Ollscoil na hÉireann, Corcaigh

National University of Ireland, Cork

Provenance investigations of Mesozoic basin infill histories in the Irish and Celtic Seas and developments in Raman spectroscopy applications for Earth Science research

Thesis presented by

Odhrán McCarthy BSc (Hons)

0000-0002-6940-1035

for the degree of

Doctor of Philosophy

University College Cork

Geology, School of Biological, Earth and Environmental Sciences

Head of School: Prof. Andrew J. Wheeler

Supervisor: Dr Patrick A. Meere

2021

Table of Contents

List of Figures

List of Abbreviations and Symbols

°C	degrees Celsius
AB	After Baseline Subtraction
ALK	alkali-rich igneous rocks
Ar-Ar	Argon-Argon
ASI	aluminium saturation index
BB	Before Baseline Subtraction
c.	circa
CL	Cathode Luminescence
CM	Cornubian Massif
cm	centimetre
cm^{-1}	Reciprocal centimetre or wavenumber
DEM	Digital elevation model
DG	Donegal Granite
DPSS	Diode-pumped solid state
EDS	Electron Dispersive Spectroscopy
FB	Fastnet Basin
FWHM	peak full width at half maxim
Ga	"billion years ago"
GIS	Geographical Information System
GS	Goban Spur Basin
HM	partial-melts/leucosomes/high-grade metamorphic
HMA	Heavy Mineral Abundance
IM	mafic I-type granitoids and mafic igneous rocks
KDE	Kernel Density Estimate
km	kilometre
LA-ICP-MS	Laser Ablation Inductively Coupled Plasma Mass Spectroscopy
LBH	London-Barbrant High
LM	(In reference to a location) Leinster Massif
LM	(In reference to apatite) low-medium grade metamorphic and metasomatic
m	meter
Ma	Mega annum
MB	Munster Basin
MCT	Monian Composite Terrane
MDS	Multi-Dimensional Scaling
n	Number of grains analysed
NCSB	North Celtic Sea Basin
nm	nanometre
ORS	Old Red Sandstone
PB	Porcupine Bank
PC	Principal Component
PCA	Principal Component Analysis
PF	peak frequency
PH	Porcupine High
pH	potential of hydrogen
PI	peak intensity
QGIS	Open-source Geographical Information System

REE	Rare Earth Elements
RSA	Raman Spectroscopy Analysis
S	S-type granitoids
SB	Slyne Basin
SCSB	South Celtic Sea Basin
SEM	Scanning Electron Microscope
SGCB	Saint George's Channel Basin
SM	Scottish Massif
SVM	Support Vector Machine
UM	Ultramafic Rocks
U-Pb	Uranium-Lead
WB	Wessex Basin
WM	Welsh Massif
µm	microns

Declaration

This is to certify that the work I am submitting is my own and has not been submitted for another degree, either at University College Cork or elsewhere. All external references and sources are clearly acknowledged and identified within the contents. I have read and understood the regulations of University College Cork concerning plagiarism.

Signed . . . .

Odhrán McCarthy
Author

Acknowledgements

"Believe you can, and you are halfway there" Theodore Roosevelt (1905). Over the course of four years I am privileged to have received support, encouragement, advice, critique, time and most importantly a good kick up the arse when I needed it from my family, friends and colleagues. In this section I will attempt to acknowledge the many personal and professional supports I have received during my time in UCC. One of these people is Dr Pat Meere. I have had the privilege of learning from Pat for over 8 years and I look forward to working together in the future. Your open-door policy, discussions, corrections, advice and support have made this project one of the most enjoyable of my life. I cannot begin to thank you enough for giving me the opportunity to work on this project and for guiding me through these many years. No matter what was going on in the background, I always felt welcome, heard and encouraged to pursue my goals after leaving your humble office. Thank you, Pat.

To Dr Brenton Fairey, thank you for your help throughout my project. Your passion for research is infectious and I think I got the bug! Your advice and generous contributions to this work were very welcome and kept me motivated and enthused. You were always there to pop a question off or just to show you something cool I was working on, thank you! I would also like to thank Prof David Chew for his continued support and advice in sample preparation, analysis, processing and interpreting data over the last four years. I learned a great deal from you about writing in particular, and I can not thank you enough for giving me so much of your valuable time. Your honest and direct approach to critiquing my work was greatly appreciated and undoubtedly enhanced the quality of this body of research. I would also like to acknowledge the help I received from Dave's fantastic group, past and present, Dr Chris Mark, Dr Gary O'Sullivan and Remi Rateau. I want to specially thank Foteini Drakau for her help in getting my apatite samples analysed during the COVID-19 crisis and keeping me calm and light-hearted during my first session of analysis after my laptop discombobulated.

A great and heartfelt thank you is extended to Prof. Andrew Wheeler, Dr Ed Jarvis, Dr John Reavy, Dr Kate Kesieva, Dr Richard Unitt and rest of the Geology faculty. You have all offered advice, facilitated analysis or just made me feel at home in UCC over the last 4-8 years. Thank you for your teachings and for creating such a wonderful atmosphere in the department. I want to extend my thanks to the wonderful administration and support staff in the school of

Biological Earth and Environmental Sciences of UCC. To Mary McSweeney, Christine Dennehy and Elaine Kelly, thank you for all your support in arranging payments, meetings, timetables, documents and stopping me from getting into a fist fight with the Finance department on more than one occasion.

A group of people that have both helped and hindered my progress are my fellow postgraduates in UCC. Ger, Luke, Jurgen, Ruaihri, Daniel, Dr Valentina Rossi, Tiffany, Darren, John, Aisling, Kate, and Dr Mohit Tunwal, thanks for all the lunches, advice and support you provided over the last few years. There is no point doing something unless you can enjoy it, and you guys made everyday a little bit more fun.

For two months of 2018, I was privileged to have been welcomed to the Department of Earth and Environmental Sciences in the University of Milano-Biccoca by Dr Sergio Andò, Prof. Eduardo Garzanti and Dr Alberto Resentini. Thank you for your generosity in sharing your lab space, teaching me about basin tectonics, sedimentary petrology and provenance research. You made Sarah and I feel so welcome. It would be difficult to find a more generous and open group of researchers who have such passion for their research, coffee and students.

To all at iCRAG and the Hydrocarbons Spoke, thank you. iCRAG is such a unique and wonderful group of researchers which has fundamentally changed geoscience research in Ireland. I want to thank Prof. John Walsh, Prof. Chriss Bean, Prof. Murray Hitzman and most importantly Dr Shane Tyrell for your work in making iCRAG and our research group what it is. I would also like to acknowledge the support and help from my fellow PhD students in iCRAG, Dr Jess Franklin, Dr Aoife Blowick, Siobhan Burke, Remi Rateau, Dr Gary O'Sullivian, Dr Pablo Rodriguez Salgado, Martin Naughton and all the others. A special mention goes to Siobhan Burke, my partner in crime for 6 years. You were like an older sister to me and I cannot thank you enough for your support, generosity and friendship. I want to thank the team in iCRAG including Dr Aoife Brady, Dr Jennifer Craig, Dr Fergus McAuliffe, Francis Manu, Elspeth Wallace and Luo Luo for their administration, financial and logistical support.

To the Pafurians of Bishopstown: Cian, Aoife, Aude and Alan, thank you for putting up with my moaning and hosting the odd party to help blow off some steam. I have also received

many words of encouragement, dinners, couches/beds to sleep on and lifts around the country by many of my friends. Specifically I want to acknowledge Kate, Mark, Luise, Brian, Thomas, Seán, Johnny, Andrew, Barry and Emily. Your friendship and support over the last four years helped to make some of these some of the most enjoyable of my life. I also want to thank my crack pot team of proof-readers, Dr Tadhg Moore, Alan, Ruaihri, Ger and Sarah. Thanks for the long nights and giving up your time to help get me over the line in the end.

To my family, I want to acknowledge all the dinners, lifts, discussions, project management sessions and proof-reading you helped with. There is a large and growing debt owed to my parents Eileen and William. Thank you for always encouraging me to question and pursue despite life's setbacks. You both gave me a stable foundation on which to build my life on, to manage my losses and acknowledge my successes. Thank you. Gwen, Gerry, Maeve and Guy, thank you for letting us live in your holiday home while I wrote up my thesis and the world shuddered because of the pandemic. You all, along with Liz, have been a huge support and a second family for me.

Above all others, I need to acknowledge the selfless and unrelenting support from my wonderful partner Sarah over the last four years. Thank you for putting our travels on hold and for the hundreds of hours of discussion, revision, proofing, correcting, teaching, advising, cooking, cleaning, tea and coffee making on top of all the lifts and financial support. I cannot describe my gratitude in this short paragraph, but I will be forever grateful to have had your support throughout this period of my life.

Acknowledgment of Funding

O.McC, P.M and D.C acknowledge the financial support of Science Foundation Ireland, Grant/Award Number: 13/RC/2092; European Regional Development Fund; PIPCO RSG. This publication uses data and survey results acquired during a project undertaken on behalf of the Irish Shelf Petroleum Studies Group (ISPSG) of the Irish Petroleum Infrastructure Programme (PIP) Group 4 (project code IS 12/05 UCC). The ISPSG comprises Atlantic Petroleum (Ireland) Ltd, Cairn Energy Plc, Chrysaor E&P Ireland Ltd, Chevron North Sea Limited, ENI Ireland BV, Europa Oil & Gas, ExxonMobil E&P Ireland (Offshore) Ltd, Husky Energy, Kosmos Energy LLC, Maersk Oil North Sea UK Ltd, Petroleum Affairs Division of the Department of Communications, Energy and Natural Resources, Providence Resources Plc, Repsol Exploración SA, San Leon Energy PLC, Serica Energy PLC, Shell E&P Ireland Ltd, Sosina Exploration Ltd, Tullow Oil Plc and Woodside Energy (Ireland) Pty Ltd.

Abstract

Part 1: Sedimentary provenance analysis is a powerful tool for interrogating the history of sedimentary basins. In this study, Quantitative provenance analysis (QPA) is applied to interpret the sedimentary infill of North Celtic Sea Basin, Saint George's Channel Basin, Fastnet Basin and Goban Spur Basin offshore of Irelands southeast coast. This research was conducted to further develop understanding of the sediment routing and infill in these basins and therefor provide insights to basin connectivity. Basin structure are important for further economic developments in carbon storage, hydrocarbon exploration and mapping of reservoir fairways in the Irish and Celtic Sea. Prior to this study, all published hypothesis addressing the provenance of Mesozoic sediments in the Irish and Celtic Sea basins have considered sediment sourcing and routing from the post Caledonian cover sequences and basement rocks of the Irish and Welsh Massifs. Multiple environmental and tectonic events took place during the Mesozoic in the Irish and Celtic sea region. However the impact of these events has not been accounted for. To test these hypotheses as well as the impact of environmental and tectonic change on the provenance of basin infill, two studies were conducted on; i) Middle Jurassic to Upper Cretaceous successions and, ii) Triassic to Lower Jurassic successions in these basins. A multi-proxy investigation of detrital zircon, white mica and apatite geochronology along with heavy mineral analysis and petrographic methods were chosen. Results from these find evidence that marine transgression-regression cycles and tectonism exhibited a first-order control on sediment routing and provenance throughout the Mesozoic. Significantly, these findings show that sediment routing and sourcing was not principally derived from the Irish and Welsh Massifs. Four distinct provenance switches are detected throughout the 185 million years of basin evolution. Contrary to previous hypothesis, the Irish and Welsh Massifs are only identified as the primary source during the Late Jurassic and Early Cretaceous. Findings of these two bodies of research have fundamentally changed our understanding of basin infill and sedimentary provenance in the Irish and Celtic Sea basins during the Mesozoic Era. More broadly, this study can be used as a case study for the impacts of environmental or tectonic activity on sedimentary provenance.

Part 2: Raman spectroscopy is a developing tool in sedimentary provenance analysis as well as the geosciences more broadly. Developing the accessibility and interoperability of this tool and derived data is of benefit to the broader geo-science community, particularly within petrographic

studies. Its appeal as a multi-faceted analytical tool is sometimes overlooked due to financial, computational or access barriers. Data processing and visualisation of large Raman data sets or mapped data sets can be an additional challenge as standard freeware has a limited capacity to processes these files or lacks a rasterization capability (e.g., R, spectralgryph and crystal sleuth). To overcome this challenge and to capitalise on recent developments in Raman spectroscopy, the fourth chapter in this thesis presents an in-house, automated Raman peak analysis and rasterization freeware called "Ramaster". To demonstrate the potential applications for this program, two case studies were chosen including; i) Raman maps of detrital zircon grains and, ii) characterisation of phosphatised dermal tissues from 40 Ma anuran (frog) skin. Ramaster significantly saved processing time and produced detailed maps of zircon growth structures and phosphatised anuran fossil tissue structures. This work has excellent potential for future development and offers a simple but effective solution for the rasterisation of mapped Raman data sets.

Part 3: Constraining the chronology of tectonic events is a ubiquitous challenge for geoscience researchers. Investigatory tools available for tectonic research are typically qualitative and lack workable data sets (e.g., Cathodoluminescence imaging) or are destructive to the sample material (e.g., LA-ICP-MS). Today there exists a broad range mineral characterization and discrimination techniques for which Raman spectroscopy is a developing tool. This study aims to demonstrate the application of Raman spectroscopy in differentiating a ubiquitous mineral throughout the earths lithosphere (quartz), which has applications in provenance research as well as other economic, social and scientific fields. In the fifth chapter of this thesis, Raman and Fluorescence spectroscopy are applied to differentiate multiple generations of vein-hosted quartz. We find that Raman spectroscopy analysis can be used to differentiate different multiple generations of quartz as well as providing insights to the origin of hydrothermal fluids, tectonic deformation histories. The differentiation of alpha quartz has not been demonstrated in an in-situ sample to date and represents a significant development in the field of mineral discrimination techniques.

Chapter 1: *Introduction*

The project originated as part of the Irish Centre for Research in Applied Geosciences (iCRAG) hydrocarbons spoke and was proposed to better constrain sediment routing pathways as well as basin and reservoir connectivity in the Irish and Celtic Sea Basins. The project focused on furthering previous research on sedimentary routing pathways and testing existing hypothesis on sediment provenance. Although the aim of this work was provenance research, the project naturally produced a number methodological developments in Raman spectroscopy in both computational processing and analysis methodologies. Due to the broad appeal of Raman spectroscopy in provenance research as well as more broadly in the geoscience community, these developments were included as part of the project.

The research presented in this PhD consists of two distinct parts comprising four main chapters. Chapter 1 of provides a broad introduction and background to each part, followed by their respective aims and objectives. Part 1, the primary focus of this research project, addresses the provenance of Mesozoic sediments in the Irish and Celtic Sea basins (Fig. 1). It is presented in Chapters 2 and 3. Part 2 is presented in Chapter 4 and Chapter 5. Chapter 4 introduces a new Raman spectroscopy software called “Ramaster”, which was developed as a side project during the course of the work outlined in Chapters 2 and 3. Ramaster is an automated peak analysis tool developed for analysing and rasterizing mapped Raman data sets. The tool’s potential applications in provenance and more broadly in geoscience research are explored in Chapter 4. Also presented in Part 2 of this thesis is Chapter 5, which is a further development on the applications of Raman spectroscopy within tectonic studies, specifically using Raman and fluorescence spectroscopy of quartz to better constrain tectonic history by characterizing differences in molecule composition and vibrational state. The conclusions of the thesis are summarised in Chapter 6.

The following sections offer a background introduction and rationale for each area of research included in this thesis.

1.1. Part 1: Provenance Research of the Irish and Celtic Sea Basins

1.1.1. Basic Concepts

Quantitative provenance analysis in geological research is "aimed at reconstructing the parent-rock assemblages of sediments and the climatic-physiographic conditions under which sediments formed" (Weltje *et al.*, 2004). Provenance research incorporates a broad range of topics within sedimentary petrology and aims to understand where sediments are generated and from where they are transported. This is important as sedimentary provenance can be used to understand how environmental change and tectonism has influenced topography, sediment drainage and deposition. It is also critical to consider post-depositional histories, and how sedimentary successions reached their current lithostratigraphic configuration, as the present-day assemblage of minerals in a sediment or rock is the product of its geologic history. Quantitativeprovenance analysis can provide evidence of source regions which no longer exist today. Previous sources may have been exhumed and eroded or subducted leaving only remnant particles within the lithosphere as evidence of their existence. These points are particularly true for the Mesozoic sedimentary basins of the Irish and Celtic Seas where numerous environmental and tectonic events have influenced the provenance of sedimentary infill (Naylor *et al.*, 2011).

Within an economic context, QPA has applications in hydrocarbon exploration for assessing sediment-dispersal patterns, unroofing of source areas and understanding the impact of diagenesis on reservoir productivity (Smyth *et al.*, 2014). It also has broader economic implications in the construction industry as part of quality assurance measures (Koglin *et al.*, 2010), and for hydrodynamic modelling (Garzanti *et al.*, 2009). Moreover, QPA methodologies can identify important factors in aggregate selection and tracing. Provenance analysis also has applications within criminal law and homicide fields as a forensic investigatory tool (Fitzpatrick *et al.*, 2019). The field of QPA has versatile application and broad appeal for several industries and societal demands.

Considering the large number of influencing factors on sedimentary provenance, a multi-proxy provenance approach using complimentary analytical methodologies is typically employed in modern provenance research (Caracciolo *et al.*, 2019; Franklin *et al.*, 2020; Nauton-Fourteu *et al.*, 2020). Analytical approaches may include bulk sediment characterisation techniques like heavy mineral analysis (Mange and Wright 2007), optical petrography (Dickinson, 1970; Pettijohn *et al.*, 2012) and geochemistry (Ramkumar, 2015). Additionally, single grain techniques like U-Pb zircon (Chew *et al.*, 2019a), rutile and titanite (McAteer *et al.*, 2010a) geochronology as well as Ar-Ar white mica (Li *et al.*, 2007) and Pb-isotope fingerprinting (Tyrrell *et al.*, 2012) can provide novel insights into sedimentary provenance histories.

Provenance tools offer a unique and exceptional insight into environmental and tectonic histories and more recent developments in geochronology methodologies have greatly enhanced the speed and volume of material that can be analysed (Zimmermann *et al.*, 2018; Chew *et al.*, 2019a). In addition, developments in Raman spectroscopy (Resentini *et al.*, 2020) and apatite trace element analysis (O'Sullivan *et al.*, 2020) have also been significant recent developments. A significant challenge when working offshore is collecting sufficient sample material for analysis. Offshore samples are expensive to collect and in particular offshore samples require significant fiscal and logistical efforts to obtain. These samples are precious and every effort to make full utility of this material was made. Provenance analysis has an excellent range of analysis techniques which can provide novel insights to earth history from a few hundred grains of sand. This thesis is a good example of how to make the most use of limited sample material. However it should be noted that working with such a small amount of precious material provides a limited insight with numerous inherited and natural biases.

1.1.2. Provenance Research in the Irish and Celtic Sea and Analytical Approach

The development of sedimentary basins in the Celtic and Irish Seas began with Carboniferous-Permian rifting of the palaeocontinent Pangea, which resulted in the opening of the Atlantic ocean (Naylor *et al.*, 1982; Allen *et al.*, 2002). The basins consist of up to 9 km of Mesozoic

sedimentary infill overlying a Permian and Carboniferous basement. From the beginning of the Mesozoic, Ireland along with the rest of the British Iles had drifted from a latitude of 30° (Petrie *et al.*, 1989; Hesselbo, 2020; Vickers *et al.*, 2020), to as far north as 50° by the beginning of the Cenozoic Era. Throughout the Mesozoic Era, the North Celtic Sea Basin (NCSB), Saint Georges Channel Basin (SGCB), Fastnet Basin, Goban Spur Basin and surrounding basins of the Irish and Celtic Sea area (Fig. 1) underwent multiple marine regression-transgression cycles (Murphy *et al.*, 1991) which were intimately associated with local and regional tectonic events (Murdoch *et al.*, 1995; Rodríguez-Salgado *et al.*, 2019). This continental drifting and the active rifting of the Atlantic ocean during this period was synchronous with a transition from arid, hot and humid conditions during the Triassic (Hounslow *et al.*, 2006) to a more temperate oceanic climate by the Paleocene (Naylor *et al.*, 2011). For a detailed breakdown of the Cretaceous – Jurassic and Jurassic to Triassic lithostratigraphy of these basins see Sections 2.2 and 3.2.

For more than 185 million years of basin development, dynamic environmental change and tectonism exhibited a strong control on the infill of these basins but also the present-day configuration of their lithostratigraphy. In some basins, significant unconformities exist as a result of Middle Jurassic (Naylor *et al.*, 2011) or Late Cretaceous tectonism (Rodríguez-Salgado *et al.*, 2019) that prohibits cross basin comparison. This makes it difficult to build a comprehensive regional picture of sediment sourcing (e.g., Middle Jurassic sediments of the Fastnet Basin). Furthermore, large sections of strata have been exhumed and eroded across multiple basins (e.g., Cretaceous sediments in the SGCB, NCSB and Fastnet Basin) as a result of regional tectonic events (Cogné *et al.*, 2016). In addition, a lack of economic interest in Triassic sediments and basement sequences has resulted in a relative scarcity of data from this period, making it difficult to investigate the early development of these basins. Despite the complex history, to date the collective agreement on the provenance of sedimentary basin infill has been limited to the Irish and Welsh Massifs implying that these two source regions were principally shedding into the opening basins (Robinson *et al.*, 1981; Ainsworth *et al.*, 1985; Millson, 1987; Petrie *et al.*, 1989; Caston, 1995; Kessler *et al.*, 1995; Tyrrell, 2005; Naylor *et al.*, 2011). These hypotheses were constructed using petrographic, paleocurrent, seismic and wireline log data. These methods provided a limited provenance insight as they cannot link a sediment with its source beyond qualitative descriptions of sediment

composition and source descriptions. Qualitative provenance techniques which fingerprint grains of sand using age dating techniques and chemical classifications of source rocks and basin infill is the optimum way of providing a more definitive insight to sedimentary provenance (Caracciolo *et al.*, 2019). As environmental and tectonic conditions continually changed throughout the Mesozoic Era in the study area, it seems highly unlikely that only two principal source areas infilled these basins. One of the primary aims of this work is to test if these early ideas on the provenance of southern Irish Mesozoic basin infill are correct, or if sediment infill was affected by the environmental and tectonic events which took place throughout the Mesozoic Era.

To consider recent developments in QPA, and to address some of the long-standing provenance questions in the study area, sample preparation and analysis methodologies were chosen to enable multi-proxy analysis of the limited sample material available. Despite the considerable improvements in QPA research methodologies in recent years, it remains crucially important to consider natural and introduced bias when sampling, preparing and analyzing material (Chew et al., 2020). Samples were separated into the 63-125 µm and 125-250 µm grain size windows to allow comparison of minerals with a similar size following the methods of Mange et al. (1992) and Morton et al. (1994). Unfortunately, the coarser fractions typically yielded too few heavy minerals (less than 200 grains) to be considered representative of the population and were therefore excluded from the reported results in this thesis. A wider grain size window (e.g., 5-500 µm) as preferred by Garzanti et al. (2009) and Andò (2020) was not chosen as the provenance of grains with different density, size and shape are more prone to the natural bias of grain texture and hydraulic sorting during transport and deposition of sediments. This was of particular concern as this study focuses on lithified sediments where the hydrodynamic setting, source areas and environment are only partially understood. The debate as to the selection of the correct grain size window within the field of heavy mineral analysis is a challenging one, and requires a balance between accuracy, sample preparation and analysis time. Each method has its own inherent bias and where possible, these biases should be taken into consideration during the interpretation of subsequent data sets. The selection of the narrow 63-125 µm grain size window provides a limited insight to sediment provenance as it excludes sources which produce naturally larger grains (E.g. tourmaline).

Zircon U-Pb geochronology analysis was chosen to capture input and recycling from igneous and significant lithostratigraphic domains of ancient paleocontinents like Laurentia and Avalonia (Fig. 1). Zircon has a high a closure temperature of c. 900 °C (Cherniak *et al.*, 2001), and is resistant to the destructive effects of weathering and erosion making it a strong provenance indicator. However, zircon U-Pb geochronology often underrepresents metamorphic and sedimentary sources as zircon fertility is highly variable in source lithologies (Malusà *et al.*, 2016). For a more rounded characterisation of source rocks, apatite U-Pb geochronology and trace element analysis (O'Sullivan *et al.*, 2020) was chosen to capture input from younger volcanic and metamorphic sources as it has a lower closure temperature of between c. 570–375 °C (Thomson *et al.*, 2012; Kirkland *et al.*, 2018). Apatite is common in metamorphic, igneous, and sedimentary rocks and is robust during transport and deposition. However it is susceptible to chemical weathering in humid conditions (Morton *et al.*, 1999).

Recent developments in apatite analysis have demonstrated how trace elements can be used to uniquely fingerprint source rocks offering a more specific sedimentary provenance than traditional U-Pb geochronology of detrital zircon or TiO_2 polymorphs (O'Sullivan *et al.*, 2020). White mica was also chosen as it is typical of igneous, metamorphic, and sedimentary sources and has a closure temperature of 445–400 °C (Harrison *et al.*, 2009), is a good indicator of metapelite, felsic igneous and hydrothermal sources (Mange *et al.*, 2007), and is often considered a first order source indicator as it is liable to mechanical disaggregation in aeolian settings, although is more durable in a subaqueous setting (Anderson *et al.*, 2017). Heavy mineral analysis was conducted to offer a more rounded insight into sedimentary provenance, and diagenetic alteration than single grain techniques. QEMSCAN analysis was chosen to characterize the heavy mineral assemblage of each sample as the 10 µm chemical maps provided the best insight to chemistry and morphology of all grains in the sample and allowed other geochronology techniques to be applied to the sample material. However it is naturally biased as it cannot differentiate polymorphs. Raman classification of heavy minerals assemblages was not chosen as the primary heavy mineral classifier as TiO_2 could not be optically or chemically differentiated, and samples would need to have been prepared differently limiting the ability for multiple analysis on a single grain. Heavy minerals analysis can better represent source regions which have low single grain fertility or sediments which

have undergone extensive weathering (e.g., zircon, apatite or white mica). Additional techniques like K-feldspar Pb fingerprinting and TiO_2 U-Pb dating were planned for this project, however due to the Coronavirus pandemic, these analyses could not be undertaken.

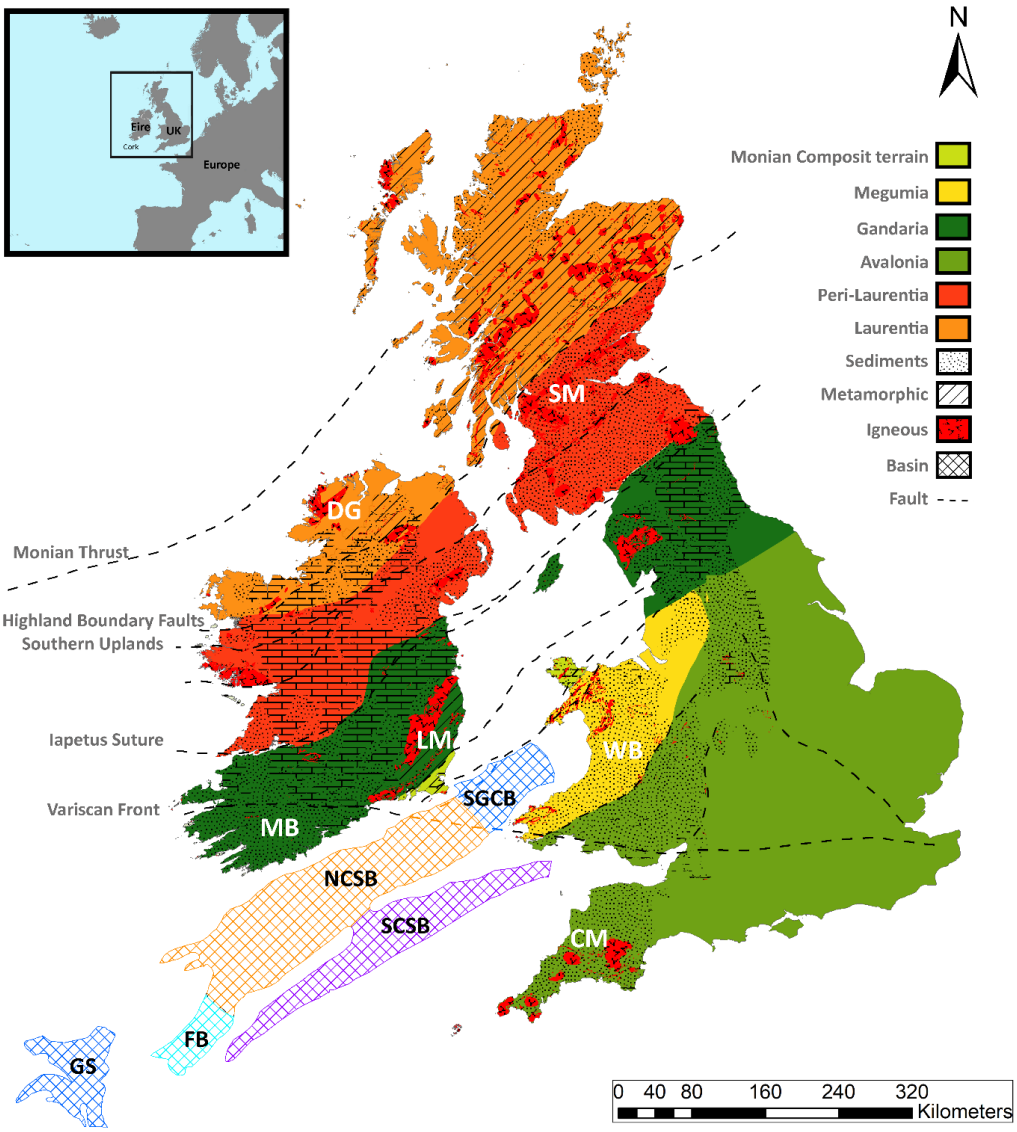

Fig. 1. *Study area with superimposed tectono-sedimentary affiliations following Waldron et al. (2019b). A broad characterisation of sediment source types which were possible available during the Mesozoic is provided for a provenance perspective. NCSB, North Celtic Sea Basin; SGCB, Saint George's Channel Basin; SCSB, South Celtic Sea Basin; FB, Fastnet Basin; GS, Goban Spur Basin.*

1.1.3. Source Regions

To provide context to the challenges associated with interpreting the provenance of Mesozoic basin infill in the Irish and Celtic Seas, a brief introduction to the tectonostratigraphic source domains, as defined by Hibbard *et al.* (2007), is offered. Source region are described in greater detail within Chapters 2 and 3 of the thesis.

Ireland and Britain are composed of a series of palaeocontinental assemblages including Laurentian (and Peri-Laurentian) domains north of the Iapetus Suture (Fig. 1) and Peri-Gondwanan domains to the south (Pollock *et al.*, 2012). Laurentian and Peri-Laurentian domains, and their cover sequences, typically comprise of U-Pb zircon populations of 2.9-0.9 Ga, as well as c. 400 Ma populations (Chew *et al.*, 2014b; McConnell *et al.*, 2016). The Peri-Gondwanan domains include all terranes that were proximal to the northern margin of western Gondwana during the Early Neoproterozoic until the break-up of Gondwana in the Early Paleozoic (Van der Voo, 1988; Nance *et al.*, 2008). These domains include Ganderia, Megumia, the Moinian Composite Terrane, Avalonia and Cadomia (Waldron *et al.*, 2019a). They are an abundant source of 690–525 Ma U-Pb zircon populations (Pothier *et al.*, 2015). Laurentian and Peri-Gondwanan sources can be readily differentiated using their respective detrital zircon populations. Conversely, it is extremely difficult to differentiate between the different Peri-Gondwanan domains using U-Pb zircon geochronology alone, as many of these sources include a dominant Peri-Gondwanan zircon population, as well as Acadian, Caledonian and Variscan zircon populations (Fairey *et al.*, 2018).

Ireland is blanketed by post-Caledonian cover sequences. In the context of this research the most important of these are the thick Carboniferous Limestone successions of central Ireland and the Upper Devonian successions of the Munster Basin, the Dingle Basin and South Munster Basin. These source regions and basins have a distinct fertility bias as heavy minerals which may be liable to chemical or physical weathering may not have been recorded in recycled sediments which infilled the Irish and Celtic Sea Basins during the Mesozoic. The Munster Basin and South Munster Basin presents a challenge to provenance interpretations of the region. It is the most proximal to the study area (see Fig. 1), and contains a dominant

Laurentian population (Fairey, 2017) making it difficult to differentiate from other Laurentian sources. For this reason, detrital U-Pb apatite and Ar-Ar white mica geochronology were chosen along with heavy mineral characterization of samples to differentiate between igneous, sedimentary and metamorphic sources. Additionally the Carboniferous limestones which blanked much of Ireland today, must have influenced sediment routing and limited the exposure of underlying successions to erosion during the Mesozoic. Unfortunately it is not possible to reconstruct the cover of these sequences throughout the Mesozoic. The Dingle Basin (Fairey *et al.*, 2018) and Clare Basin (Nauton-Fourteu *et al.*, 2020) which lies along the West coast of Ireland, are also potential source regions which contain a mixed Peri-Gondwanan and Laurentian detrital zircon signature. There has been very limited work to characterize the heavy mineral composition of these different source's excluding the Clare Basin.

1.1.4. Aims and Objectives

The primary aims of this study of the Mesozoic basin infill histories in the Irish and Celtic Seas are:

- **1.1.A.** to test if Mesozoic basin infill was primarily sourced from the Upper Devonian Munster Basin, South Munster Basin, Leinster Massif and Welsh Massif;
- **1.1.B.** to profile the influence of transgression and regression cycles on sedimentary provenance throughout the Mesozoic Era in these basins;
- **1.1.C.** to profile the influence of tectonic events on sedimentary provenance and recycling throughout the Mesozoic Era in these basins;
- **1.1.D.** to constrain the temporal evolution of sedimentary provenance in the region.

1.2. Part 2: Developments in Raman Spectroscopy methodologies and applications

1.2.1. "Ramaster" Software application for Raman imaging and chemical characterisation; Automated peak analysis and imaging of Raman data sets

1.2.1.1. Basic Concepts

Raman spectroscopy has become a popular analytical tool in geoscience research since the discovery of the Raman effect in 1928 (Raman, 1928). Raman analysis allows researchers to identify organic (Norell *et al.*, 2020) and inorganic materials (Andò *et al.*, 2014) including mineral polymorphs. It allows for the measurement of molecular bond variance induced by pressure (Chandrabhas *et al.*, 1992) and temperature making it useful in geobarometry and geothermometry (Beyssac *et al.*, 2002). In more recent years, Raman spectroscopy has become increasingly popular among provenance researchers for automated mineral identification (Lünsdorf *et al.*, 2019), geochronology (Chew *et al.*, 2017; Anderson *et al.*, 2020), combined Raman fingerprinting and geochronology (Resentini *et al.*, 2020). Raman spectroscopy has a broader appeal in the science (Smith *et al.*, 2019a) community and developments in this sector are beneficial all.

An important consideration in any research project is the choice of sample preparation and analysis methodologies. Ideally, one method could provide insights to numerous facets of a mineral's chemistry and structure, while being cost effective and simple. When correctly applied, Raman spectroscopy offers this multi-faceted insight into material science which is demonstrated by its inclusion on the ExoMars Rover mission (Rull *et al.*, 2017). However, the cost associated with modern Raman technology means that access is often limited while older systems lack modern mapping and analytical capabilities. Moreover, processing and interpreting spot and mapped Raman data sets can be time-consuming with required processing software often being costly, inflexible, and limited in accessibility. Furthermore, there is a distinct lack of software available for rasterising these data sets.

Chapter 4 of this thesis presents a simplification of the data processing, analysis and interpretation processes involved in Raman spectroscopy by introducing a Python 2.7 fully-stacked freeware called “Ramaster''. Ramaster automates peak analysis of mapped Raman data sets by using a Fourier analysis peak fitting algorithm on every spectrum, generating a georeferenced map of the results. This tool has broad appeal as single peak analysis is a commonly applied analysis technique and can offer insights to bond variance within a sample allowing the user to differentiate between polymorphs, mineral phases and identify alteration effects.

The first case study uses Raman maps of 160 zircon grains to generate zircon peak intensity maps which offer insights to mineralisation chronology, thermal annealing and metamictisation processes which are used for geochronology investigations in Chapters 2 and 3 (Fig. 2). A conventional challenge in working with heavy mineral mounts is the cathode luminescence (CL) imaging of detrital zircon grains prior to U-Pb geochronology as each grain is scattered throughout the sample. CL imaging of each grain individually is time consuming and may not be possible in circumstances where machine time is limited or costly. Recent developments in Raman mapping and analysis of zircon offer a novel solution. Raman maps that are comparable to CL images have been produced and provide insights into mineral structure and chemistry allowing for the optimal selection of ablation spots (Chew *et al.*, 2017; Anderson *et al.*, 2020). Raman mapping of detrital zircon grains can therefore serve a similar purpose to CL images in geochronological and provenance investigations. The second case study takes Raman data sets from the dermal tissue of a 40-million-year-old-anuran (frog) which has been preserved through phosphatisation in a karst landscape. The full width at half maximum, peak intensity and peak frequency Raman maps revealed the exceptional preservation of the anuran’s epidermis and glands structures through variations in apatite and D- and G-band carbon molecules in the dermal tissue. Raman characterisation of molecule structure and order is a growing field in geoscience and Ramaster offers an accessible, time-saving and flexible alternative to available free and commercial software.

1.2.2. Aims and Objectives

In Chapter 4 of this thesis applications for Ramaster in i) provenance research and ii) palaeontology case studies are demonstrated. This work aims to:

1.2.A. simplify processing of mapped Raman data sets for provenance applications;

1.2.B. reduce processing time;

1.2.C. demonstrate the application of the software in two separate fields of research;

1.2.D. make Raman science more accessible by offering a free, automated processing solution.

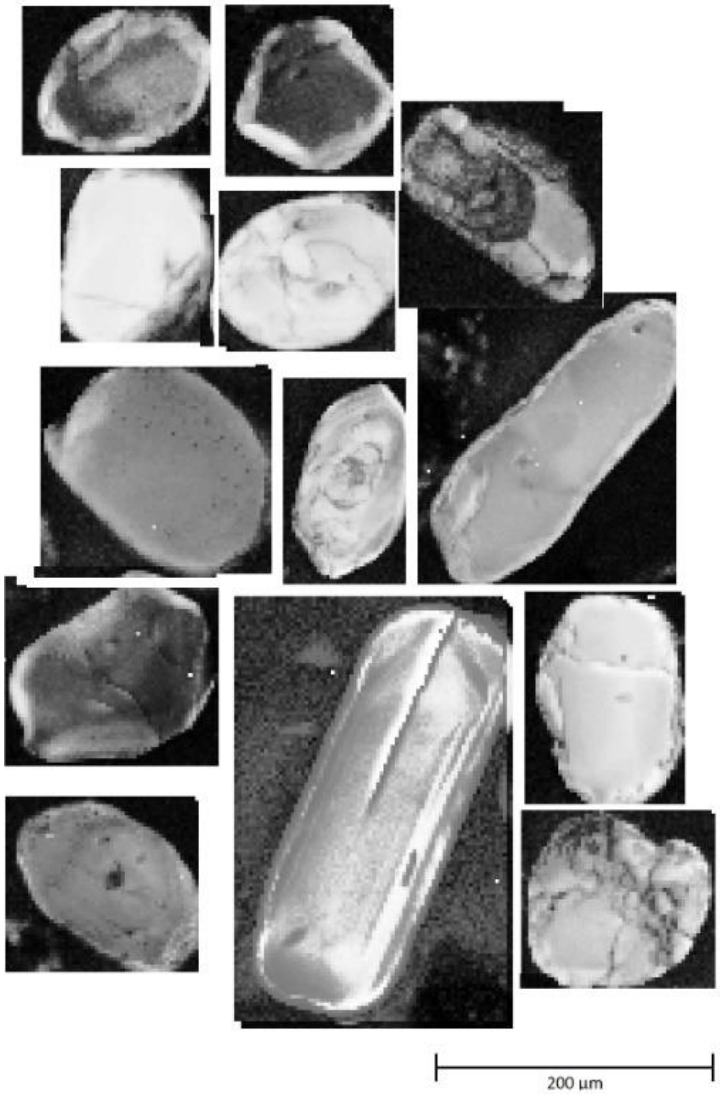

Fig. 2. *Raman maps of detrital zircon grains generated with Ramaster.*

1.2.3. Raman Spectroscopy of Vein-hosted Alpha Quartz

1.2.3.1. Basic Concepts

Raman spectroscopy analysis has the capacity to differentiate minerals based on their molecular composition and state of molecular order. This has already been demonstrated in a lab setting with quartz (Shapiro *et al.*, 1967; Etchepare *et al.*, 1974) and field setting with zircon (Nasdala *et al.*, 1995; Nasdala *et al.*, 1998). In tectonic studies, optical and geochemical techniques are typically used to differentiate the order of vein formation in a fractured rock to elucidate tectonic or deformation histories. Veins can often fracture multiple times and can become infilled with different generations of minerals such as quartz. If these generations could be reliably differentiated, one can determine the order in which tectonic events occurred. With some further development, Raman spectroscopy could provide an excellent approach to accomplishing this task. These insights can help a provenance researcher understand the deformation history of a source region, as well as helping to test thermobarometery and geothermometry data from minerals like apatite (Cogné *et al.*, 2016) and mica (Hames *et al.*, 1997). Additionally, this Raman differentiation of multiple crystallization phases of a single phase, could be used to differentiate diagenetic overgrowths and alteration patterns within sediment petrography.

Raman analysis has been shown to differentiate alpha quartz in a lab setting by measuring the different vibrational modes in each generation of quartz, namely these include the 206 and 464 cm–1 A1 modes (Shapiro *et al.*, 1967; Schmidt *et al.*, 2000). This application of Raman spectroscopy has not yet been applied in a field setting to interpret the deformation sequence of a vein's opening history. Chapter 5 of this thesis presents research which differentiates generations of vein-hosted quartz in the historic Allihies Copper Mine of the Beara Peninsula in West Cork, Ireland. This is the first Raman spectroscopy differentiation of vein-hosted alpha quartz by mapping material-fluorescence and Si-O bond variations in a real-world scenario. Findings of this study have direct application in both academia and industry as quartz is an abundant mineral that can record the deformation history of Earth's upper crust.

As the entire spectrum was important in these processes, Ramaster (see

Section 1.2) was not utilised in this study. Instead a multivariate spectral analysis approach was chosen using principal component analysis to allow for multiple bond variations to be used in differentiating generations of quartz.

1.2.4. Aims and Objectives

The primary aim of this work is to demonstrate that Raman spectroscopy can be used to differentiate multiple generations of mineralisation within a vein. Analysis of two data sets compiling 917,278 Raman spectra are used to characterise Si-O bonds in the SiO_4 quartz tetrahedron. The aims of this work are to demonstrate that:

1.2.E. alpha quartz Raman modes can be used to differentiate generations of quartz mineralisation in a vein;

1.2.F. material fluorescence in Raman spectra can be used to differentiate between different generations of quartz.

1.2.G. Raman spectroscopy can be used in-situ to characterize the mineralisation history of a mineral and that this has great potential for application in provenance research

1.3. **References**

Ainsworth, N. R., Horton, N. F., & Penney, R. A. (1985). Lower Cretaceous micropalaeontology of the Fastnet Basin, offshore south-west Ireland. *Marine and Petroleum Geology, 2*(4), 341-349. doi:https://doi.org/10.1016/0264-8172(85)90029-7

Allen, P. A., Bennett, S. D., Cunningham, M. J. M., Carter, A., Gallagher, K., Lazzaretti, E., Galewsky, J., Densmore, A. L., Phillips, W. E. A., Naylor, D., & Hach, C. S. (2002). The post-Variscan thermal and denudational history of Ireland. *Geological Society, London, Special Publications, 196*(1), 371-399. doi:10.1144/gsl.sp.2002.196.01.20

Anderson, A. J., Hanchar, J. M., Hodges, K. V., & van Soest, M. C. (2020). Mapping radiation damage zoning in zircon using Raman spectroscopy: Implications for zircon chronology. *Chemical Geology, 538*, 119494. doi:https://doi.org/10.1016/j.chemgeo.2020.119494

Anderson, C. J., Struble, A., & Whitmore, J. H. (2017). Abrasion resistance of muscovite in aeolian and subaqueous transport experiments. *Aeolian Research, 24*, 33-37. doi:https://doi.org/10.1016/j.aeolia.2016.11.003

Andò, S. (2020). Gravimetric separation of heavy minerals in sediments and rocks. *Minerals, 10*(3), 273.

Andò, S., & Garzanti, E. (2014). Raman spectroscopy in heavy-mineral studies. *Geological Society, London, Special Publications, 386*(1), 395-412. doi:https://doi.org/10.1144/SP386.2

Beyssac, O., Goffé, B., Chopin, C., & Rouzaud, J. (2002). Raman spectra of carbonaceous material in metasediments: a new geothermometer. *Journal of metamorphic Geology, 20*(9), 859-871. doi: https://doi.org/10.1046/j.1525-1314.2002.00408.x

Caracciolo, L., Andò, S., Vermeesch, P., Garzanti, E., McCabe, R., Barbarano, M., Paleari, C., Rittner, M., & Pearce, T. (2019). A multidisciplinary approach for the quantitative provenance analysis of siltstone: Mesozoic Mandawa Basin, southeastern Tanzania. *Geological Society, London, Special Publications, 484*, SP484-2018-2136. doi:https://doi.org/10.1144/SP484-2018-136

Caston, V. (1995). The Helvick oil accumulation, Block 49/9, North Celtic Sea Basin. *Geological Society, London, Special Publications, 93*(1), 209-225. doi:10.1144/gsl.sp.1995.093.01.15

Chandrabhas, N., Shashikala, M., Muthu, D., Sood, A., & Rao, C. (1992). Pressure-induced orientational ordering in C60 crystals as revealed by Raman spectroscopy. *Chemical physics letters, 197*(3), 319-323. doi:https://doi.org/10.1016/0009-2614(92)85776-7

Cherniak, D., & Watson, E. (2001). Pb diffusion in zircon. *Chemical Geology, 172*(1-2), 5-24.

Chew, D., Drost, K., & Petrus, J. A. (2019). Ultrafast,> 50 Hz LA-ICP-MS Spot Analysis Applied to U–Pb Dating of Zircon and other U-Bearing Minerals. *Geostandards and Geoanalytical Research, 43*(1), 39-60. doi:https://doi.org/10.1111/ggr.12257

Chew, D., O'Sullivan, G., Caracciolo, L., Mark, C., & Tyrrell, S. (2020). Sourcing the sand: Accessory mineral fertility, analytical and other biases in detrital U-Pb provenance analysis. *Earth-Science Reviews*, 103093. doi:https://doi.org/10.1016/j.earscirev.2020.103093

Chew, D. M., Petrus, J. A., Kenny, G. G., & McEvoy, N. (2017). Rapid high-resolution U–Pb LA-Q-ICPMS age mapping of zircon. *Journal of Analytical Atomic Spectrometry, 32*(2), 262-276. doi:https://doi.org/10.1039/C6JA00404K

Chew, D. M., & Strachan, R. A. (2014). The Laurentian Caledonides of Scotland and Ireland. *Geological Society, London, Special Publications, 390*(1), 45-91. doi:https://doi.org/10.1144/SP390.16

Cogné, N., Doepke, D., Chew, D., Stuart, F. M., & Mark, C. (2016). Measuring plume-related exhumation of the British Isles in Early Cenozoic times. *Earth and Planetary Science Letters, 456*, 1-15. doi:https://doi.org/10.1016/j.epsl.2016.09.053

Dickinson, W. R. (1970). Interpreting detrital modes of graywacke and arkose. *Journal of Sedimentary Research, 40*(2), 695-707. doi:https://doi.org/10.1306/74D72018-2B21-11D7-8648000102C1865D

Etchepare, J., Merian, M., & Smetankine, L. (1974). Vibrational normal modes of SiO2. I. α and β quartz. *The Journal of Chemical Physics, 60*(5), 1873-1876. doi:https://doi.org/10.1063/1.1681287

Fairey, B. J. (2017). *Sediment routing and recycling through multiple basins from Palaeozoic to Mesozoic times: a provenance study of the Devonian Old Red Sandstone of southern Ireland and neighbouring offshore Mesozoic basins.* PhD thesis, University College Cork,

Fairey, B. J., Kerrison, A., Meere, P. A., Mulchrone, K. F., Hofmann, M., Gärtner, A., Sonntag, B.-L., Linnemann, U., Kuiper, K. F., & Ennis, M. (2018). The provenance of the Devonian Old Red Sandstone of the Dingle Peninsula, SW Ireland; the earliest record of Laurentian and peri-Gondwanan sediment mixing in

Ireland. *Journal of the Geological Society, London*, jgs2017-2099. doi:https://doi.org/10.1144/jgs2017-099 |
Fitzpatrick, R. W., & Raven, M. D. (2019). The forensic comparison of trace amounts of soil on a pyjama top with hypersulfidic subaqueous soil from a river as evidence in a homicide cold case. *Geological Society, London, Special Publications, 492*, SP492-2019-2059.
Franklin, J., Tyrrell, S., O'Sullivan, G., Nauton-Fourteu, M., & Raine, R. (2020). Provenance of Triassic sandstones in the basins of Northern Ireland—Implications for NW European Triassic palaeodrainage. *Geological Journal*. doi:https://doi.org/10.1002/gj.3697
Garzanti, E., Andò, S., & Vezzoli, G. (2009). Grain-size dependence of sediment composition and environmental bias in provenance studies. *Earth and Planetary Science Letters, 277*(3), 422-432. doi:https://doi.org/10.1016/j.epsl.2008.11.007
Harrison, T. M., Célérier, J., Aikman, A. B., Hermann, J., & Heizler, M. T. (2009). Diffusion of 40Ar in muscovite. *Geochimica et Cosmochimica Acta, 73*(4), 1039-1051. doi:https://doi.org/10.1016/j.gca.2008.09.038
Hibbard, J. P., Van Staal, C. R., & Rankin, D. W. (2007). A comparative analysis of pre-Silurian crustal building blocks of the northern and the southern Appalachian orogen. *American Journal of Science, 307*(1), 23-45. doi:https://doi: 10.2475/01.2007.02
Kessler, L., & Sachs, S. D. (1995). Depositional setting and sequence stratigraphic implications of the Upper Sinemurian (Lower Jurassic) sandstone interval, North Celtic Sea/St George's Channel Basins, offshore Ireland. *Geological Society, London, Special Publications, 93*(1), 171-192. doi:https://doi.org/10.1144/GSL.SP.1995.093.01.13
Kirkland, C., Yakymchuk, C., Szilas, K., Evans, N., Hollis, J., McDonald, B., & Gardiner, N. (2018). Apatite: a U-Pb thermochronometer or geochronometer? *Lithos, 318*, 143-157.
Koglin, N., Frimmel, H. E., Minter, W. L., & Brätz, H. (2010). Trace-element characteristics of different pyrite types in Mesoarchaean to Palaeoproterozoic placer deposits. *Mineralium Deposita, 45*(3), 259-280.
Li, Z.-X., Wartho, J.-A., Occhipinti, S., Zhang, C.-L., Li, X.-H., Wang, J., & Bao, C. (2007). Early history of the eastern Sibao Orogen (South China) during the assembly of Rodinia: new mica 40Ar/39Ar dating and SHRIMP U–Pb detrital zircon provenance constraints. *Precambrian Research, 159*(1-2), 79-94.
Malusà, M. G., Resentini, A., & Garzanti, E. (2016). Hydraulic sorting and mineral fertility bias in detrital geochronology. *Gondwana Research, 31*, 1-19.
Mange, M. A., & Maurer, H. (1992). *Heavy minerals in colour*: Springer Science & Business Media.
Mange, M. A., & Wright, D. T. (2007). *Heavy minerals in use*: Elsevier.
McAteer, C. A., Daly, J. S., Flowerdew, M. J., Connelly, J. N., Housh, T. B., & Whitehouse, M. J. (2010). Detrital zircon, detrital titanite and igneous clast U–Pb geochronology and basement–cover relationships of the Colonsay Group, SW Scotland: Laurentian provenance and correlation with the Neoproterozoic Dalradian Supergroup. *Precambrian Research, 181*(1-4), 21-42.
McConnell, B., Rogers, R., & Crowley, Q. (2016). Sediment provenance and tectonics on the Laurentian margin: implications of detrital zircons ages from the Central Belt of the Southern Uplands–Down–Longford Terrane in Co. Monaghan, Ireland. *Scottish Journal of Geology, 52*(1), 11-17. doi:https://doi.org/10.1144/sjg2015-013
Millson, J. (1987). *The Jurassic evolution of the Celtic Sea basins.* Paper presented at the Conference on petroleum geology of North West Europe. 3.
Morton, A. C., & Hallsworth, C. (1994). Identifying provenance-specific features of detrital heavy mineral assemblages in sandstones. *Sedimentary Geology, 90*(3-4), 241-256. doi:https://doi.org/10.1016/0037-0738(94)90041-8
Morton, A. C., & Hallsworth, C. R. (1999). Processes controlling the composition of heavy mineral assemblages in sandstones. *Sedimentary Geology, 124*(1), 3-29.
Murdoch, L. M., Musgrove, F. W., & Perry, J. S. (1995). Tertiary uplift and inversion history in the North Celtic Sea Basin and its influence on source rock maturity. *Geological Society, London, Special Publications, 93*(1), 297-319. doi:10.1144/gsl.sp.1995.093.01.22
Murphy, N. J., & Ainsworth, N. R. (1991). Stratigraphy of the Triassic, Lower Jurassic and Middle Jurassic (Aalenian) from the Fastnet Basin, offshore south-west Ireland. *Marine and Petroleum Geology, 8*(4), 417-429. doi:https://doi.org/10.1016/0264-8172(91)90064-8
Nance, R. D., Murphy, J. B., Strachan, R. A., Keppie, J. D., Gutiérrez-Alonso, G., Fernández-Suárez, J., Quesada, C., Linnemann, U., D'lemos, R., & Pisarevsky, S. A. (2008). Neoproterozoic-early Palaeozoic tectonostratigraphy and palaeogeography of the peri-Gondwanan terranes: Amazonian v. West

African connections. *Geological Society, London, Special Publications, 297*(1), 345-383. doi:https://doi.org/10.1144/SP297.17
Nasdala, L., Irmer, G., & Wolf, D. (1995). The degree of metamictization in zircons: a Raman spectroscopic study. *European Journal of Mineralogy-Ohne Beihefte, 7*(3), 471-478. doi:https://doi.org/10.1127/ejm/7/3/0471
Nasdala, L., Pidgeon, R., Wolf, D., & Irmer, G. (1998). Metamictization and U-Pb isotopic discordance in single zircons: a combined Raman microprobe and SHRIMP ion probe study. *Mineralogy and Petrology, 62*(1-2), 1-27. doi:https://doi.org/10.1007/BF01173760
Nauton-Fourteu, M., Tyrrell, S., Morton, A., Mark, C., O'Sullivan, G. J., & Chew, D. M. (2020). Constraining recycled detritus in quartz-rich sandstones: insights from a multi-proxy provenance study of the Mid-Carboniferous, Clare Basin, western Ireland. *Basin Research*. doi:https://doi.org/10.1111/bre.12469
Naylor, D., & Shannon, P. (1982). *Geology of offshore Ireland and west Britain*. United Kingdom.
Naylor, D., & Shannon, P. (2011). *Petroleum geology of Ireland*: Dunedin Academic Press Limited.
Norell, M. A., Wiemann, J., Fabbri, M., Yu, C., Marsicano, C. A., Moore-Nall, A., Varricchio, D. J., Pol, D., & Zelenitsky, D. K. (2020). The first dinosaur egg was soft. *Nature*. doi:https://doi.org/10.1038/s41586-020-2412-8
O'Sullivan, G., Chew, D., Kenny, G., Henrichs, I., & Mulligan, D. (2020). The trace element composition of apatite and its application to detrital provenance studies. *Earth-Science Reviews, 201*, 103044. doi:https://doi.org/10.1016/j.earscirev.2019.103044
Petrie, S., Brown, J., Granger, P., & Lovell, J. (1989). Mesozoic history of the Celtic Sea basins. *Extensional Tectonics and Stratigraphy of the North Atlantic Margins American Association of Petroleum Geologists Memoirs, 46*, 433-445.
Pettijohn, F. J., Potter, P. E., & Siever, R. (2012). *Sand and sandstone*: Springer Science & Business Media.
Pollock, J. C., Hibbard, J. P., & van Staal, C. R. (2012). A paleogeographical review of the peri-Gondwanan realm of the Appalachian orogen. *Canadian Journal of Earth Sciences, 49*(1), 259-288. doi:https://doi.org/10.1139/e11-049
Pothier, H. D., Waldron, J. W., Schofield, D. I., & DuFrane, S. A. (2015). Peri-Gondwanan terrane interactions recorded in the Cambrian–Ordovician detrital zircon geochronology of North Wales. *Gondwana Research, 28*(3), 987-1001. doi:https://doi.org/10.1016/j.gr.2014.08.009
Raman, C. V. (1928). A change of wave-length in light scattering. *Nature, 121*(3051), 619. doi:https://doi.org/10.1038/121619b0
Ramkumar, M. (2015). Toward standardization of terminologies and recognition of chemostratigraphy as a formal stratigraphic method. In *Chemostratigraphy* (pp. 1-21): Elsevier.
Resentini, A., Andò, S., Garzanti, E., Malusà, M. G., Pastore, G., Vermeesch, P., Chanvry, E., & Dall'Asta, M. (2020). Zircon as a provenance tracer: Coupling Raman spectroscopy and UPb geochronology in source-to-sink studies. *Chemical Geology*, 119828. doi:https://doi.org/10.1016/j.chemgeo.2020.119828
Robinson, K., Shannon, P., & Young, G. M. (1981). The Fastnet Basin: An integrated analysis. In L. G. Illing & G. D. Hobson (Eds.), *Petroleum Geology of the Continental Shelf of North-West Europe* (pp. 444–454). London: Heyden and Son Ltd.
Rodríguez-Salgado, P., Childs, C., Shannon, P. M., & Walsh, J. J. (2019). Structural evolution and the partitioning of deformation during basin growth and inversion: A case study from the Mizen Basin Celtic Sea, offshore Ireland. *Basin Research*. doi:https://doi.org/10.1111/bre.12402
Rull, F., Maurice, S., Hutchinson, I., Moral, A., Perez, C., Diaz, C., Colombo, M., Belenguer, T., Lopez-Reyes, G., & Sansano, A. (2017). The Raman laser spectrometer for the ExoMars rover mission to Mars. *Astrobiology, 17*(6-7), 627-654. doi:https://doi.org/10.1089/ast.2016.1567
Schmidt, C., & Ziemann, M. A. (2000). In-situ Raman spectroscopy of quartz: A pressure sensor for hydrothermal diamond-anvil cell experiments at elevated temperatures. *American Mineralogist, 85*(11-12), 1725-1734. doi:https://doi.org/10.2138/am-2000-11-1216
Shapiro, S. M., O'Shea, D. C., & Cummins, H. Z. (1967). Raman scattering study of the alpha-beta phase transition in quartz. *Physical Review Letters, 19*(7), 361. doi:https://doi.org/10.1103/PhysRevLett.19.361
Smyth, H. R., Morton, A., Richardson, N., & Scott, R. A. (2014). Sediment provenance studies in hydrocarbon exploration and production: An introduction. *Geological Society, London, Special Publications, 386*(1), 1-6.

Thomson, S. N., Gehrels, G. E., Ruiz, J., & Buchwaldt, R. (2012). Routine low-damage apatite U-Pb dating using laser ablation–multicollector–ICPMS. *Geochemistry, Geophysics, Geosystems, 13*(2). doi:https://10.1029/2011GC003928

Tyrrell, S. (2005). *Investigations of Sandstone Provenance.* (PhD). University College Dublin,

Tyrrell, S., Haughton, P. D., Souders, A. K., Daly, J. S., & Shannon, P. M. (2012). Large-scale, linked drainage systems in the NW European Triassic: insights from the Pb isotopic composition of detrital K-feldspar. *Journal of the Geological Society, London, 169*(3), 279-295. doi:https://doi.org/10.1144/0016-76492011-104

Van der Voo, R. (1988). Paleozoic paleogeography of North America, Gondwana and intervening. displaced terranes: Comparisons of palaeomagnetism with paleoclimatology and biogeographical patterns. *Geological Society of America Bulletin, 100*, 411-423. doi:https://doi.org/10.1130/0016-7606(1988)100<0311:PPONAG>2.3.CO;2

Waldron, J. W., Schofield, D. I., & Murphy, J. B. (2019a). Diachronous Paleozoic accretion of peri-Gondwanan terranes at the Laurentian margin. *Geological Society, London, Special Publications, 470*(1), 289-310. doi:https://doi.org/10.1144/SP470.11

Waldron, J. W., Schofield, D. I., Pearson, G., Sarkar, C., Luo, Y., & Dokken, R. (2019b). Detrital zircon characterization of early Cambrian sandstones from East Avalonia and SE Ireland: implications for terrane affinities in the peri-Gondwanan Caledonides. *Geological Magazine, 156*(7), 1217-1232. doi:https://doi.org/10.1017/S0016756818000407

Weltje, G. J., & von Eynatten, H. (2004). Quantitative provenance analysis of sediments: review and outlook. *Sedimentary Geology, 171*(1-4), 1-11.

Zimmermann, S., Mark, C., Chew, D., & Voice, P. J. (2018). Maximising data and precision from detrital zircon U-Pb analysis by LA-ICPMS: The use of core-rim ages and the single-analysis concordia age. *Sedimentary Geology, 375*, 5-13. doi:https://doi.org/10.1016/j.sedgeo.2017.12.020

Chapter 2: *The Provenance of Middle Jurassic to Cretaceous sediments in the Irish and Celtic Sea basins: Environmental and tectonic controls on sediment sourcing*

Authors

Odhrán McCarthy[1], Brenton Fairey[2], Patrick Meere[1], David Chew [3], Aidan Kerrison[4], David Wray[5], Mandy Hofmann[6], Andreas Gärtner[6], Benita-Lisette Sonntag[6], Ulf Linnemann[6], Klaudia F. Kuiper[7].

Affiliations

[1]School of Biological, Environmental and Earth Sciences and iCRAG, University College Cork

[2]Chemostrat, Welshpool, United Kingdom

[3]Department of Geology and iCRAG, Trinity College Dublin, Dublin, Ireland

[4]School of Earth and Atmospheric Sciences, Queensland University of Technology, Brisbane, QLD, Australia

[5]School of Sciences, University of Greenwich, Kent, UK, ME4TB

[6]Senckenberg Naturhistorische Sammlungen Dresden, Museum für Mineralogie und Geologie, Königsbrücker Landstraße 159, D-01109 Dresden, Germany

[7]Department of Earth Sciences, Vrije Universiteit Amsterdam, De Boelelaan 1085, NL-1081 HV Amsterdam, The Netherlands

Correspondence: odhranm04@hotmail.com

Abstract

The Jurassic and Cretaceous sedimentary infill of the Irish and Celtic Sea basins is intimately associated with the breakup of the supercontinent Pangea, and the opening of the Atlantic margin. Previous basin studies have constrained tectonism, basin uplift and sediment composition, but sediment provenance and routing have not received detailed consideration. Current hypotheses for basin infill suggest localised sediment sourcing throughout the

Jurassic and Cretaceous, despite a dynamic tectonic and palaeo-environmental history spanning more than 100 million years. We present detrital zircon, white mica and apatite geochronology alongside heavy mineral data from five basins. Findings reveal that basin infill derived predominantly from distal sources with lesser periods of local sourcing. We deduce that tectonically induced marine transgression and regression events had a first-order control on distal (Laurentia) *versus* proximal (Peri-Gondwana) sedimentary sourcing. Additionally, tectonism which uplifted the Fastnet Basin region during the Middle-Late Jurassic recycled basin sediments into the connected Celtic and Irish Sea basins. Detrital geochronology and heavy mineral evidence support three distinct provenance switches throughout the Jurassic and Cretaceous in these basins. Overall an integrated multi-proxy provenance approach provides novel insights to tectonic and environmental controls on basin infill as demonstrated in the Irish and Celtic Sea basins.

2.1. **Introduction**

Provenance investigations provide useful insights into important environmental and tectonic events as well as the origin and routing of sediments. This is especially true for the Mesozoic sedimentary basins of the Irish and Celtic Seas, which formed after the rifting and breakup of the palaeocontinent Pangea, and during the protracted opening of the Atlantic margin (Naylor *et al.*, 1982; Allen *et al.*, 2002). Previous research has primarily focused on the basin tectonics and structure, hydrocarbon potential and palaeo-environmental history, furthering our understanding of the evolution of this offshore segment of the Atlantic Margin (Shannon, 1991a; Shannon *et al.*, 2001; Naylor *et al.*, 2011). Evidence of more than two kilometers of basin exhumation during the Jurassic and Cretaceous indicates that tectonism played an integral role in the sourcing, routing and preservation of the basin infill (Cogné *et al.*, 2014; Cogné *et al.*, 2016; Rodríguez-Salgado *et al.*, 2019). However, there is a distinct gap in our understanding of the interplay of environmental and tectonic controls on the provenance of the Irish Mesozoic basin infill. Despite more than 40 years of economic exploration in the Jurassic and Cretaceous successions, there have been no dedicated provenance studies in the North Celtic Sea Basin (NCSB) (Fig. 3), Saint George's Channel Basin (SGCB), South Celtic Sea Basin (SCSB), Fastnet Basin and Goban Spur Basin (O'Reilly *et al.*, 1991; Shannon, 1996). Sediment is thought to have been locally derived from the Upper Devonian Munster Basin and the adjacent, Early to Middle Paleozoic, Leinster Massif (Fig. 1) throughout the Jurassic and Cretaceous (Robinson *et al.*, 1981; Ainsworth *et al.*, 1985; Millson, 1987; Caston, 1995; Naylor *et al.*, 2011). However, while this simple model is consistent with biostratigraphic data, sedimentary petrography, paleocurrent data and seismic investigations, these observations provide limited insight into the detailed sedimentary provenance. Considering the active tectonism and fluctuating environmental signals observed in the region during the Mesozoic (Naylor *et al.*, 2011), it seems unlikely that only two sediment sources were active throughout the Jurassic and Cretaceous Periods. Given that the major tectonic and environmental events that shaped these basins are well-constrained, the basins make for an ideal testing ground for investigating the effects of such events on sediment provenance.

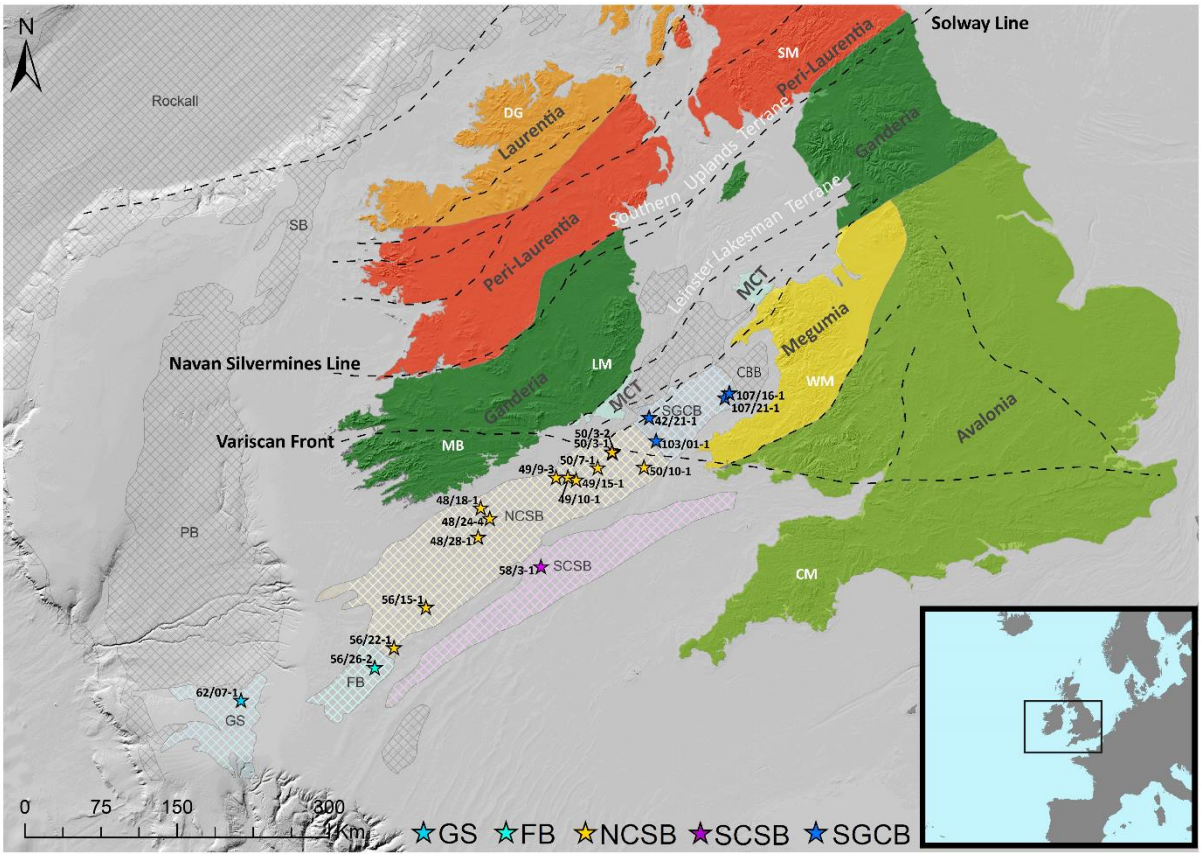

Fig. 3. *Map of the present-day study area with onshore and offshore bathymetry (EMODnet, 2018). Stars are coloured by basin and mark sampled well locations. DG, Dalradian Supergroup; LM, Leinster Massif; MB, Munster Basin; WM, Welsh Massif; CM, Cornubia Massif; SM, Scottish Massif; PB, Porcupine Basin; SB, Slyne Basin; NCSB, North Celtic Sea Basin; SCSB, South Celtic Sea Basin; SGCB, Saint George's Channel Basin; FB, Fastnet Basin; GS, Goban Spur Basin; MCT, Monian Composite Terrane (Nance et al., 2015; Waldron et al., 2019b).*

The study area includes five sedimentary basins on the continental shelf off the coast of southeast Ireland in the Irish and Celtic Seas (Fig. 3). Mesozoic and Cenozoic stratigraphy in the study area has been truncated by multiple exhumation events driven by either; i) epeirogenic mechanisms related to the proto-Iceland plume (Brodie *et al.*, 1994; Jones *et al.*, 2002; Cogné *et al.*, 2016) or, ii) far-field tectonic influences from the Mesozoic Cimmerian (Early Alpine) orogeny (Rawson *et al.*, 1982), and the Cenozoic Alpine orogeny (Ziegler *et al.*, 1995). These first-order tectonic controls on basin development drove localised marine transgression-regression cycles throughout the Mesozoic Period. Recently, a revised stratigraphic nomenclature was proposed for Irish offshore stratigraphy (ISPSG, 2019) and is incorporated into Fig. 4, which summarises the stratigraphy, tectonism and sea level change in the SGCB, NCSB and Fastnet Basin. Of the 105 wells drilled across these basins, 35 samples were taken from Jurassic and Cretaceous sandstone units across 19 wells. Investigating the

provenance of these basins is challenging as numerous potential paleocontinental sources yield similar detrital zircon populations (e.g., Peri-Gondwanan sources such as Avalonia, Megumia, Iberia and Armorica) requiring alternative analytical techniques like apatite and mica geochronology or feldspar analysis for diagnostic source fingerprinting. Such techniques have been successfully applied in the Slyne (Franklin *et al.*, 2020), Munster (Fairey, 2017), Dingle (Fairey *et al.*, 2018) and Clare basins (Nauton-Fourteu *et al.*, 2020) in the Irish offshore and mainland.

This study aims to test the hypothesis that the Leinster Massif and Munster Basin were the primary sediment sources throughout the Middle Jurassic to Late Cretaceous in the North Celtic Sea Basin (NCSB), Saint George's Channel Basin (SGCB), Fastnet Basin and Goban Spur Basin (Fig. 3). Additionally, we aim to better characterise the influence of tectonic and environmental controls on sediment provenance in the study area. A multi-proxy approach of single grain geochronology (U-Pb zircon and apatite, and $^{40}Ar/^{39}Ar$ mica dating), apatite trace element analysis and bulk sediment characterisation of heavy mineral abundance (HMA) was undertaken. To contextualise changes in sediment provenance during basin development, sandstones within larger stratigraphical units which mark potentially significant changes in tectonic and environmental conditions were sampled (see Fig. 4and Table 7 of supplementary materials for further detail). More broadly, findings of this study could have implications for other basins along the Atlantic Margin.

2.2. **Geological Background**

2.2.1. Overview

The NCSB is linked to the SGCB to the north, and Fastnet Basin and South Celtic Sea Basin to the south (Fig. 3). It records the thickest (9 km maximum thickness) stratigraphic succession of Mesozoic stratigraphy (Rodriguez-Salgado, 2019) of these basins and is well profiled with 2D and 3D seismic surveys (Sibuet *et al.*, 1990; O'Reilly *et al.*, 1991; Rodríguez-Salgado *et al.*, 2019), 88 drilled wells as well as gravity and magnetic surveys (Sibuet *et al.*, 1990). The Fastnet Basin (16 wells in total) preserves a limited succession of Middle-Upper Jurassic stratigraphy due to Cimmerian uplift (Fig. 4), but was an important igneous centre throughout the

Mesozoic Era (Caston *et al.*, 1981; Ainsworth *et al.*, 1985; Murphy *et al.*, 1991; Ewins *et al.*, 1995). The SGCB contains a complete section of Triassic and Jurassic stratigraphy but has limited Cretaceous successions due to Cenozoic exhumation and erosion. The Goban Spur Basin is the least studied of these basins with only one well, and limited 2D and 3D seismic survey data (Yang *et al.*, 2020). Generally, offshore well records tend to focus on Cretaceous intervals across the Irish and Celtic Sea, and of the 114 wells drilled in the Celtic Sea, only 26 penetrate basement rock. Due to limited well penetration, numerous unconformities, and poor quality 2D seismic data, the Jurassic and Triassic stratigraphy of these units is only partially understood in the study area.

2.2.2. Pre-Mesozoic to Early Jurassic Tectonic Framework

Basin development offshore of the south and east of Ireland (the Celtic and Irish Sea basins) initiated towards the end of the Carboniferous and into the early Permian and was associated with the breakup of the supercontinent of Pangea (Chadwick *et al.*, 1995). By the Early Triassic, renewed rifting of Pangea followed a northeast-southwest Caledonian structural fabric in the region (Shannon, 1991a) (Fig. 3). The Early Triassic basins are interpreted to have been disconnected, long and narrow and of varying size and were located 15-20° north of the equator with an arid climate (Warrington *et al.*, 1992). By the Late Triassic to Early Jurassic, rift chains extended along Pangea from the Tethys Ocean to the central Atlantic. These rift chains were associated with further development of early Permian-Triassic rift basins, and deepening transgressive marine conditions resulting in the deposition of the Mercia Mudstone Group throughout the study area (Ruffell *et al.*, 1999).

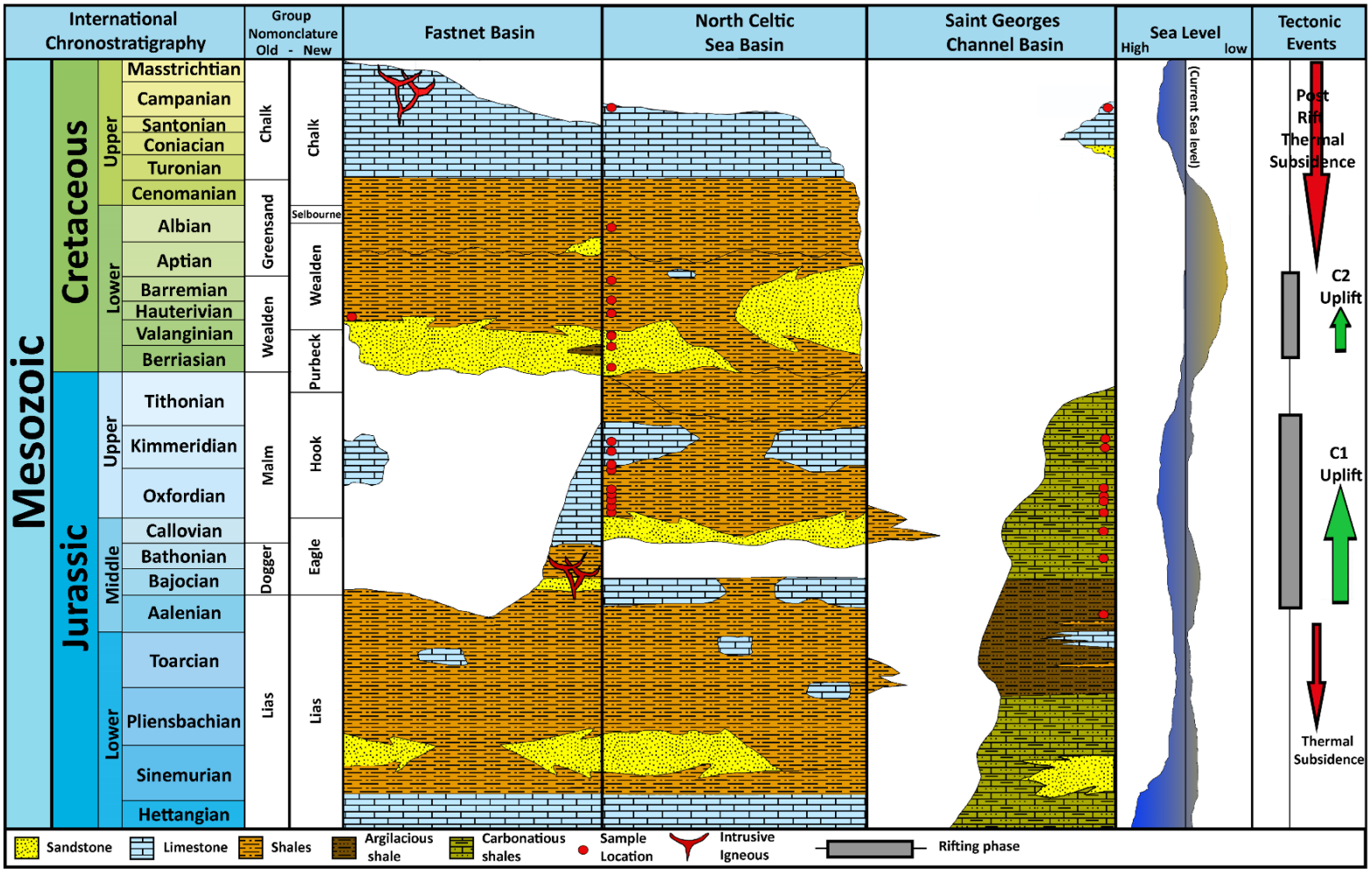

Fig. 4. *Summary of the Mesozoic lithostratigraphy of the Fastnet Basin, NCSB and SGCB. Lithostratigraphy adapted from Tyrrell (2005) and interpretations from well logs. Red circles indicate sample locations. New group nomenclature is taken from a new standard lithostratigraphic framework for offshore Ireland (ISPSG, 2019). Old group nomenclature and sea level data are taken from Murphy et al. (1991); Ewins et al. (1995); Shannon (1995); Welch et al. (2000); Hounslow et al. (2006).*

Open marine conditions developed during the latest Triassic to Early Jurassic resulting in the deposition of the Lias Group (Fig. 4), with regional transgressive marine sedimentation during the Rhaetian slowing and shallowing into carbonate dominated marine environments by the Hettangian. The study area had drifted north to a latitude of c. 30° by the Early-Middle Jurassic (Bassoulet, 1993). Marine conditions persisted until a thermal subsidence induced regression event in the Late Sinemurian led to the deposition of localised deltaic and shallow marine sandstones along the margins of the SGCB, northern NCSB and Fastnet Basin (Naylor *et al.*, 2011). Terrestrial clastic sediment is thought to have been sourced from the Old Red Sandstone of the Munster Basin or the Fastnet Spur during the Sinemurian, while the eastern half of the NCSB is thought to have sourced sediment from the Leinster Massif (Petrie *et al.*, 1989). There then followed a localised transgression back into mixed, shallow marine carbonate and sandstone deposition by the Pliensbachian (Kessler *et al.*, 1995). The SGCB is thought to have received input from the Leinster Massif at this time as the progradation of deltaic and shallow marine clastic sediments feeding from the Leinster Massif switched from south to east (Petrie *et al.*, 1989). The Toarcian brought a widespread, thermal subsidence-related transgression, resulting in mudstone and shale deposition throughout the Celtic Sea basins (Murphy *et al.*, 1991).

2.2.3. Middle to Late Jurassic Sedimentation and Cimmerian Tectonism

Middle Jurassic sedimentation was strongly affected by the onset of Cimmerian tectonism which exerted a strong control on exhumation and relative sea level changes (C1 uplift, Fig. 4) in the Celtic and Irish Sea basins (Ziegler, 1990). In this study, Cimmerian tectonism refers to the pulsed, far-field effects of the Cimmerian orogeny of central Asia and Mediterranean-Alpine Europe, which was associated with the closure of Palaeotethys and opening of Neotethys (Stampfli *et al.*, 2006). It is linked to stages of rift-related, Middle Jurassic to Late Cretaceous tectonism, initiating in the Aalenian as outlined by Naylor *et al.* (2011) and Rodríguez-Salgado *et al.* (2019) in the study area. Continued regression during the Aalenian developed thick nearshore deltaic sequences in the east, and argillaceous and calcareous sand beds in the west of the SGCB. Sea level started to rise into the Late Bajocian, likely because of thermal subsidence, and argillaceous deposits became more frequent (Eagle

Group, Fig. 4). More than 700 m of Middle Jurassic successions (Lias-Hook Groups) are preserved in the NCSB. The Fastnet Basin preserves 233 m (well 56/26-1) of the Middle Jurassic Eagle Group which was exhumed and eroded later in in the Middle Jurassic by Cimmerian tectonism (Fig. 4). During the Bajocian, six sills and possible volcanic plugs intruded along northeast-trending fault zones in the Fastnet Basin (Caston *et al.*, 1981; Rodríguez-Salgado *et al.*, 2019). During the Bathonian, a localised marine regression resulted in shallow marine conditions in the northeast NCSB and SGCB, where bioclastic sands were deposited as part of the Eagle Group. Carbonate shelves developed in the NCSB and SGCB and shallow marine conditions developed in the Cardigan Bay Basin (Fig. 3) (Caston, 1995).

During the Bathonian, another phase of Cimmerian tectonism uplifted and eroded Middle to Upper Jurassic successions in the Fastnet Basin and the western margin of the NCSB (Fig. 4). Though speculative, a hot spot may have caused doming of the Goban Spur Basin, Fastnet Basin and western NCSB which drove uplift and erosion (Shannon, 1996), while the SGCB and northern NCSB remained as marine environments with deposition of calcareous mud, silt and thin intervals of sand (325 m Well 50/3-2 & 700 m Well 103/2-1). Sedimentation has been interpreted as syn-rift, continental to shallow marine in origin, possibly sourced from the re-activated basin margins including the Munster Basin, Leinster, Cornubian and Welsh massifs (Fig. 4). Rising sea levels and progressive rifting produced marine conditions in the NCSB and SGCB. A further regressive event developed during the Late Bathonian, resulting in a freshwater to a brackish environment throughout the Irish Sea. The Callovian-Oxfordian is marked by deposition of cross bedded, current rippled and braided fluvial sediments of the Hook Group (1157 m Well 50/3-2) in most areas of the NCSB which rest unconformably (Fig. 4) on carbonaceous Bathonian strata as a result of Cimmerian tectonism. The Fastnet Basin records 433 m (Well 63/8-1) of the Hook Group. Sediment sourcing during this period is thought to have been derived from the exhumed and eroded basin margins in the NCSB (Caston, 1995). The SGCB had a marginal marine-lacustrine environment at this time comprising calcareous muds interbedded with sparse sandstones and occasionally fluvial braided sequences. Evidence of fault-bounded sedimentation in a warm and wet palaeo-climate is provided by non-marine, *Classopollis* pollen and red oxidised kaolinite-smectite dominated clays in Middle-Upper Jurassic successions on the southeast Irish mainland (Higgs *et al.*, 1986), which contrasts with the thick, clastic sequences developed in the adjacent

offshore. During the Oxfordian-Tithonian, the facies distribution changed from fluvial drained sediments to increasingly lacustrine/marginal-marine in the NCSB. Throughout this period, the SGCB remined a marginal-marine environment depositing, carbonate-rich sands, silts and calcareous mudstone units (Naylor *et al.*, 2011).

2.2.4. Cretaceous Sedimentation

Crustal extension along Atlantic fault systems occurred at the Jurassic-Cretaceous boundary as part of a late phase of Cimmerian tectonism (Rawson *et al.*, 1982). Consequently, in the vicinity of southern Ireland, continental shelves and upland areas were exhumed (C2 uplift Fig. 4) along with the adjacent offshore basins (Rodríguez-Salgado *et al.*, 2019). This coincided with a fall in sea level globally from the Tithonian-Valanginian (Haq, 2014). Marginal basin areas were eroded and continental, fluvial and deltaic sediments were deposited, as part of the Purbeck Group, lying unconformably upon Upper Jurassic successions in the Irish and Celtic Sea regions (Fig. 4). The Purbeck units contain non-marine, white-pink, fine-coarse grained sandstone with greenish grey calcareous claystones and marls (Caston, 1995). These units have an average thickness of 230 m across the basins and a maximum thickness of 560 m (well 57/2-2). Brackish-freshwater Berriasian sediments were followed by Valanginian-Hauterivian alluvial shales, while fluvial sandstones likely derived from a western source, like the Leinster Massif and Munster Basin, are also identified in the Fastnet Basin and NCSB (Robinson *et al.*, 1981; Ainsworth *et al.*, 1985). The study area was in a mid-latitude region at the time (Allen, 1981; Culver *et al.*, 2006), closer to its current latitude, and observed a change from arid to humid climate conditions during the Valanginian (Ruffell *et al.*, 1994). A global transgression (Haq, 2014) in the Hauterivian-Albian is recorded by deposition across much of the Irish and Celtic Seas, of the marginal-marine to marine Wealden Group (Rowell, 1995) and later the Selbourne Group and coincides with a period of post-rift thermal subsidence (Fig. 2). Marine conditions continued into the Cenomanian, resulting in regional deposition of the Chalk Group (1200 m thick well 93/2-1, and 191 m well 50/2-1) (Payton, 1977; Haq, 2014). Later, during the Cenozoic, the basin margins were exhumed and eroded as part of the initial phase of prolonged uplift and subsidence associated with the opening of the Atlantic (Anell *et al.*, 2009). This uplift event removed Upper Jurassic and Cretaceous material from the SGCB producing major unconformities overlain by Cenozoic strata (Fig. 4). Throughout the

Cretaceous, periods of igneous activity in the Porcupine Basin, Western Approaches, Goban Spur Basin and Fastnet Basin (Fig. 4) were common and typically coincided with rifting phases in the Atlantic and opening of the Bay of Biscay, while the NCSB, SCSB and SGCB regions were volcanically quiescent throughout the Mesozoic (Croker *et al.*, 1987; Tate *et al.*, 1988; García-Mondéjar, 1996; Rodríguez-Salgado *et al.*, 2019). The common occurrence of unconformities, and the evident removal of basin margins is crucial in this investigation as potential proximal sediment sources, available during the Jurassic and Cretaceous, are no longer preserved in the geological record.

2.3. **Potential Sediment Sources**

Potential sediment sources are considered in terms of tectonostratigraphic domains (Hibbard *et al.*, 2007) as their unique geological histories help to determine the ultimate source of the Mesozoic infill. The exact boundaries, and tectonic history of each domain are continually debated (Waldron *et al.*, 2019b). Two broad palaeocontinental assemblages can be found in Britain and Ireland. These are Laurentian (and Peri-Laurentian) domains north of the Iapetus Suture, and Peri-Gondwanan domains to the south (Fig. 3) (Hibbard *et al.*, 2007; Pollock *et al.*, 2012). Peri-Gondwanan domains are separated into Ganderia, the Monian Composite Terrane, Avalonia and Megumia (Waldron *et al.*, 2019b). More recent tectonomagmatic events are also included in the characterisation of source regions as they further help in fingerprinting sources (e.g., Permian igneous activity within Avalonia).

2.3.1. Laurentia

Laurentian crustal provinces in the North Atlantic region comprise amalgamated Archean-Paleoproterozoic cratonic blocks such as the North Atlantic Craton in Greenland and Eastern Canada (Buchan *et al.*, 2000). In Ireland and Britain Laurentian sources include the Lewisian Complex (2.9–1.7 Ga) (Rainbird *et al.*, 2001; McAteer *et al.*, 2014), the Annagh Gneiss Complex (1.8–1.0 Ga)(Daly *et al.*, 2005) of northwest Ireland and the Rhinns Complex (1.8–1.7 Ga) of northern Ireland and Scotland (Daly, 1996; Chew *et al.*, 2014b). Broadly, Laurentian domains have been affected by Archean, the Trans-Hudson/Nagssugtoqidian (2.0–1.8 Ga)(Hoffman, 1990; Henrique-Pinto *et al.*, 2017), Labradorian (1.7–1.6 Ma), Pinwarian (1.5–1.4 Ga) (Gower,

1996; McAteer *et al.*, 2014), and Grenville (1.3–0.9 Ga) orogenic events. Not all of these orogenic phases affected the Laurentian basement units in Britain and Ireland, but many of these orogenic episodes are typically captured by detrital zircon ages in Laurentian cover sequences. In Scotland and Ireland, these cover sequences include the Neoproterozoic Moine Supergroup and Neoproterozoic to Early Paleozoic Dalradian Supergroup, which both exhibit a broad range of detrital zircon populations from 3.1–0.9 Ga characteristic of a Laurentian provenance (See Chew *et al.* (2014b)). The Laurentian Caledonides of Scotland and Ireland were intruded by a series of granitic bodies from 470-400 Ma, with the major peak in granitic magmatism at 430–400 Ma (Miles *et al.*, 2018; Murphy *et al.*, 2019).

2.3.2. Peri-Laurentia

Peri-Laurentia, refers to the domain along the south-eastern Laurentian margin which is associated with subduction and closure of the Iapetus Ocean (McConnell *et al.*, 2016). The Southern Uplands – Longford-Down Terrane is bounded by the Southern Uplands Fault to the north, and the Iapetus Suture to the south in Ireland and northern Britain (Fig. 3). Detrital zircon spectra from the Southern Uplands terrane are comprised of 2.0–0.9 Ga Laurentian zircon with a particularly prominent 1.5–1.0 Ga population, with Ordovician 490–470 Ma zircon becoming more prominent in the southern tracts (Waldron *et al.*, 2014). Permian to Carboniferous extensional volcanism in the Midland Valley of southern Scotland is dated from 342–329 Ma by the $^{40}Ar/^{39}Ar$ method, with a shorter-lived second phase at c. 298 Ma (Monaghan *et al.*, 2004; Kirstein *et al.*, 2006). The Southern Upland Terrane is thus comprised of sediment primarily derived from Laurentia and includes Paleozoic magmatic detritus.

2.3.3. Peri-Gondwanan Domains

The Peri-Gondwanan domain includes all terranes that were proximal to the northern margin of western Gondwana during the Early Neoproterozoic until the breakup of Gondwana in the Early Paleozoic (Van der Voo, 1988; Nance *et al.*, 2008). These domains include Ganderia, Megumia, the Monian Composite Terrane, Avalonia and Cadomia, and are a source of abundant 690–525 Ma zircon (Pothier *et al.*, 2015).

2.3.3.1. Ganderia and the Monian Composite Terrane

To the immediate south of the Iapetus Suture in Ireland and Britain lies Ganderia, sometimes referred to as Avalonia (Tyrrell *et al.*, 2007; Fullea *et al.*, 2014; Todd, 2015) and more rarely Cadomia in the literature (Soper *et al.*, 1984; Max *et al.*, 1990). The Leinster Massif is an important potential source area. It is comprised of Neoproterozoic basement (the Rosslare Complex) intruded by the Saint Helens Gabbro (618 Ma), the Saltees Granite (437 Ma), the Carrigmore Diorite (415 Ma) and three intrusive phases of the Leinster Batholith (417, 409 and 404 Ma) (Brück *et al.*, 1974; O'Connor *et al.*, 1978; Long *et al.*, 1983; Max *et al.*, 1990; Fritschle *et al.*, 2018). The Leinster Massif forms part of the Leinster-Lakesman Terrane, an eastward extension of the Ganderian terrane of Newfoundland. It has long been considered a likely source of recycled material into the Irish and Celtic Sea regions (Winn Jr, 1994; Hartley, 1995; Taber *et al.*, 1995; Naylor *et al.*, 2011). Zircon populations from these Ganderian domains are typically dominated by 700–500 Ma and c. 400 Ma populations, often with subordinate 2.2–1.0 Ga Amazonian populations (Strachan *et al.*, 2007). The Monian Composite Terrane incorporates the Isle of Anglesey and the southern margin of the Leinster Massif (Fig. 3) (Waldron *et al.*, 2014; Pothier *et al.*, 2015; Waldron *et al.*, 2019a). Like Ganderia, this terrane represents a significant source of metamorphic and igneous detritus with U-Pb detrital zircon populations like those of Ganderia.

2.3.3.2. Megumia

The term “Megumia” was suggested by Waldron *et al.* (2011) for the Meguma Terrane in Nova Scotia and the Harlech Dome in Wales because of their similar biostratigraphy and geochronological signatures and the existence of this domain is further supported by the work of White *et al.* (2012) and Nance *et al.* (2015). Avalonia and Megumia are challenging sources to distinguish using detrital zircon geochronology alone (Collins *et al.*, 2004; Strachan *et al.*, 2007; Pothier *et al.*, 2015). The Welsh Massif was likely an important sediment source region for the Celtic Sea basins and incorporated the Megumian domain to the north and the Avalonian domain to the south (Fig. 3).

2.3.3.3. Avalonia

Avalonia in southern England is identified as Caledonian 'East Avalonia' (as opposed to Appalachian 'West Avalonia') and typically is a source for abundant 650–540 Ma detrital zircon grains (Waldron *et al.*, 2019b). For a more detailed description of the distinction between East versus West Avalonia see van Staal *et al.* (1996) and Pothier *et al.* (2015). Topographic highs of Avalonian basement during the Mesozoic include the Cornubian Massif and the London-Brabant High (Fig. 3). The Cornubian Massif also contains post-Variscan extrusive and intrusive igneous rocks (Smith *et al.*, 2019b).

2.3.3.4. Cadomia

Cadomia includes terranes of the southern Variscan Belt, the Armorican Massif in north-western France and the Iberian Massif in Spain. For a detailed description of these Cadomian terranes see Nance *et al.* (2008) and Henderson *et al.* (2016). The Iberian and Armorican Massif contains Cambrian marine sediments overlying Neoproterozoic volcano-sedimentary successions. The Variscan Orogeny resulted in regional metamorphism of these crustal blocks and the emplacement of associated igneous intrusions (Guerrot *et al.*, 1990; Dallmeyer *et al.*, 2013). These domains would be expected to yield abundant Variscan, Paleozoic and Neoproterozoic zircon and mica like other Peri-Gondwanan domains in NW Europe (Fernández-Suárez *et al.*, 2000; Gutiérrez-Alonso *et al.*, 2005).

2.3.4. Post-Caledonian Cover Sequences

Important cover sequences which are likely sources of recycled Peri-Gondwanan and Laurentian material to the Celtic and Irish Sea basins include the Dingle Basin (Fairey *et al.*, 2018), the Upper Devonian Munster Basin, the Carboniferous Clare Basin (Nauton-Fourteu *et al.*, 2020) and other coeval clastic sequences in central Ireland . The Munster Basin comprises an Upper Devonian to Lower Carboniferous volcano-sedimentary succession affected by Variscan orogenesis (Meere *et al.*, 2006). Fairey (2017) demonstrated that the Upper Devonian Old Red Sandstone of the Munster Basin typically contains two distinct U-Pb zircon populations including; i) Silurian (c. 430 Ma) and Grenville (1.0 Ga) populations which appear to have a Laurentian affinity (e.g., the Gyleen and Kiltorcan formations) and ii) Silurian and

Peri-Gondwanan (c. 700 Ma) populations with subordinate 2.2–0.9 Ga populations (e.g., the Harryloch Formation). The former of these two populations appears to be the most common in the Munster Basin, making it challenging to differentiate from Laurentian sources. Nauton-Fourteu *et al.* (2020) established that the Clare Basin contains a similar population of detrital zircon to the Munster Basin reflecting input from the Northern Laurentian domains, the Southern Peri-Gondwanan domains and igneous intrusive sediment from the Caledonian orogenic cycle. Carboniferous sediments blanket much of central Ireland today, but it is difficult to establish the extent to which these sequences may have covered the Leinster Massif and Munster Basin during the Mesozoic. As these are carbonate successions, they have a heavy mineral fertility and likely represent a minor contribution to offshore basin infill compared to the Leinster granites and Devonian sandstones of the east and south of the Ireland. In addition, Visean volcanism was sporadically developed in central Ireland (c. 337 Ma) and was broadly coeval with volcanism in the Midland Valley of Scotland (Somerville *et al.*, 1992). Apatite fission track data from the Galtee Mountains, Lugnaquilla and Mount Leinster record three phases of onshore exhumation during the Triassic-Early Jurassic (200-170 Ma), Jurassic-Cretaceous boundary (c. 145 Ma) and Early Cretaceous (c. 110 Ma) and comprised a total of 1.5 3 km of exhumation over 150 Ma (Cogné *et al.*, 2016).

2.4. **Methods**

2.4.1. Rationale

A multi-proxy approach of single grain geochronology (U-Pb zircon and apatite, and $^{40}Ar/^{39}Ar$ mica dating), apatite trace element analysis and bulk sediment characterisation of HMA was undertaken in this study to minimise analytical bias and to capture diverse metamorphic, igneous and sedimentary sources (Hietpas *et al.*, 2011; Chew *et al.*, 2020). Due to limited sample size, the conventional approach of splitting samples for heavy mineral and geochronology analysis was not possible. Heavy mineral concentrates were mounted in resin directly after separation and mapped via Qualitative Evaluation of Minerals by Scanning Electron Microscopy (QEMSCAN) analysis for mineral identification and subsequent U-Pb geochronology (Pascoe *et al.*, 2007; Zhang *et al.*, 2015). Six core and 27 drill cutting samples

were taken from the core stores of the Irish Petroleum Affairs Division (PAD) in Dublin and the British Geological Survey Core Shed in Keyworth, UK (see supplementary data table 7).

2.4.2. Sample Preparation

2.4.2.1. Zircon, Apatite and Heavy Mineral Analysis

Processing of samples was conducted at University College Cork (UCC), Ireland. Samples from core and drill cuttings were cleaned by thoroughly washing samples through a < 250 µm sieve and then cleaned with an ultrasonic bath to remove remaining clay material. Samples were disaggregated using a jaw crusher and sieved into 63-125 µm and 125-250 µm grain size fractions where the 63 – 125 was chosen for heavy mineral analysis (Morton, 1984; Mange *et al.*, 1992; Morton *et al.*, 1994). Density separation was conducted with lithium polytungstate (density ca 2.85 $g.cm^{-3}$) by centrifuge and recovered by partial freezing with liquid nitrogen (Garzanti, 2017). Where the recovered heavy fraction was large enough, the cone and quarter method was used to reduce samples for mounting. Samples were then mounted on double-sided sticky tape, cast in epoxy resin and grains were ground and polished to half thickness. Samples are labelled by basin where NC indicates the North Celtic Sea Basin, SG - Saint George's Channel Basin, SC - South Celtic Sea Basin, GS - Goban Spur Basin and FB - the Fastnet Basin. Fifteen Zircon and four mica samples NC1, NC6-NC8, NC17 – NC20, NC26&NC27, SC1, GS1 and FB1 – FB6 were processed and analysed as in Fairey et al. (2018) (see Table 2). Zircon U-Pb geochronology is commonly utilized in provenance studies as zircon has a high closure temperature of > 900 °C, is resistant to weathering and chemical alteration effects, and can be analysed with rapid sample throughput (Gehrels *et al.*, 2006; Chew *et al.*, 2017; Vermeesch *et al.*, 2017). However, zircon has a natural fertility bias wherein it is under-represented in mafic and some metamorphic sources (Hietpas *et al.*, 2011). To capture zircon-poor sources, a combination of detrital white mica and apatite geochronology was also undertaken. The combination of apatite trace element analysis and U-Pb geochronology (closure temperature window of c. 375–550 °C) is effective in identifying the age and composition of both igneous and metamorphic sources (O'Sullivan *et al.*, 2020).

2.4.2.2. White Mica

White mica samples were prepared in the geochronology laboratory, Vrije Universiteit Amsterdam, Amsterdam, Netherlands. Grains were disaggregated by jaw crusher and disc mill. To preserve coarse grains, sieving took place between incrementally decreasing crush sizes. Grains of 200-500 μm were retained after each sieving step. Mica-rich samples were further processed using a shaking table to concentrate platy minerals. Samples with a poor mica yield were further separated by density separation using diluted diiodomethane with a density of 2.78 g/cm^{-3}in an overflow centrifuge. A Franz magnetic separator was used to remove magnetic and paramagnetic impurities. Finally, grains for $^{40}Ar/^{39}Ar$ geochronology were handpicked under an optical microscope to avoid inclusions or impurities. White mica has a closure temperature of 445–400 °C (Harrison *et al.*, 2009), is a good indicator of metapelite, felsic igneous and hydrothermal sources (Mange *et al.*, 2007), and is often considered a first-order source indicator as it is liable to mechanical disaggregation in aeolian settings, although is more durable in a subaqueous setting (Anderson *et al.*, 2017).

2.4.2.3. Heavy Mineral Analysis

Twenty-one samples from the Jurassic and Cretaceous successions of the northern NCSB and SGCB were processed for heavy mineral analysis. After mounting, samples were ground and polished to half thickness and processed for QEMSCAN analysis at 10 μm resolution by Rocktype Ltd in their Oxford laboratory. The FEI-trademarked QEMSCAN® technique is an automated mineralogy method which combines Energy Dispersive Spectroscopy (EDS) with software that enables automated pixel by pixel spectral acquisition and post-analysis mineral classification. Drill cuttings can sometimes be contaminated with drilling additives or caved materials, and it is important to note that datasets derived from these sources can sometimes be contaminated and should be interpreted with caution (see Table 7 for full sample details). Core samples (which do not experience this effect) are identified throughout the text and in figures for this reason. Upon reviewing mud logs, the minerals barite and fluorite which are commonly encountered in drilling mud were excluded from the HMA results with the remaining phases normalised to 100 %. Raman spectroscopy was used to differentiate between kyanite, sillimanite and andalusite and between REE phosphate minerals at

University College Cork (UCC). A Renishaw inVia™ confocal Raman microscope with a 50 mW DPSS (diode-pumped, solid-state) 532 nm laser, at 1 second residence time, 10 % laser strength and a x50 long working distance objective was used for these spot analyses. Raman spectra were identified using the RUFF database (Lafuente *et al.*, 2015) and in-house libraries. Mineral phases considered as provenance indicator minerals include zircon, tourmaline, TiO_2 phases, apatite, sphalerite, garnet, titanite, monazite, clinopyroxene, kyanite, staurolite and chrome-spinel. Other phases include abundant pyrite, chalcopyrite, biotite, muscovite and siderite. Once classified, light phases were excluded and heavy mineral groups were normalised to 100% of the total HMA (Zhang *et al.*, 2015). The reported total volume percentage of mineral abundance from the QEMSCAN analysis can introduce biases as naturally larger minerals (e.g., tourmaline) have a higher modal volume than if point counting was undertaken. QEMSCAN analysis also does not differentiate between authigenic and detrital or mineral polymorphs which can also introduce bias; the influence of these biases was considered when interpreting the heavy mineral results. Heavy mineral GZi (garnet vs zircon) and MZi (monazite vs zircon) indices were calculated following Morton *et al.* (1994).

2.4.3. Geochronology

2.4.3.1. Zircon and Apatite U-Pb

A maximum of up to 175 zircon grains in four samples were randomly selected and their positions on grain mounts located in UCC using a Renishaw inVia™ confocal Raman microscope. Zircon and apatite isotopic analysis was conducted using an Agilent 7900 Quadrupole ICPMS coupled to a Photon Machines Analyte Excite 193 nm ArF Excimer laser ablation system with a Helex 2-volume ablation cell at the Department of Geology, Trinity College Dublin. The spot size was 24 µm and 30 µm spots for zircon and apatite analysis, respectively. The primary reference materials were Plešovice zircon (Slama et al., 2008) and Madagascar apatite (Wiedenbeck *et al.*, 1995; Thomson *et al.*, 2012) respectively. The weighted mean ^{206}Pb-^{238}U ages for secondary zircon standards are: in-house zircon standard WRS 1348 (Pointon et al., 2012) = 529.4 ± 2.6 Ma (n = 50), 91500 zircon (Wiedenbeck et al. 1995) = 1055.1 ± 4.6 Ma (n=42) and GZ7 (Nasdala *et al.*, 2018) = 528.6 ± 2.0 Ma (n=50). The ^{207}Pb-corrected apatite secondary standard ages are: McClure Mountain (Schoene & Bowring,

2006) = 526.3 ± 4.7 Ma (n=38) and Durango (McDowell et al., 20025) = 30.4 ± 1.0 Ma (n=45). When compared with the published reference age values, all results are within 2σ uncertainty of their published ages. Reduction of raw isotope data was conducted in Igor Pro software with the Iolite 2.5 package extension. The primary standards Madagascar apatite and Plešovice zircon were used to correct for mass bias, downhole U-Pb fractionation and intra-session instrument drift using the data reduction schemes' VisualAge' for zircon and 'VisualAge_UcomPbine' for apatite (Paton *et al.*, 2011; Petrus *et al.*, 2012; Chew *et al.*, 2014a; Chew *et al.*, 2019a). Apatite is a challenging mineral to accurately date as it can incorporate high levels of common lead (Pb_c) during crystallisation which can result in high Pb_c to radiogenic lead (Pb*) ratios. An iterative Pb_C correction was employed for all detrital apatite unknowns after Chew *et al.* (2014a). As apatite often yields large U-Pb age uncertainties, particularly in grains with high Pb_c / Pb* ratios, the results were filtered using an age dependent uncertainty threshold (Chew *et al.*, 2020), with a 2σ uncertainly filter of 50% employed for grains younger than 100 Ma, 15% for 1000-–100 Ma and 5% for 3.6–1.0 Ga. To maximise precision, zircon single grain concordia ages were calculated using the Isoplot v4.15 Excel add-on for all zircon samples in this study (Ludwig, 2012). Concordant ages for zircon are displayed for a probability of concordance > 0.001 (Zimmermann *et al.*, 2018). Kernel density estimate (KDE) curves were plotted using IsoplotR (Vermeesch, 2018). A 25 Ma bandwidth was chosen for zircon and apatite to limit over smoothing and facilitate cross-sample comparison.

Zircon sample NC22a was analysed in the Department for Science, University of Greenwich. U-Pb LA-ICP-MS analysis was conducted using a Thermo Scientific iCAP Q Quadrupole ICP-MS coupled to an Elemental Scientific NWR213 laser ablation unit fitted with a TwoVol2 ablation chamber. Calibration was achieved using the zircon 91500 reference material which was measured after every 10 unknown grains throughout the measurement run. Accuracy was independently verified by regular measurement of the Plešovice zircon standard, which was treated as an unknown. The weighted mean value of Plešovice single grain ages was calculated at 339.0 ± 4.0 Ma (n=30) and is within published uncertainties (Sláma *et al.*, 2008). A 25 µm spot size was used. Optimum grain sampling during the unattended run was maintained via the use of 'Imagelock' within the laser ablation software platform. The resultant measurements were processed with Iolite v3.7 using its U_Pb_Geochron4 data

reduction scheme. Zircon samples NC1, NC6-NC8, NC17-NC21, GS1 and FB1-FB5 were processed following Fairey *et al.* (2018), from unpublished PhD data.

2.4.3.2. Detrital White Mica

Four white mica samples were irradiated together with Fish Canyon sanidine (FCs) for 18 hours at the Oregon State University TRIGA reactor in the cadmium-shielded CLICIT facility. $^{40}Ar/^{39}Ar$ analyses were performed at the geochronology laboratory of the VU University on a Helix MC noble gas 66 mass spectrometer. Single mica grains were fused with a Synrad CO_2 laser beam and released gas was exposed to NP10 and St172 getters and analysed on the Helix MC. The five argon isotopes were measured simultaneously with ^{40}Ar on the H2-Faraday position with a 10^{13} Ω resistor amplifier, ^{39}Ar on the H1-Faraday with a 10^{13} Ω resistor amplifier, ^{38}Ar on the AX-CDD (CDD – Compact Discrete Dynode), ^{37}Ar on the L1-CDD and ^{36}Ar on the L2-CDD. Gain calibration for the CDDs are done by peak jumping a CO_2 reference beam on all detectors in dynamic mode. All intensities are corrected relative to the L2 detector. Air pipettes are run every ten hours and are used for mass discrimination corrections. The atmospheric air value of 298.56 from Lee *et al.* (2006) is used. Detailed analytical procedures for the Helix MC are described in Monster (2016). The calibration model of Kuiper *et al.* (2008) with an FCs age of 28.201 ± 0.046 Ma and the decay constants of Min *et al.* (2000) are used in age calculations. The correction factors for neutron interference reactions are (2.64 ± 0.02) $x10^{-4}$ for $(^{36}Ar/^{37}Ar)^{Ca}$, (6.73 ± 0.04) $x10^{-4}$ for $(^{39}Ar/^{37}Ar)^{Ca}$, (1.21 ± 0.003) $x10^{-2}$ for $(^{38}Ar/^{39}Ar)^{K}$ and (8.6 ± 0.7) $x10^{-4}$ for $(^{40}Ar/^{39}Ar)^{K}$. All uncertainties are quoted at the 2σ level and include all analytical errors. A 25 Ma bandwidth was chosen for mica to limit over smoothing and facilitate cross-sample comparison with zircon and apatite.

2.4.3.3. Apatite Trace Elements

During U-Pb isotope analysis of apatite, trace element concentrations were simultaneously obtained. The primary standard employed used was NIST 612 standard glass, and a crushed aliquot of Durango apatite, whose trace element abundances are characterised by solution ICP-MS (Chew *et al.*, 2016), was used as a secondary standard. The trace element data were reduced using the Iolite "Trace Elements" data reduction scheme. The apatite trace element chemistry was interrogated using the approach of O'Sullivan *et al.* (2020), which employs

Support Vector Machine (SVM) discrimination to a literature database of apatite-bedrock compositions. This method allows the user to utilise the light rare earth element (LREE, sum of La-Nd) and Sr/Y trace element data collected during U-Pb analysis to differentiate between alkali-rich igneous rocks (ALK), mafic I-type granitoids and mafic igneous rocks (IM), low- and medium-grade metamorphic and metasomatic rocks (LM), partial-melts, leucosomes and high-grade metamorphic rocks (HM), S-type and high aluminium saturation index, 'felsic' I-types granitoids (S) and ultramafic rocks including carbonatites, lherzolites and pyroxenites (UM) (O'Sullivan et al., 2020). The apatite trace element analyses are then plotted on a bivariate (sum LREE vs Sr/Y plot), with each analysis coloured according to its ^{207}Pb-corrected age (Fig. 7). Grains which fail the uncertainty threshold are coloured grey.

2.5. **Results**

Heavy mineral datasets from 21 samples are summarised in Fig. 3. Kernel density estimate (KDE) diagrams of age data from 1144 zircon (15 samples), 214 mica (4 samples) and 176 apatite grains (3 samples including trace element data) from the NCSB, SGCB, Fastnet and Goban Spur Basins are presented. The age data are grouped into six tectonomagmatic populations to facilitate sample comparison (Table 1). These include grain populations — P1; Atlantic rift-related volcanism, P2; Variscan and Acadian, P3; Caledonian, Scandian and Grampian, P4; Peri-Gondwanan, P5; Grenvillian and Pinwarian and P6; Labradorian and Lewisian (see potential sediment sources section for references). It is important to note that the zircon, apatite and mica yield in some samples is limited, and the age data from these small populations should be interpreted with caution. Samples NC7, NC8, NC11, NC17, NC19 and SG5 are from core samples while the remainder are drill cuttings.

Fig. 5. *Total heavy mineral abundance of samples from the Middle Jurassic to Upper Cretaceous sequences of the NCSB and SGCB. Note that three samples contained 130 – 200 HM grains and should be interpreted with caution (see Table 6).*

2.5.1. Heavy Mineral Analysis

QEMSCAN analysis of 21 heavy mineral separates characterised between 137 – 7993 heavy mineral grains per sample. These results are summarised as a percentage of total volume in Fig. 5 (Zhang *et al.*, 2015). Three out of 21 samples contained less than 200 grains (137; 177; 188) and may not fully represent the heavy mineral population (Morton, 1982). Mineral ratios were calculated after Morton *et al.* (1994) where mineral counts were substituted for total volume %. In addition, multivariate principal component analysis (PCA) using the R package "Provenance" was chosen to identify mineral correlations (Vermeesch *et al.*, 2016) (Fig. 6). TiO_2 polymorphs like anatase/brookite as well as sphalerite are common authigenic phases (Mange *et al.*, 1992) and have not been differentiated from authigenic and detrital phases. Therefore, TiO_2 phases may represent authigenic (anatase/brookite) or detrital (rutile) grains.

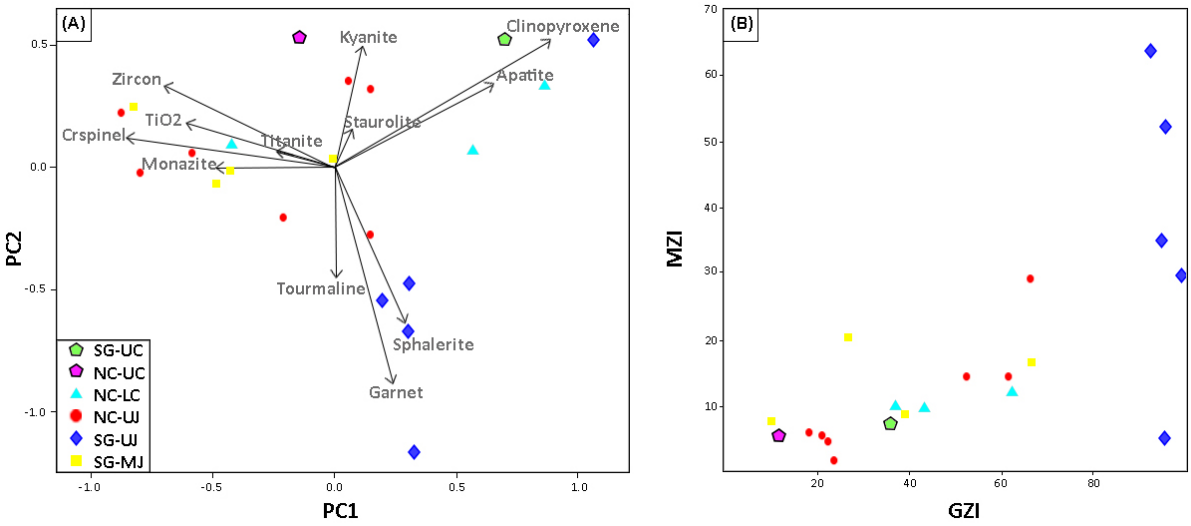

Fig. 6. *PCA biplot of HMA results from Middle Jurassic to Upper Cretaceous samples. (B) Biplot of GZi vs MZi ratios. Symbols used in both figures represent the same samples. NC-UJ, NCSB Upper Jurassic; SG-UJ, SGCB Upper Jurassic; SG-MJ, SGCB Middle Jurassic samples; NC-LC, NCSB Lower Cretaceous; SG-UC, SGCB Upper Cretaceous; NC-UC, NCSB Upper Cretaceous.*

2.5.1.1. Middle Jurassic – Upper Jurassic Samples

Middle Jurassic sediments of the SGCB comprise abundant TiO_2 phases, apatite, tourmaline, garnet and zircon with some clinopyroxene, sphalerite, monazite and titanite in places (Fig. 5). Upper Jurassic samples of the SGCB contain abundant apatite, tourmaline and garnet with limited TiO_2 phases and sphalerite. Upper Jurassic samples of the NCSB have abundant zircon,

tourmaline, TiO_2 phases and apatite with some garnet and traces of sphalerite, titanite and staurolite indicative of a metamorphic, igneous or hydrothermal source. Upper Jurassic samples from the SGCB generally contain less zircon and more tourmaline, garnet and sphalerite than those of the NCSB.

2.5.1.2. Cretaceous Samples

The Lower Cretaceous samples NC23 – NC25 (Wells 50/03-01 and 50/03-02) are composed of 18% to > 42% apatite along with TiO_2 phases, tourmaline and garnet. Limited zircon and chrome spinel make up the remainder of the samples, like the Upper Jurassic samples of the SGCB (Fig. 5 and Fig. 6). Principal component analysis of the heavy mineral data shows that the Lower Cretaceous samples positively correlate with PC1 because of the increase in staurolite and kyanite. The Upper Cretaceous sample NC22 (Well 50/07-01) also contains significant apatite and TiO_2 phases but with a marked increase in staurolite and kyanite. Sample SG16 (Well 106/28-1) also contains abundant TiO_2 phases and apatite, with more clinopyroxene than any other sample from the NCSB or SGCB (Fig. 6). This further supports the presence of a proximal igneous source.

Principal component analysis of the HMA data is summarised in Fig. 6A. PC1 correlates positively with clinopyroxene and apatite and to a lesser extent with sphalerite and garnet and negatively correlates with zircon, TiO_2 phases, chrome spinel and monazite. As sphalerite is positively correlated with garnet and tourmaline, it is likely from a metamorphic or igneous source, but may also be related to authigenic growth. Kyanite, apatite, zircon and clinopyroxene positively correlate with PC2 and there is a strong negative correlation with garnet, sphalerite and tourmaline. The PCA and MZi *vs* GZi ratio plots successfully distinguish the garnet-rich and zircon-poor Late Jurassic sediments of the SGCB from all other samples (Fig. 6b).

2.5.2. Zircon U-Pb Geochronology

2.5.2.1. Middle Jurassic

The Middle Jurassic (Callovian) sample GS1 (Well 62/07-1) from the Goban Spur Basin has a dominant c. 1.7 Ga (Labradorian – Lewisian) population (Fig. 7). Caledonian – Grampian zircon, and some Archean and Grenville grains comprise the rest of the sample population. The Bathonian sample SG5 (core from Well 107/16-1) from the SGCB contains a dominant Grenville population centered around 1.0 Ga with some Pinwarian and Archean detritus. In both samples, the absence of significant late Neoproterozoic zircon is noteworthy and indicates an absence of Peri-Gondwanan input.

Table 1. Single grain age groups based on significant orogenic events where P = Population. Groupings are defined as discussed in Potential Sediment Sources section.

Grain Population	Min (Ga)	Max (Ga)	Tectonic Association
Gpop6	1.5	2.9	Labradorian, Lewisian
Gpop5	0.9	1.5	Grenville, Pinwarian
Gpop4	0.5	0.7	Peri-Gondwanan
Gpop3	0.39	0.47	Caledonian, Grampian, Scandian
Gpop2	0.29	0.39 /0.4	Acadian, Variscan
Gpop1	0.07	0.27	Atlantic rift related volcanism

2.5.2.2. Upper Jurassic

The Upper Jurassic samples NC6 (Well 49/15-1), NC7 (core from Well 49/9-3), NC8 (core from Well 49/10-1), NC9 (Well 50/03-1) and NC10 (Well 50/03-02) from the NCSB share similar diverse zircon U-Pb age populations from 0.4 to 2.7 Ga, with abundant sub-peaks (Fig. 7). Unlike the Middle Jurassic samples above, zircon of Peri-Gondwanan affinity is abundant in all samples. Core sample NC7 contains a young 176 Ma zircon population (n = 3).

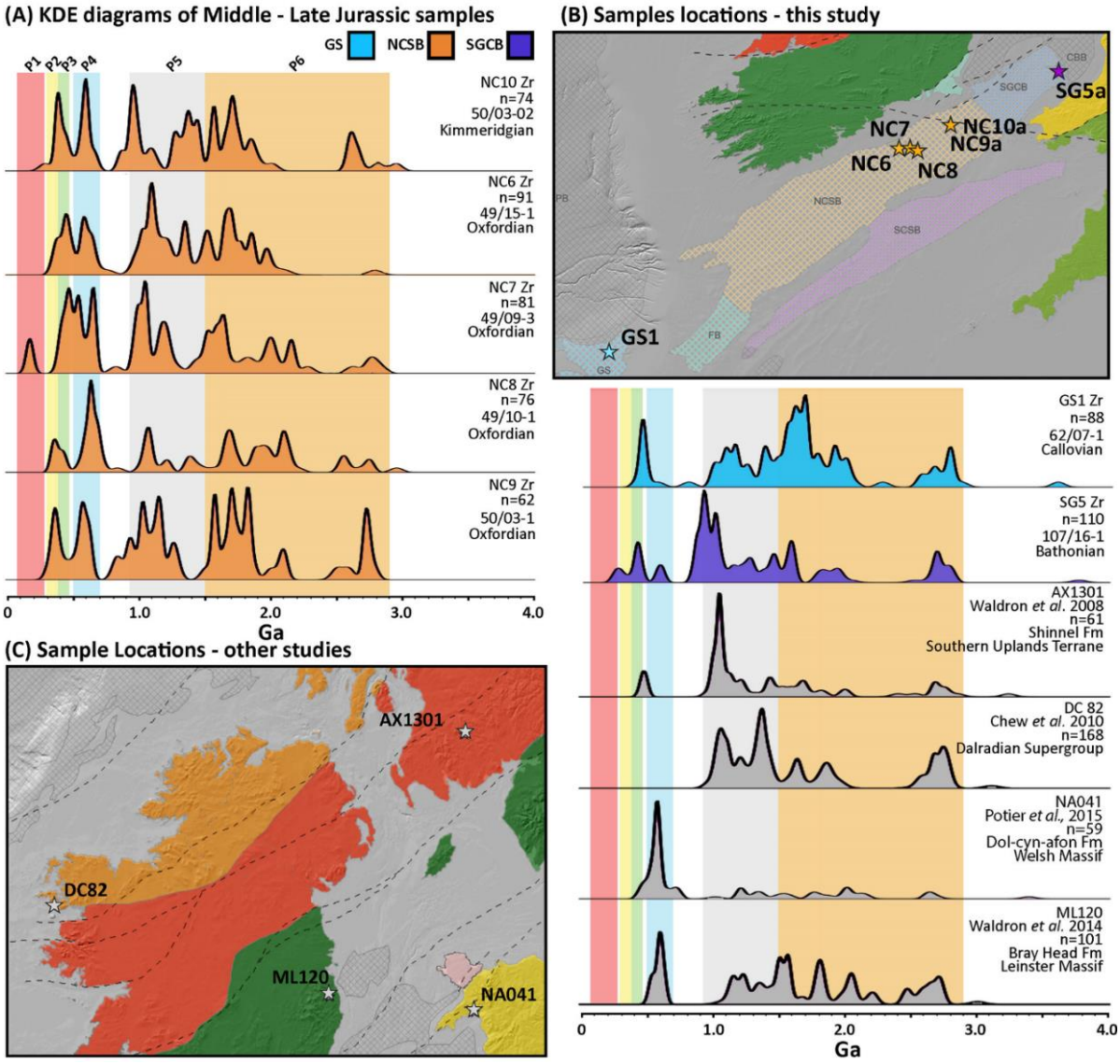

Fig. 7. *(A) KDE diagrams of detrital zircon from Middle to Upper Jurassic samples. (B) Sample locations. For further details see Table 2 supplementary information. (C) Representative source samples from Waldron et al. (2008), Chew et al. (2010), Waldron et al. (2014) and (Pothier et al., 2015).*

2.5.2.3. Cretaceous

The Variscan-Acadian (P2) and Caledonian-Scandian-Grampian populations (P3) dominate in the Lower Cretaceous (Valanginian – Barremian) zircon samples NC18 (Well 48/18-1), NC19 (Core sample, Well 48/24-4), NC20 (Well 48/28-1), NC26 (Well 56/22-1) and FB4 (Well 56/26-2). These samples lack significant Grenville-Pinwarian (P5) and Labradorian-Lewisian (P6) U-Pb zircon populations, which marks an important provenance switch compared to the Jurassic samples (Fig. 8). The Albian sample NC17 (Well 49/9-2) comprises mostly Proterozoic, Peri-Gondwanan (P4) and Caledonian (P3) grains with a single 128 Ma zircon, the youngest zircon

found in this study, and broadly mirrors the zircon age population seen in the Campanian sample NC22 (Well 50/07-01). Samples NC22 and NC17 lack a 2.0 Ga population and have subordinate Peri-Gondwanan and dominant Paleozoic populations.

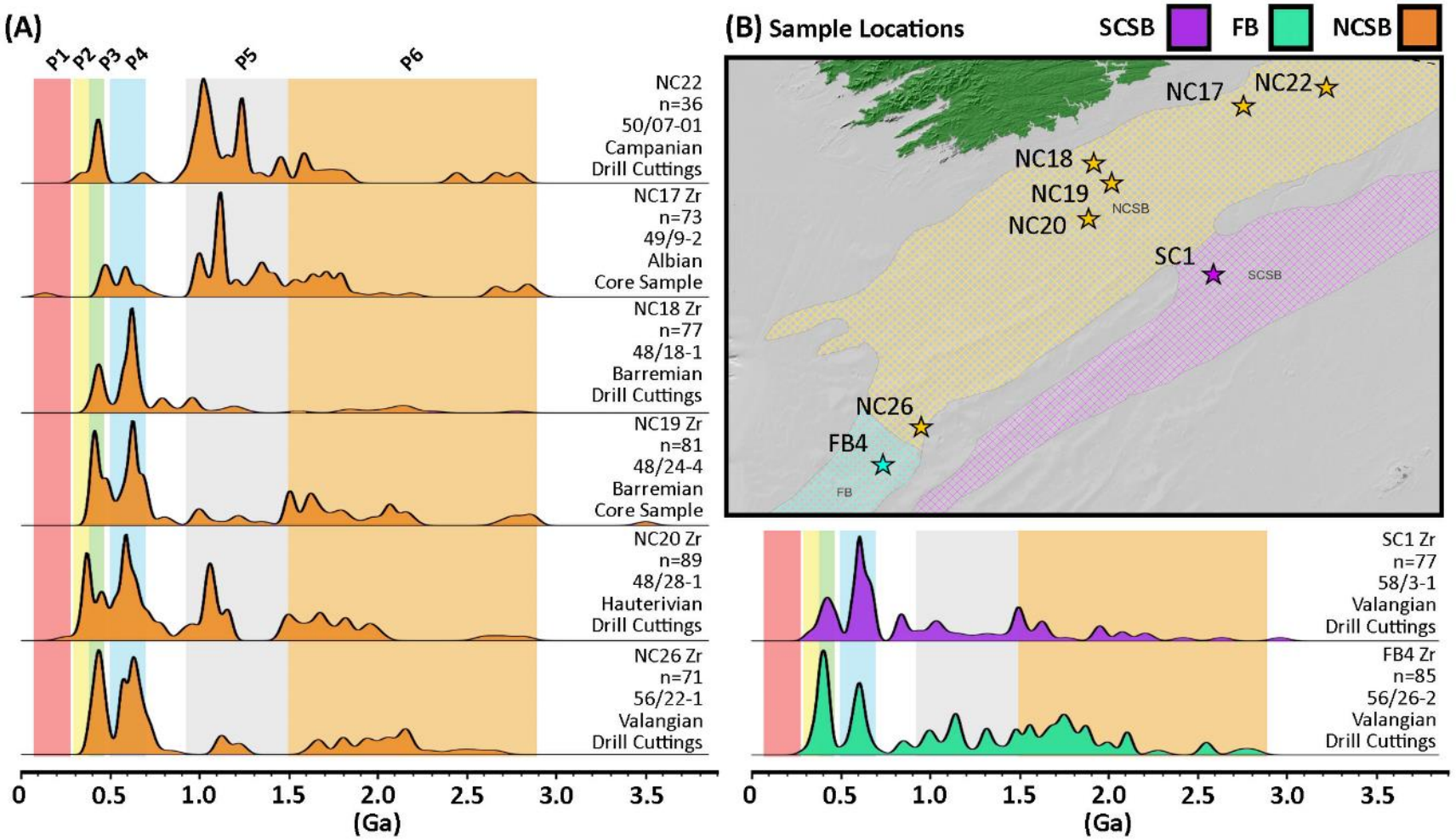

Fig. 8. *(A) Lower and Upper Cretaceous detrital zircon results summarised in KDE diagrams from the NCSB and SGCB. For classification of the population groupings, see Table 1. (B) Well locations for sampling. For further details see Table 2 supplementary information.*

2.5.3. Apatite U-Pb Geochronology and Trace Elements

2.5.3.1. Middle Jurassic

Apatite from the Bathonian core sample SG5 comprises a multi-source trace element signature (Fig. 9). The broadly syn-depositional (230-160 Ma) population has a mixed mafic/I-type granite affinity, while the 320–280 Ma Variscan grains have a mafic/I-type granite affinity along with apatite grains derived from low-grade metamorphic rocks. Older (late Grenville, c. 900 Ma) apatites have a mixed metamorphic and igneous affinity. Much of the ultramafic and low-grade metamorphic apatite resulted in ages with large uncertainties which fail the U-Pb age uncertainty filter and are hence underrepresented in the U-Pb geochronology KDE plots (Fig. 9C). The absence of Mesoproterozoic and older apatite in this sample is noteworthy compared to the zircon age spectra from the same sample while the younger 300–160 Ma sources are clearly underrepresented in the zircon populations of SG5 (Fig. 7). The youngest apatite age population in sample SG5a suggests an active igneous source of ultramafic-mafic affinity in or near the NCSB and SGCB during the Middle-Late Jurassic (See Table 4); this is only poorly recorded in the zircon dataset (e.g., a sub-population at 176 Ma in core sample NC7, Fig. 7).

2.5.3.2. Cretaceous

Cenomanian apatite sample SG16 (Well 106/28-1) contains Scandian-Caledonian and syn-depositional Cretaceous populations with distinct c. 95 Ma and c. 420 Ma peaks. Apatite trace element plots for this sample show a mafic/I-type igneous signature for all grains with two distinct populations within this field on the SVM plot (Fig. 9A). In sample NC22 (Well 50/07-01), the apatite is derived from a single Cretaceous (c. 95 Ma) population with a mafic to ultramafic igneous affinity. The abundant Cretaceous apatite (and a single zircon dated at 128 Ma in sample NC17) demonstrate a syn-depositional igneous source unrecognised in the NCSB and SGCB to date.

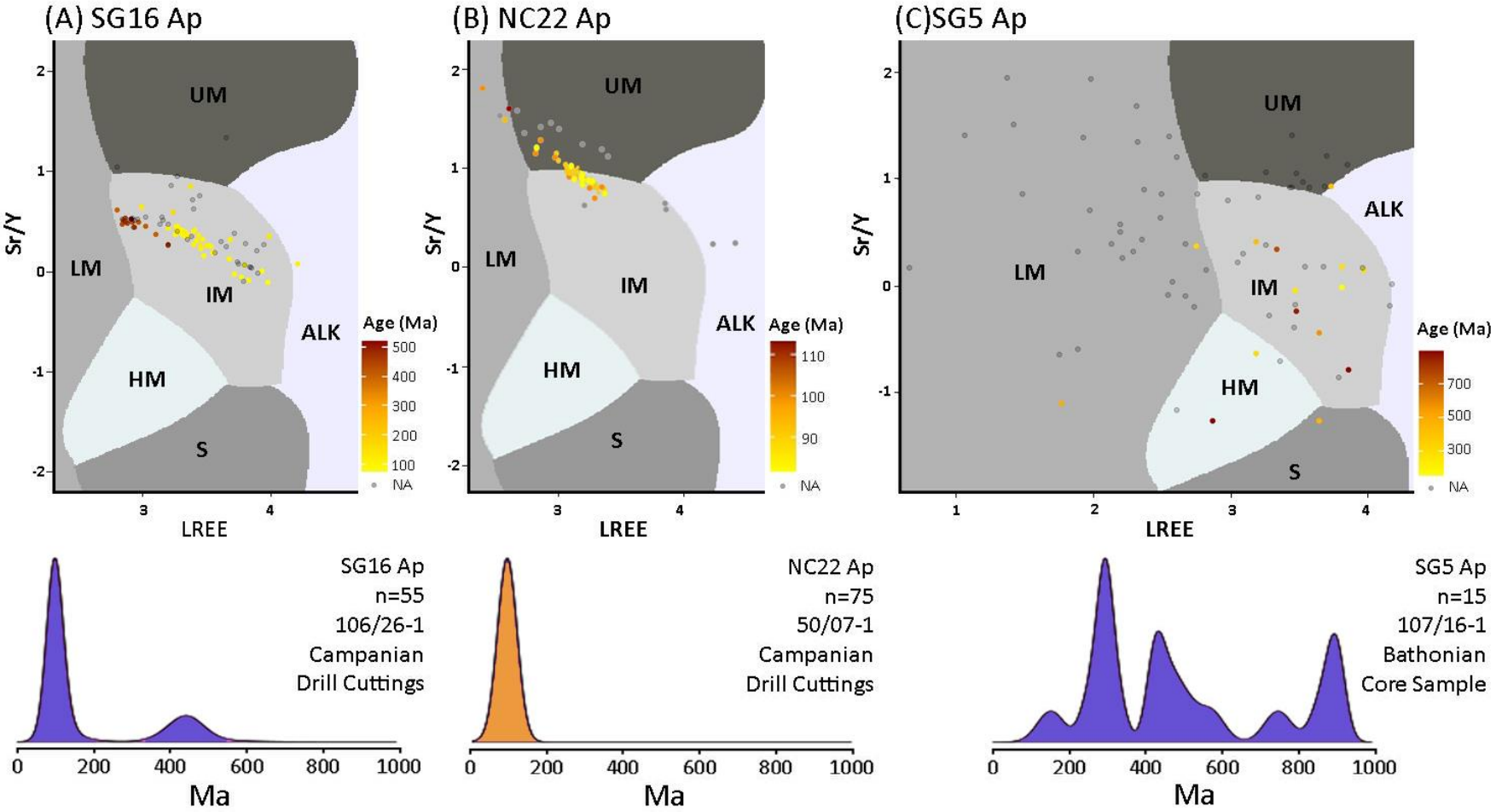

Fig. 9. *Apatite trace element SVM biplots with corresponding KDE U-Pb apatite diagrams from Jurassic and Cretaceous samples. (A) SG16 from the Upper Cretaceous. (B) NC22 from the Upper Cretaceous (C) SG5 from the Middle Jurassic. ALK, alkali-rich igneous rocks; IM, mafic I-type granitoids and mafic igneous rocks; LM, low-medium grade metamorphic and metasomatic; HM, partial-melts/leucosomes/high-grade metamorphic; S, S-type granitoids and high aluminium saturation index (ASI) 'felsic' I-types; UM, ultramafic rocks including carbonatites, lherzolites and pyroxenites (O'Sullivan et al., 2020). For further details see Table 3 for U-Pb and Table 4 for trace element information.*

2.5.4. White Mica Ar-Ar Geochronology

Jurassic core sample NC7 (Well 49/9-03), along with Cretaceous samples NC19 (core from Well 48/24-4) and NC17 (Well 49/9-02) yield white mica of late Caledonian or Acadian affinity (main peak at 435 Ma), an age peak which is also detected in zircon populations of the NCSB (Fig. 10). The Valanginian sample NC27 (Well 56/15-01) located toward the southern margin of the NCSB contains a slightly younger Caledonian – Acadian population (395 Ma) with an additional Peri-Gondwanan sub-population and a single white mica dated at 1423 Ma.

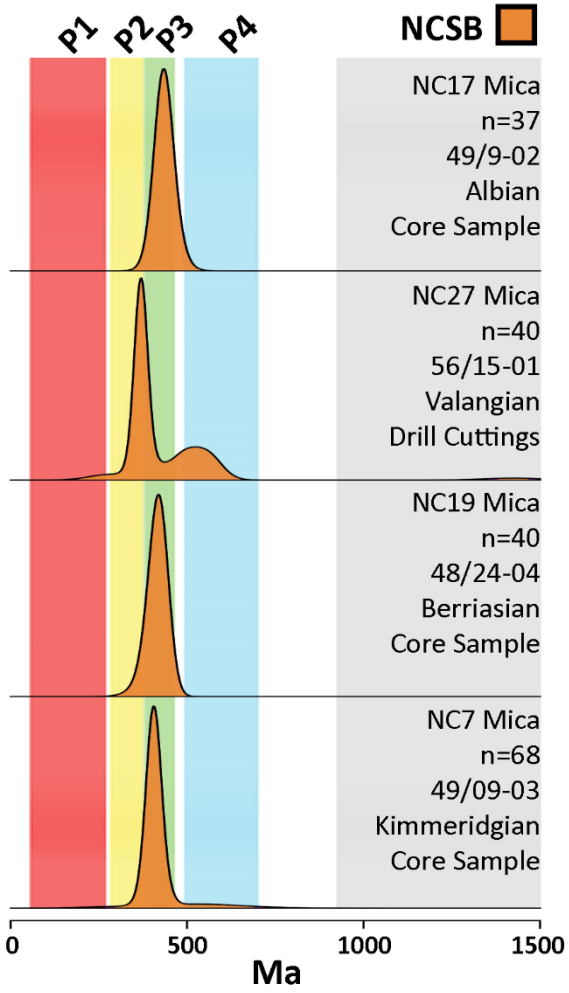

Fig. 10. *$^{40}Ar/^{39}Ar$ dating of detrital white mica samples from Jurassic and Cretaceous sediments of the NCSB. For further details see Table 5 supplementary information.*

2.6. **Discussion**

2.6.1. Middle Jurassic Provenance

During the Middle Jurassic, the initial phases of far-field Cimmerian tectonism uplifted the entire southern margin of the study area (Rodríguez-Salgado *et al.*, 2019). Heavy mineral assemblages from the SGCB indicate a metamorphic, igneous or hydrothermal source for these sediments (Fig. 5). The Callovian sample GS1 from the Goban Spur Basin, and the Bathonian core sample SG5 from the SGCB, were deposited prior to or during, this uplift event when the Irish and Celtic Sea regions were connected (Fig. 9). U-Pb Zircon populations in these samples differ, with the Goban Spur sample GS1 exhibiting a dominant 1.7 Ga Proterozoic KDE peak while the SGCB has an asymmetric series of Proterozoic KDE peaks culminating in a 1.0 Ga Grenville population (Fig. 7).

This Grenville population in the SGCB (core sample SG5) is likely sourced predominantly from the north. A c. 1.9–1.0 Ga zircon population is prominent in the Longford Down – Southern Uplands terrane and the Silurian sequences of the Lake District (Waldron *et al.*, 2014) (see Fig. 7). The apatite U-Pb data (sample SG5) also support dominant north-derived input into the SGCB, as 275 Ma mafic/I-type granitoids are indicative of the Midland Valley Terrane of the Scottish Massif (Monaghan *et al.*, 2004). The c. 900 Ma (late Grenville) apatite is likely derived from a northern source – either the Southern Uplands – Longford Down terrane (for which no apatite U-Pb data are available), or from portions of the Laurentian basement which record post-Grenville cooling with no significant Caledonian (*sensu lato*) tectonothermal overprinting (Fig. 9C). The c. 170 Ma ultramafic-mafic apatite is likely sourced from Middle Jurassic volcanism in the Fastnet Basin (Caston *et al.*, 1981), suggesting a dominant northern and subordinate southern input to the SGCB (Fig. 11). If these magmatic sources were eroded and the resulting sediment transported by marine currents or littoral drift into the SGCB, this would indicate inter-basin connectivity, but a pyroclastic origin is also possible (Fig. 9C). Material from the Goban Spur Basin (GS1) has a more prominent 1.7 Ga population. This dominant Laurentian signature in GS1 is likely from a Laurentian source to the north, of which the most proximal sources would include the Dalradian Supergroup (Chew *et al.*, 2010), Rhinns Complex, or granitic orthogneisses of the Porcupine High (Chew *et al.*, 2019b).

Importantly, Late Neoproterozoic populations in GS1 and SG5 are either minor or absent. This indicates that there was minimal sourcing from Cadomia to the south or from recycling of post-Caledonian cover sequences of onshore Ireland such as the Leinster Massif and Clare Basin (Morton *et al.*, 2016; Nauton-Fourteu *et al.*, 2020). Potential sourcing from the Upper Devonian Munster Basin is more difficult to establish. The Upper Old Red Sandstone of the Munster Basin contains little Neoproterozoic detrital zircon and abundant Silurian and Grenville detrital zircon (Fairey, 2017), similar to sample SG5. Thus it is not possible to definitively rule out this potential source as a significant contributor of Laurentian detrital zircon in this sample. However when the detrital zircon data are combined with the U-Pb and trace element data and the heavy mineral abundance results, a more distal northern source region is thought more likely.

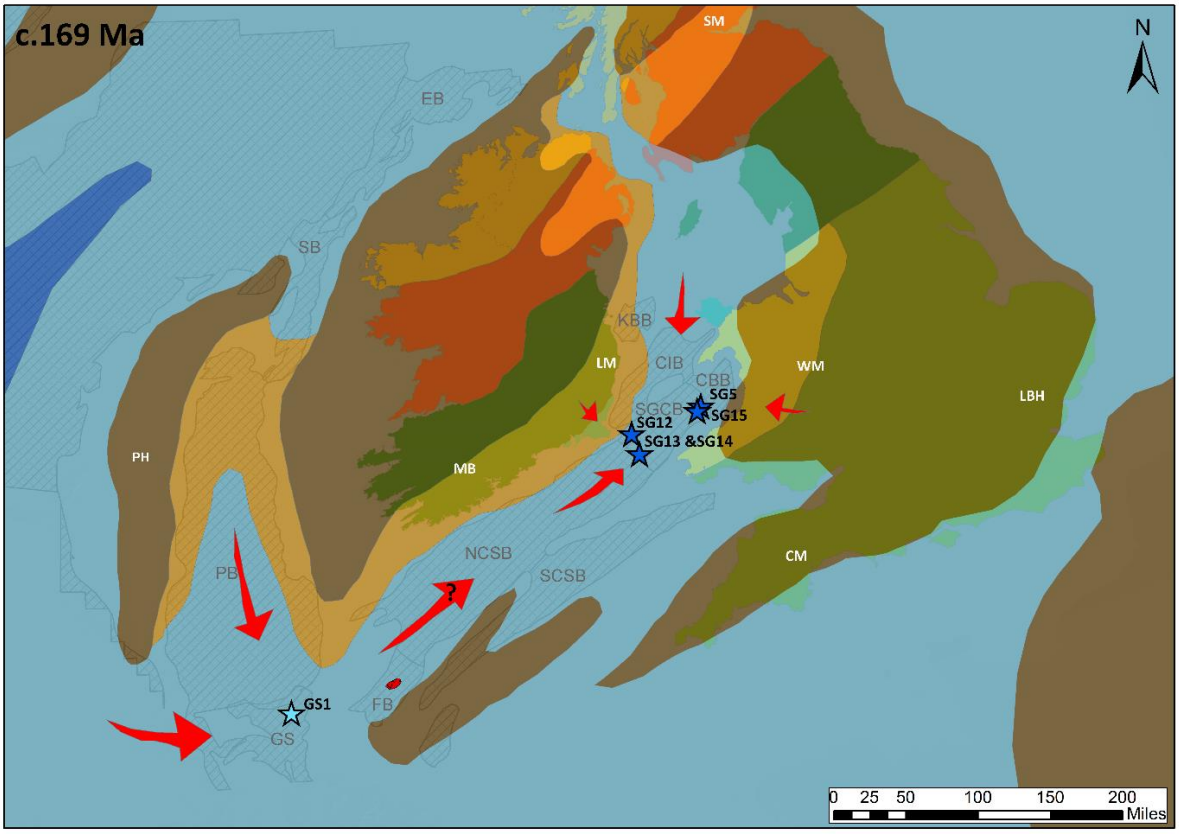

Fig. 11. *Bajocian palaeoenvironmental reconstruction after Shannon et al. (1998), Naylor et al. (2011) and Keeley (1995). Dark brown – topographical highs, light brown – topographical lows, light blue – shallow marine environments, navy – deeper marine, red – igneous centre. Cross-hatch polygons mark basin boundaries and red arrows indicate sediment transport direction. MB, Munster Basin; LM, Leinster Massif; CM, Cornubian Massif; LBH, London Barbrant High; WM, Welsh Massif; MCT, Monian Composite Terrane; PH, Porcupine High.*

2.6.2. Late Jurassic Provenance

By the Late Jurassic, Cimmerian exhumation had established a land barrier which separated the Celtic and Irish Sea Basins from the Goban Spur Basin (Fig. 12). Uplift in the SGCB region resulted in shallow marine conditions while the NCSB persisted as an open marine environment. Sediment is thought to have been derived from the basin margins producing sand-prone marine carbonates, and continental fluvial deposits with limited basin connectivity in the Irish and Celtic Sea Regions (Caston, 1995; Naylor *et al.*, 2011). The HMA principal component analysis, and MZI and GZI ratios show that Middle Jurassic samples in the SGCB (SG5, SG12, SG13 and SG15) and Upper Jurassic samples in the NCSB (NC9-NC11 and NC13-NC16) are rich in zircon and TiO_2 phases (albeit some may be authigenic), while Upper Jurassic samples in the SGCB (SG7 – SG10) are zircon-poor and tourmaline- and garnet-rich and are highly distinctive on the PCA and MZI *vs* GZI plots (Fig. 6). These results signal a provenance switch from the Middle to Late Jurassic in the SGCB, and that the NCSB and SGCB were likely not connected during the Late Jurassic. The negative correlation with PC1, and positive correlation with PC2 of the Middle Jurassic SGCB and Upper Jurassic NCSB HMA samples in Fig. 6A, indicates a similar provenance of mixed metamorphic, igneous and recycled sedimentary successions.

The Upper Jurassic NCSB U-Pb detrital zircon spectra (NC6-NC10) contain diverse Laurentian 2.9–0.9 Ga populations, but also, significantly, a prominent c. 700 Ma Peri-Gondwanan population. Comparatively, Bathonian sample SG5 (Fig. 7) contains dominant Grenville and subordinate Peri-Gondwanan and Labradorian U-Pb zircon populations supporting the Middle-Late Jurassic provenance switch observed in SGCB HMA samples. This implies that the Leinster Massif and Welsh Massif, which contain dominant Peri-Gondwanan populations (Waldron *et al.*, 2014; Pothier *et al.*, 2015) and the uplifted Fastnet Basin and onshore Munster Basin, which containing mixed Laurentian and Peri-Gondwanan populations, were potential sources into the NCSB. Assuming the Oxfordian biostratigraphic age assigned to sample core NC7 is accurate, then the small but conspicuous 176 Ma zircon population present in this sample (weighted average age of three grains = 176.6 ± 1.9 Ma) supports recycling from the Fastnet Basin, as no other intrusive or volcanic body of this age is found in the surrounding area (Caston *et al.*, 1981). These findings partially support local sediment

sourcing as proposed by Caston (1995), with an additional, previously unrecognised, component of recycled detritus from the uplifted Fastnet Basin region.

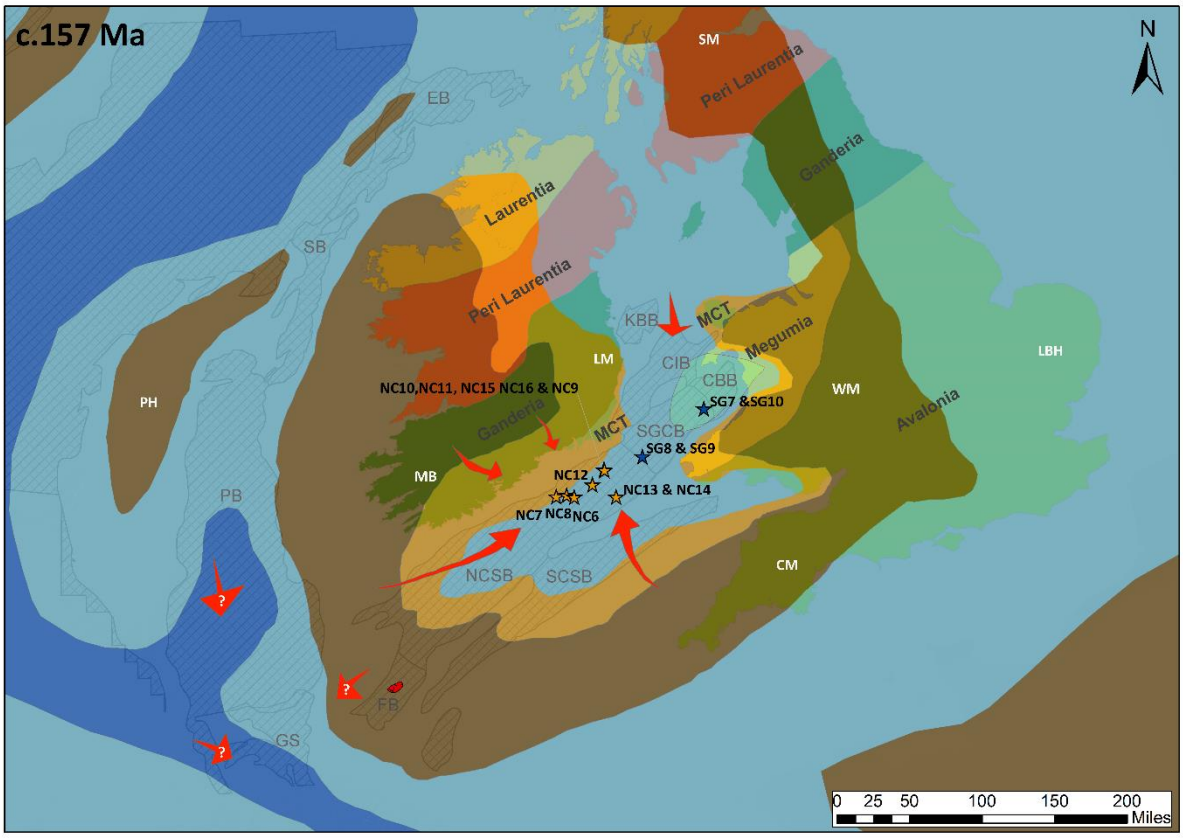

Fig. 12. *Palaeoenvironmental model during the Kimmeridgian and Oxfordian after Shannon and Naylor (1998), Naylor and Shannon (2011) and Keeley (1995). Dark brown – topographical highs, light brown – topographical lows, light blue – shallow marine environments, navy – deeper marine, red – igneous centre. Crosshatch polygons mark basin boundaries and red arrows indicate sediment transport direction. MB, Munster Basin; LM, Leinster Massif; CM, Cornubian Massif; LBH, London Barbrant High; WM, Welsh Massif; MCT, Monian Composite Terrane; PH, Porcupine High.*

2.6.3. Early Cretaceous Provenance

A late phase of Cimmerian tectonism induced a regression during the Early Cretaceous causing fluvial sedimentation of the Purbeck and Wealden Groups in the Irish and Celtic Sea basins (Rodríguez-Salgado *et al.*, 2019) (Fig. 13). Exhumation of the Leinster Massif and Munster Basin regions was also ongoing throughout this period (Cogné *et al.*, 2016). Heavy mineral samples from the northern margin of the NCSB (NC23-NC25) contain abundant apatite and TiO_2 phases, some tourmaline, staurolite, sphalerite, zircon and limited kyanite,

monazite and titanite. This broadly reflects input from igneous and metamorphic sources, supporting sediment derivation from the Monian Composite Terrane, and Welsh and Leinster Massifs (Fig. 6). U-Pb zircon and Ar-Ar mica results from the Lower Cretaceous (Valangian-Barremian) successions (NC18-NC20, NC26, SC1 and FB4) contain dominant Neoproterozoic-Palaeozoic and subordinate 2.9–0.9 Ga (Laurentian) detrital zircon populations (Fig. 8 & 10), indicating sourcing from the Munster Basin (Fairey, 2017), Welsh Massif (Pothier *et al.*, 2015) and/or Leinster Massifs (Waldron *et al.*, 2014). This therefore supports earlier models such as Robinson *et al.* (1981) and Ainsworth *et al.* (1985) that proposed sediment sourcing from western sources like the Munster Basin and Leinster massif. The decrease in Laurentian-derived populations in the Early Cretaceous is attributed to a marine regression disconnecting Laurentian sources with the Celtic Sea, and tectonic quiescence limiting inter-basin recycling.

During the Albian, sedimentation was significantly influenced by transgressive conditions initiated by post-rift related thermal subsidence (Taber *et al.*, 1995) (Fig. 14). Isopach, sediment facies and petrographic analysis on the Greensand and Wealden/Selbourne groups by Winn Jr (1994), Taber *et al.* (1995) and Hartley (1995) suggest that sediment was sourced locally from reworked Wealden Group to the south, or the Leinster and Welsh massifs and the Munster Basin. Detrital zircon U-Pb spectra from the Albian core sample NC17 (Well 49/9-2) comprises an asymmetric 1.1 Ga Grenville population, and a significantly reduced Neoproterozoic (peri-Gondwanan) population compared to the underlying Valanginian-Barremian sequences. This population is likely sourced from the Gyleen Formation of the Munster Basin (Fairey, 2017) proximal to the sample site of NC17 (Well 49/9-2) which has a Laurentian provenance, or more distally from the Southern Uplands – Longford Down terrane (cf Waldron *et al.* (2014);Fig. 7). These data do not support reworking from the Wealden Group, Leinster or Welsh Massifs, as these units are all characterised by prominent Peri-Gondwanan zircon peaks (e.g., see Wealdon Group samples NC18-NC20 in Fig. 8).

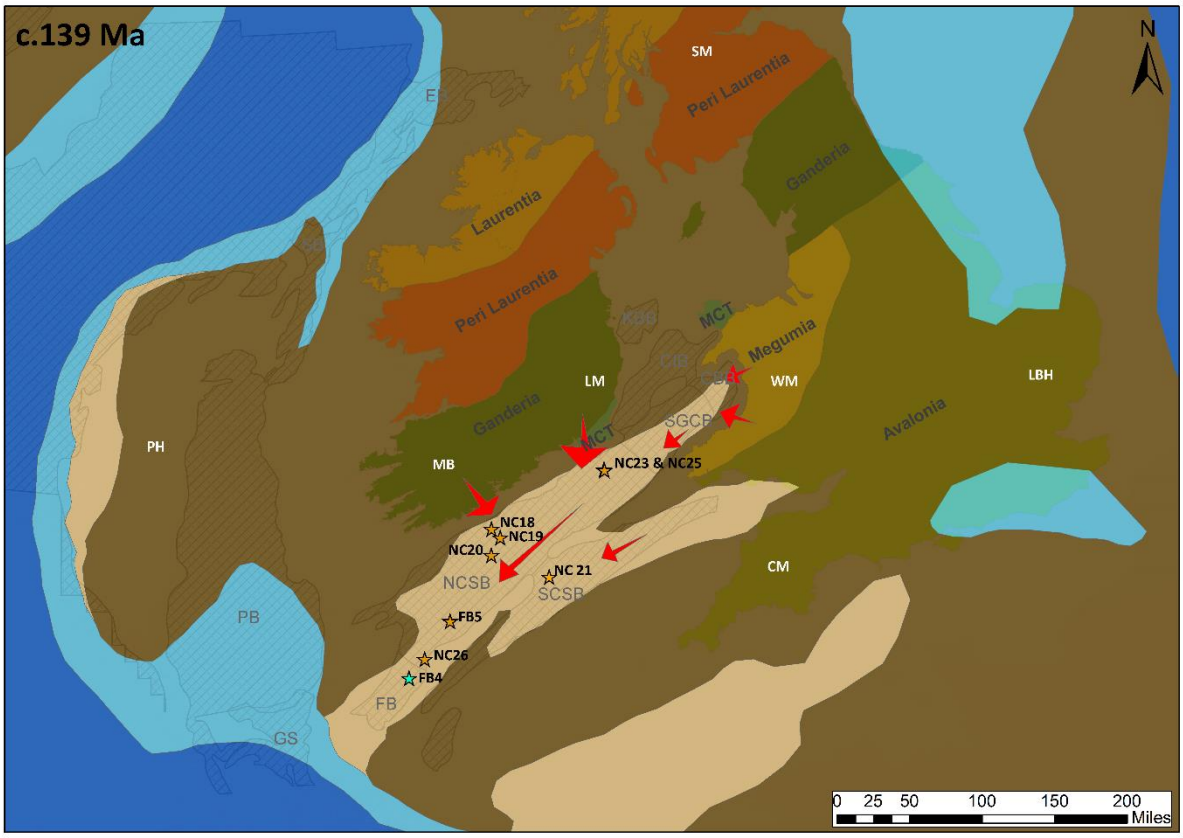

Fig. 13. *Palaeoenvironmental reconstruction during the Early Cretaceous (Hauterivian) after Rodríguez-Salgado et al. (2019),; (Naylor et al., 2011), Ewins et al. (1995) and Ainsworth et al. (1985). Dark brown – topographical highs, light brown – topographical lows, light blue – shallow marine environments, navy - deeper marine, red – igneous centre. Cross hatch polygons mark basin boundaries and red arrows indicate sediment transport direction. MB, Munster Basin; LM, Leinster Massif; CM, Cornubian Massif; LBH, London Barbrant High; WM, Welsh Massif; MCT, Monian Composite Terrane; PH, Porcupine High.*

2.6.4. Late Cretaceous Provenance

By the Turonian, initial deposition of the Chalk Group had begun as transgressive conditions progressed across northern Europe (Fig. 14) (Hancock, 1989). U-Pb apatite and trace element analysis combined with HMA data from samples SG16 and NC22 indicates an ultramafic-mafic source region with continuous igneous activity from 130–85 Ma such as, the Porcupine, Goban Spur and Fastnet Basins mixed with older Caledonian sources like the Leinster and Welsh Massifs. The presence of kyanite, garnet and staurolite indicates an additional metamorphic source. Additionally, the abundance of apatite with an igneous trace element chemistry in NC22 and SG16 support a significant magmatic source. Given that the detrital

zircon spectrum from NC22 favours a Laurentian source, the metamorphic source terrane is more likely a terrane with a Laurentian affinity such as the Dalradian Supergroup in northwest Ireland possibly transported by long-distance marine mechanisms into the Celtic Sea, like the ultra-long distance littoral transport observed along the west coast of Namibia (Garzanti *et al.*, 2014). The Munster Basin likely contributed some Laurentian detritus to these Upper Cretaceous successions also (Fig. 8A). The syn-depositional (c. 95 Ma) Cretaceous apatite population in samples NC22 and SG16, are probably from the pyroclastic ash cloud deposits from magmatism along the Fastnet Basin or another rift-related magmatic sources in the region.

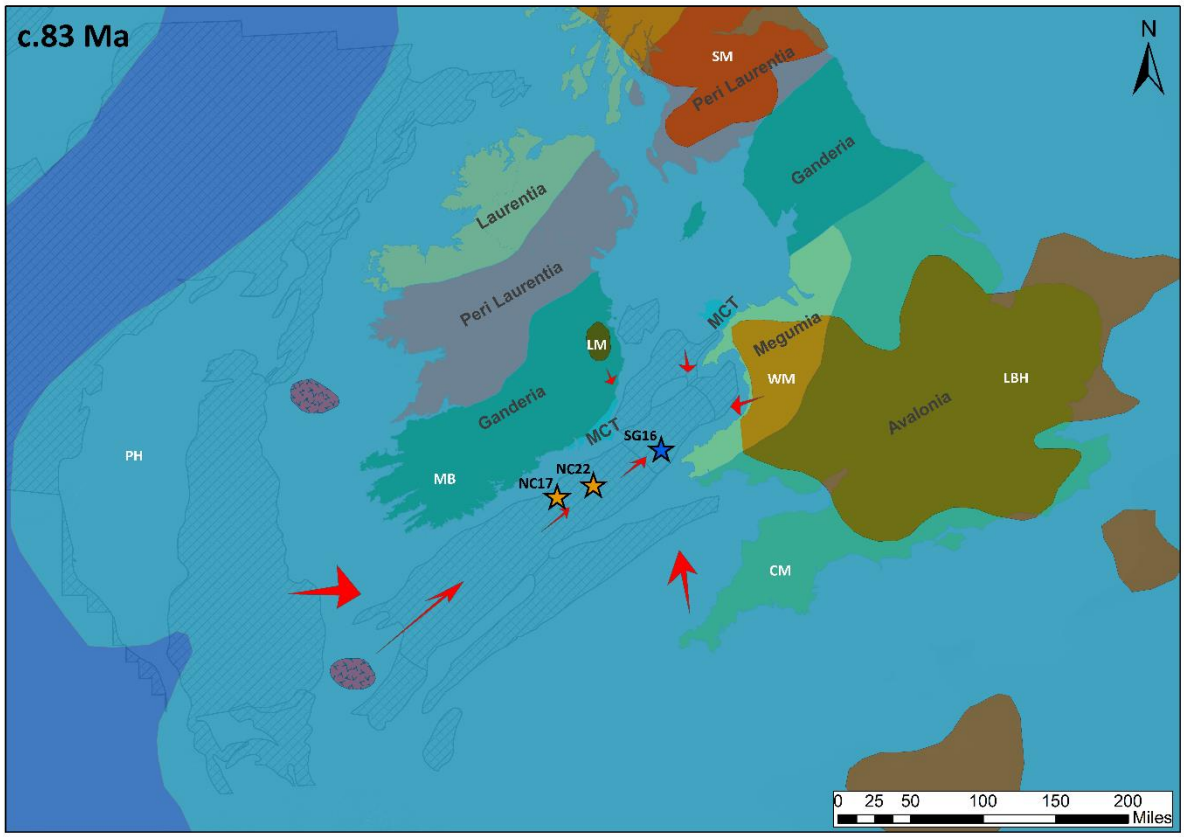

Fig. 14. *Palaeoenvironmental reconstruction during the Late Cretaceous (Campanian) after Naylor et al. (2011), (Shannon, 1991a) and Hancock (1989). Sediment routing is indicated by red arrows. Dark brown – topographical highs, light brown – topographical lows, light blue – shallow marine environments, navy – deeper marine, red – igneous centre. Cross hatch polygons mark basin boundaries and red arrows indicate sediment transport direction. MB, Munster Basin; LM, Leinster Massif; CM, Cornubian Massif; LBH, London Barbrant High; WM, Welsh Massif; MCT, Monian Composite Terrane; PH, Porcupine High.*

2.7. **Conclusions**

Transgression-regression cycles and Cimmerian tectonism exhibited strong control on distal *versus* proximal sediment sourcing in the Irish and Celtic Sea basins during the Middle Jurassic to Late Cretaceous. Recycling of sediments from the Munster Basin into the offshore domain remains a significant provenance challenge and requires a multi-proxy provenance approach. These controls resulted in three distinct provenance switches demonstrating that sediment did not principally derive from local sources. These findings suggest the following:

1. Laurentian-derived sediment was the dominant source in the connected Goban Spur Basin, Fastnet Basin, NCSB and SGCB during the Middle Jurassic.
2. Possible derivation from a Middle Jurassic volcanic source in the Fastnet Basin is identified in the SGCB implying basin connectivity or ash fall sedimentation into the surrounding basins.
3. Late Jurassic Cimmerian tectonism reworked strata from the Fastnet Basin and marginal basin regions into the Celtic sea and SGCB inhibiting sediment exchange between the NCSB and SGCB.
4. Fluvial sedimentation during the Early Cretaceous drained from the Irish and Welsh Massifs into the NCSB, SCSB, SGCB, and Fastnet Basins.
5. During a transgression in the Late Cretaceous, Laurentian-derived sediment likely transported from the Dalradian Supergroup of western Ireland by marine mechanisms into the NCSB and SGCB, along with pyroclastic deposits from syn-rift ultramafic-mafic magmatism.

2.8. **References**

Ainsworth, N. R., Horton, N. F., & Penney, R. A. (1985). Lower Cretaceous micropalaeontology of the Fastnet Basin, offshore south-west Ireland. *Marine and Petroleum Geology, 2*(4), 341-349. doi:https://doi.org/10.1016/0264-8172(85)90029-7

Allen, P. (1981). Pursuit of Wealden models. *Journal of the Geological Society, London, 138*(4), 375-405. doi:https://doi.org/10.1144/gsjgs.138.4.0375

Allen, P. A., Bennett, S. D., Cunningham, M. J. M., Carter, A., Gallagher, K., Lazzaretti, E., Galewsky, J., Densmore, A. L., Phillips, W. E. A., Naylor, D., & Hach, C. S. (2002). The post-Variscan thermal and

denudational history of Ireland. *Geological Society, London, Special Publications, 196*(1), 371-399. doi:10.1144/gsl.sp.2002.196.01.20

Anderson, C. J., Struble, A., & Whitmore, J. H. (2017). Abrasion resistance of muscovite in aeolian and subaqueous transport experiments. *Aeolian Research, 24*, 33-37. doi:https://doi.org/10.1016/j.aeolia.2016.11.003

Anell, I., Thybo, H., & Artemieva, I. (2009). Cenozoic uplift and subsidence in the North Atlantic region: Geological evidence revisited. *Tectonophysics, 474*(1-2), 78-105. doi:https://doi.org/10.1016/j.tecto.2009.04.006

Bassoulet, J.-P., Elmi, S., Poisson, A., Cecca, F., Bellion, Y., Guiraud, R., Baudin, F.,. (1993). Middle Toarcian (184-182 Ma). In J. Dercourt, Ricou, L.E., Vrielynck, B. (Ed.), *Atlas Tethys Paleoenvironmental Maps* (pp. 63-84). Gauthier-Villars, Paris.

Brodie, J., & White, N. (1994). Sedimentary basin inversion caused by igneous underplating: Northwest European continental shelf. *Geology, 22*(2), 147-150. doi:https://doi.org/10.1130/0091-7613(1994)022<0147:SBICBI>2.3.CO;2

Brück, P., Potter, T. L., & Downie, C. (1974). *The Lower Palaeozoic stratigraphy of the northern part of the Leinster Massif.* Paper presented at the Proceedings of the Royal Irish Academy. Section B: Biological, Geological, and Chemical Science.

Buchan, K., Mertanen, S., Park, R., Pesonen, L., Elming, S.-Å., Abrahamsen, N., & Bylund, G. (2000). Comparing the drift of Laurentia and Baltica in the Proterozoic: the importance of key palaeomagnetic poles. *Tectonophysics, 319*(3), 167-198. doi:https://doi.org/10.1016/S0040-1951(00)00032-9

Caston, V. (1995). The Helvick oil accumulation, Block 49/9, North Celtic Sea Basin. *Geological Society, London, Special Publications, 93*(1), 209-225. doi:10.1144/gsl.sp.1995.093.01.15

Caston, V., Dearnley, R., Harrison, R., Rundle, C., & Styles, M. (1981). Olivine-dolerite intrusionsin the Fastnet Basin. *Journal of the Geological Society, London, 138*(1), 31-46. doi:https://doi.org/10.1144/gsjgs.138.1.0031

Chadwick, R., & Evans, D. (1995). The timing and direction of Permo-Triassic extension in southern Britain. *Geological Society, London, Special Publications, 91*(1), 161-192. doi:https://doi.org/10.1144/GSL.SP.1995.091.01.09

Chew, D., Drost, K., & Petrus, J. A. (2019a). Ultrafast,> 50 Hz LA-ICP-MS Spot Analysis Applied to U–Pb Dating of Zircon and other U-Bearing Minerals. *Geostandards and Geoanalytical Research, 43*(1), 39-60. doi:https://doi.org/10.1111/ggr.12257

Chew, D., O'Sullivan, G., Caracciolo, L., Mark, C., & Tyrrell, S. (2020). Sourcing the sand: Accessory mineral fertility, analytical and other biases in detrital U-Pb provenance analysis. *Earth-Science Reviews*, 103093. doi:https://doi.org/10.1016/j.earscirev.2020.103093

Chew, D., Tyrrell, S., Daly, J. S., Cogné, N., Sun, K., & Badenszki, E. (2019b). *The Basement geology of the Porcupine High - A Key Transatlantic link between the Caledonides and Apalachians.* Paper presented at the GSA Annual Meeting in Phoenix, Arizona, USA-2019.

Chew, D. M., Babechuk, M. G., Cogné, N., Mark, C., O'Sullivan, G. J., Henrichs, I. A., Doepke, D., & McKenna, C. A. (2016). (LA, Q)-ICPMS trace-element analyses of Durango and McClure Mountain apatite and implications for making natural LA-ICPMS mineral standards. *Chemical Geology, 435*, 35-48. doi:https://doi.org/10.1016/j.chemgeo.2016.03.028

Chew, D. M., Daly, J. S., Magna, T., Page, L. M., Kirkland, C. L., Whitehouse, M. J., & Lam, R. (2010). Timing of ophiolite obduction in the Grampian orogen. *Bulletin, 122*(11-12), 1787-1799. doi:https://doi.org/10.1130/B30139.1

Chew, D. M., Petrus, J. A., & Kamber, B. S. (2014a). U–Pb LA–ICPMS dating using accessory mineral standards with variable common Pb. *Chemical Geology, 363*, 185-199. doi:https://doi.org/10.1016/j.chemgeo.2013.11.006

Chew, D. M., Petrus, J. A., Kenny, G. G., & McEvoy, N. (2017). Rapid high-resolution U–Pb LA-Q-ICPMS age mapping of zircon. *Journal of Analytical Atomic Spectrometry, 32*(2), 262-276. doi:https://doi.org/10.1039/C6JA00404K

Chew, D. M., & Strachan, R. A. (2014b). The Laurentian Caledonides of Scotland and Ireland. *Geological Society, London, Special Publications, 390*(1), 45-91. doi:https://doi.org/10.1144/SP390.16

Cogné, N., Chew, D., & Stuart, F. M. (2014). The thermal history of the western Irish onshore. *Journal of the Geological Society, London, 171*(6), 779-792. doi:https://doi.org/10.1144/jgs2014-026

Cogné, N., Doepke, D., Chew, D., Stuart, F. M., & Mark, C. (2016). Measuring plume-related exhumation of the British Isles in Early Cenozoic times. *Earth and Planetary Science Letters, 456*, 1-15. doi:https://doi.org/10.1016/j.epsl.2016.09.053

Collins, A., & Buchan, C. (2004). Provenance and age constraints of the South Stack Group, Anglesey, UK: U–Pb SIMS detrital zircon data. *Journal of the Geological Society, London, 161*(5), 743-746. doi:https://doi.org/10.1144/0016-764904-036

Croker, P., & Shannon, P. (1987). *The evolution and hydrocarbon prospectivity of the Porcupine Basin, offshore Ireland.* Paper presented at the Conference on petroleum geology of North West Europe. 3.

Culver, S. J., & Rawson, P. F. (2006). *Biotic response to global change: the last 145 million years*: Cambridge University Press.

Dallmeyer, R. D., Franke, W., & Weber, K. (2013). *Pre-Permian geology of central and eastern Europe*: Springer Science & Business Media.

Daly, J. S. (1996). Pre-Caledonian history of the Annagh Gneiss Complex North-Western Ireland, and correlation with Laurentia-Baltica. *Irish Journal of Earth Sciences*, 5-18.

Daly, J. S., & Flowerdew, M. J. (2005). Grampian and late Grenville events recorded by mineral geochronology near a basement–cover contact in north Mayo, Ireland. *Journal of the Geological Society, London, 162*(1), 163-174. doi:https://doi.org/10.1144/0016-764903-150

EMODnet, B. C. (2018). EMODnet Digital Bathymetry (DTM 2018) (Publication no. https://doi.org/10.12770/18ff0d48-b203-4a65-94a9-5fd8b0ec35f6). https://sextant.ifremer.fr/record/18ff0d48-b203-4a65-94a9-5fd8b0ec35f6/

Ewins, N. P., & Shannon, P. M. (1995). Sedimentology and diagenesis of the Jurassic and Cretaceous of the North Celtic Sea and Fastnet Basins. *Geological Society, London, Special Publications, 93*(1), 139-169. doi:https://doi.org/10.1144/GSL.SP.1995.093.01.12

Fairey, B. J. (2017). *Sediment routing and recycling through multiple basins from Palaeozoic to Mesozoic times: a provenance study of the Devonian Old Red Sandstone of southern Ireland and neighbouring offshore Mesozoic basins.* PhD thesis, University College Cork,

Fairey, B. J., Kerrison, A., Meere, P. A., Mulchrone, K. F., Hofmann, M., Gärtner, A., Sonntag, B.-L., Linnemann, U., Kuiper, K. F., & Ennis, M. (2018). The provenance of the Devonian Old Red Sandstone of the Dingle Peninsula, SW Ireland; the earliest record of Laurentian and peri-Gondwanan sediment mixing in Ireland. *Journal of the Geological Society, London*, jgs2017-2099. doi:https://doi.org/10.1144/jgs2017-099 |

Fernández-Suárez, J., Gutiérrez-Alonso, G., Jenner, G., & Tubrett, M. (2000). New ideas on the Proterozoic-Early Palaeozoic evolution of NW Iberia: insights from U–Pb detrital zircon ages. *Precambrian Research, 102*(3-4), 185-206. doi:https://doi.org/10.1016/S0301-9268(00)00065-6

Franklin, J., Tyrrell, S., O'Sullivan, G., Nauton-Fourteu, M., & Raine, R. (2020). Provenance of Triassic sandstones in the basins of Northern Ireland—Implications for NW European Triassic palaeodrainage. *Geological Journal*. doi:https://doi.org/10.1002/gj.3697

Fritschle, T., Daly, J. S., Whitehouse, M. J., McConnell, B., & Buhre, S. (2018). Multiple intrusive phases in the Leinster Batholith, Ireland: geochronology, isotope geochemistry and constraints on the deformation history. *Journal of the Geological Society, London, 175*(2), 229-246. doi:https://doi.org/10.1144/jgs2017-034

Fullea, J., Muller, M., Jones, A., & Afonso, J. (2014). The lithosphere–asthenosphere system beneath Ireland from integrated geophysical–petrological modeling II: 3D thermal and compositional structure. *Lithos, 189*, 49-64. doi:https://doi.org/10.1016/j.lithos.2013.09.014

García-Mondéjar, J. (1996). Plate reconstruction of the Bay of Biscay. *Geology, 24*(7), 635-638. doi:https://doi.org/10.1130/0091-7613(1996)024<0635:PROTBO>2.3.CO;2

Garzanti, E. (2017). The Maturity Myth In Sedimentology and Provenance AnalysiS. *Journal of Sedimentary Research, 87*(4), 353-365. doi:https://doi.org/10.2110/jsr.2017.17

Gehrels, G., Valencia, V., & Pullen, A. (2006). Detrital zircon geochronology by laser-ablation multicollector ICPMS at the Arizona LaserChron Center. *The Paleontological Society Papers, 12*, 67-76. doi:DOI: https://doi.org/10.1017/S1089332600001352

Gower, C. F. (1996). The evolution of the Grenville Province in eastern Labrador, Canada. *Geological Society, London, Special Publications, 112*(1), 197-218. doi:https://doi.org/10.1144/GSL.SP.1996.112.01.11

Guerrot, C., & Peucat, J. (1990). U-Pb geochronology of the Upper Proterozoic Cadomian orogeny in the northern Armorican Massif, France. *Geological Society, London, Special Publications, 51*(1), 13-26. doi:https://doi.org/10.1144/GSL.SP.1990.051.01.02

Gutiérrez-Alonso, G., Fernández-Suárez, J., Collins, A. S., Abad, I., & Nieto, F. (2005). Amazonian Mesoproterozoic basement in the core of the Ibero-Armorican Arc: 40Ar/39Ar detrital mica ages complement the zircon's tale. *Geology, 33*(8), 637-640. doi:https://doi.org/10.1130/G21485AR.1

Hancock, J. M. (1989). Sea-level changes in the British region during the Late Cretaceous. *Proceedings of the Geologists' Association, 100*(4), 565-IN561.
Haq, B. U. (2014). Cretaceous eustasy revisited. *Global and Planetary change, 113*, 44-58. doi:https://doi.org/10.1016/j.gloplacha.2013.12.007
Harrison, T. M., Célérier, J., Aikman, A. B., Hermann, J., & Heizler, M. T. (2009). Diffusion of 40Ar in muscovite. *Geochimica et Cosmochimica Acta, 73*(4), 1039-1051. doi:https://doi.org/10.1016/j.gca.2008.09.038
Hartley, A. (1995). Sedimentology of the Cretaceous Greensand, Quadrants 48 and 49, North Celtic Sea Basin: a progradational shoreface deposit. *Geological Society, London, Special Publications, 93*(1), 245-257. doi:https://doi.org/10.1144/GSL.SP.1995.093.01.17
Henderson, B. J., Collins, W. J., Murphy, J. B., Gutierrez-Alonso, G., & Hand, M. (2016). Gondwanan basement terranes of the Variscan–Appalachian orogen: Baltican, Saharan and West African hafnium isotopic fingerprints in Avalonia, Iberia and the Armorican Terranes. *Tectonophysics, 681*, 278-304. doi:https://doi.org/10.1016/j.tecto.2015.11.020
Henrique-Pinto, R., Guilmette, C., Bilodeau, C., & McNicoll, V. (2017). Evidence for transition from a continental forearc to a collisional pro-foreland basin in the eastern Trans-Hudson Orogen: Detrital zircon provenance analysis in the Labrador Trough, Canada. *Precambrian Research, 296*, 181-194. doi:https://doi.org/10.1016/j.precamres.2017.04.035
Hibbard, J. P., Van Staal, C. R., & Rankin, D. W. (2007). A comparative analysis of pre-Silurian crustal building blocks of the northern and the southern Appalachian orogen. *American Journal of Science, 307*(1), 23-45. doi:https://doi: 10.2475/01.2007.02
Hietpas, J., Samson, S., Moecher, D., & Chakraborty, S. (2011). Enhancing tectonic and provenance information from detrital zircon studies: assessing terrane-scale sampling and grain-scale characterization. *Journal of the Geological Society, London, 168*(2), 309-318. doi:https://doi.org/10.1144/0016-76492009-163
Higgs, K., & Beese, A. (1986). A Jurassic microflora from the Colbond Clay of Cloyne, County Cork. *Irish Journal of Earth Sciences*, 99-109.
Hoffman, P. F. (1990). Subdivision of the Churchill Province and the extent of the Trans-Hudson Orogen. *The Early Proterozoic Trans-Hudson Orogen of North America*, 15-39.
Hounslow, M., & Ruffell, A. (2006). Triassic: seasonal rivers, dusty deserts and saline lakes. In *The Geology of England & Wales* (pp. 295-325): Geological Society of London.
ISPSG, I. S. P. S. G. (2019). *The Standard Stratigraphic Nomenclature of Offshore Ireland: An Integrated Lithostratigraphic, Biostratigraphic and Sequence Stratigraphic Framework, Dublin: Irish Petroleum Infrastructure Programme (PIP).* Retrieved from
Jones, S. M., White, N., Clarke, B. J., Rowley, E., & Gallagher, K. (2002). Present and past influence of the Iceland Plume on sedimentation. *Geological Society, London, Special Publications, 196*(1), 13-25. doi:https://doi.org/10.1144/GSL.SP.2002.196.01.02
Keeley, M. (1995). New evidence of Permo-Triassic rifting, onshore southern Ireland, and its implications for Variscan structural inheritance. *Geological Society, London, Special Publications, 91*(1), 239-253. doi:https://doi.org/10.1144/GSL.SP.1995.091.01.12
Kessler, L., & Sachs, S. D. (1995). Depositional setting and sequence stratigraphic implications of the Upper Sinemurian (Lower Jurassic) sandstone interval, North Celtic Sea/St George's Channel Basins, offshore Ireland. *Geological Society, London, Special Publications, 93*(1), 171-192. doi:https://doi.org/10.1144/GSL.SP.1995.093.01.13
Kirstein, L., Davies, G., & Heeremans, M. (2006). The petrogenesis of Carboniferous–Permian dyke and sill intrusions across northern Europe. *Contributions to Mineralogy and Petrology, 152*(6), 721-742. doi:https://doi.org/10.1007/s00410-006-0129-9
Kuiper, K., Deino, A., & Hilgen, F. (2008). Synchronizing Rock Clocks of Earth History. *Synchronizing rock clocks of Earth history: Science, 320*, 500-504. doi:https://doi:10.1126/science.1154339
Lafuente, B., Downs, R., Yang, H., & Stone, N. (2015). The power of databases: the RRUFF project. In "Highlights in mineralogical crystallography", Armbruster, T. & Danisi, RM, eds. W. *De Gruyter, Berlin, Germany, 1*, 30. doi:https://doi.org/10.1515/9783110417104-003
Lee, J.-Y., Marti, K., Severinghaus, J. P., Kawamura, K., Yoo, H.-S., Lee, J. B., & Kim, J. S. (2006). A redetermination of the isotopic abundances of atmospheric Ar. *Geochimica et Cosmochimica Acta, 70*(17), 4507-4512. doi:https://doi.org/10.1016/j.gca.2006.06.1563
Long, C. B., Max, M. D., & Yardley, B. W. (1983). Compilation Caledonian metamorphic map of Ireland. In *Regional Trends in the Geology of the Appalachian-Caledonian-Hercynian-Mauritanide Orogen* (pp. 221-233): Springer.

Ludwig, K. (2012). Isoplot 3.75-4.15 manual. *A Geochronological Toolkit for Microsoft Excel, 4*, 1-70.
Mange, M. A., & Maurer, H. (1992). *Heavy minerals in colour*: Springer Science & Business Media.
Mange, M. A., & Wright, D. T. (2007). *Heavy minerals in use*: Elsevier.
Max, M., Barber, A., & Martinez, J. (1990). Terrane assemblage of the Leinster Massif, SE Ireland, during the Lower Palaeozoic. *Journal of the Geological Society, London, 147*(6), 1035-1050. doi:https://doi.org/10.1144/gsjgs.147.6.1035
McAteer, C. A., Daly, J. S., Flowerdew, M. J., Whitehouse, M. J., & Kirkland, C. L. (2010). A Laurentian provenance for the Dalradian rocks of north Mayo, Ireland, and evidence for an original basement–cover contact with the underlying Annagh Gneiss Complex. *Journal of the Geological Society, London, 167*(5), 1033-1048. doi:https://doi.org/10.1144/0016-76492009-147
McAteer, C. A., Daly, J. S., Flowerdew, M. J., Whitehouse, M. J., & Monaghan, N. M. (2014). Sedimentary provenance, age and possible correlation of the Iona Group SW Scotland. *Scottish Journal of Geology, 50*(2), 143-158. doi:https://doi.org/10.1144/sjg2013-019
McConnell, B., Rogers, R., & Crowley, Q. (2016). Sediment provenance and tectonics on the Laurentian margin: implications of detrital zircons ages from the Central Belt of the Southern Uplands–Down–Longford Terrane in Co. Monaghan, Ireland. *Scottish Journal of Geology, 52*(1), 11-17. doi:https://doi.org/10.1144/sjg2015-013
Meere, P. A., & Mulchrone, K. F. (2006). Timing of deformation within Old Red Sandstone lithologies from the Dingle Peninsula, SW Ireland. *Journal of the Geological Society, London, 163*(3), 461-469. doi:https://doi.org/10.1144/0016-764905-099
Miles, A. J., & Woodcock, N. (2018). A combined geochronological approach to investigating long lived granite magmatism, the Shap granite, UK. *Lithos, 304*, 245-257. doi:https://doi.org/10.1016/j.lithos.2018.02.012
Millson, J. (1987). *The Jurassic evolution of the Celtic Sea basins.* Paper presented at the Conference on petroleum geology of North West Europe. 3.
Min, K., Mundil, R., Renne, P. R., & Ludwig, K. R. (2000). A test for systematic errors in 40Ar/39Ar geochronology through comparison with U/Pb analysis of a 1.1-Ga rhyolite. *Geochimica et Cosmochimica Acta, 64*(1), 73-98. doi:https://doi.org/10.1016/S0016-7037(99)00204-5
Monaghan, A., & Pringle, M. (2004). 40Ar/39Ar geochronology of Carboniferous-Permian volcanism in the Midland Valley, Scotland. *Geological Society, London, Special Publications, 223*(1), 219-241. doi:https://doi.org/10.1144/GSL.SP.2004.223.01.10
Monster, M. W. L. (2016). *Multi-method palaeointensity data of the geomagnetic field during the past 500 kyrs from European volcanoes.* UU Dept. of Earth Sciences, Retrieved from https://dspace.library.uu.nl/handle/1874/340862
Morton, A. (1984). Stability of detrital heavy minerals in Tertiary sandstones from the North Sea Basin. *Clay minerals, 19*(3), 287-308.
Morton, A., Knox, R., & Frei, D. (2016). Heavy mineral and zircon age constraints on provenance of the Sherwood Sandstone Group (Triassic) in the eastern Wessex Basin, UK. *Proceedings of the Geologists' Association, 127*(4), 514-526. doi:https://doi.org/10.1016/j.pgeola.2016.06.001
Morton, A. C. (1982). The provenance and diagenesis of Palaeogene sandstones of southeast England as indicated by heavy mineral analysis. *Proceedings of the Geologists' Association, 93*(3), 263-274.
Morton, A. C., & Hallsworth, C. (1994). Identifying provenance-specific features of detrital heavy mineral assemblages in sandstones. *Sedimentary Geology, 90*(3-4), 241-256. doi:https://doi.org/10.1016/0037-0738(94)90041-8
Murphy, J. B., Nance, R. D., Gabler, L. B., Martell, A., & Archibald, D. A. (2019). Age, geochemistry and origin of the Ardara appinite plutons, northwest Donegal, Ireland. *Geoscience Canada: Journal of the Geological Association of Canada/Geoscience Canada: journal de l'Association Géologique du Canada, 46*(1), 31-48. doi:https://doi.org/10.12789/geocanj.2019.46.144
Murphy, N. J., & Ainsworth, N. R. (1991). Stratigraphy of the Triassic, Lower Jurassic and Middle Jurassic (Aalenian) from the Fastnet Basin, offshore south-west Ireland. *Marine and Petroleum Geology, 8*(4), 417-429. doi:https://doi.org/10.1016/0264-8172(91)90064-8
Nance, R. D., Murphy, J. B., Strachan, R. A., Keppie, J. D., Gutiérrez-Alonso, G., Fernández-Suárez, J., Quesada, C., Linnemann, U., D'lemos, R., & Pisarevsky, S. A. (2008). Neoproterozoic-early Palaeozoic tectonostratigraphy and palaeogeography of the peri-Gondwanan terranes: Amazonian v. West African connections. *Geological Society, London, Special Publications, 297*(1), 345-383. doi:https://doi.org/10.1144/SP297.17

Nance, R. D., Neace, E. R., Braid, J. A., Murphy, J. B., Dupuis, N., & Shail, R. K. (2015). Does the Meguma terrane extend into SW England? *Geoscience Canada*, 61-76. doi:https://doi.org/10.12789/geocanj.2014.41.056

Nasdala, L., Corfu, F., Schoene, B., Tapster, S. R., Wall, C. J., Schmitz, M. D., Ovtcharova, M., Schaltegger, U., Kennedy, A. K., & Kronz, A. (2018). GZ 7 and GZ 8–Two Zircon Reference Materials for SIMS U-Pb Geochronology. *Geostandards and Geoanalytical Research, 42*(4), 431-457. doi: https://doi.org/10.1111/ggr.12239

Nauton-Fourteu, M., Tyrrell, S., Morton, A., Mark, C., O'Sullivan, G. J., & Chew, D. M. (2020). Constraining recycled detritus in quartz-rich sandstones: insights from a multi-proxy provenance study of the Mid-Carboniferous, Clare Basin, western Ireland. *Basin Research*. doi:https://doi.org/10.1111/bre.12469

Naylor, D., & Shannon, P. (1982). *Geology of offshore Ireland and west Britain*. United Kingdom.

Naylor, D., & Shannon, P. (2011). *Petroleum geology of Ireland*: Dunedin Academic Press Limited.

O'Connor, P., & Brück, P. (1978). Age and origin of the Leinster Granite. *Journal of Earth Sciences*, 105-113.

O'Reilly, B. M., Shannon, P. M., & Vogt, U. (1991). Seismic studies in the North Celtic Sea Basin: implications for basin development. *Journal of the Geological Society, London, 148*(1), 191-195. doi:https://10.1144/gsjgs.148.1.0191

O'Sullivan, G., Chew, D., Kenny, G., Henrichs, I., & Mulligan, D. (2020). The trace element composition of apatite and its application to detrital provenance studies. *Earth-Science Reviews, 201*, 103044. doi:https://doi.org/10.1016/j.earscirev.2019.103044

Pascoe, R., Power, M., & Simpson, B. (2007). QEMSCAN analysis as a tool for improved understanding of gravity separator performance. *Minerals engineering, 20*(5), 487-495. doi:https://doi.org/10.1016/j.mineng.2006.12.012

Paton, C., Hellstrom, J., Paul, B., Woodhead, J., & Hergt, J. (2011). Iolite: Freeware for the visualisation and processing of mass spectrometric data. *Journal of Analytical Atomic Spectrometry, 26*(12), 2508-2518. doi:https://10.1039/C1JA10172B

Payton, C. E. (1977). *Seismic stratigraphy: applications to hydrocarbon exploration* (Vol. 26): American Association of Petroleum Geologists Tulsa, OK.

Petrie, S., Brown, J., Granger, P., & Lovell, J. (1989). Mesozoic history of the Celtic Sea basins. *Extensional Tectonics and Stratigraphy of the North Atlantic Margins American Association of Petroleum Geologists Memoirs, 46*, 433-445.

Petrus, J. A., & Kamber, B. S. (2012). VizualAge: A Novel Approach to Laser Ablation ICP-MS U-Pb Geochronology Data Reduction. *Geostandards and Geoanalytical Research, 36*(3), 247-270. doi:https://10.1111/j.1751-908X.2012.00158.x

Pollock, J. C., Hibbard, J. P., & van Staal, C. R. (2012). A paleogeographical review of the peri-Gondwanan realm of the Appalachian orogen. *Canadian Journal of Earth Sciences, 49*(1), 259-288. doi:https://doi.org/10.1139/e11-049

Pothier, H. D., Waldron, J. W., Schofield, D. I., & DuFrane, S. A. (2015). Peri-Gondwanan terrane interactions recorded in the Cambrian–Ordovician detrital zircon geochronology of North Wales. *Gondwana Research, 28*(3), 987-1001. doi:https://doi.org/10.1016/j.gr.2014.08.009

Rainbird, R. H., Hamilton, M. A., & Young, G. M. (2001). Detrital zircon geochronology and provenance of the Torridonian, NW Scotland. *Journal of the Geological Society, London, 158*(1), 15-27. doi:https://doi.org/10.1144/jgs.158.1.15

Rawson, P., & Riley, L. (1982). Latest Jurassic-Early Cretaceous events and the "late Cimmerian unconformity" in North Sea area. *AAPG Bulletin, 66*(12), 2628-2648. doi:https://doi.org/10.1306/03B5AC87-16D1-11D7-8645000102C1865D

Robinson, K., Shannon, P., & Young, G. M. (1981). The Fastnet Basin: An integrated analysis. In L. G. Illing & G. D. Hobson (Eds.), *Petroleum Geology of the Continental Shelf of North-West Europe* (pp. 444–454). London: Heyden and Son Ltd.

Rodriguez-Salgado, P. (2019). *Structural and Kinematic Analysis of the Celtic Sea Basins.* (PhD). University College Dublin,

Rodríguez-Salgado, P., Childs, C., Shannon, P. M., & Walsh, J. J. (2019). Structural evolution and the partitioning of deformation during basin growth and inversion: A case study from the Mizen Basin Celtic Sea, offshore Ireland. *Basin Research*. doi:https://doi.org/10.1111/bre.12402

Rowell, P. (1995). Tectono-stratigraphy of the North Celtic Sea Basin. *Geological Society, London, Special Publications, 93*(1), 101-137. doi:10.1144/gsl.sp.1995.093.01.11

Ruffell, A., & Shelton, R. (1999). The control of sedimentary facies by climate during phases of crustal extension: examples from the Triassic of onshore and offshore England and Northern Ireland. *Journal of the Geological Society, London, 156*(4), 779-789. doi:https://doi.org/10.1144/gsjgs.156.4.0779

Ruffell, A. H., & Rawson, P. F. (1994). Palaeoclimate control on sequence stratigraphic patterns in the late Jurassic to mid-Cretaceous, with a case study from Eastern England. *Palaeogeography, Palaeoclimatology, Palaeoecology, 110*(1-2), 43-54. doi:https://doi.org/10.1016/0031-0182(94)90109-0

Shannon, P. (1991). The development of Irish offshore sedimentary basins. *Journal of the Geological Society, London, 148*(1), 181-189. doi:https://doi.org/10.1144/gsjgs.148.1.0181

Shannon, P. (1996). Current and future potential of oil and gas exploration in Ireland. In K. Glennie & A. Hurst (Eds.), *AD1995-NW Europe's Hydrocarbon Industry. Geol. Soc, London* (Vol. 1, pp. 51-62): Journal of the Geological Society, London.

Shannon, P., & Naylor, D. (1998). An assessment of Irish offshore basins and petroleum plays. *Journal of Petroleum Geology, 21*(2), 125-152. doi:https://doi.org/10.1111/j.1747-5457.1998.tb00651.x

Shannon, P. M. (1995). Permo-Triassic development of the Celtic Sea region, offshore Ireland. *Geological Society London Special Publication, 91*, 215-237. doi:https://doi.org/10.1144/GSL.SP.1995.091.01.11

Shannon, P. M., Corcoran, D. V., & Haughton, P. D. W. (2001). The petroleum exploration of Ireland's offshore basins: introduction. *Geological Society, London, Special Publications, 188*(1), 1-8. doi:https://10.1144/gsl.sp.2001.188.01.01

Sibuet, J. C., Dyment, J., Bois, C., Pinet, B., & Ondreas, H. (1990). Crustal structure of the Celtic Sea and Western Approaches from gravity data and deep seismic profiles: constraints on the formation of continental basins. *Journal of Geophysical Research: Solid Earth, 95*(B7), 10999-11020. doi:https://doi.org/10.1029/JB095iB07p10999

Sláma, J., Košler, J., Condon, D. J., Crowley, J. L., Gerdes, A., Hanchar, J. M., Horstwood, M. S., Morris, G. A., Nasdala, L., & Norberg, N. (2008). Plešovice zircon—a new natural reference material for U–Pb and Hf isotopic microanalysis. *Chemical Geology, 249*(1-2), 1-35. doi:https://doi.org/10.1016/j.chemgeo.2007.11.005

Smith, W. D., Darling, J., Bullen, D., Lasalle, S., Pereira, I., Moreira, H., Allen, C. J., & Tapster, S. (2019). Zircon perspectives on the age and origin of evolved S-type granites from the Cornubian Batholith, Southwest England. *Lithos, 336*, 14-26. doi:https://doi.org/10.1016/j.lithos.2019.03.025

Somerville, I. D., Strogen, P., & Jones, G. L. (1992). Biostratigraphy of Dinantian limestones and associated volcanic rocks in the Limerick Syncline, Ireland. *Geological Journal, 27*(3), 201-220. doi:https://doi.org/10.1002/gj.3350270302

Soper, N., & Hutton, D. (1984). Late Caledonian sinistral displacements in Britain: implications for a three-plate collision model. *Tectonics, 3*(7), 781-794. doi:https://10.1029/TC003i007p00781

Stampfli, G. M., & Kozur, H. W. (2006). Europe from the Variscan to the Alpine cycles. *Journal of the Geological Society, London, 32*, 57-82. doi:https://doi.org/10.1144/GSL.MEM.2006.032.01.04

Strachan, R., Collins, A., Buchan, C., Nance, R., Murphy, J., & D'Lemos, R. (2007). Terrane analysis along a Neoproterozoic active margin of Gondwana: insights from U–Pb zircon geochronology. *Journal of the Geological Society, London, 164*(1), 57-60. doi:https://doi.org/10.1144/0016-76492006-014

Taber, D., Vickers, M., & Winn, R. (1995). The definition of the Albian 'A'Sand reservoir fairway and aspects of associated gas accumulations in the North Celtic Sea Basin. *Geological Society, London, Special Publications, 93*(1), 227-244. doi:https://doi.org/10.1144/GSL.SP.1995.093.01.16

Tate, M., & Dobson, M. (1988). Syn-and post-rift igneous activity in the Porcupine Seabight Basin and adjacent continental margin W of Ireland. *Geological Society, London, Special Publications, 39*(1), 309-334. doi:https://doi.org/10.1144/GSL.SP.1988.039.01.28

Thomson, S. N., Gehrels, G. E., Ruiz, J., & Buchwaldt, R. (2012). Routine low-damage apatite U-Pb dating using laser ablation–multicollector–ICPMS. *Geochemistry, Geophysics, Geosystems, 13*(2). doi:https://10.1029/2011GC003928

Todd, S. (2015). Structure of the Dingle Peninsula, SW Ireland: evidence for the nature and timing of Caledonian, Acadian and Variscan tectonics. *Geological Magazine, 152*(2), 242-268. doi:https://doi.org/10.1017/S0016756814000260

Tyrrell, S. (2005). *Investigations of Sandstone Provenance.* (PhD). University College Dublin,

Tyrrell, S., Haughton, P. D., & Daly, J. S. (2007). Drainage reorganization during breakup of Pangea revealed by in-situ Pb isotopic analysis of detrital K-feldspar. *Geology, 35*(11), 971-974. doi:https://doi.org/10.1130/G4123A.1

Van der Voo, R. (1988). Paleozoic paleogeography of North America, Gondwana and intervening. displaced terranes: Comparisons of palaeomagnetism with paleoclimatology and biogeographical patterns. *Geological Society of America Bulletin, 100*, 411-423. doi:https://doi.org/10.1130/0016-7606(1988)100<0311:PPONAG>2.3.CO;2

van Staal, C. R., Sullivan, R. W., & Whalen, J. B. (1996). Provenance of tectonic history of the Gander Zone in the Caledonian/Appalachian Orogen: Implications for the origin and assembly of Avalon. In M. D. T. Damian Nance (Ed.), *Avalonian and Related Peri-Gondwanan Terranes of the Circum-North Atlantic* (Vol. 304, pp. 347-367): Geological Society of America.

Vermeesch, P. (2018). IsoplotR: A free and open toolbox for geochronology. *Geoscience Frontiers, 9*(5), 1479-1493. doi:https://doi.org/10.1016/j.gsf.2018.04.001

Vermeesch, P., Resentini, A., & Garzanti, E. (2016). An R package for statistical provenance analysis. *Sedimentary Geology, 336*, 14-25. doi:https://doi.org/10.1016/j.sedgeo.2016.01.009

Vermeesch, P., Rittner, M., Petrou, E., Omma, J., Mattinson, C., & Garzanti, E. (2017). High throughput petrochronology and sedimentary provenance analysis by automated phase mapping and LAICPMS. *Geochemistry, Geophysics, Geosystems, 18*(11), 4096-4109. doi:https://doi.org/10.1002/2017GC007109

Waldron, J. W., Floyd, J. D., Simonetti, A., & Heaman, L. M. (2008). Ancient Laurentian detrital zircon in the closing Iapetus ocean, Southern Uplands terrane, Scotland. *Geology, 36*(7), 527-530. doi:https://doi.org/10.1130/G24763A.1

Waldron, J. W., Schofield, D. I., Dufrane, S. A., Floyd, J. D., Crowley, Q. G., Simonetti, A., Dokken, R. J., & Pothier, H. D. (2014). Ganderia–Laurentia collision in the Caledonides of Great Britain and Ireland. *Journal of the Geological Society, London, 171*(4), 555-569. doi:https://doi.org/10.1144/jgs2013-131

Waldron, J. W., Schofield, D. I., & Murphy, J. B. (2019a). Diachronous Paleozoic accretion of peri-Gondwanan terranes at the Laurentian margin. *Geological Society, London, Special Publications, 470*(1), 289-310. doi:https://doi.org/10.1144/SP470.11

Waldron, J. W., Schofield, D. I., Pearson, G., Sarkar, C., Luo, Y., & Dokken, R. (2019b). Detrital zircon characterization of early Cambrian sandstones from East Avalonia and SE Ireland: implications for terrane affinities in the peri-Gondwanan Caledonides. *Geological Magazine, 156*(7), 1217-1232. doi:https://doi.org/10.1017/S0016756818000407

Waldron, J. W., Schofield, D. I., White, C. E., & Barr, S. M. (2011). Cambrian successions of the Meguma Terrane, Nova Scotia, and Harlech Dome, North Wales: dispersed fragments of a peri-Gondwanan basin? *Journal of the Geological Society, London, 168*(1), 83-98. doi:https://doi.org/10.1144/0016-76492010-068

Warrington, G., & Ivimey-Cook, H. (1992). Triassic. In J. Cope, J. Ingham, & P. Rawson (Eds.), *Atlas of palaeogeography and lithofacies.* (Vol. 13, pp. 97-106): Geological Society of London Memoir.

Welch, M. J., & Turner, J. P. (2000). Triassic–Jurassic development of the St. George's Channel basin, offshore Wales, UK. *Marine and Petroleum Geology, 17*(6), 723-750. doi:https://doi.org/10.1016/S0264-8172(00)00017-9

White, C., Palacios, T., Jensen, S., & Barr, S. (2012). Cambrian–Ordovician acritarchs in the Meguma terrane, Nova Scotia, Canada: Resolution of early Paleozoic stratigraphy and implications for paleogeography. *GSA Bulletin, 124*(11-12), 1773-1792. doi:https://doi.org/10.1130/B30638.1

Wiedenbeck, M., Alle, P., Corfu, F., Griffin, W., Meier, M., Oberli, F. v., Quadt, A. v., Roddick, J., & Spiegel, W. (1995). Three natural zircon standards for U-Th-Pb, Lu-Hf, trace element and REE analyses. *Geostandards newsletter, 19*(1), 1-23. doi:https://doi.org/10.1111/j.1751-908X.1995.tb00147.x

Winn Jr, R. D. (1994). Shelf sheet-sand reservoir of the Lower Cretaceous Greensand, North Celtic Sea Basin, offshore Ireland. *AAPG Bulletin, 78*(11), 1775-1789. doi:https://doi.org/10.1306/A25FF28D-171B-11D7-8645000102C1865D

Yang, P., Welford, J. K., Peace, A. L., & Hobbs, R. (2020). Investigating the Goban Spur rifted continental margin, offshore Ireland, through integration of new seismic reflection and potential field data. *Tectonophysics, 777*, 228364. doi:https://doi.org/10.1016/j.tecto.2020.228364

Zhang, X., Pease, V., Omma, J., & Benedictus, A. (2015). Provenance of Late Carboniferous to Jurassic sandstones for southern Taimyr, Arctic Russia: a comparison of heavy mineral analysis by optical and QEMSCAN methods. *Sedimentary Geology, 329*, 166-176. doi:https://doi.org/10.1016/j.sedgeo.2015.09.008

Ziegler, P. A. (1990). *Geological Atlas of Western and Central Europe* (2 ed.): Shell Internationale Petroleum Maatschappij B.V. 239pp.

Ziegler, P. A., Cloetingh, S., & van Wees, J.-D. (1995). Dynamics of intra-plate compressional deformation: the Alpine foreland and other examples. *Tectonophysics, 252*(1-4), 7-59.

Zimmermann, S., Mark, C., Chew, D., & Voice, P. J. (2018). Maximising data and precision from detrital zircon U-Pb analysis by LA-ICPMS: The use of core-rim ages and the single-analysis concordia age. *Sedimentary Geology, 375*, 5-13. doi:https://doi.org/10.1016/j.sedgeo.2017.12.020

Chapter 3: *The provenance of Triassic and Lower Jurassic successions in the North Celtic Sea, St. George's Channel and Fastnet Basins: Insights on the evolution of Mesozoic basin provenance in the Celtic and Irish Seas*

Authors

Odhrán McCarthy[(1)], Brenton Fairey[(2)], Patrick Meere[(1)], David Chew [(3)], Aidan Kerrison[(4)], Mandy Hofmann[(5)], Andreas Gärtner[(5)], Benita-Lisette Sonntag[(5)], Ulf Linnemann[(5)], Klaudia F. Kuiper[(6)].

Affiliations

[1]School of Biological, Environmental and Earth Sciences and iCRAG, University College Cork

[2]Chemostrat, Welshpool, United Kingdom

[3]Department of Geology and iCRAG, Trinity College Dublin, Dublin, Ireland

[4]School of Earth, Environmental and Biological Sciences, Brisbane, Australia

[5]Senckenberg Naturhistorische Sammlungen Dresden, Museum für Mineralogie und Geologie, Königsbrücker Landstraße 159, D-01109 Dresden, Germany

[6]Faculty of Earth Sciences, Vrije Universiteit Amsterdam, De Boelelaan 1085, NL-1081 HV Amsterdam, The Netherlands

Abstract

The provenance of the sedimentary infill of the Irish and Celtic Sea basins demonstrates the importance of marine transgression-regression cycles, and rift related tectonics which exhibit a first-order control on distal *versus* proximal sediment sourcing. However, our understanding of these influencing factors is incomplete as the provenance of Triassic and Early Jurassic basin infill is yet to be investigated with a multi-proxy provenance approach. Existing hypothesis are based on petrographic and 2D seismic data which provide a limited provenance insight, and do not account for environmental and tectonic factors indicating near-field sediment

sourcing despite a marine transgression event between the Triassic and Early Jurassic. This study aims to better constrain the provenance of Triassic and Lower Jurassic successions in the Irish and Celtic Sea basins, and to further characterize the temporal evolution of sedimentary provenance throughout these Mesozoic successions. A multi-proxy investigation of detrital U-Pb zircon and apatite geochronology, apatite trace element analysis combined with Ar-Ar white mica geochronology and heavy mineral analysis were chosen. Findings support sedimentation from the Peri-Gondwanan, Iberian Massif into the Fastnet, North Celtic Sea, and Saint George's Channel Basins during the Early Triassic. By the Early Jurassic, a clear provenance switch occurred coinciding with transgressive sedimentation as Peri-Gondwanan detritus is replaced by distally sourced Laurentian detritus. Additionally, we present a Mesozoic scale provenance model for the Irish and Celtic Sea basins using a large, multi-proxy data set, collected from across the Mesozoic successions of these basins.

3.1. **Introduction**

The provenance of basin infill can be influenced by environmental conditions, tectonism, the proximity of source regions as well as their exposure to weathering processes (Garzanti *et al.*, 2009; Garzanti, 2017). Due to the potential influence of these controls on sediment sourcing, routing, and preservation, a multi-proxy approach is commonly utilized in modern provenance research to asses the origin of sediments (Caracciolo, 2020; Chew *et al.*, 2020).

The basins of the Irish and Celtic Seas (Fig. 15) were subject to significant tectonic and environmental change throughout the Mesozoic Era (Fig. 16). However, previous hypotheses addressing the provenance of Cretaceous (Robinson *et al.*, 1981; Ainsworth *et al.*, 1985; Hartley, 1995; Taber *et al.*, 1995) and Jurassic (Caston, 1995) basin infill, within the Irish and Celtic Sea region have not been able to account for the influence of these factors on sedimentary provenance. This is primarily because these hypotheses were constructed with seismic, petrographic, paleocurrent and biostratigraphic data, providing a limited insight into sedimentary provenance. Recent provenance work has evidenced the importance of tectonic and environmental controls on sediment sourcing in these basins, as well as the need for a multi-proxy approach in assessing sediment provenance (see Chapter 1). It is likely that tectonism and environmental factors influenced Early Jurassic and Triassic basin infill, as a prolonged marine transgression and rift related faulting and subsidence occurred throughout this period (Fig. 16). To date there is no established provenance hypothesis for the Triassic basin infill of the Irish and Celtic Sea region, while Early Jurassic infill is thought to derive from the Irish onshore and basin margins including the Munster Basin and Leinster Massif (Petrie *et al.*, 1989; Keeley, 1995; Kessler *et al.*, 1995).

Findings from Chapter 1 raise important questions concerning the provenance of Lower Jurassic and Triassic successions. The provenance of Triassic, Sherwood Sandstone Group sediments in the Fastnet Basin, North Celtic Sea Basin (NCSB) and Saint George's Channel Basin (SGCB) have been under investigated, despite these successions representing more than 3000 m of the 9 km of Mesozoic infill in these Basins. The Fastnet Basin, NCSB and SGCB may have been infilled with detritus from local sources such as the Leinster Massif, Munster Basin, Welsh Massif and Cornubian Massif which all surround the Celtic Sea Region (Fig. 15).

Alternatively they may have infilled with sediment from the Iberian Massif or Armorican Massif to the south which were topographical highs at the time (Morton *et al.*, 2016). Each of these sources have a Peri-Gondwanan tectonic affinity making them difficult to differentiate. They each contain similar Neoproterozoic and Paleozoic populations, with limited or subordinate populations of Mesoproterozoic and Archean populations (Waldron *et al.*, 2014; Pothier *et al.*, 2015; Fairey, 2017; Fairey *et al.*, 2018). The Munster Basin is the exception to this rule as it contains a significant amount of Silurian (c. 420) and Grenville (c. 1.1 Ga) aged zircon as well as minor occurrences of peri-Gondwanan type detrital zircon (Fairey, 2017).

Regional provenances studies of Triassic infill have shown a large scale drainage from the Variscan uplands (e.g., Armorican Massif) in the south, through the Wessex Basin (Morton *et al.*, 2016), and through a series of connected basins through central Britain (Dunford *et al.*, 2001) and as far north as the Slyne Basin via the large 500+ km "Budleighensis" river system (Tyrrell *et al.*, 2012; Zoleikhaei *et al.*, 2016; Franklin *et al.*, 2020). This extensive river system contained multiple channels draining sediment from the northern margin of Armorican Massif (Morton *et al.*, 2016). The scale of this system makes it difficult to interpret the extent of its reach and connectivity with the Celtic Sea or southern margin of the Irish Sea during the Early Triassic. Importantly, in the SGCB, St. Tudwals Arch was a northern topographical high along with the Welsh Massif and may have prevented fluvial systems draining west into the SGCB during the Early Triassic (Fig. 15) (Ruffell *et al.*, 1999; Dunford *et al.*, 2001). If the Budleighensis system drained south, or east from the central UK basins, sediments of the SGCB should contain similar apatite, zircon and mica populations to the Triassic sediments of the Wessex Basin (Morton *et al.*, 2016) and Northern Ireland (Franklin *et al.*, 2020). Alternatively, the Budleighensis system may have entered the Celtic Sea via the Goban Spur and Fastnet Basins to the south (Fig. 15), circumnavigating the Cornubian Massif which partially blocked drainage from the east into the southern margin of the Celtic Sea.

Lower Jurassic marine sediments of the NCSB, SGCB and Fastnet Basin are thought to derive from the local Munster Basin and Leinster Massif to the west, and Welsh Massif to the east (Petrie *et al.*, 1989; Keeley, 1995; Kessler *et al.*, 1995). Considering more recent findings of Middle Jurassic infill, this locally sourced hypothesis seems unlikely as more distal, Laurentian

sediment would be expected in a marine setting as observed in Middle Jurassic sediments of the SGCB and Goban Spur Basin (see Section 2.7).

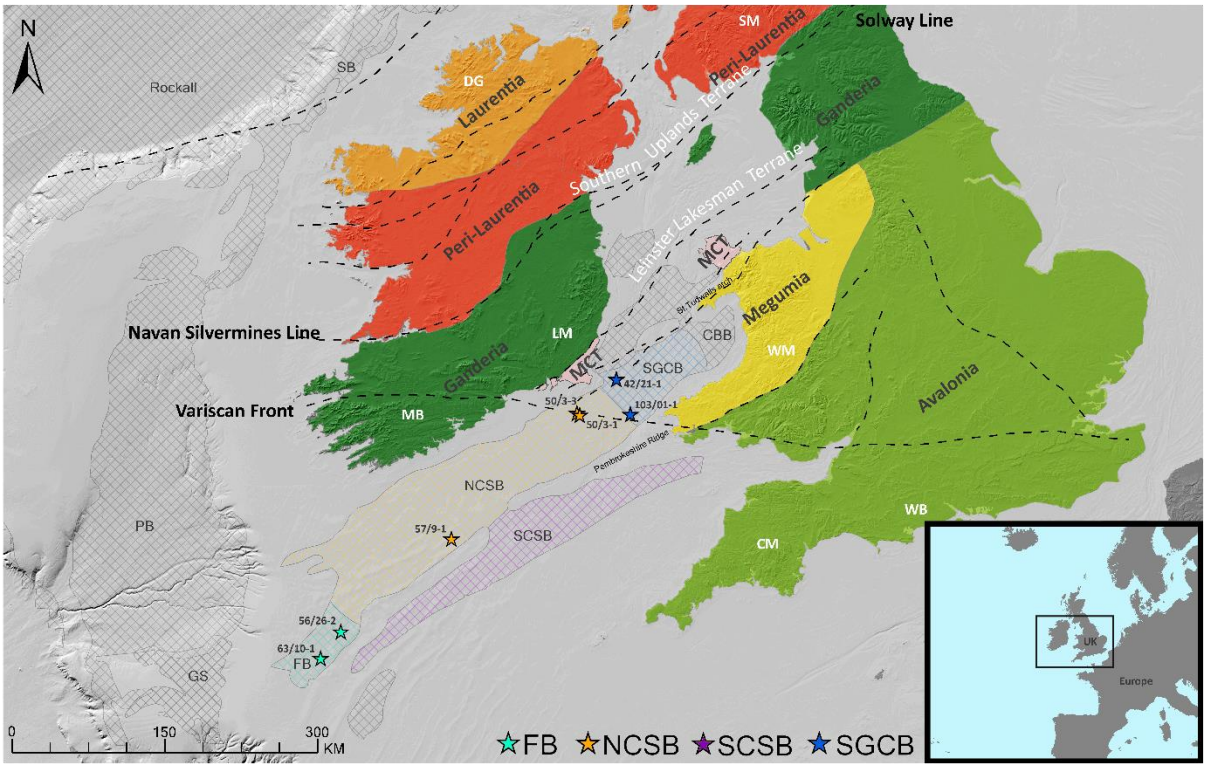

Fig. 15. *Study area offshore of Ireland's south-east coastline. Markers indicate sampled wells from all stratigraphic intervals included in this study. Background offshore bathymetry from EMODnet (2018). CBB, Cardigan Bay Basin; DG, Dalradian Supergroup; LM, Leinster Massif; MB, Munster Basin; WM, Welsh Massif; CM, Cornubia Massif; SM, Scottish Massif; PB, Porcupine Basin; SB, Slyne Basin; NCSB, North Celtic Sea Basin; SCSB, South Celtic Sea Basin; SGCB, Saint George's Channel Basin; FB, Fastnet Basin; GS, Goban Spur Basin; MCT, Monian Composite Terrane (Nance et al., 2015; Waldron et al., 2019b).*

Historically, the challenges associated with addressing provenance in these basins are numerous. The primary challenge is the large number of similar source terrains proximal to the Irish and Celtic Seas, making differentiation of sources and sediment recycling difficult. Neoproterozoic and Palaeozoic zircon populations dominate sources from the British and Irish Peri-Gondwanan Domains south of the Iapetus Suture (Waldron *et al.*, 2011; Waldron *et al.*, 2014; Waldron *et al.*, 2019b). Sources south of the British Isles, like Iberia and Armorica, also contain this signature having a Peri-Gondwanan tectonic affinity (Fernández-Suárez *et al.*, 2000; Morton *et al.*, 2015). Furthermore, a lack of core material and limited cuttings from offshore drilling disqualified many samples collected for this study from being analysed or

included in results. To investigate provenance and make full utility of limited sample material, a multi-proxy investigation of single grain U-Pb zircon, apatite and Ar-Ar mica geochronology was undertaken. Apatite trace element analysis and bulk sediment characterization of heavy mineral analysis (HMA) was conducted where processed samples contained enough material. Revised palaeogeographic models of two periods are used to contextualise results with basin development, environmental change and provenance. This study aims to investigate the provenance of basin infill from the Early Triassic to the Early Jurassic and test existing theories on sediment sourcing in the Fastnet Basin, NCSB and SGCB. In addition, we present a Mesozoic scale provenance model incorporating 20 detrital zircon data sets from Section 2.8.1, with unpublished PhD data (Fairey, 2017), and data from this study to summarise the broader influence of environmental and tectonic controls on sediment sourcing in these basins. Given the understanding of large scale tectonic and environmental changes in the basin, a Mesozoic scale study of sedimentary provenance provides an excellent testing ground for demonstrating the influence of these first-order controls on sedimentary provenance.

3.2. Tectonic Development and Source Terrains

3.2.1. General Background

Triassic-Lower Jurassic successions are found across the Irish and Celtic Sea basins, however due to extensive tectonism (Fig. 16), these sequences are typically fault bounded with varying thickness. In the Fastnet Basin, Triassic and Lower Jurassic successions comprise up to c. 3163 m (Well 56/26-2) across five wells. The NCSB contains up to 1119 m (Well 47/29-1) of Triassic material with only 6 wells penetrating the Sherwood Sandstone group. Up to 3620.5 m (Well 56/18-1) of the Lias Group are also recorded across 14 wells in the NCSB. The SGCB has 10 exploration wells which record 1594 m (Well 106/28-1) of Triassic successions and 1550 m of the Lias Group successions (Well 106/28-1) and are reported to contain up to 8000 m of post-Variscan basin infill (Maddox *et al.*, 1995; Naylor *et al.*, 2011). The current understanding of both Triassic and Jurassic stratigraphy in the Irish offshore region is restricted by limited well penetration as well as limited penetration of 2D seismic data to these depths (Naylor *et al.*, 2011; Rodríguez-Salgado *et al.*, 2019). Research on Triassic successions in the region has focused on basin development and palaeoenvironmental conditions (Shannon, 1995;

Hounslow *et al.*, 2006), fault structures like the St. Georges Fault (Welch *et al.*, 2000) and their potential for hydrocarbon exploration (Shannon *et al.*, 1993; Maddox *et al.*, 1995). While more regional studies have investigated large scale drainage systems across western Europe in Triassic sandstones (Tyrrell *et al.*, 2012; Morton *et al.*, 2016; Franklin *et al.*, 2019) and the opening Atlantic Margin (SÌtolfovÃ¡ *et al.*, 2009).

3.2.2. Pre-Mesozoic Tectonic Framework and Triassic Sedimentation

Basin development offshore of Ireland's south and east coast initiated toward the end of the Carboniferous period and continued into the Early Permian. Pangea began to rift and break up, resulting in the early development of the Celtic and Irish sea Basins (Chadwick *et al.*, 1995). This early rifting followed inherent Variscan tectonic fabrics which penetrated carboniferous and Permian basement rock (Shannon, 1991b). By the Early Triassic, renewed rifting of Pangea resulted in the Boreal Norway – Greenland and Bay of Biscay rift systems developing in the Irish Sea, following a Caledonian, northeast-southwest structural fabric (Shannon, 1991b; Warrington *et al.*, 1992). This rifting resulted in a series of large horst and graben structures forming in the Irish and Celtic Sea which significantly influenced sediment infill of these early basins (Welch *et al.*, 2000). A marine environment existed at the time because of the Bay of Biscay rift system linking the Tethyan Ocean in the east to the Boreal Sea. The study area was located 10-15° north of the equator with a humid equatorial climate. Regression of the Boreal Sea accompanied by equatorial, humid conditions resulted in an arid continental setting prevailing across the Irish and Celtic Sea by the Early Triassic. These conditions led to ferric oxidation of sediment producing the characteristic regional red bed sequence of the Lower Triassic, Sherwood Sandstone Group (Shannon, 1991b; Shannon *et al.*, 1993) (Fig. 16). The Sherwood Sandstone Group sediments have an average thickness of 65.9 m and a maximum of 114.5 m (Well 56/15-1) in the Fastnet Basin and NCSB. Five wells penetrate Sherwood Sandstone Group material in the Fastnet Basin and NCSB, with only 3 in the SGCB.

Broadly, Triassic successions in the Celtic Sea basins follow that of onshore Britain and the Irish Sea. The basal sandstone rich succession known as the Sherwood Sandstone Group is conformably overlain by the mudstone and saliferous successions of the Mercia Mudstone Group followed by thin marls of the Penarth Group (Shannon, 1991b; Shannon *et al.*, 1993;

Shannon *et al.*, 2001; SÌtolfovÃ¡ *et al.*, 2009) (Fig. 16). The primary driver for sedimentation in these basins is still the subject of debate, with two hypotheses currently proposed. The first argues for a rift-controlled Sherwood Sandstone sequence draining from local highs whilst the Mercia Mudstone resulted from post-rift thermal sagging which extended onto the surrounding basins, returning to a shallow marine environment by the Middle Triassic (Naylor *et al.*, 2011). The second argues for control of lowland areas by faults infilled by upland Variscan massifs forming the Sherwood Sandstone, with Mercia Mudstone lithologies deposited during rift phases, as conditions became increasingly marine in the Middle Triassic (Ruffell *et al.*, 1999). Importantly, both theories indicate sedimentation from the surrounding uplands without distal input. As discussed in the introduction, the extent to which the Budleighensis system connected with the NCSB, SGCB and Fastnet Basin is unknown. However, the Irish and Celtic sea basins show evidence of fluvial systems draining into a lagoonal/playa lake setting across the Irish Sea (Shannon *et al.*, 1993; Ruffell *et al.*, 1999). From the Late Triassic to Early Jurassic, rift chains extended from the Tethys Ocean to the central Atlantic along Pangea. This further established Early Permian-Triassic rift basins, deepening transgressive marine conditions resulting in the deposition of the Mercia Mudstone Group. Mercia Mudstone sequences in the SGCB are interpreted to be deltaic to marginal-marine, with halite and mudstone persistent throughout from the Late Triassic to Early Jurassic (Fig. 16). From the Anisian onward, the NCSB and SGCB had a marginal-marine setting, transitioning into a fully marine environment because of basin subsidence by the Late Triassic and into the Early Jurassic (Fig. 16). This marine transition is recorded in Penarth Groups calcareous marl successions. Of the wells in the NCSB and Fastnet Basin, a maximum thickness of 449.5 m (Well 56/26-2) of Penarth, Mercia Mudstone and Sherwood Sandstone successions are penetrated.

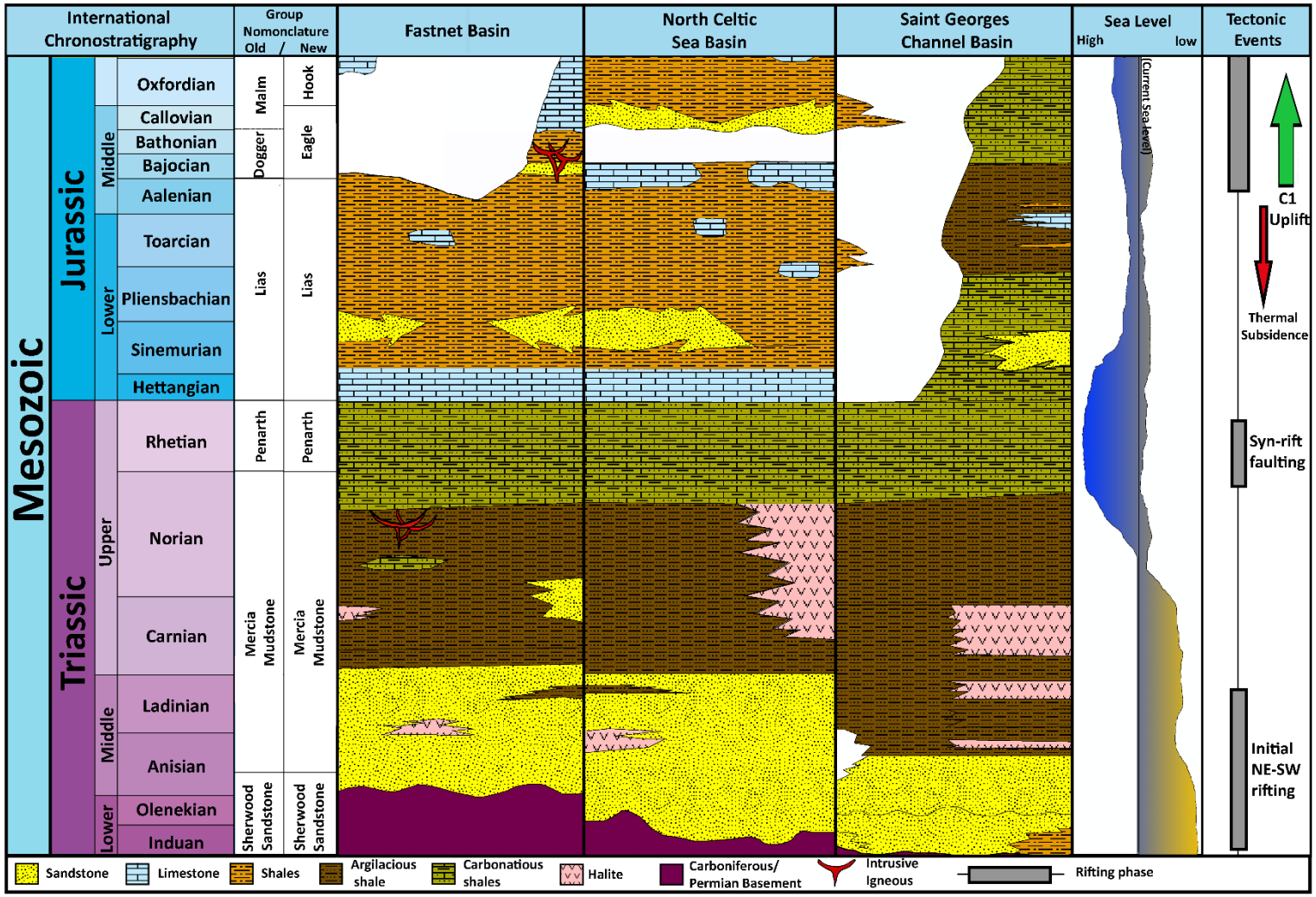

Fig. 16. *Summarized stratigraphy of the Irish and Celtic Sea regions throughout the Mesozoic period, including sea level variation and major tectonic events after Murphy et al. (1991); Ewins et al. (1995); Shannon (1995); Welch et al. (2000); Hounslow et al. (2006); Tyrrell et al. (2012). New nomenclature follows ISPSG (2019).*

3.2.3. Early Jurassic Period

By the Late Rhaetian, the open marine setting gave way to shallow marine conditions by the Hettangian, resulting in transgressive sedimentation. The Fastnet Basin records up to 3282.5 m (Well 63/10-1) of the Lias Group. This transition was recorded regionally in the deposition of the Penarth and Liassic sequences (Rowell, 1995) (Fig. 16). Carbonates dominate much of the Fastnet Basin by the Sinemurian, which thinned eastward into the NCSB. Thinning reflects the transition from marine conditions in the Fastnet Basin to marginal-marine conditions in the SGCB. A regression event by the end of the Sinemurian led to the deposition of deltaic sandstone in the SGCB, northern NCSB and Fastnet Basin (Fig. 16). Sediment transported during these deltaic conditions is thought to have been clastic, terrestrial sourced material from onshore old red sandstone or the Fastnet Spur based on sandstone isopach maps (Ewins *et al.*, 1995; Tyrrell, 2005). Deposition in the eastern half of the NCSB possibly shed from the Leinster Massif (Petrie *et al.*, 1989).

Much of the fault activation influenced sediment deposition where horst and graben structures of the NCSB and SGCB made deep depocenters thought to limit sedimentation to the south (Welch *et al.*, 2000). For example, the Saint George's Fault played an influential role in sediment transport as footwall readjustment at the northern margin of the NCSB and SGCB deepened marine conditions northeast of the fault. Deltaic, shallow marine and marine conditions are interpreted at this time (Ewins *et al.*, 1995). Conditions then transgressed back into a shallow carbonate and sandstone deposits by the Pleinsbachian as a consequence (Kessler *et al.*, 1995). By the Pleinsbachian, clastic sedimentation with mudstone and marine conditions prevailed into the Late Pleinsbachian in the NCSB and SGCB. The Pembroke Ridge was reportedly a topographical high at the time directing northern sourced, Leinster and Welsh Massifs, sediments to the southeast (Fig. 15). The Leinster Massif is thought to have been a primary source of clastic material at this time (Petrie *et al.*, 1989). By the Toarcian, a major transgression related to thermal subsidence resulted in mudstone and shale deposition throughout the Celtic Sea (Murphy *et al.*, 1991). Upward grading mudstones indicate marine conditions with carbonates in the NCSB, grading into deltaic and shallow marine clastic deposits in the SGCB (Petrie *et al.*, 1989).

3.2.4. Early Jurassic and Triassic Sediment Sources

Sediment source regions are broadly grouped into two tectonostratigraphic domains which include Laurentia and Peri–Laurentia to the north of the Iapetus Suture (Fig. 15) and Peri-Gondwanan affiliated sources to the South (including Gandaria, Monian composite terrains, Megumia, Avalonia and Cadomia) (Waldron *et al.*, 2019b). The characterization of Laurentian and Peri-Gondwanan domains as well as post-Caledonian cover sequences is addressed in Section 2.3.. However, considering the special importance of Cadomian domains during the Triassic, these are discussed in greater detail below.

The Armorican and Iberian Massifs are Cadomian domains, with an inherent upland Variscan topography (Nance *et al.*, 2008; Henderson *et al.*, 2016), metamorphosed in places by the Variscan orogeny and associated magmatic activity (Guerrot *et al.*, 1990; Dallmeyer *et al.*, 2013). Sediment draining from the central or northern margin of the Iberian Massif would likely have a dominant Variscan population of I- type and S-type igneous sources along with allochthonous Ediacaran metamorphosed material (Fernández-Suárez *et al.*, 2014; Grobe *et al.*, 2014; Pereira *et al.*, 2018). While sediment draining from the Armorican Massif would be expected to contain a similar Peri-Gondwanan zircon population with autochthonous c. 315 Ma mica and zircon from sources like the Lizio granite, however allochthonous Ediacaran sediment is also located toward the south of the Armorican Massif (Tartese *et al.*, 2011; von Raumer *et al.*, 2015). These Cadomian sources are expected to shed abundant Paleozoic and Neoproterozoic zircon and mica, however the Iberian Massif is expected to shed Ediacaran mica more readily to the North (Fernández-Suárez *et al.*, 2000; Gutiérrez-Alonso *et al.*, 2005).

3.3. Methods

3.3.1. Rationale

Quantitative provenance analysis has a wide range of tools for interrogating the routing systems of ancient sediments (Chew *et al.*, 2020). Analytical tools were chosen to complement each other, minimise bias and to make full use of very limited sample materials. Detrital zircon U-Pb geochronology was chosen as this system has a high closure temperature

and is resistance to chemical and weathering induced alterations (Gehrels *et al.*, 2006; Chew *et al.*, 2017; Vermeesch *et al.*, 2017). However, its natural bias under-represents metamorphic and mafic igneous sources (Hietpas *et al.*, 2011). Coupling zircon with apatite U-Pb geochronology is more representative of igneous sources and metamorphic sources whilst also providing a trace element signature describing the age and chemistry of a source terrain (O'Sullivan *et al.*, 2020). Detrital white mica further compliments these methods acting as an additional tracker for igneous and metamorphic sources (Von Eynatten *et al.*, 2003). Bulk sediment characterisation techniques, like heavy mineral analysis (HMA) and petrographic analysis, better capture sediment composition and may provide additional insights to provenance and sediment history including diagenetic alteration (Morton *et al.*, 1994; Mange *et al.*, 2007; Andò *et al.*, 2014). In this study, HMA results were very limited due to samples often lacking more than 200 detrital, opaque heavy minerals. These samples were excluded from results, and the remaining 5 samples are included to better describe sample composition and to make full utility of precious sample material. It is important to note that heavy mineral abundance summarised by total volume is biased by naturally larger grains, like tourmaline, and may occupy more of a sample than if point counted. In addition, QEMSCAN analysis cannot differentiate between mineral polymorphs or authigenic and detrital grains, and these analytical biases were considered while interpreting results. TiO_2 minerals could not be confidently differentiated between authigenic and detrital grains along with sphalerite. Interpretations of sediment sourcing involving these minerals in particular were made cautiously.

For a full description of sample preparation, see Section 2.4. This preparation technique was chosen to optimise data extraction from very limited sample material. However this methodology made optical identification of grains difficult as a high level of polishing was not possible. Prepared samples are labelled by basin where NC indicates the NCSB, SG the SGCB and FB the Fastnet Basin. Detrital white mica and zircon samples FB1, FB2 and NC1 were processed and analysed as outlined in Fairey *et al.* (2018) and are taken from an unpublished PhD data set. Samples in this study are from offshore cuttings (11 samples) or from a core sample (sample NC4 only). Inherently these have a risk of contamination from cave ins as well as drill fluid suspension minerals like barite, fluorite and sometimes mica. Samples which are

from core samples are identified in text and diagrams while all other samples are from drill cuttings.

3.3.2. Heavy Mineral Analysis

Five samples prepared for heavy mineral analysis were mounted, ground and polished to the approximate centre of grains and sent for Qemscan analysis at 10 µm resolution by Rocktype Ltd in their Oxford laboratory. QEMSCAN analysis was used to identify all heavy mineral suites. As samples are taken from offshore core and cuttings, all barite and fluorite minerals are excluded with the remainder normalised to 100% of the excluded values. Further Raman and optical investigations of REE phosphates minerals, kyanite, sillimanite and andalusite polymorphs were conducted using an Renishaw inVia™ confocal Raman microscope in University College Cork (Andò *et al.*, 2014). A Renishaw inVia™ confocal Raman microscope with a 50 mW DPSS (diode-pumped, solid-state) 532 nm laser, at 1 second residence time, 10% laser strength and a x50 long working distance objective was used for these spot analyses. Sample spectra were identified using the Ruff database (Lafuente *et al.*, 2015). Phases considered indicator minerals including zircon, tourmaline, grouped TiO_2 phases, apatite, sphalerite, garnet, titanite, monazite, clinopyroxene, kyanite, staurolite and chromespinel are included in results. Other identified minerals include abundant pyrite, chalcopyrite, biotite, muscovite, siderite and traces of galena. Reported heavy mineral values were normalised to 100% of the total heavy mineral volume of the sample.

3.3.3. Zircon, Apatite and Mica Geochronology

Zircon, apatite and mica samples were analysed and processed following Section 2.6. Single grain concordant ages were calculated for all zircon samples using the isoplot v4.15 excel add in (Ludwig, 2012). The primary reference materials were Plešovice zircon (Slama et al., 2008) and Madagascar apatite (Wiedenbeck *et al.*, 1995; Thomson *et al.*, 2012) respectively. The weighted mean ^{206}Pb-^{238}U ages for secondary zircon standards are: in-house zircon standard WRS 1348 (Pointon et al., 2012) = 529.4 ± 2.6 Ma (n = 50), 91500 zircon (Wiedenbeck et al. 1995) = 1055.1 ± 4.6 Ma (n=42) and GZ7 (Nasdala *et al.*, 2018) = 528.6 ± 2.0 Ma (n=50). All

standards for this analysis are within uncertainty ranges when compared to the published reference materials (Wiedenbeck *et al.*, 1995). A common Pb correction was applied to apatite samples for high common lead to radiogenic lead ratios, after Cogné *et al.* (2014). As apatite often yields discordant U-Pb ages, an iterative 2σ error filter of 50% was applied for grains less than 100 Ma, 15% for 1000–100 Ma and 6% for 3.6 – 1.0 Ga (O'Sullivan *et al.*, 2020). Concordant zircon ages are displayed for a probability of concordance > 0.001 after Zimmermann *et al.* (2018). Kernel density estimates (KDEs) were generated using the IsoplotR package (Vermeesch, 2018). A 25 Ma bandwidth was chosen for zircon and apatite, and a 5 Ma bandwidth was chosen was for mica sample NC1.

3.3.4. Apatite Trace Element Analysis

During U-Pb isotope analysis of apatite, trace element concentrations were obtained simultaneously. The primary standard employed was NIST 612 standard glass, and the secondary standards Durango and McClure apatites were employed (Chew *et al.*, 2016). Flowing the multivariate analysis approach of O'Sullivan *et al.* (2020), combined SNV-PCA analysis was used to discriminate apatite trace element chemistry. This method allows the user to utilise the LREE (La-Nd) and Sr/Y trace element data collected during ablation to differentiate between alkali-rich igneous rocks (ALK), mafic I-type granitoids and mafic igneous rocks (IM), low- and medium-grade metamorphic and metasomatic (LM), partial-melts, leucosomes and high-grade metamorphics (HM), S-type granitoids and high aluminium saturation index, 'felsic' I-types (S) and ultramafic rocks including carbonatites, lherzolites and pyroxenites (UM). Ages reported in these data sets are filtered as of those from Section 2.6.1. while all apatite grains are included regardless of their discordance. Analytical error and phosphate abundance were used to filter analysis which may have missed apatite grains or grains which were dislodged during the ablation processes.

3.4. **Results**

Heavy mineral abundance (5 samples) as well as Kernel Density Estimate (KDE) diagrams of 479 zircons (5 samples), 68 micas (1 sample), and 105 apatites (2 samples) are presented, with trace element analysis of 205 apatite (2 samples) grains from two samples. Age data from

multiple geochronology methods are grouped into 6 populations relating to their orogenic and tectonic affinities (Table 2). Geochronological populations follow that of Section 2.8. and references therein for ease of cross sample comparison. These data are then contextualised with Mesozoic provenance evolution in a Multi Dimensional Scaling (MDS) model incorporating a further 15 detrital zircon U-Pb data sets from McCarthy, *et al.* (2020) produced using the MDS function in the R package "Provenance" (Vermeesch, 2018). In addition, a ratio calculation of samples above and below 720 Ma is used to distinguish dominantly Peri-Gondwanan and Laurentian populations.

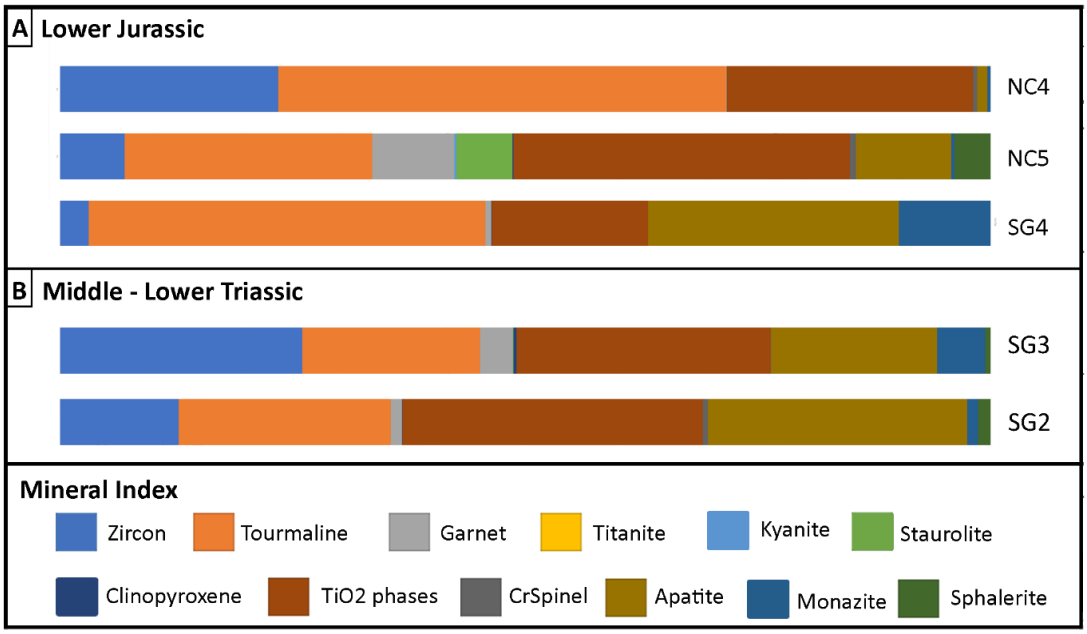

Fig. 17. *Heavy mineral Abundance for (A) Lower Jurassic samples and (B) Lower-Middle Triassic samples. Mineral index is for Sections A and B (See Appendix D Table 6 for all heavy mineral samples).*

3.4.1. Heavy Mineral Abundance

Five heavy mineral samples from the SGCB and NCSB are summarised in Fig. 17. Lower Jurassic samples of the NCSB contain zircon, tourmaline and TiO_2 phases, however, sample NC5 (cuttings Well 50/03-3) appears to contain an additional metamorphic or hydrothermal input as indicated by the presence of sphalerite (possibly authigenic), staurolite and garnet. Sample NC4 (core Well 50/03-1) represents a compositionally mature sediment containing 95% zircon, tourmaline and TiO_2 minerals (Fig. 17). Jurassic and Triassic samples (SG2-SG4 cuttings wells 103/01-2 and 42/21-1) of the SGCB contain more monazite with some garnet and

clinopyroxene, and less tourmaline than the NCSB. Together, clinopyroxene, apatite and TiO_2 phases indicate a volcanic source. Garnet, monazite and tourmaline indicate a metamorphic source.

Table 2. Detrital single grain age groups based on regional tectonic events.

Grain Population	Min (Ga)	Max (Ga)	Tectonic Association
Gpop6	1.5	2.9	Labradorian, Lewisian
Gpop5	0.9	1.5	Grenville, Pinwarian
Gpop4	0.5	0.7	Peri-Gondwanan
Gpop3	0.39	0.47	Caledonian, Grampian, Scandian
Gpop2	0.29	0.39 /0.4	Acadian, Variscan
Gpop1	0.07	0.27	Atlantic rift related volcanism

3.4.2. Lower Triassic Zircon U-Pb Geochronology

Sample FB2 (Cuttings Well 57/09-1) from the eastern margin of the NCSB is dominated by a c. 600 Ma Peri-Gondwanan population with subordinate Acadian and Variscan populations (Fig. 18). Limited Grenville and Labradorean aged zircon are present. Sample NC1 (Cuttings well 56/26-2) has a homogenised Acadian-Peri-Gondwanan population (Fig. 18). This sample also contains limited Laurentian detritus, indicating a dominant Peri-Gondwanan source for these samples.

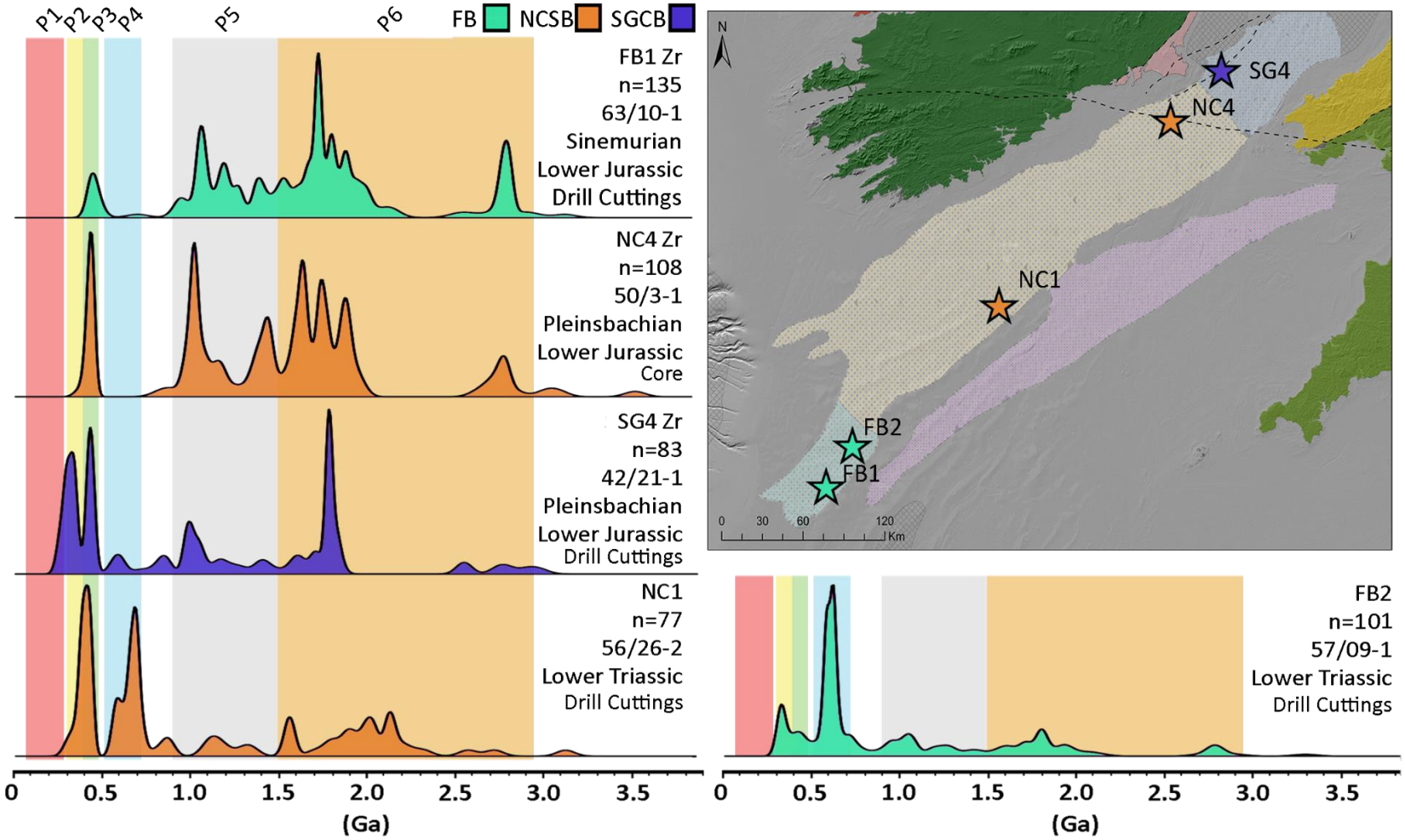

Fig. 18. *Zircon KDE diagrams of Triassic and Lower Jurassic sediments in the NCSB, North Celtic Sea Basin; SGCB, St. George's Channel Basin; FB, Fastnet Basin (See Appendix D Table 2 U-Pb data for all detrital zircon data).*

3.4.3. Lower Jurassic Zircon U-Pb Geochronology

Pleinsbachian sample SG4 (Cuttings Well 42/21-1) has three dominant populations of 1.8 Ga Labradorean, c. 430 Ma Caledonian, and 310 Ma Variscan affinity (Fig. 18). In addition, this sample contains a subordinate 1.0 Ga Grenville peak with some older Archean material. NCSB sample NC4 (Core Well 50/03-1) has two dominant populations, and a series of subordinate populations. The c. 440 Ma Caledonian-Grampian population and 1.0 Ga Grenville populations are dominant peaks along with a series of subordinate Labradorean peaks making up the rest of the sample with some Archean material. Fastnet Basin sample FB1 contains a distinct Laurentian population of 1.7 Ga zircon along with some 1.1 Ga Grenville material and older Archean zircon. This sample also contains a subordinate 460 Ma population of Grampian affinity. The Lower Jurassic samples reflect a distinct change in provenance, contrasting from Laurentian dominated populations to Peri-Gondwanan populations of the Lower Triassic samples. Sample SG4 has an additional input of Peri-Gondwanan population.

3.4.4. Apatite Geochronology and Trace Element Analysis

Lower Triassic sample SG2 (Cuttings Well 103/01-2) contains a single, dominant Variscan population c.325 Ma. Trace element analysis distinguishes several subgroups within this age group. There is a significant proportion of multiple high-grade metamorphic grains with compositional variation in this group. Ultramafic-mafic apatite of the same age is present with a single older 465 Ma grain (Fig. 19A). Some S-type granitoid and felsic I-type grains c. 325 Ma are also present of ultramafic affinity. Multiple I-type granitoid and mafic apatites make up the remainder of the sample, with a single 960 Ma grain in this group. Lower Jurassic sample SG4 (Cuttings Well 42/21-1) apatite contains two dominant populations: a Paleoproterozoic c. 1.8 Ga and late Permian population c. 280 Ma. Several subordinate populations make up the remainder of this sample, from Peri-Gondwanan to Laurentian affinity. Trace element modelling identifies a distinct I-type granitoid/mafic igneous source of 280 Ma apatite and medium-low grade metamorphic and igneous sources for all other grains. (Fig. 19B.).

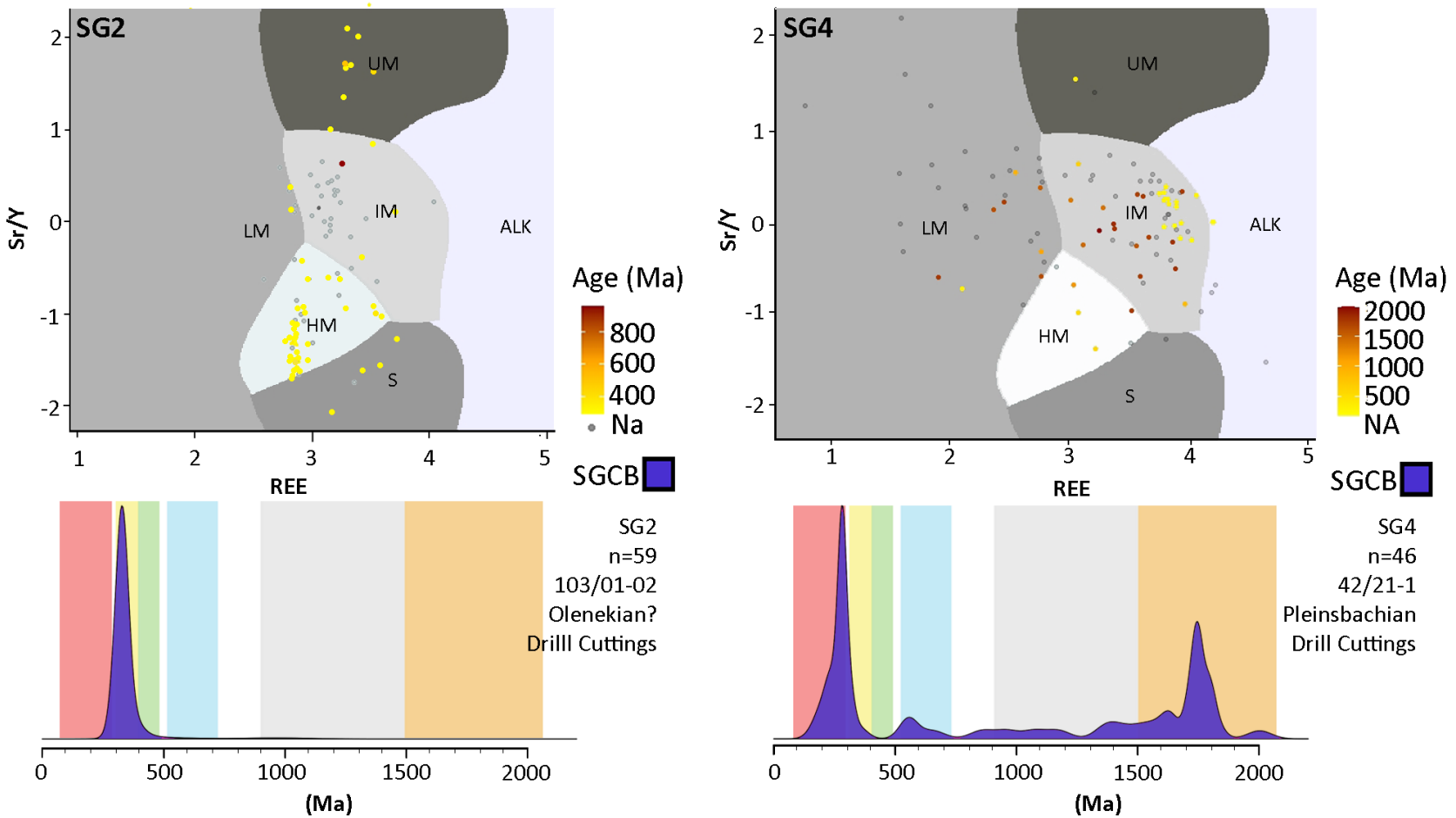

Fig. 19. *Apatite trace element SVM biplot and accompanying KDE diagrams for: Triassic sample SG2a of the SGCB and Lower Jurassic sample SG4a of the SGCB. Trace element plots were generated following O'Sullivan et al. (2020) where ALK, alkali-rich igneous rocks; IM, mafic I-type granitoids and mafic igneous rocks; LM, low-medium grade metamorphic and metasomatic; HM, partial-melts/leucosomes/high-grade metamorphic; S, S-type granitoids and high aluminium saturation index (ASI) 'felsic' I-types; UM, ultramafic rocks including carbonatites, lherzolites and pyroxenites (O'Sullivan et al., 2020). For further details see Table 3 for U-Pb and Table 4 for trace element information.*

3.4.5. Triassic White Mica Geochronology

NC1 (Cuttings Well 52/26-2) contains a conspicuous Ediacaran white mica population of Peri-Gondwanan affinity (Fig. 20). In addition, two grains of Scandian and Variscan age are present. Despite the abundance of Acadian and Caledonian zircon in NC1, it is devoid of comparative mica. Mica of this age is not found in other mica samples from younger Jurassic and Cretaceous sequences.

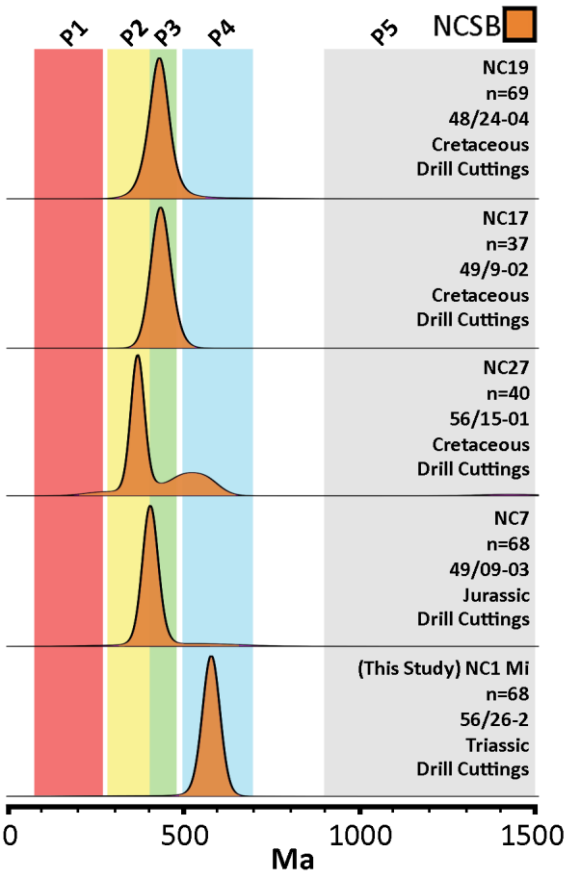

Fig. 20. *$^{40}Ar/^{39}Ar$ dating of detrital white mica samples from the Cretaceous (NC19,NC17 & NC27), Jurassic (NC7) and Triassic (NC1). Kernel bandwidth of 25 Ma. (See Appendix D Table 5 Ar-Ar data for all detrital mica samples)*

3.5. **Discussion**

3.5.1. Triassic Anisian-Ladinian Provenance

During the initial phase of basin opening, infill of sedimentary basins south of the Iapetus suture is thought to have drained drain from the Armorican Massifs as far as Northern Ireland via the central basins of the Britain (Tyrrell *et al.*, 2012). Heavy mineral samples SG2 & SG3 contain chromespinel, clinopyroxene, garnet, monazite and sphalerite (possibly authigenic), which are indicative of metamorphic and igneous sources (Mange *et al.*, 1992). It is therefore unsurprising to find abundant c. 700 Ma and Caledonian-Acadian and Peri-Gondwanan U-Pb zircon populations in Triassic samples NC1 (cuttings Well 56/26-2) and FB2 (cuttings Well 57/09-1). These samples are like those of comparative Sherwood Sandstone Group of the Wessex Basin infilled from the Cadomian, Armorican massif (Morton *et al.*, 2013; Morton *et al.*, 2016). However, this is not directly indicative of a southern provenance for sediments of the Celtic Sea as these Triassic samples also match those of the Lower Cretaceous in the NCSB, which drained from the Irish and Welsh Massifs (see Section 2.8.3.1). More indicative of a Cadomian provenance is Ediacaran aged Ar-Ar white mica in the NCSB sample NC1 (Well 56/26-2) and Variscan, U-Pb dated apatite in the SGCB sample SG2 (Well 103/01-2) (Fig. 19). A probable source of Ediacaran mica is the basement complexes of north-western Iberia which preserve Peri-Gondwanan, late Cambrian-Neoproterozoic zircon and mica (Fernández-Suárez *et al.*, 2000; Gutiérrez-Alonso *et al.*, 2005; von Raumer *et al.*, 2015).

The Munster Basin is an unlikely source despite being the most proximal as it contains significant Grenville aged zircon populations as well as limited Peri-Gondwanan and Silurian U-Pb zircon populations (Fairey, 2017). Furthermore, a source marginal to the NCSB basin is very unlikely, as younger Jurassic and Cretaceous mica samples (NC17, NC19, NC27) from the NCSB do not contain mica of this age, with only one sample (NC7 Upper Jurassic cuttings Well 49/09-3) preserving a single Ediacaran grain (Fig. 20). The absence of these signatures is likely a consequence of Permian-Triassic rifting which produced horst and graben structures limiting Triassic sedimentation from the north (Irish and Welsh Massifs) to the south into the NCSB (Ruffell *et al.*, 1999). However, the absence of 500–270 Ma Ar-Ar white mica populations is confounding as both northern and southern sources contain these populations

(Fig. 20). One possible explanation for this is selective drainage from the north-eastern Iberian Massif (von Raumer *et al.*, 2015) into the NCSB, where Cambrian basement is exposed with less Variscan material.

Apatite sample SG2 (cuttings Well 103/01-2) is also diagnostic of a southern provenance from the Iberian Massif. The ultramafic-mafic igneous and low-high grade metamorphic trace element signatures of 350–294 Ma U-Pb dated apatite (O'Sullivan *et al.*, 2020) are likely from the northern, western and central regions of the Iberian Massif. Here, Variscan aged S-type granites intruded and caused greenschist-amphibolite facies metamorphism (Cabrera *et al.*, 2004; Grobe *et al.*, 2014) of Neoproterozoic to Early Paleozoic metasediments in the Galicia region of north-western Spain (Fernández-Suárez *et al.*, 2000; Dallmeyer *et al.*, 2012; Pereira *et al.*, 2018; Ferreira *et al.*, 2019). Variscan orogenic magmatism and associated low-high grade metamorphism are thus the likely source of these Variscan aged metamorphic apatites. This is supported by the mixed metamorphic and igneous HMA results of samples SG3 and SG2 (Fig. 17).

Alternatively, the Cornubian Massif in southwest England contains granitic intrusions and some volcanic material, including S-type granites and volcanics active from 325–270 Ma (Smith *et al.*, 2019b). However, if sediment were transported from this source, a more significant proportion of 300–270 Ma apatite and mica of this age would be expected in NC1 (cuttings well 56/26-2) and SG2 (cuttings well 103/01-2). Additionally, 2D seismic evidence of sediments onlapping the Labadie Bank and Pembrokeshire Ridge (Fig. 21) indicate that the NCSB and South Celtic Sea Basin were disconnected at this time (Tyrrell, 2005; Rodriguez-Salgado, 2019). Though the Armorican Massif contains granitic and volcanic sources of Variscan age (Hounslow *et al.*, 2006; Ducassou *et al.*, 2011; Tartese *et al.*, 2011; Dallmeyer *et al.*, 2013; Augier *et al.*, 2015), its evident drainage north into the Wessex basin, distance from the Celtic Sea, and the numerous obstructive topographical highs likely precludes sedimentation from this source into the Fastnet Basin or SGCB (Fig. 21). Detrital Ar-Ar mica, combined U-Pb and trace element analysis of apatite and U-Pb zircon geochronology provide strong evidence that sediment was transported from the Iberian Massif into the Fastnet Basin, NCSB and SGCB during the Early Triassic.

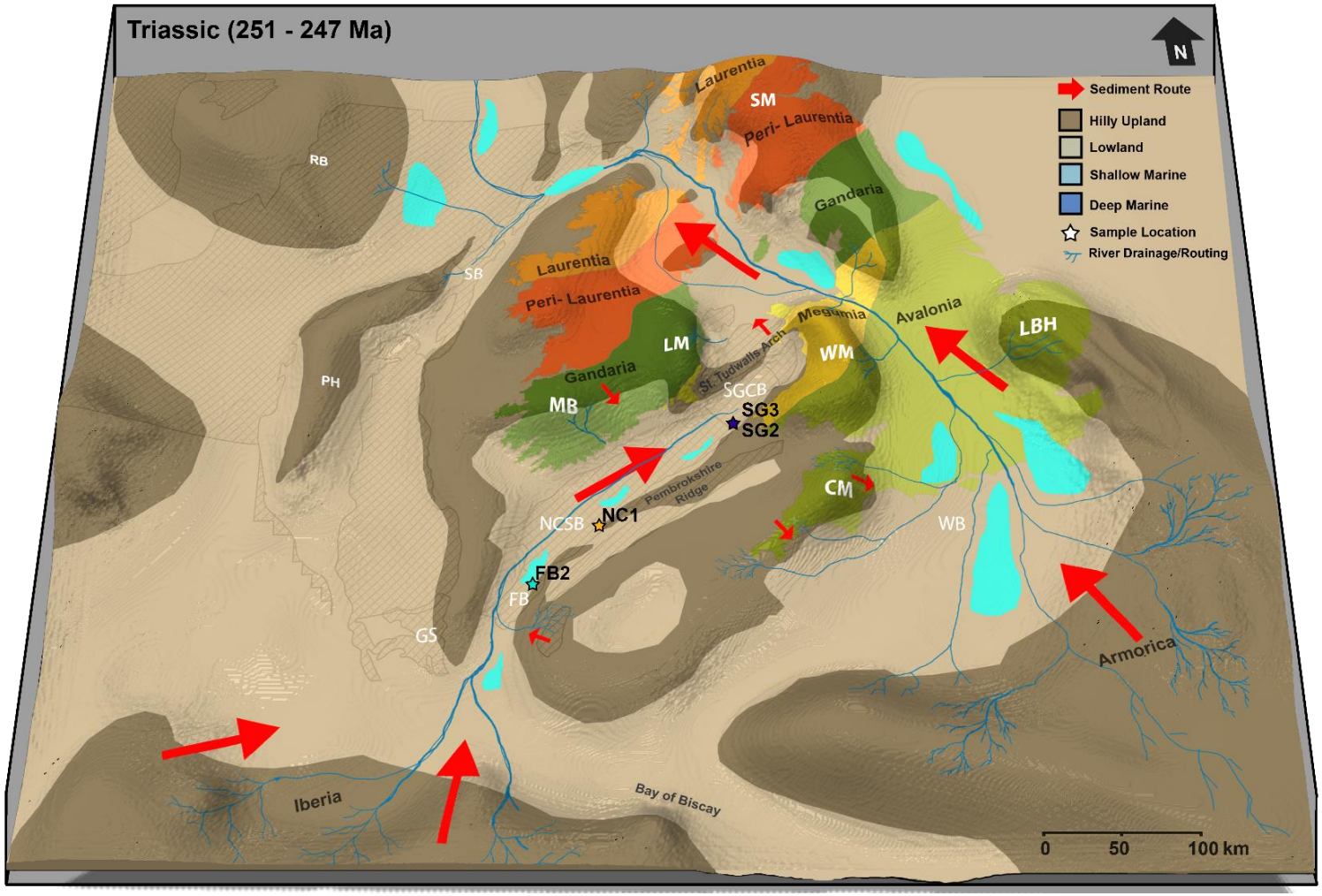

Fig. 21. *Interpreted palaeoenvironmental map of the Induan-Olenekian after Dunford et al. (2001), Hounslow et al. (2006), De La Horra et al. (2008), Naylor et al. (2011), Tyrrell et al. (2012), Morton et al. (2013) and Franklin et al. (2020). Arrows indicate sediment transport direction while rivers indicate possible drainage patterns, and turquoise pools are intermittently wet/dry playa. CM, Cornubian Massif; GS, Goban Spur Basin; LBH, London-Barbrant High; LM, Leinster Massif; MB, Munster Basin; NCSB, North Celtic Sea Basin; SB, Slyne Basin; SGCB, Saint George's Channel Basin; SM, Scottish Massif; WB, Wessex Basin; WM, Welsh Massif.*

3.5.2. Early Jurassic Provenance

During the Early Jurassic, continued Pangean rifting initiated a basin-wide marine transgression with shelf deposits and deltaic sedimentation in localised marginal settings (Fig. 22). Previous interpretations of provenance have considered sedimentation primarily from the Old Red Sandstone sources in the Fastnet Spur (Petrie *et al.*, 1989; Ewins *et al.*, 1995), while eastern NCSB sediments were thought to derive from the Leinster Massif (Petrie *et al.*, 1989; Kessler *et al.*, 1995).

Heavy mineral results from Liassic sandstones sample NC5 (cuttings Well 50/03-3) comprise staurolite with some kyanite, garnet and apatite indicative of a metamorphic or igneous lithium pegmatite source like the Leinster Massif (Jennings *et al.*, 2011). Contrastingly, NC4 (core Well 50/03-1) HMA results reflect mature sediment comprised of 98% zircon, tourmaline and TiO_2 minerals (possibly authigenic). Unlike NC5, this indicates distal sediment transport, recycling or chemical alteration as labile minerals susceptible to weathering and erosion are absent (Garzanti, 2017) (e.g., apatite and clinopyroxene). As both samples are Pleinsbachian, shallow shelf marine with intermittent deltaic deposits, this variation possibly reflects the interplay between distal sedimentation from a western Laurentian source and localised deltaic input from the Irish Massif during a transgressive period (Fig. 18B).

Lower Jurassic U-Pb zircon samples (FB1, NC4 and SG4) signal a distinct provenance switch from Peri-Gondwanan c. 700 Ma populations of the Lower Triassic (FB2 and NC1) with Laurentian, 1.0 Ga Grenville and 1.9–1.7 Ga Pinwarian-Labradorian populations (Fig. 18). The most proximal Laurentian sources include the Munster Basin (Fairey, 2017) or Dalradian Supergroup (Chew *et al.*, 2010), Rhinns Complex, granitic orthogneisses of the Porcupine High offshore of Ireland's west coast (Chew *et al.*, 2019b), or the Southern Uplands Terrane of northern Ireland and Scotland (Waldron *et al.*, 2008). Alternatively, FB1 (cuttings Well 63/10-1), similar to GS1 (cuttings Well 62/07-1) of the Middle Jurassic NCSB (Fig. 5, Section 2.8.1.), may represent derivation from Greenland or the eastern Canadian Trans-Hudson Orogeny Laporte Group(Willner *et al.*, 2014; Gilligan *et al.*, 2016; Henrique-Pinto *et al.*, 2017).

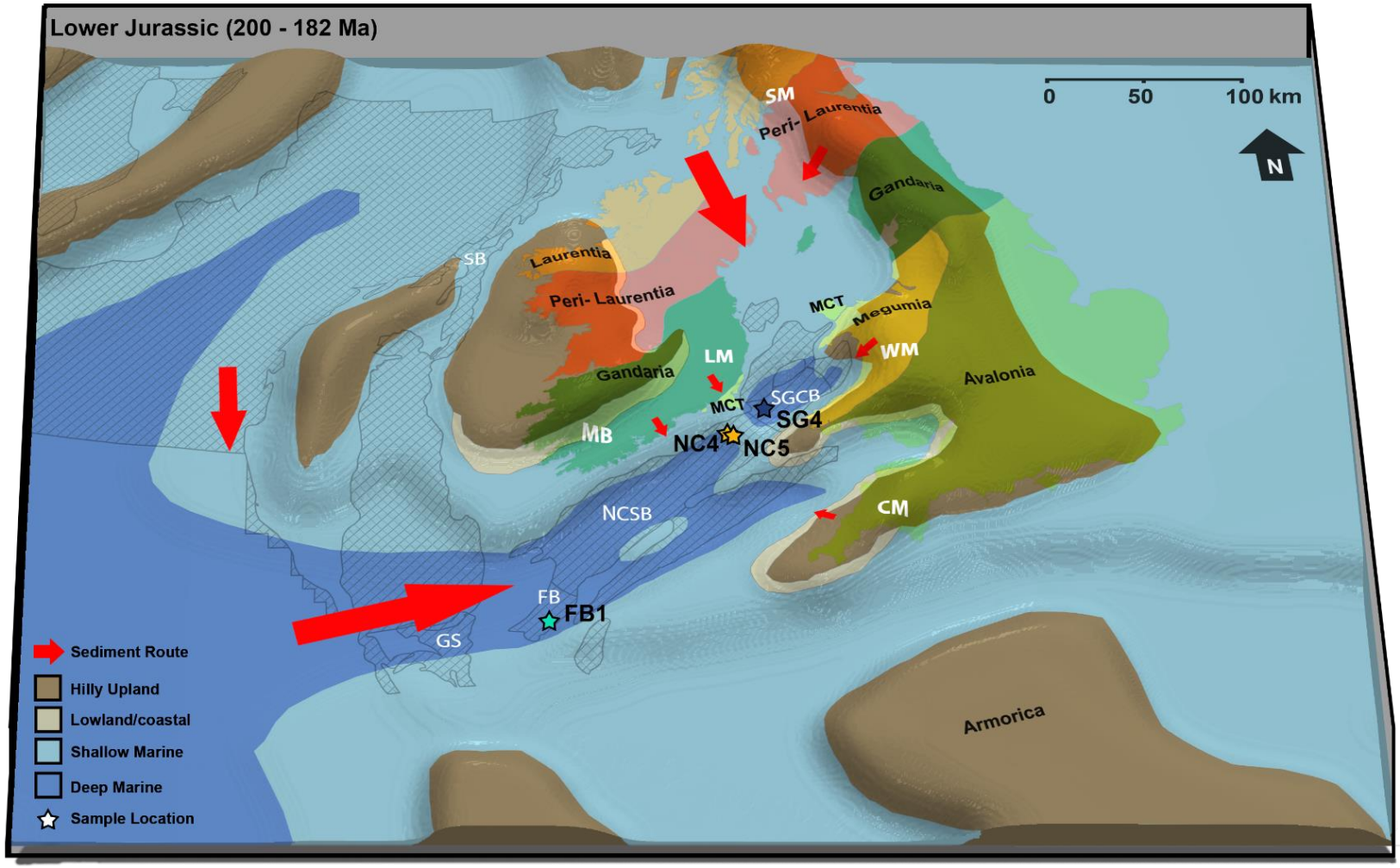

Fig. 22. *Interpreted palaeoenvironmental map of the Lower Jurassic after Roberts (1989) and Naylor et al. (2011). Sediment routing is indicated by red arrows. Cross hatch polygons mark basin boundaries. CM, Cornubian Massif; GS, Goban Spur Basin; LBH, London-Barbrant High; LM, Leinster Massif; MB, Munster Basin; NCSB, North Celtic Sea Basin; SB, Slyne Basin; SGCB, Saint George's Channel Basin; SM, Scottish Massif; WB, Wessex Basin; WM, Welsh Massif.*

Such a dominant 1.7 Ga population lacking Peri-Gondwanan detritus is unlikely to have come from a northern source which had to circumnavigated the Irish (Fairey, 2017; Fairey *et al.*, 2018; Nauton-Fourteu *et al.*, 2020) and Welsh Massifs (Waldron *et al.*, 2014). Laurentian sources west of the Irish Massif shed sediment into the opening Atlantic prior to the Mesozoic (Tyrrell *et al.*, 2012; Franklin *et al.*, 2019; Franklin *et al.*, 2020), and may have continued as marine conditions returned during the Late Triassic and Early Jurassic. These sources delineate a long-distance sediment routing mechanism likely facilitated by transgressive conditions as observed in Middle Jurassic-Upper Cretaceous sediments of the Irish and Celtic Sea basins (see Section 2.9)**.** Sample NC4 (Well 50/3-1) may be derived from the Munster basin as it contains an asymmetric Grenville peak similar to that identified in the Glyeen Formation (Fairey, 2017), and without apatite or mica geochronology, it is difficult to differentiate these sources. This supports HMA results indicating a mix of near- and far-field sediment sourcing to the NCSB at the time.

Pleinsbachian sample SG4 (cuttings Well 42/21-1) differs to NCSB core sample NC4 (Well 50/3-1) and Fastnet Basin sample FB1 (cuttings Well 63/10-1) containing some c. 700 Ma Peri-Gondwanan material as well as 286 Ma zircon along with, c. 275 Ma and 200–173 Ma apatite (Fig. 19B). Trace element analysis of c. 275 Ma grains identifies a mafic/I-type igneous source, likely from volcanism associated with the Midland Valley Terrain to the north which occurred because of post Variscan orogenic collapse across northwest Europe during the Carboniferous and Early Permian (Monaghan & Pringle, 2004). Further, 1.85–1.0 Ga metamorphic and igneous apatite and the dominant 1.85 Ga zircon population in SG4 (Well 42/21-1) are possibly recycled from the Dalradian Supergroup (Chew *et al.*, 2010), Rhinns Complex, Iona Group (McAteer *et al.*, 2014) or Colonsay Group of southwest Scotland (McAteer *et al.*, 2010b). An alternate source of these Permian apatites is the Dartmoor, Isles of Scilly or Haig Fras granites to the south, which intruded as part of the Cornubian batholith during the Early Permian c. 280 Ma (Dyment *et al.*, 1991; Taylor, 2007; Warr, 2012). The 650–550 Ma zircon and apatite are likely from Welsh or Leinster Massif (Waldron *et al.*, 2014) as southern samples NC4 (core Well 50/03-1) and FB1 (cuttings Well 63/10-1) lack these populations precluding a Peri-Gondwanan source to the south. It is not possible to derive the relative northern and southern sediment contributions to the SGCB currently, however, there is clear evidence of a dominantly northern source with a plausible southern input.

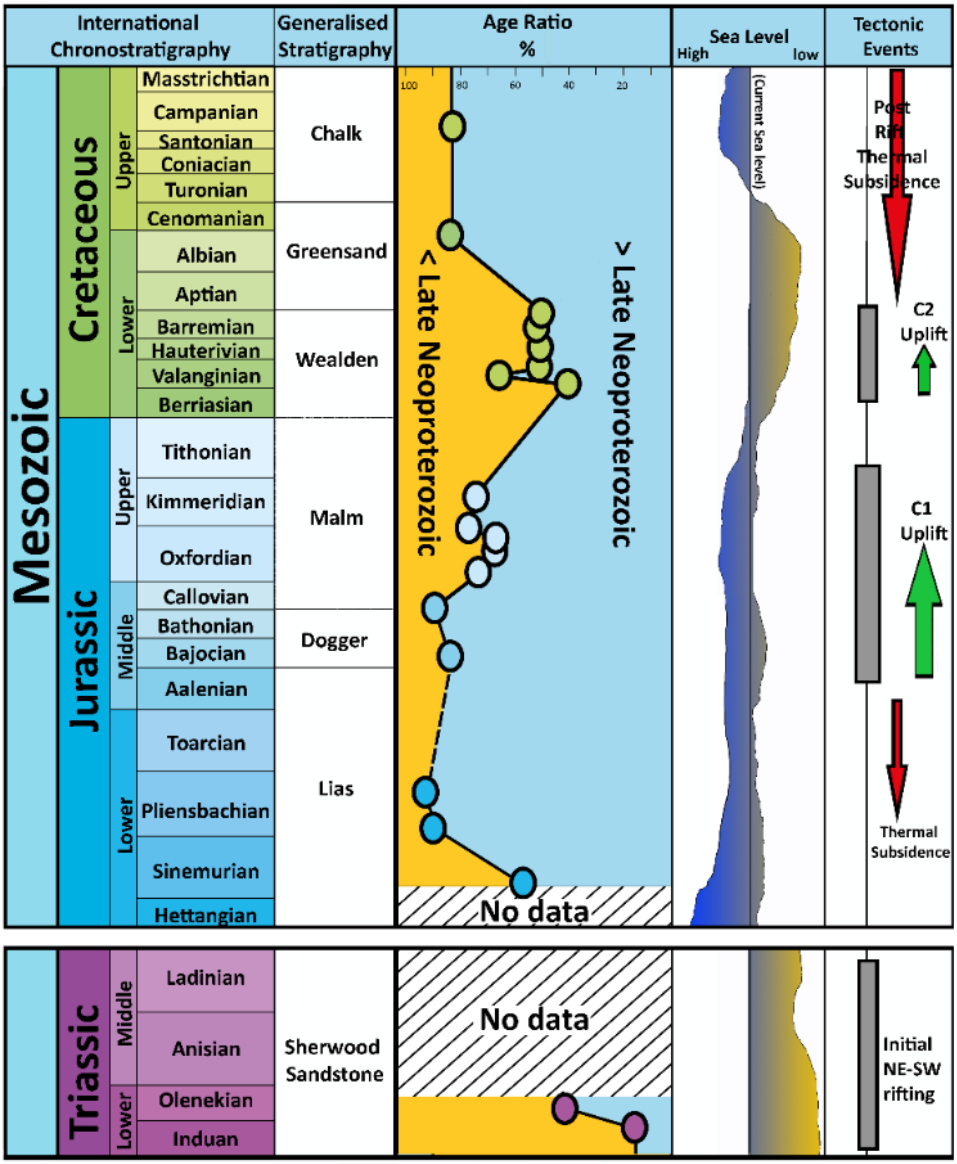

Fig. 23. *Lithostratigrphic summary of the zircon ratio above and below the Late Neoproterozoic (720 Ma) with adapted sea level estimates and tectonic events from Murphy et al. (1991), Shannon (1991a) and Rodríguez-Salgado et al. (2019). Age ratio samples from the Middle Jurassic-Upper Cretaceous samples are taken from Section 2.8.1.. As this covers multiple basins, Sea level colours show the interpreted range of environments within each basin from terrestrial (yellow) – marine (blue).*

3.5.3. Mesozoic Infill Model for the Celtic and Irish Seas

Data from this study combined with 15 samples (see Table 7 of appendixes E) from Middle Jurassic to Upper Cretaceous sequences of the Goban Spur, Fastnet Basin, SCSB, NCSB and SGCB are used to model temporal provenance evolution throughout the Mesozoic. By calculating the ratio of detrital zircon grains above and below the Late Neoproterozoic (720

Ma) (Fig. 23), and using MDS modelling of these 20 detrital zircon samples, four distinct groupings are observed which highlight the first-order control of environmental and tectonic factors on sediment provenance (Fig. 24).

Samples (FB2, SC1, NC1, NC18, NC19, NC20 and NC26) within MDS Group 1 contain dominant Peri-Gondwanan (700-500 Ma) and Scandian-Variscan (470 – 290Ma) populations, with limited amounts of Laurentian (0.9-2.2 Ga) associated detritus (Fig. 24). These samples are from non-marine successions where fluvial derived sediments drained directly from post Caledonian cover sequences of Peri-Gondwanan domains with minimal recycling or distal input (Fig. 23). During the Triassic, these sources include the Iberian Massif within the Cadomian domain (see Section 3.2.3). During the Early Cretaceous, sources include the Leinster Massif (Waldron *et al.*, 2014)and Welsh Massif (Pothier *et al.*, 2015), all of which have a dominant Peri-Gondwanan affinity (Section 2.8.1.3).

Group 2 samples (FB4, SG4, NC7, NC8 and NC10) contain a mixed Peri-Gondwanan and 1.0-2.9 Ga Laurentian signature often with a prominent c. 1.7 Ga population (e.g., SG4 Fig. 18). These sediments were deposited in a shallow marine-continental shelf setting with significant terrestrial input from Peri-Gondwanan Domains and post Caledonian cover sequences (Munster basin, Leinster Massif and Welsh Massif). This occurred because of significant tectonically (Cimmerian) induced exhumation and erosion (Upper Jurassic Samples) or proximity to Peri-Gondwanan rich sources (SG4 as discussed above).

Group 3 samples (NC4, NC6, NC7, NC10, NC9 NC22 and SG5) are very similar to Group 2, however, they contain a dominant asymmetric 1.0 Ga Grenville population, likely from the Munster Basin, Dalradian supergroup or Southern Uplands Terrain, often with less Peri-Gondwanan material. Zircon populations within this group are a result of tectonic

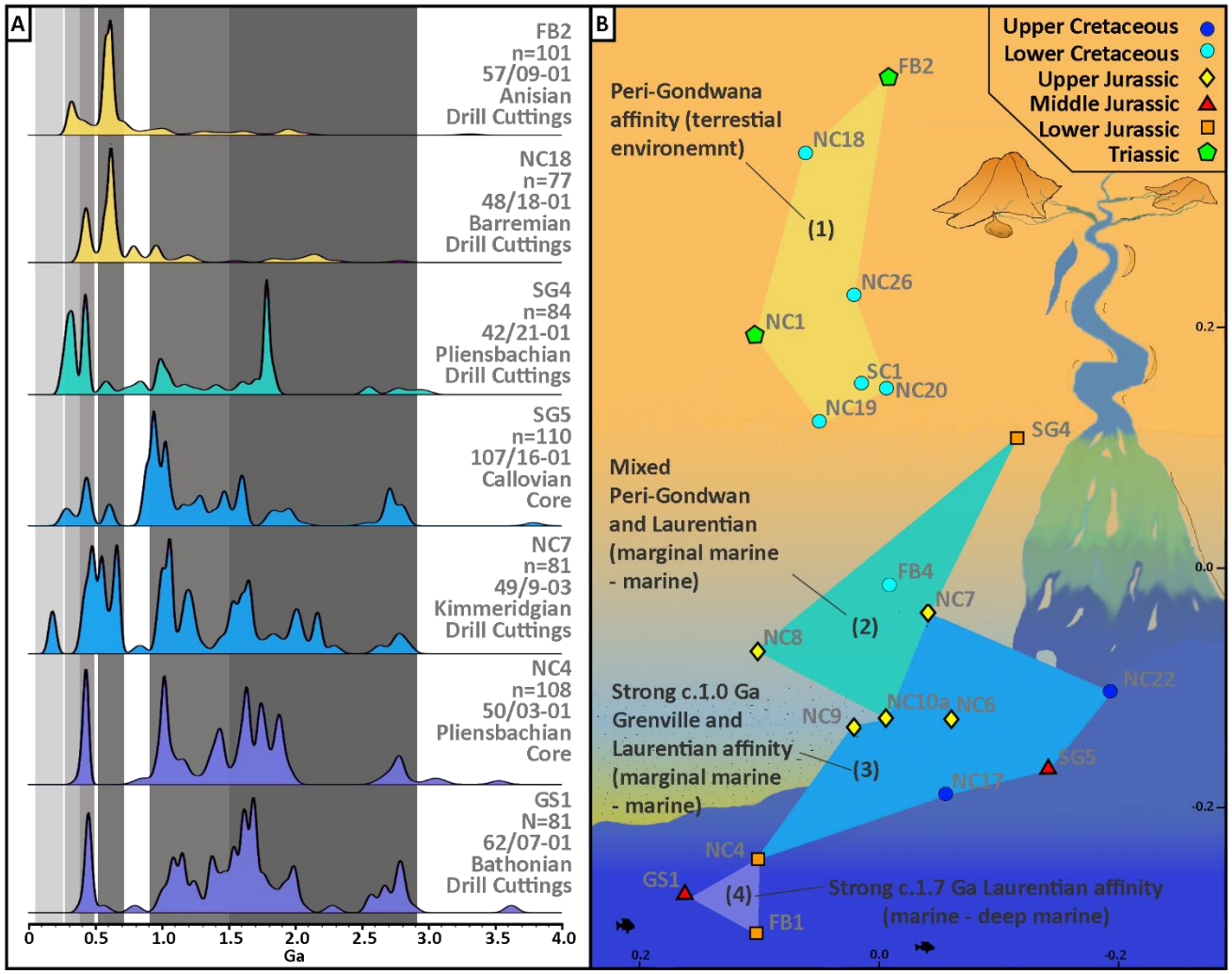

Fig. 24. *Multi-Dimensional Scale (MDS) model of detrital zircon populations with illustrations linking environmental conditions with MDS groupings. (A) 7/20 KDE diagrams of detrital zircon U-Pb single grain concordant age data. Data used for this model are taken from this study and combined with data from Section 2.8.1, where KDE colour corresponds to MDS groupings 1-4. (B) Four distinct groupings are observed where; Group 1 (Yellow): During regressive marine periods (Early Triassic and Early Cretaceous drainage form local sources dominate basin infill lacking Laurentian input. Group 2 (Turquoise): Dominant Peri-Gondwanan populations with some Laurentian material in a shallow marine environment; Group 3 (Blue): Tectonic uplift mixed with shallow to marginal-marine conditions inputs a homogenised signature; Group 4 (Purple): Deep Marine – shallow marine conditions transport Laurentian dominated material into the Celtic Sea region.*

exhumation and recycling as well as a significant northern derived input into the NCSB facilitated by transgressive conditions.

Group 4 samples (GS1, FB1 and NC4) represent a different Laurentian signature with a dominant 1.7 Ga population. This signature is found in Lower to Middle Jurassic samples which were deposited in open marine conditions with minimal or no tectonic recycling recorded. It represents input from an ultimately Laurentian source. The interplay between 1.0 Ga and 1.7 Ga zircon populations aids in distinguishing northern (Laurentian) or local western sources (Munster Basin) from distant western Laurentian sources associated sediments which have not tracked near an actively shedding Peri-Gondwanan domain or post Caledonian cover sequence. MDS groupings and age ratio calculations from Detrital zircon populations evidence a first-order tectonic and environmental control on sediment provenance.

3.6. **Conclusions**

By combining a multi-proxy approach with a large detrital zircon data set, the findings of this study can provide the first interpretations of the temporal evolution of provenance in the Irish and Celtic Sea basins. Findings from this study suggest:

1. Triassic sediments in the Fastnet Basin, NCSB and SGCB derived from the Iberian Massif during a regressive marine period.
2. Early Jurassic transgressive sedimentation introduced Laurentian sediment, possibly from the Munster Basin into the NCSB. The SGCB received input form the Midland Valley and Southern Uplands Terranes to the north. The Fastnet Basin appears to have received input from a Laurentian source west of the study area like the Dalradian Metasediments of western Ireland or farther west.
3. MDS modelling of detrital zircon data sets highlights the first-order control which environmental and tectonic factors have on the temporal evolution of sedimentary provenance throughout the Mesozoic Era in the Celtic and Irish Sea basins.

3.7. **References**

Ainsworth, N. R., Horton, N. F., & Penney, R. A. (1985). Lower Cretaceous micropalaeontology of the Fastnet Basin, offshore south-west Ireland. *Marine and Petroleum Geology, 2*(4), 341-349. doi:https://doi.org/10.1016/0264-8172(85)90029-7

Andò, S., & Garzanti, E. (2014). Raman spectroscopy in heavy-mineral studies. *Geological Society, London, Special Publications, 386*(1), 395-412. doi:https://doi.org/10.1144/SP386.2

Augier, R., Choulet, F., Faure, M., & Turrillot, P. (2015). A turning-point in the evolution of the Variscan orogen: the ca. 325 Ma regional partial-melting event of the coastal South Armorican domain (South Brittany and Vendée, France). *Bulletin de la Société géologique de France, 186*(2-3), 63-91. doi:https://doi.org/10.2113/gssgfbull.186.2-3.63

Cabrera, L., Roca, E., Garcés, M., & de Porta, J. (2004). Estratigrafía y evolución tectonosedimentaria oligocena superior-neógena del sector central del margen catalán (Cadena Costero-Catalana). *Geología de España*, 569-572.

Caracciolo, L. (2020). Sediment generation and sediment routing systems from a quantitative provenance analysis perspective: Review, application and future development. *Earth-Science Reviews*, 103226. doi:https://doi.org/10.1016/j.earscirev.2020.103226

Caston, V. (1995). The Helvick oil accumulation, Block 49/9, North Celtic Sea Basin. *Geological Society, London, Special Publications, 93*(1), 209-225. doi:10.1144/gsl.sp.1995.093.01.15

Chadwick, R., & Evans, D. (1995). The timing and direction of Permo-Triassic extension in southern Britain. *Geological Society, London, Special Publications, 91*(1), 161-192. doi:https://doi.org/10.1144/GSL.SP.1995.091.01.09

Chew, D., O'Sullivan, G., Caracciolo, L., Mark, C., & Tyrrell, S. (2020). Sourcing the sand: Accessory mineral fertility, analytical and other biases in detrital U-Pb provenance analysis. *Earth-Science Reviews*, 103093. doi:https://doi.org/10.1016/j.earscirev.2020.103093

Chew, D., Tyrrell, S., Daly, J. S., Cogné, N., Sun, K., & Badenszki, E. (2019). *The Basement geology of the Porcupine High - A Key Transatlantic link between the Caledonides and Apalachians.* Paper presented at the GSA Annual Meeting in Phoenix, Arizona, USA-2019.

Chew, D. M., Babechuk, M. G., Cogné, N., Mark, C., O'Sullivan, G. J., Henrichs, I. A., Doepke, D., & McKenna, C. A. (2016). (LA, Q)-ICPMS trace-element analyses of Durango and McClure Mountain apatite and implications for making natural LA-ICPMS mineral standards. *Chemical Geology, 435*, 35-48. doi:https://doi.org/10.1016/j.chemgeo.2016.03.028

Chew, D. M., Daly, J. S., Magna, T., Page, L. M., Kirkland, C. L., Whitehouse, M. J., & Lam, R. (2010). Timing of ophiolite obduction in the Grampian orogen. *Bulletin, 122*(11-12), 1787-1799. doi:https://doi.org/10.1130/B30139.1

Chew, D. M., Petrus, J. A., Kenny, G. G., & McEvoy, N. (2017). Rapid high-resolution U–Pb LA-Q-ICPMS age mapping of zircon. *Journal of Analytical Atomic Spectrometry, 32*(2), 262-276. doi:https://doi.org/10.1039/C6JA00404K

Cogné, N., Chew, D., & Stuart, F. M. (2014). The thermal history of the western Irish onshore. *Journal of the Geological Society, London, 171*(6), 779-792. doi:https://doi.org/10.1144/jgs2014-026

Dallmeyer, R. D., Franke, W., & Weber, K. (2013). *Pre-Permian geology of central and eastern Europe*: Springer Science & Business Media.

Dallmeyer, R. D., & Garcia, E. M. (2012). *Pre-mesozoic geology of Iberia*: Springer Science & Business Media.

De La Horra, R., Benito, M. I., LÓPEZ-GÓMEZ, J., Arche, A., Barrenechea, J. F., & Luque, J. (2008). Palaeoenvironmental significance of Late Permian palaeosols in the South-Eastern Iberian Ranges, Spain. *Sedimentology, 55*(6), 1849-1873. doi:https://doi.org/10.1111/j.1365-3091.2008.00969.x

Ducassou, C., Poujol, M., Hallot, E., Bruguier, O., & Ballevre, M. (2011). Petrology and geochronology of the high-K calc-alkaline Mésanger magmatism (Armorican massif, France): a ca. 320 Ma old volcano-plutonic association. *Bulletin de la Société géologique de France, 182*(6), 467-477. doi:https://doi.org/10.2113/gssgfbull.182.6.467

Dunford, G., Dancer, P., & Long, K. (2001). Hydrocarbon potential of the Kish Bank Basin: integration within a regional model for the Greater Irish Sea Basin. *Geological Society, London, Special Publications, 188*(1), 135-154. doi:https://doi.org/10.1144/GSL.SP.2001.188.01.07

Dyment, J., & Bano, M. (1991). Deep crustal features of the Celtic Sea from complementary processing on the SWAT data. *Geophysical Journal International, 105*(1), 71-83. doi:10.1111/j.1365-246X.1991.tb03445.x

EMODnet, B. C. (2018). EMODnet Digital Bathymetry (DTM 2018) (Publication no. https://doi.org/10.12770/18ff0d48-b203-4a65-94a9-5fd8b0ec35f6). https://sextant.ifremer.fr/record/18ff0d48-b203-4a65-94a9-5fd8b0ec35f6/

Ewins, N. P., & Shannon, P. M. (1995). Sedimentology and diagenesis of the Jurassic and Cretaceous of the North Celtic Sea and Fastnet Basins. *Geological Society, London, Special Publications, 93*(1), 139-169. doi:https://doi.org/10.1144/GSL.SP.1995.093.01.12

Fairey, B. J. (2017). *Sediment routing and recycling through multiple basins from Palaeozoic to Mesozoic times: a provenance study of the Devonian Old Red Sandstone of southern Ireland and neighbouring offshore Mesozoic basins.* PhD thesis, University College Cork,

Fairey, B. J., Kerrison, A., Meere, P. A., Mulchrone, K. F., Hofmann, M., Gärtner, A., Sonntag, B.-L., Linnemann, U., Kuiper, K. F., & Ennis, M. (2018). The provenance of the Devonian Old Red Sandstone of the Dingle Peninsula, SW Ireland; the earliest record of Laurentian and peri-Gondwanan sediment mixing in Ireland. *Journal of the Geological Society, London*, jgs2017-2099. doi:https://doi.org/10.1144/jgs2017-099 |

Fernández-Suárez, J., Gutiérrez-Alonso, G., Jenner, G., & Tubrett, M. (2000). New ideas on the Proterozoic-Early Palaeozoic evolution of NW Iberia: insights from U–Pb detrital zircon ages. *Precambrian Research, 102*(3-4), 185-206. doi:https://doi.org/10.1016/S0301-9268(00)00065-6

Fernández-Suárez, J., Gutiérrez-Alonso, G., Pastor-Galán, D., Hofmann, M., Murphy, J., & Linnemann, U. (2014). The Ediacaran–Early Cambrian detrital zircon record of NW Iberia: possible sources and paleogeographic constraints. *International Journal of Earth Sciences, 103*(5), 1335-1357. doi:https://doi.org/10.1007/s00531-013-0923-3

Ferreira, J., dos Santos, T. B., Pereira, I., & Mata, J. (2019). Tectonically assisted exhumation and cooling of Variscan granites in an anatectic complex of the Central Iberian Zone, Portugal: constraints from LA-ICP-MS zircon and apatite U–Pb ages. *International Journal of Earth Sciences, 108*(7), 2153-2175. doi:https://doi.org/10.1007/s00531-019-01755-1

Franklin, J., Tyrrell, S., Morton, A., Frei, D., & Mark, C. (2019). Triassic sand supply to the Slyne Basin, offshore western Ireland–new insights from a multi-proxy provenance approach. *Journal of the Geological Society, 176*(6), 1120-1135. doi:https://doi.org/10.1144/jgs2019-085

Franklin, J., Tyrrell, S., O'Sullivan, G., Nauton-Fourteu, M., & Raine, R. (2020). Provenance of Triassic sandstones in the basins of Northern Ireland—Implications for NW European Triassic palaeodrainage. *Geological Journal*. doi:https://doi.org/10.1002/gj.3697

Garzanti, E. (2017). The Maturity Myth In Sedimentology and Provenance AnalysiS. *Journal of Sedimentary Research, 87*(4), 353-365. doi:https://doi.org/10.2110/jsr.2017.17

Garzanti, E., Andò, S., & Vezzoli, G. (2009). Grain-size dependence of sediment composition and environmental bias in provenance studies. *Earth and Planetary Science Letters, 277*(3), 422-432. doi:https://doi.org/10.1016/j.epsl.2008.11.007

Gehrels, G., Valencia, V., & Pullen, A. (2006). Detrital zircon geochronology by laser-ablation multicollector ICPMS at the Arizona LaserChron Center. *The Paleontological Society Papers, 12*, 67-76. doi:DOI: https://doi.org/10.1017/S1089332600001352

Gilligan, A., Bastow, I. D., & Darbyshire, F. A. (2016). Seismological structure of the 1.8 Ga Trans-Hudson Orogen of North America. *Geochemistry, Geophysics, Geosystems, 17*(6), 2421-2433. doi:https://doi.org/10.1002/2016GC006419

Grobe, R., Alvarez-Marrón, J., Glasmacher, U., & Stuart, F. (2014). Mesozoic exhumation history and palaeolandscape of the Iberian Massif in eastern Galicia from apatite fission-track and (U+ Th)/He data. *International Journal of Earth Sciences, 103*(2), 539-561. doi:https://doi.org/10.1007/s00531-013-0976-3

Guerrot, C., & Peucat, J. (1990). U-Pb geochronology of the Upper Proterozoic Cadomian orogeny in the northern Armorican Massif, France. *Geological Society, London, Special Publications, 51*(1), 13-26. doi:https://doi.org/10.1144/GSL.SP.1990.051.01.02

Gutiérrez-Alonso, G., Fernández-Suárez, J., Collins, A. S., Abad, I., & Nieto, F. (2005). Amazonian Mesoproterozoic basement in the core of the Ibero-Armorican Arc: 40Ar/39Ar detrital mica ages complement the zircon's tale. *Geology, 33*(8), 637-640. doi:https://doi.org/10.1130/G21485AR.1

Hartley, A. (1995). Sedimentology of the Cretaceous Greensand, Quadrants 48 and 49, North Celtic Sea Basin: a progradational shoreface deposit. *Geological Society, London, Special Publications, 93*(1), 245-257. doi:https://doi.org/10.1144/GSL.SP.1995.093.01.17

Henderson, B. J., Collins, W. J., Murphy, J. B., Gutierrez-Alonso, G., & Hand, M. (2016). Gondwanan basement terranes of the Variscan–Appalachian orogen: Baltican, Saharan and West African hafnium isotopic

fingerprints in Avalonia, Iberia and the Armorican Terranes. *Tectonophysics, 681*, 278-304. doi:https://doi.org/10.1016/j.tecto.2015.11.020
Henrique-Pinto, R., Guilmette, C., Bilodeau, C., & McNicoll, V. (2017). Evidence for transition from a continental forearc to a collisional pro-foreland basin in the eastern Trans-Hudson Orogen: Detrital zircon provenance analysis in the Labrador Trough, Canada. *Precambrian Research, 296*, 181-194. doi:https://doi.org/10.1016/j.precamres.2017.04.035
Hietpas, J., Samson, S., Moecher, D., & Chakraborty, S. (2011). Enhancing tectonic and provenance information from detrital zircon studies: assessing terrane-scale sampling and grain-scale characterization. *Journal of the Geological Society, London, 168*(2), 309-318. doi:https://doi.org/10.1144/0016-76492009-163
Hounslow, M., & Ruffell, A. (2006). Triassic: seasonal rivers, dusty deserts and saline lakes. In *The Geology of England & Wales* (pp. 295-325): Geological Society of London.
ISPSG, I. S. P. S. G. (2019). *The Standard Stratigraphic Nomenclature of Offshore Ireland: An Integrated Lithostratigraphic, Biostratigraphic and Sequence Stratigraphic Framework, Dublin: Irish Petroleum Infrastructure Programme (PIP).* Retrieved from
Jennings, E., Marschall, H., Hawkesworth, C., & Storey, C. (2011). Characterization of magma from inclusions in zircon: Apatite and biotite work well, feldspar less so. *Geology, 39*(9), 863-866. doi:https://doi.org/10.1130/G32037.1
Keeley, M. (1995). New evidence of Permo-Triassic rifting, onshore southern Ireland, and its implications for Variscan structural inheritance. *Geological Society, London, Special Publications, 91*(1), 239-253. doi:https://doi.org/10.1144/GSL.SP.1995.091.01.12
Kessler, L., & Sachs, S. D. (1995). Depositional setting and sequence stratigraphic implications of the Upper Sinemurian (Lower Jurassic) sandstone interval, North Celtic Sea/St George's Channel Basins, offshore Ireland. *Geological Society, London, Special Publications, 93*(1), 171-192. doi:https://doi.org/10.1144/GSL.SP.1995.093.01.13
Lafuente, B., Downs, R., Yang, H., & Stone, N. (2015). The power of databases: the RRUFF project. In "Highlights in mineralogical crystallography", Armbruster, T. & Danisi, RM, eds. W. *De Gruyter, Berlin, Germany, 1*, 30. doi:https://doi.org/10.1515/9783110417104-003
Ludwig, K. (2012). Isoplot 3.75-4.15 manual. *A Geochronological Toolkit for Microsoft Excel, 4*, 1-70.
Maddox, S. J., Blow, R., & Hardman, M. (1995). Hydrocarbon prospectivity of the Central Irish Sea Basin with reference to Block 42/12, offshore Ireland. *Geological Society, London, Special Publications, 93*(1), 59-77. doi:https://doi.org/10.1144/GSL.SP.1995.093.01.08
Mange, M. A., & Maurer, H. (1992). *Heavy minerals in colour*: Springer Science & Business Media.
Mange, M. A., & Wright, D. T. (2007). *Heavy minerals in use*: Elsevier.
McAteer, C. A., Daly, J. S., Flowerdew, M. J., Whitehouse, M. J., & Kirkland, C. L. (2010). A Laurentian provenance for the Dalradian rocks of north Mayo, Ireland, and evidence for an original basement–cover contact with the underlying Annagh Gneiss Complex. *Journal of the Geological Society, London, 167*(5), 1033-1048. doi:https://doi.org/10.1144/0016-76492009-147
McAteer, C. A., Daly, J. S., Flowerdew, M. J., Whitehouse, M. J., & Monaghan, N. M. (2014). Sedimentary provenance, age and possible correlation of the Iona Group SW Scotland. *Scottish Journal of Geology, 50*(2), 143-158. doi:https://doi.org/10.1144/sjg2013-019
Morton, A., Hounslow, M. W., & Frei, D. (2013). Heavy-mineral, mineral-chemical and zircon-age constraints on the provenance of Triassic sandstones from the Devon coast, southern Britain. *Geologos, 19*(1-2), 67-85.
Morton, A., Knox, R., & Frei, D. (2016). Heavy mineral and zircon age constraints on provenance of the Sherwood Sandstone Group (Triassic) in the eastern Wessex Basin, UK. *Proceedings of the Geologists' Association, 127*(4), 514-526. doi:https://doi.org/10.1016/j.pgeola.2016.06.001
Morton, A., Waters, C., Fanning, M., Chisholm, I., & Brettle, M. (2015). Origin of Carboniferous sandstones fringing the northern margin of the Wales-Brabant Massif: insights from detrital zircon ages. *Geological Journal, 50*(5), 553-574. doi:https://doi.org/10.1002/gj.2572
Morton, A. C., & Hallsworth, C. (1994). Identifying provenance-specific features of detrital heavy mineral assemblages in sandstones. *Sedimentary Geology, 90*(3-4), 241-256. doi:https://doi.org/10.1016/0037-0738(94)90041-8
Murphy, N. J., & Ainsworth, N. R. (1991). Stratigraphy of the Triassic, Lower Jurassic and Middle Jurassic (Aalenian) from the Fastnet Basin, offshore south-west Ireland. *Marine and Petroleum Geology, 8*(4), 417-429. doi:https://doi.org/10.1016/0264-8172(91)90064-8
Nance, R. D., Murphy, J. B., Strachan, R. A., Keppie, J. D., Gutiérrez-Alonso, G., Fernández-Suárez, J., Quesada, C., Linnemann, U., D'lemos, R., & Pisarevsky, S. A. (2008). Neoproterozoic-early Palaeozoic

tectonostratigraphy and palaeogeography of the peri-Gondwanan terranes: Amazonian v. West African connections. *Geological Society, London, Special Publications, 297*(1), 345-383. doi:https://doi.org/10.1144/SP297.17

Nasdala, L., Corfu, F., Schoene, B., Tapster, S. R., Wall, C. J., Schmitz, M. D., Ovtcharova, M., Schaltegger, U., Kennedy, A. K., & Kronz, A. (2018). GZ 7 and GZ 8–Two Zircon Reference Materials for SIMS U-Pb Geochronology. *Geostandards and Geoanalytical Research, 42*(4), 431-457. doi: https://doi.org/10.1111/ggr.12239

Nauton-Fourteu, M., Tyrrell, S., Morton, A., Mark, C., O'Sullivan, G. J., & Chew, D. M. (2020). Constraining recycled detritus in quartz-rich sandstones: insights from a multi-proxy provenance study of the Mid-Carboniferous, Clare Basin, western Ireland. *Basin Research*. doi:https://doi.org/10.1111/bre.12469

Naylor, D., & Shannon, P. (2011). *Petroleum geology of Ireland*: Dunedin Academic Press Limited.

O'Sullivan, G., Chew, D., Kenny, G., Henrichs, I., & Mulligan, D. (2020). The trace element composition of apatite and its application to detrital provenance studies. *Earth-Science Reviews, 201*, 103044.

Pereira, M. F., Fernández, R. D., Gama, C., Hofmann, M., Gärtner, A., & Linnemann, U. (2018). S-type granite generation and emplacement during a regional switch from extensional to contractional deformation (Central Iberian Zone, Iberian autochthonous domain, Variscan Orogeny). *International Journal of Earth Sciences, 107*(1), 251-267.

Petrie, S., Brown, J., Granger, P., & Lovell, J. (1989). Mesozoic history of the Celtic Sea basins. *Extensional Tectonics and Stratigraphy of the North Atlantic Margins American Association of Petroleum Geologists Memoirs, 46*, 433-445.

Pothier, H. D., Waldron, J. W., Schofield, D. I., & DuFrane, S. A. (2015). Peri-Gondwanan terrane interactions recorded in the Cambrian–Ordovician detrital zircon geochronology of North Wales. *Gondwana Research, 28*(3), 987-1001. doi:https://doi.org/10.1016/j.gr.2014.08.009

Roberts, D. G. (1989). Basin inversion in and around the British Isles. *Geological Society, London, Special Publications, 44*(1), 131-150. doi:10.1144/gsl.sp.1989.044.01.09

Robinson, K., Shannon, P., & Young, G. M. (1981). The Fastnet Basin: An integrated analysis. In L. G. Illing & G. D. Hobson (Eds.), *Petroleum Geology of the Continental Shelf of North-West Europe* (pp. 444–454). London: Heyden and Son Ltd.

Rodriguez-Salgado, P. (2019). *Structural and Kinematic Analysis of the Celtic Sea Basins.* (PhD). University College Dublin,

Rodríguez-Salgado, P., Childs, C., Shannon, P. M., & Walsh, J. J. (2019). Structural evolution and the partitioning of deformation during basin growth and inversion: A case study from the Mizen Basin Celtic Sea, offshore Ireland. *Basin Research*. doi:https://doi.org/10.1111/bre.12402

Rowell, P. (1995). Tectono-stratigraphy of the North Celtic Sea Basin. *Geological Society, London, Special Publications, 93*(1), 101-137. doi:10.1144/gsl.sp.1995.093.01.11

Ruffell, A., & Shelton, R. (1999). The control of sedimentary facies by climate during phases of crustal extension: examples from the Triassic of onshore and offshore England and Northern Ireland. *Journal of the Geological Society, London, 156*(4), 779-789. doi:https://doi.org/10.1144/gsjgs.156.4.0779

Shannon, P. (1991a). The development of Irish offshore sedimentary basins. *Journal of the Geological Society, London, 148*(1), 181-189. doi:https://doi.org/10.1144/gsjgs.148.1.0181

Shannon, P., & MacTiernan, B. (1993). Triassic prospectivity in the Celtic Sea, Ireland-a case history. *First Break, 11*(2), 47-57. doi:https://doi.org/10.3997/1365-2397.1993003

Shannon, P. M. (1991b). The development of Irish offshore sedimentary basins. *Journal of the Geological Society, London, 148*(1), 181-189. doi:https://doi.org/10.1144/gsjgs.148.1.0181

Shannon, P. M. (1995). Permo-Triassic development of the Celtic Sea region, offshore Ireland. *Geological Society London Special Publication, 91*, 215-237. doi:https://doi.org/10.1144/GSL.SP.1995.091.01.11

Shannon, P. M., Corcoran, D. V., & Haughton, P. D. W. (2001). The petroleum exploration of Ireland's offshore basins: introduction. *Geological Society, London, Special Publications, 188*(1), 1-8. doi:https://10.1144/gsl.sp.2001.188.01.01

SÌtolfovÃ¡, K. i., & Shannon, P. M. (2009). Permo-Triassic development from Ireland to Norway: basin architecture and regional controls. *Geological Journal, 44*(6), 652-676. doi:10.1002/gj.1187

Smith, W. D., Darling, J., Bullen, D., Lasalle, S., Pereira, I., Moreira, H., Allen, C. J., & Tapster, S. (2019). Zircon perspectives on the age and origin of evolved S-type granites from the Cornubian Batholith, Southwest England. *Lithos, 336*, 14-26. doi:https://doi.org/10.1016/j.lithos.2019.03.025

Taber, D., Vickers, M., & Winn, R. (1995). The definition of the Albian 'A'Sand reservoir fairway and aspects of associated gas accumulations in the North Celtic Sea Basin. *Geological Society, London, Special Publications, 93*(1), 227-244. doi:https://doi.org/10.1144/GSL.SP.1995.093.01.16

Tartese, R., Poujol, M., Ruffet, G., Boulvais, P., Yamato, P., & Košler, J. (2011). New U-Pb zircon and 40Ar/39Ar muscovite age constraints on the emplacement of the Lizio syn-tectonic granite (Armorican Massif, France). *Comptes Rendus Geoscience, 343*(7), 443-453. doi:https://doi.org/10.1016/j.crte.2011.07.005

Taylor, G. K. (2007). Pluton shapes in the Cornubian Batholith: new perspectives from gravity modelling. *Journal of the Geological Society, London, 164*(3), 525-528. doi:https://doi.org/10.1144/0016-76492006-104

Thomson, S. N., Gehrels, G. E., Ruiz, J., & Buchwaldt, R. (2012). Routine low-damage apatite U-Pb dating using laser ablation–multicollector–ICPMS. *Geochemistry, Geophysics, Geosystems, 13*(2). doi:https://10.1029/2011GC003928

Tyrrell, S. (2005). *Investigations of Sandstone Provenance.* (PhD). University College Dublin,

Tyrrell, S., Haughton, P. D., Souders, A. K., Daly, J. S., & Shannon, P. M. (2012). Large-scale, linked drainage systems in the NW European Triassic: insights from the Pb isotopic composition of detrital K-feldspar. *Journal of the Geological Society, London, 169*(3), 279-295. doi:https://doi.org/10.1144/0016-76492011-104

Vermeesch, P. (2018). IsoplotR: A free and open toolbox for geochronology. *Geoscience Frontiers, 9*(5), 1479-1493. doi:https://doi.org/10.1016/j.gsf.2018.04.001

Vermeesch, P., Rittner, M., Petrou, E., Omma, J., Mattinson, C., & Garzanti, E. (2017). High throughput petrochronology and sedimentary provenance analysis by automated phase mapping and LAICPMS. *Geochemistry, Geophysics, Geosystems, 18*(11), 4096-4109. doi:https://doi.org/10.1002/2017GC007109

Von Eynatten, H., & Wijbrans, J. (2003). Precise tracing of exhumation and provenance using 40Ar/39Ar geochronology of detrital white mica: the example of the Central Alps. *Geological Society, London, Special Publications, 208*(1), 289-305. doi:https://doi.org/10.1144/GSL.SP.2003.208.01.14

von Raumer, J. F., Stampfli, G. M., Arenas, R., & Martínez, S. S. (2015). Ediacaran to Cambrian oceanic rocks of the Gondwana margin and their tectonic interpretation. *International Journal of Earth Sciences, 104*(5), 1107-1121. doi:https://doi.org/10.1007/s00531-015-1142-x

Waldron, J. W., Floyd, J. D., Simonetti, A., & Heaman, L. M. (2008). Ancient Laurentian detrital zircon in the closing Iapetus ocean, Southern Uplands terrane, Scotland. *Geology, 36*(7), 527-530. doi:https://doi.org/10.1130/G24763A.1

Waldron, J. W., Schofield, D. I., Dufrane, S. A., Floyd, J. D., Crowley, Q. G., Simonetti, A., Dokken, R. J., & Pothier, H. D. (2014). Ganderia–Laurentia collision in the Caledonides of Great Britain and Ireland. *Journal of the Geological Society, London, 171*(4), 555-569. doi:https://doi.org/10.1144/jgs2013-131

Waldron, J. W., Schofield, D. I., Pearson, G., Sarkar, C., Luo, Y., & Dokken, R. (2019). Detrital zircon characterization of early Cambrian sandstones from East Avalonia and SE Ireland: implications for terrane affinities in the peri-Gondwanan Caledonides. *Geological Magazine, 156*(7), 1217-1232. doi:https://doi.org/10.1017/S0016756818000407

Waldron, J. W., Schofield, D. I., White, C. E., & Barr, S. M. (2011). Cambrian successions of the Meguma Terrane, Nova Scotia, and Harlech Dome, North Wales: dispersed fragments of a peri-Gondwanan basin? *Journal of the Geological Society, London, 168*(1), 83-98. doi:https://doi.org/10.1144/0016-76492010-068

Warr, L. (2012). The Variscan orogeny: the welding of Pangaea. In N. Woodcock & R. Strachan (Eds.), *Geological history of Britain and Ireland* (2nd ed., pp. 274-298): John Wiley & Sons.

Warrington, G., & Ivimey-Cook, H. (1992). Triassic. In J. Cope, J. Ingham, & P. Rawson (Eds.), *Atlas of palaeogeography and lithofacies.* (Vol. 13, pp. 97-106): Geological Society of London Memoir.

Welch, M. J., & Turner, J. P. (2000). Triassic–Jurassic development of the St. George's Channel basin, offshore Wales, UK. *Marine and Petroleum Geology, 17*(6), 723-750. doi:https://doi.org/10.1016/S0264-8172(00)00017-9

Wiedenbeck, M., Alle, P., Corfu, F., Griffin, W., Meier, M., Oberli, F. v., Quadt, A. v., Roddick, J., & Spiegel, W. (1995). Three natural zircon standards for U-Th-Pb, Lu-Hf, trace element and REE analyses. *Geostandards newsletter, 19*(1), 1-23. doi:https://doi.org/10.1111/j.1751-908X.1995.tb00147.x

Willner, A. P., Gerdes, A., Massonne, H.-J., van Staal, C. R., & Zagorevski, A. (2014). Crustal evolution of the northeast Laurentian margin and the Peri-Gondwanan microcontinent Ganderia prior to and during closure of the Iapetus Ocean: detrital zircon U–Pb and Hf isotope evidence from Newfoundland. *Geoscience Canada*, 345-364. doi:https://doi.org/10.12789/geocanj.2014.41.046

Zimmermann, S., Mark, C., Chew, D., & Voice, P. J. (2018). Maximising data and precision from detrital zircon U-Pb analysis by LA-ICPMS: The use of core-rim ages and the single-analysis concordia age. *Sedimentary Geology, 375*, 5-13. doi:https://doi.org/10.1016/j.sedgeo.2017.12.020

Zoleikhaei, Y., Frei, D., Morton, A., & Zamanzadeh, S. M. (2016). Roundness of heavy minerals (zircon and apatite) as a provenance tool for unraveling recycling: A case study from the Sefidrud and Sarbaz rivers in N and SE Iran. *Sedimentary Geology, 342*, 106-117. doi:https://doi.org/10.1016/j.sedgeo.2016.06.016

Chapter 4: *"Ramaster" Software application for Raman imaging and chemical characterisation; Automated peak analysis and imaging of Raman data sets*

Authors

Odhrán McCarthy[(1)], Artsiom Vahin, Gerard Summers[(1,2)], Pat Meere[(1)], Alberto Resentini[(3)], Mohit Tunwal[(1)], Sergio Ando[(3)], Ninon Robin[(1)].

Affiliations

[1] School of Biological, Earth and Environmental Sciences and iCRAG, University College Cork, Distillery Fields, North Mall, Cork Ireland

[2]Environmental Research Institute, University College Cork, Ireland

[3]Department of Earth and Environmental Sciences, University of Milano –Bicocca.

Abstract

Raman spectroscopy can provide novel insights to the molecular order and state of earth materials. Processing and interpreting spot and mapped Raman data sets can be time consuming with processing software often being costly, inflexible, and limited in access. In addition, there is a distinct lack of software available for rasterising these data sets. To reduce processing time, improve the interpretability and the capacity of statistical testing of data sets, a python 2.7 programmed, full-stack freeware called "Ramaster" was developed for automated peak analysis, data reduction and image processing. Using two case studies we demonstrate the potential benefits of using a single program to automatically analysing spectra and generate georeferenced maps of peak intensity, full width at half maximum and peak frequency. The first case study uses Raman maps of 160 zircon grains to generate zircon peak intensity maps which offer insights to mineralisation chronology, thermal annealing and metamictisation processes which are important factors when considering U-Pb geochronology analysis. As each zircon map is georeferenced to the sample, the user does not need to spend time cross referencing samples images to overlay maps and select ablation

spots for U-Pb dating. The second case study takes Raman data set from the dermal tissue of a 40-million-year-old anuran (frog) which has been preserved through phosphatisation in a karst landscape. Full width at half maximum, peak intensity and peak frequency maps enables the user to observe the preservation of the epidermis, fossil glands and variation in the mineralisation of apatite and preservation of carbon molecules. Raman characterisation of molecule structure and state is a growing field in geoscience and Ramaster offers a more accessible, time saving and flexible alternative to available software.

4.1. **Introduction**

Raman Spectroscopy Analysis (RSA) is a powerful analytical tool used in both industry and science fields for identifying and measuring the vibrations of molecules providing insights to composition, strength, and material history. Geoscience applications of RSA include detailed mineral identification and mapping (Lünsdorf *et al.*, 2019), thermobarometer (Henry *et al.*, 2019; Muirhead *et al.*, 2019) as well as diagenetic alteration (Norell *et al.*, 2020), strain analysis (Chandrabhas *et al.*, 1992) and carbonaceous material studies with applications for planetary studies (Beyssac *et al.*, 2002; Rull *et al.*, 2017). In geochronology RSA is becoming more popular as a chemical fingerprinting tool (Resentini *et al.*, 2020) to better understand the thermal annealing and alpha decay effects on zircon growth rims (Anderson *et al.*, 2020) with Raman mapping and spot analysis (Nasdala *et al.*, 1995). Despite the vast range of applications, a significant challenge in working with Raman spectroscopy is data manipulation and processing. As this research field continually grows, a "big data" effect has come into place where new autonomous machines can run for days collecting hundreds of gigabits of data across a number of sessions (Lünsdorf *et al.*, 2019). Processing, analysing, and rasterising these data sets can be a significant challenge for which a limited set of tools are commercially (e.g., Wire™, GRAMS/AI™, and OriginLab™) and freely available (e.g., Spectragryph (Menges, 2020) or Crystal Sleuth) with few of these tools offering a rasterisation solution for mapped data sets. Raman map images are typically constructed using the whole spectra with a multi-variate data reduction approach like principal component analysis (PCA) or with singular variate mapping through analysis of peak variables like peak frequency/position (PF), peak intensity (PI) or Full width at half maximum (FWHM). Powerful commercial software like WIRE™ can generate an image using the geographical XY coordinates and a data stretching algorithm and colour ramp from the analysis results to colour the XY coordinates. Commercial software is often expensive and may not generate maps from Raman systems other than their own (e.g., Wire™ will only generate maps from a Renishaw system). Additionally, these proprietary software lack the flexibility of open software which enables the user to develop their own set of tools and methods for analysing and interpreting data. Alternate freeware is often unable to perform analytical processes which are commercially available. Batch analysis and processing of spectra is not commonly available in free or commercial software meaning that the user must develop their own tools from scratch (using MATLAB, R, or another

programming language) or each file must be analysed and digitised individually which is very time consuming and laborious. In addition, generated maps are typically not georeferenced meaning that if the data is spatially significant (e.g. a map of a thin section or grain), the user must overlay the RSA map manually using a geographical information system like ArcMap (ArcGIS-Pro, 2018), QGIS (QGIS.org, 2021) or an image manipulation software like Adobe Photoshop.

To address some of these challenges "Ramaster" was developed as a freeware based spectral imaging software to perform batched single peak analysis of multiple files and generate georeferenced images of PI, PF and FWHM which are output as a tabulated file (.csv) and a raster image file (.ascii). The utility and potential application of this software is demonstrated in two case studies. Case study one includes 160 RSA maps of detrital zircon grains in a heavy mineral mount (Fig. 25) to generate 160 georeferenced PI maps of the V2 SiO_2 (1008cm^{-1}) vibrational mode of zircon revealing concentric growth patterns, zones affected by metamictisation (Nasdala *et al.*, 1995) and thermal annealing as demonstrated in Chew *et al.* (2017) and Anderson *et al.* (2020). Case study two includes an RSA mapped cross section of 40 Ma dermal tissue from an anuran (frog) to generate nine maps of three peaks of interest. These results reveal the degradation of complex carbon groups to simple carbon structures and phosphatisation of epidermal and gland structures which preserve the dermal structure of the fossilised anuran. These case studies demonstrate the application of Ramaster software to automate batch analyse, rasterize and georeferenced Raman maps. Ramaster saves time, improves the capacity for researchers to interrogate Raman data sets and most importantly, offers a freely available data processing tool which has great potential for future development (See Appendix D for Ramaster Software and test data).

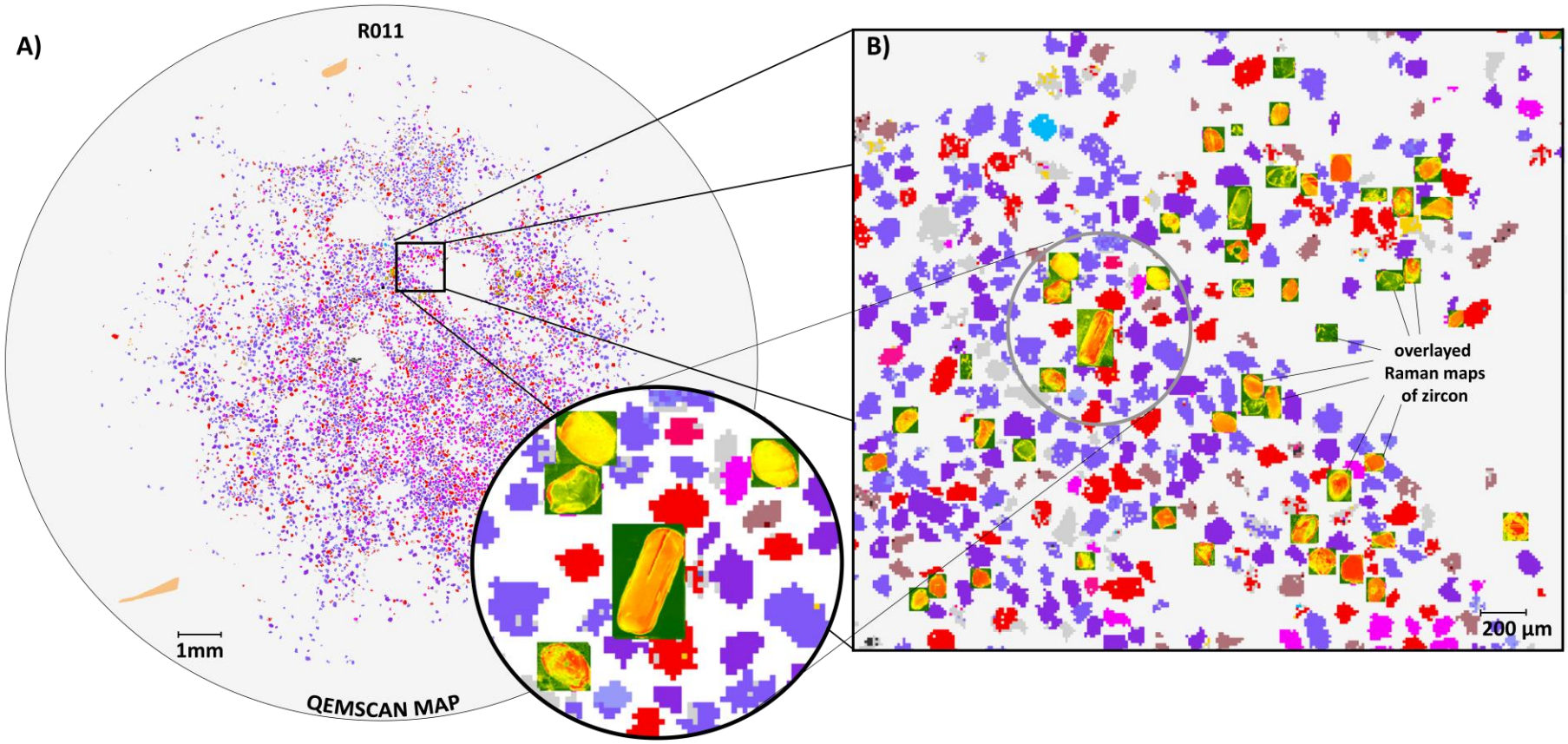

Fig. 25. *(A) Qemscan map of heavy mineral mount R011. (B) Close up of Raman spectroscopy maps of detrital zircon peak intensity (PI) at 1008 cm^{-1} with underlying QEMSCAN map R011. Raman maps were generated using Ramaster and overlayed using ArcGIS (ArcGIS-Pro, 2018).*

4.1.1. Single Variate vs Multi Variate Analysis of Raman Spectra

With any analytical or statistical interrogation of a data set, it is important to consider the pros and cons of each method. In Raman spectroscopy, the selection of a single *versus* multi-variate spectroscopy analysis method is dependent on the aim of the research. When interpreting large spectral data sets, a multi-variate statistical approach for data reduction is often employed to broadly describe common trends across a data set (e.g., Principal Component Analysis (Lee *et al.*, 2008). Multi-variate analysis or dimensionality reduction techniques can be very effective in reducing the amount of data required to interpret results. PCA analysis is often the best choice offering insights to the state and distribution of molecules throughout a sample (Naemat *et al.*, 2015). However, this approach is inherently biased as it can overlook subtle changes in peak variables which may not have a sufficiently high eigenvalue as they do not represent the majority of variance in the data set which can lead to important information being excluded (Lee *et al.*, 2008). In addition, as this utilises every peak in the spectra, it does not provide detailed information on the state of a single molecular vibrational mode and may not address the aims of the research. A more thorough approach to measuring the state of a molecule's vibration is single peak analysis. Peak analysis characterises in detail, the variables (PI, PF, FWHM) of a single peak which can offer insights to thermal histories (Lünsdorf, 2016), decay states (Anderson *et al.*, 2020), stress orientation (Chandrabhas *et al.*, 1992) and the concentration of molecules(Burke, 2001). There are numerous types of peak characterisation and transformation which commonly use Fourier analysis least squared curve finding and fitting algorithms like Linear Least Squares (Locher, 2018), multicomponent spectroscopy, and non-linear iterative curve fitting which are described in detail in O'Haver (2020). To enable the user to interpret single vibrational states, single peak analysis was chosen as the analytical method of choice for Ramaster. Multi-variate approaches like PCA, or multivariate calculations of single peak variables (e.g., α-dose as shown in Andersen (2002) or the ID/IG ratio of (Cançado *et al.*, 2006) may be integrated at a later date.

4.2. **Methods**

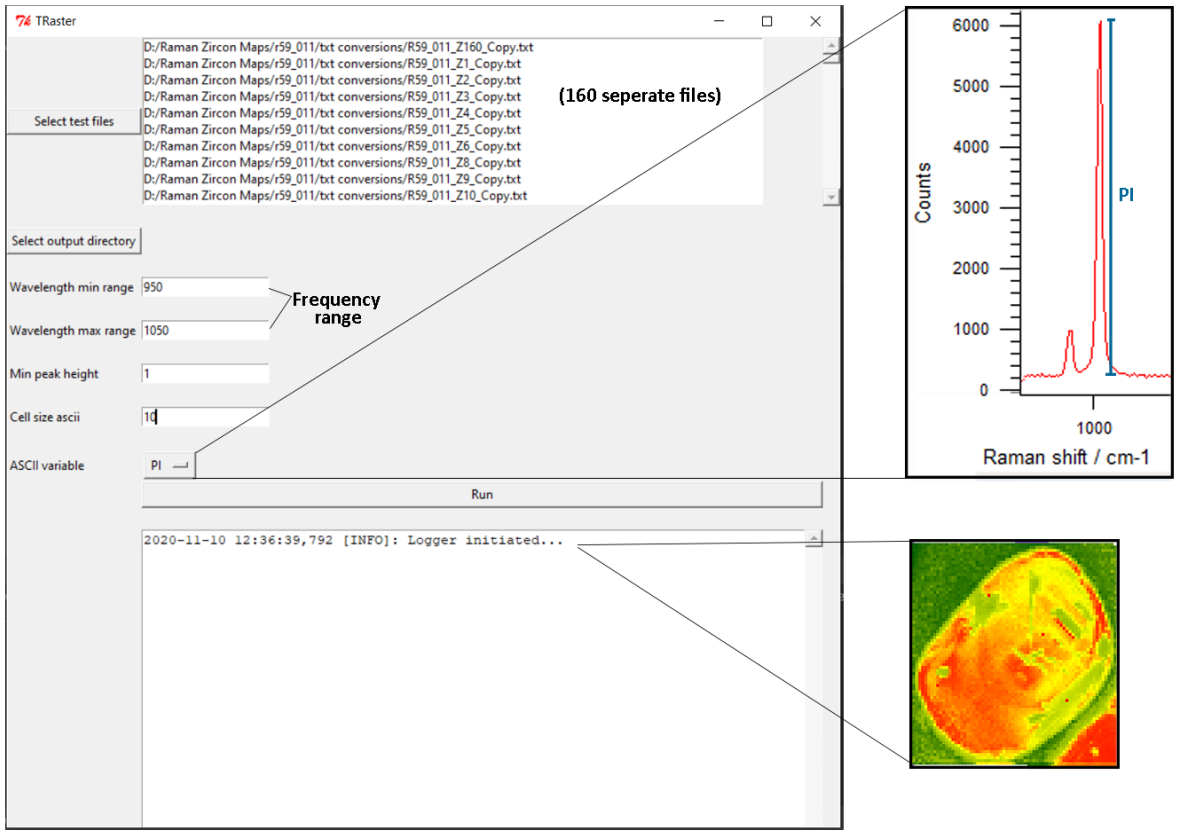

Fig. 26. *User interface and input parameters constructed using the Tkinter library.*

4.2.1. Python Structure

Ramaster is programmed to perform two primary functions which are discussed in the following sections. The first function is parsing (reading and listing) of the .txt spectral files for batch processing, peak analysis and, tabulation of results in a .csv format. The second primary function rasterises the tabulated peak variable results into a georeferenced .ascii file. To create a rasterised image of the Raman data, the software requires the XY coordinates of each analysis point to plot the map in the correct size, location and orientation. Prior to collection of Raman spectra, the user would have created a reference map of the sample. The user should record three reference points on the reference map which will have the same coordinate system as the Raman maps. These reference points can be used to overlay the reference map with the Raman maps generated with Ramaster. If no reference points are provided, the user will have to manually georeference the reference map. To create an intuitive user interface, the Tkinter package (Lumholt *et al.*, 2020) was chosen (Fig. 26).

Ramaster was originally developed in the statistical software “R” using the “peaks” function of IDPmisc (Locher, 2018) and then translated into a Python 2.7 script for a more flexible development which can more readily processes large files (R has a default memory constraint of 300+ MB). See Appendix D for Ramaster Software and test data.

4.2.2. Data Parsing and Peak Analysis

Raman data is imported to Ramaster as a .txt file to facilitate the most basic output format from most Raman systems. Parsing is conducted by counting the total number of unique X and Y coordinates as well as the number of times the Raman frequencies range is repeated if the file has multiple spectra. This process continues until all selected files are read from the input directory creating a file list which will enable batch processing later. Taking the user specified “Wavelength min range” and “Wavelength max range” (Fig. 26) a separate vector is created to speed up data processing and only the maximum peak in this range is identified to allow for the construction of a specified peak variable. The peak characterisation Fourier Analysis algorithm uses the python package SciPy 1.0 (Virtanen *et al.*, 2020) Gaussian function “find_peaks” which searches for the maximum values in each interval to find the maximum peak intensity (PI) and the frequency (PF) at which this value is found. It then automatically calculates “peak prominence” and “peak width” variables required to calculate full width at half maximum. This process does not involve peak deconvolution, so it is important to consider if the peak of interest is overlapped by another peak or noise. Once the peak of interest is measured, the PI, FWHM and PF and unique geographical X and Y coordinates for each spectrum are recorded in a .csv file and saved in the user specified output directory. Batch processing is conducted looping the peak analysis processes through the list parsed files in the input directory. It is important to consider the level of background noise, the intensity of the peak of interest and the potential for frequency variance when choosing a peak frequency range. If an overly wide frequency range is chosen, then a peak with greater intensity or even background noise may be selected over the peak of interest resulting in a biased data set/map. To reduce the amount of background noise in the output file, the user must pre-process the data using a noise reduction scheme or alternatively, input a minimum peak intensity value which is greater than the background noise. Any peaks below this threshold will then be omitted from results. The .csv output format was chosen to optimise

usability across statistical software. If the user does not require a map to be generated, the software will still perform peak characterisation and act as peak characterisation tool. It is noteworthy that FWHM and PF values will have a discretization effect if data are not sufficiently smooth or have a low spectral resolution. The discretization effect is not an issue for PI calculations and consequently, this tool is best suited for the characterisation of PI variance and not FWHM or PF. A more effective method of calculating FWHM and PF is described by O'Haver (2020).

4.2.3. .CSV-.ASCII Map Generation

The second primary function takes the tabulated output file (the .csv file) from the peak characterisation algorithm and the user defined "cell_size" (the mapping resolution used in the Raman mapping process e.g., 2 µm, 4 µm etc.) and "Ascii variable" (e.g., PI, FWHM or PF) to generate an .ascii file. Parsing is conducted to record the number of files for rasterisation into .ascii format. An empty .ascii with a replicated file name is generated for each of these files. Using numpy and Pandas packages the ascii grid is generated using the total number of X and Y columns to create an array where the cell size defines the size of each pixel in that array. The numpy array is then translated into an .ascii formatted header which is required for reading and georeferencing by a geographical information system (e.g. GIS or QGIS). The .ascii grid file acts like a digital elevation map (DEM) where different image stretches can be applied to highlight different statistical properties of the target sites which is less feasible with .tiff or .jpeg images.

4.2.4. Raman Spectroscopy Analysis

4.2.4.1. Case Study 1: Zircon Imaging in Geochronology

Heavy mineral separates from sample NC4a (see sample list Appendixes B) were processed and sampled as of Section 2.5.. After mounting, samples were ground and polished to half thickness and processed for Qualitative Evaluation of Minerals by Scanning Electron Microscopy (QEMSCAN®) analysis at 10 µm resolution by Rocktype Ltd in their Oxford laboratory (See Fig. 25 and Appendix D). The FEI-trademarked QEMSCAN® technique is an automated mineralogy method which combines Energy Dispersive Spectroscopy (EDS) with

software that enables automated pixel by pixel spectral acquisition and post-analysis mineral classification. After QEMSCAN analysis, generated maps were used to locate zircon grains for Raman mapping in the school of Biological, Earth and Environmental Sciences (BEES), University College Cork. Zircon grains were mapped at 2 µm resolution using a Renishaw inVia™ confocal Raman microscope with a 50 mW DPSS (diode-pumped, solid-state) 532 nm laser, at 0.5 second residence time, 10% laser strength and a x50 long working distance objective was used. To ensure beam focus was maintained throughout analysis, the "LiveTrack" function of the Renishaw inVia™ Raman system was used. This function auto-focuses to maintain a specific beam diameter as the laser moves across the sample surface. Cosmic ray removal and baseline subtraction processing was conduct. Spectra were identified using the RUFF database (Lafuente *et al.*, 2015) and in-house libraries and saved as .txt files. Using Ramaster, the 950-1020 cm^{-1} frequency range was analysed to target the $v_3(SiO_4)$ vibrational mode of zircon(See Appendix D for Ramaster Software and test data). Generated maps were then loaded into ArcGIS where a histogram equalized stretching and green-yellow-red colour ramp was chosen to illustrate the variance in PI values in each grain (Fig. 27).

4.2.4.2. Case Study 2: Investigations of Apatite Replacement in Fossilised Anuran

Sample MNHN QU 17281 was taken from a fossilized anuran specimen found in the karst Jurassic sequences of the Quercy massif (Filhol, 1877). A piece of dermal tissue was sampled from the anuran and mounted on a 1.75 cm scanning election microscope (SEM) stub. Backscatter images of the sample were made using a Joel SEM in the BEES, University College Cork. Raman spectroscopy analysis was conducted at 2 µm resolution using a 50 mW DPSS (diode-pumped, solid-state) 532 nm laser and a x50 long working distance objective. A total of 9348 spectra were collected using an exposure time of 1 s and 50% laser strength with no accumulations. Spectral data were processed in Wire 5.3 by removing cosmic rays, applying a baseline correction using a least squares polynomial fit, noise reduction and smoothing of each data set. Noise reduction within Wire 5.3 uses Principal Components Analysis (PCA) to generate hundreds of components from the data set which are used to differentiate real spectral components from background noise (a spectra which no distinctive Raman peak) components. Using this method, noise components were carefully identified and extracted from each data set. Spectra in each data set were compared before and after noise reduction to ensure that peak characteristics had not been altered by data processing. Spectra in Fig. 28

were then smoothed using a (Savitzky *et al.*, 1964) algorithm with a smoothing window of 11 and a polynomial order of four. Peak analysis of three frequency ranges was then conducted using Ramaster. These include the 400-200 cm^{-1} range to characterise baseline noise, the 930-990 cm^{-1} targeting the v1 PO_4^3 asymmetric stretch molecules of apatite and the 1520-1620 cm^{-1} range targeting the G- band carbon molecules to generate maps of PI, PF and FWHM for each of these peak frequency ranges (Fig. 28).

4.3. **Results and Discussion**

4.3.1. Case Study 1: Zircon Imaging in Geochronology

A total of 160 Raman data sets of mapped zircon grains from sample NC4a were automatically analysed for their maximum PI, FWHM and PF in the 950-1020 cm^{-1} frequency range targeting the v_3 SiO_4 vibrational mode of zircon (see Appendixes D Table 7 for raw data). Of these 160 maps, eight maps of PI are displayed in Fig. 27 where each is accompanied by a PI transect graph. PI along with FWHM and PF are known to correlate strongly with the amount of radiation damage (resulting in metamictisation) caused by the decay of radioactive actinides which emit alpha decay radiation resulting in the progressive amorphization of the crystalline structure (Nasdala *et al.*, 1995; Lenz *et al.*, 2015a; Lenz *et al.*, 2015b). Inversely, the thermal annealing which can take effect from > 600 °C (Mezger *et al.*, 1997) can recover the metamictisation damage and improve the crystallinity of grains increasing the PI or molecule order of the v_3 SiO4 molecule. Interpreting whether grains are from the same melt is difficult as grains can crystalize at different rates and times, even within the same melt. Further, it is unlikely that the melts composition would be evenly homogenised resulting in one grain accumulating more REE or Si and O than another grain of the same age. Our results reflect this complexity and aid in the interpretation of the crystallisation histories.

In Fig. 27 eight Raman maps of detrital zircon grains display clear concentric growth rims as well as zoning which indicates a secondary or third phase of zircon growth. The crystallisation of zircon in a melt is influenced by several factors including temperature, the availability of Si, O, U, Pb, and other radioactive actinide group elements. To understand the crystallisation history, it is helpful to observe the relative peak intensity, width and frequency of the v_3 SiO_4

vibrational mode of zircon. Across the transect observed in Z127 (Fig. 27), peak intensity variation reveals the inner structure of the mineral and the crystallisation history. The core-rim (A'-A) transect reveals a rounded inner core with a peak intensity of 4086 counts. Due to the rounded shape of this core it may reflect a history of extensive metamictisation resulting in its current amorphous shape, or it may have been exhumed and rounded by erosional processes. The second zone in Z127 has a concentric prismatic rim with an average peak intensity of 4600 counts. Due to the prismatic nature of this zone and the higher peak intensity, these likely reflect a period of slow cooling allowing for well ordered tetrahedron shape to develop around the core as well as a reduction in the abundance or radiogenic elements relative to the core or outer rims. The third and fourth zones of this grain are identified by a progressive reduction in peak intensity. These are less structured and do not display the concentric zonation of the second zone, possibly because of an increase in the amount of radiogenic actinides or U in the melt.

Sample Z11 of Fig. 27 reveals a different history of two primary growth periods. The inner core (ca. 1200 counts) of Z11 has a relatively lower PI value than the rim (6000 counts). This may be a consequence of the sequestration of radiogenic Pb and U in the core resulting in metamictisation of the sample over time. The rim displays more concentric and prismatic growth rims indicating that the rim is much younger and has not undergone extensive decay effects or it has a lower concentration of radiogenic nuclides than the core. Zircon samples Z3 and Z87 demonstrate a more consistent and prolonged growth recording numerous injections of fresh magmatic material into the melt as zircon was crystalizing. The alternating PI values in Z3 can only be explained by variations in the abundance of available Si-O or radiogenic actinides which crystallised within the melt as the zircon grew over time.

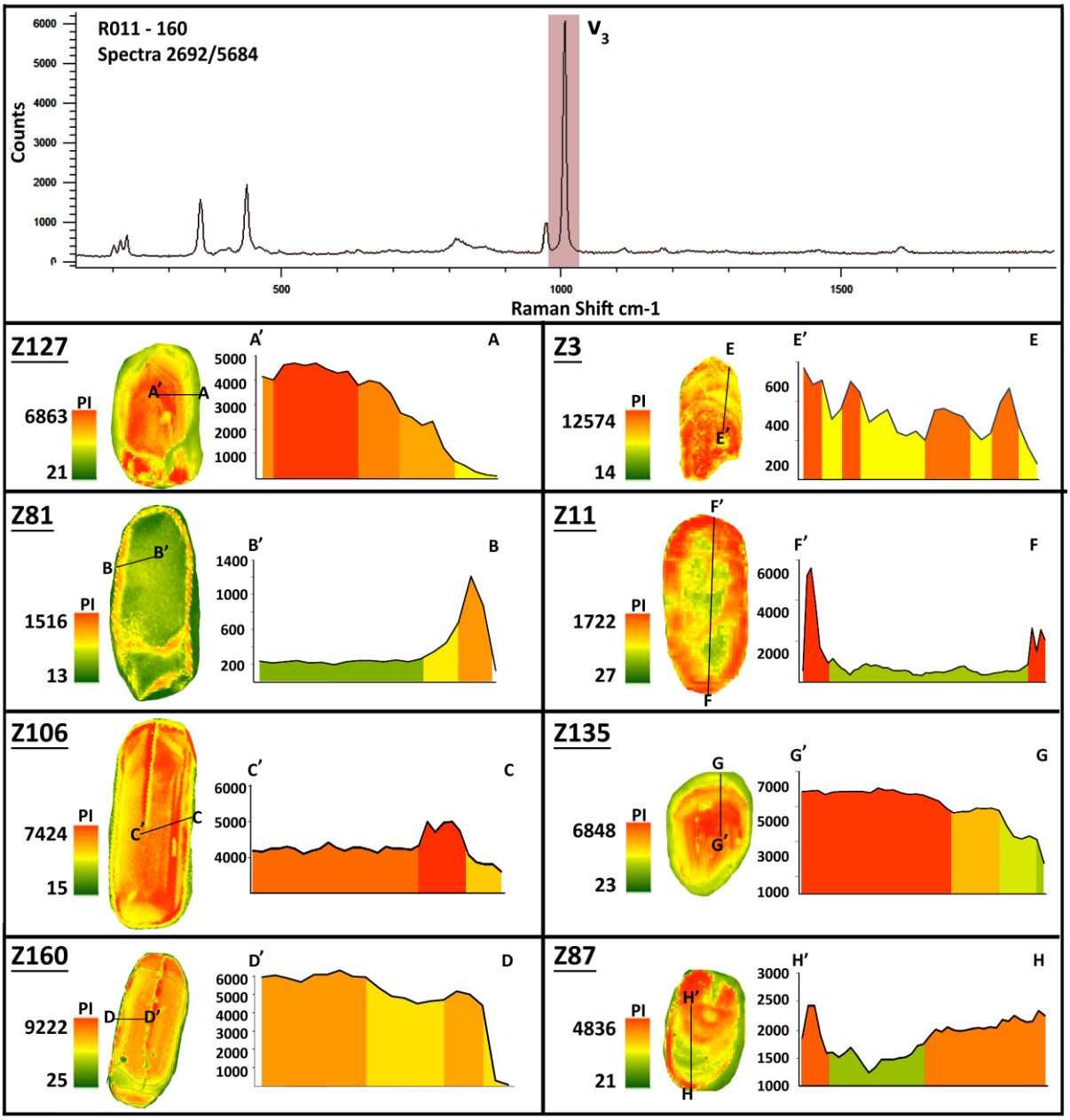

Fig. 27. *Raman spectroscopy maps of detrital zircon peak intensity (PI) at 1008 cm^{-1}. Maps and line transects of PI across the marked line transect on each grain illustrating the difference in PI across different growth phases in each grain (See Table 7 Appendixes D for all detrital zircon data).*

Raman spectroscopy imaging of zircon is often overlooked for traditional Cathodoluminescence (CL) imaging. This is because CL imaging provides high resolution images of internal growth structures useful for identifying growth rims and requires no post acquisition image processing. However, CL imaging does not provide information regarding molecule structure or state, inclusion composition or the degree of metamictisation while

RSA analysis can (Andersen, 2012). In addition, CL imaging requires sample coating of a conductive material (e.g., Carbon or graphite) prior to imaging which is removed before isotope analysis. Produced images then need to be analysed and referenced to identify core and rim locations for the selection of laser ablation spots. With the development of automated Raman mapping systems, detailed and informative analysis can be conducted over a short period of time, in situ or in prepared samples. This offers flexibility where identified grains can be georeferenced to the navigation map used during analysis removing the need for laborious multi-method image overlapping and comparison. For this method to work effectively, the Raman data for each grain needs to have X and Y coordinates in the same georeferencing system as the navigation map (e.g., Fig. 25). Each grain in this sample displays a unique crystallisation history which is accurately reflected in Ramaster generated .ascii maps. Combining this method with CL imaging, REE maps or U-Pb geochronology maps could offer an excellent bases in which to interpret the crystallisation and morphology history of zircon.

4.3.2. Case Study 2: Investigations of Apatite Replacement in Fossilized Anuran

A cross section of sample MNHN QU 17281 was mapped (see Appendixes D Table 8 for raw data). Spectra from this data set (Fig. 28B) typically show a dominant peak at 958 cm^{-1}, identified as the v1 PO_4^3 symmetric stretching mode associated with subordinate peaks v_2 (450 cm^{-1}), v_{3a} (1010 cm^{-1}), v_{3b} (1055 cm^{-1}), v_{3c} (1095 cm^{-1}) and v_4 (590 cm^{-1}) which are all hydroxyapatite PO_4^{3-} modes (Thomas *et al.*, 2011; Andò *et al.*, 2014; France *et al.*, 2014). A lower frequency v_1 PO_4^{3-} of 951 cm^{-1} reflects the presence of vivianite $Fe_3(PO_4)^2$ (Child, 1995; McGowan1 *et al.*, 2006; Keenan *et al.*, 2017), which is commonly associated with phosphate mineralisation in an environment with high organic content and acidic pH (Fig. 28B & 28G). In addition, several broad, low intensity peaks occur at 1310 cm^{-1} and 1580 cm^{-1} Fig. 28B, corresponding to altered D- and G- bands (Muirhead *et al.*, 2019). Peak analysis mapping results from this data set reveal a more detailed preservation of dermal structures than is visible with the use of SEM imagery (A -K).

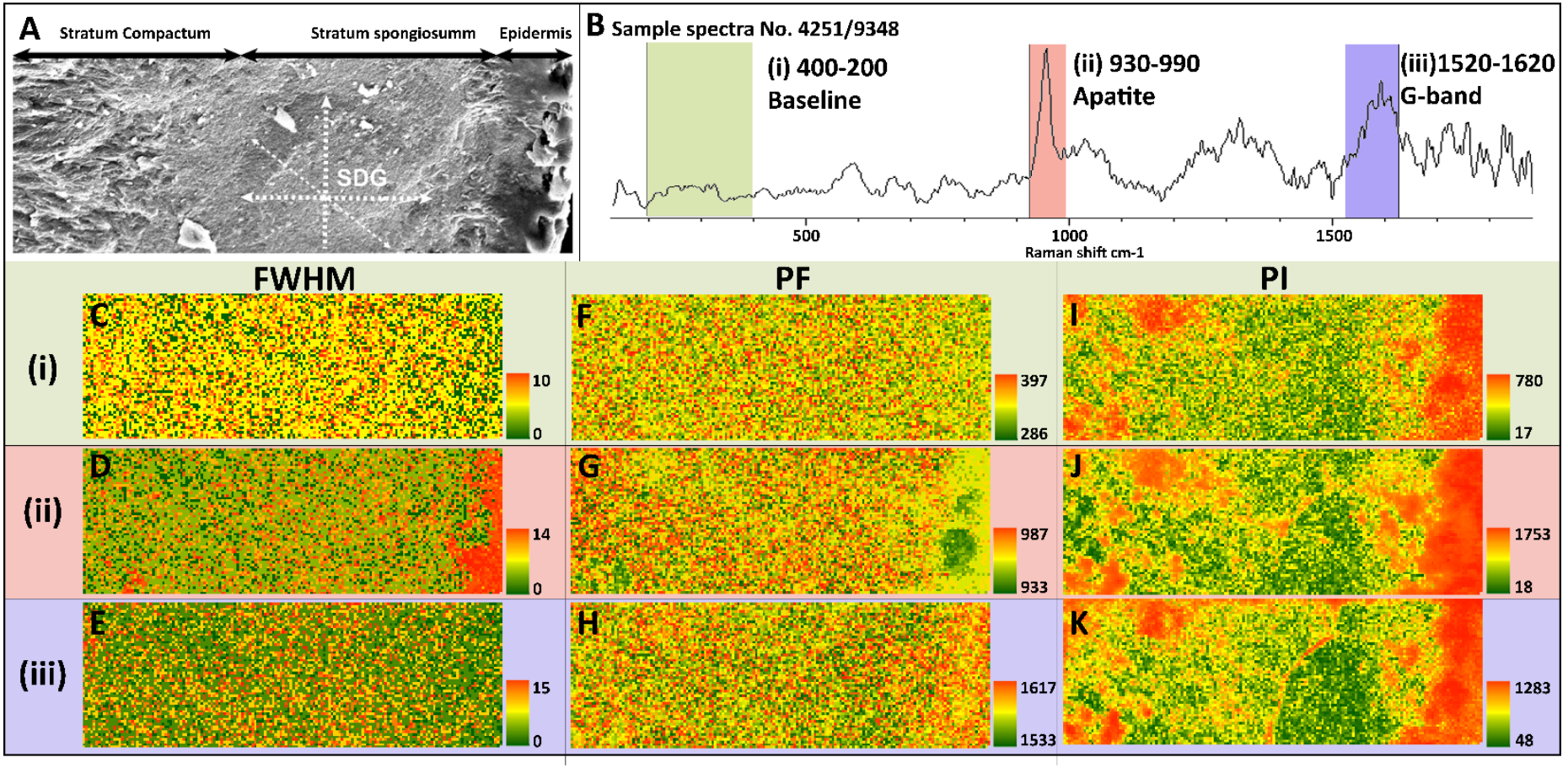

Fig. 28. *Maps of frog dermal tissue. A) SEM scan of area SDG; Suspect dermal gland. B)Raman spectra from data set with three frequency ranges (i-iii) chosen for mapping. C – D) Full width at half maximum (FWHM) maps at each frequency range. F-H) Peak frequency (PF) maps of each frequency range. I-K) Peak intensity (PI) maps of each frequency range (See Table 8 Appendixes D for Raman Data from sample MNHN QU 17281).*

The epidermis has a greater peak intensity in all frequency ranges indicating an increase in (i) background noise, (ii) apatite mineralisation and (iii) G-band carbon (Fig. 28B). Carbon rich materials often produce more fluorescence in a sample than mineralised regions and as this corresponds strongly with G-band carbon and apatite, this increase in noise is attributed to a fluorescence effect from a compositional variation within the sample. Within the stratum corneum/transitional layer from the stratum germinativium and lower gland regions (Fig. 28A), the rim of the gland and two layers of outer skin are best preserved by G-band carbon and apatite PI (Fig. 28 G-K). Apatite can readily mineralise in environments with organic rich materials and a high pH (Briggs *et al.*, 1993; Fabbri *et al.*, 2019). The gland rim and epidermal regions which produced fatty oils and skin may have created a more suitable environment for apatite and degraded G-Band carbon than the deeper dermal tissue layers. It is also helpful to look at the PF and FWHM maps as it is clear that vivianite (951 cm^{-1}) has mineralised in a more localised area than hydroxyapatite (956 cm^{-1}) further suggesting that the structural integrity of the dermal layer was maintained during phosphitization resulting in the current spatially distinct mineralisation. This also implies that these features are not artifacts of background noise or fluorescence (Yang *et al.*, 2013).

4.4. **Conclusions**

"Ramaster" allows for the quick and detailed interpretation of peak variables with a demonstrated application in geochronology, minerology and palaeontology and potential application across other geological fields. Here we demonstrate the benefits of having a batched peak analysis and image processing software. Raman maps of detrital zircon can be quickly imaged and cross-referenced with other methods allowing for characterisation of growth zones and crystal history. The benefit of having each image georeferenced saves considerable time for spatially sensitive applications like U-Pb zircon geochronology. It is important to note that PI is sensitive to beam focus and crystal orientation and for a more reliable indicator of crystalline histories, PW, PF or derived alpha dose calculations can also be used as demonstrated by Resentini *et al.* (2020) and Anderson *et al.* (2020). Ramaster generated Raman maps from the anuran dermal layer revealed preferential mineralisation of dermal structures after 40 million years. In addition, by generating multiple maps of the same area, the user can cross-compare peak variables from multiple peaks. This tool offers a unique

processing service which saves time and enhances the interpretability of complex data sets. Future work may include the incorporation of multi-variate analysis methods and in-application calculations enabling maps of D- and G- band carbon ratios for the interpretation of organic thermal maturation histories (Cançado *et al.*, 2006) or alpha dose emissions in zircon (Anderson *et al.*, 2020). In addition, spectral smoothing and different peak profiling and characterisation techniques could also be applied to produce higher resolution results.

4.5. **References**

Andersen, T. O. M. (2012). Age, Hf isotope and trace element signatures of detrital zircons in the Mesoproterozoic Eriksfjord sandstone, southern Greenland: are detrital zircons reliable guides to sedimentary provenance and timing of deposition? *Geological Magazine, 150*(03), 426-440. doi:https://doi.org/10.1017/S0016756812000623

Anderson, A. J., Hanchar, J. M., Hodges, K. V., & van Soest, M. C. (2020). Mapping radiation damage zoning in zircon using Raman spectroscopy: Implications for zircon chronology. *Chemical Geology, 538*, 119494. doi:https://doi.org/10.1016/j.chemgeo.2020.119494

Andò, S., & Garzanti, E. (2014). Raman spectroscopy in heavy-mineral studies. *Geological Society, London, Special Publications, 386*(1), 395-412. doi:https://doi.org/10.1144/SP386.2

Beyssac, O., Goffé, B., Chopin, C., & Rouzaud, J. (2002). Raman spectra of carbonaceous material in metasediments: a new geothermometer. *Journal of metamorphic Geology, 20*(9), 859-871. doi: https://doi.org/10.1046/j.1525-1314.2002.00408.x

Briggs, D., Kear, A., Martill, D., & Wilby, P. (1993). Phosphatization of soft-tissue in experiments and fossils. *Journal of the Geological Society, London, 150*(6), 1035-1038. doi:https://doi.org/10.1144/gsjgs.150.6.1035

Cançado, L., Takai, K., Enoki, T., Endo, M., Kim, Y., Mizusaki, H., Jorio, A., Coelho, L., Magalhaes-Paniago, R., & Pimenta, M. (2006). General equation for the determination of the crystallite size L a of nanographite by Raman spectroscopy. *Applied Physics Letters, 88*(16), 163106. doi:https://doi.org/10.1063/1.2196057

Chandrabhas, N., Shashikala, M., Muthu, D., Sood, A., & Rao, C. (1992). Pressure-induced orientational ordering in C60 crystals as revealed by Raman spectroscopy. *Chemical physics letters, 197*(3), 319-323. doi:https://doi.org/10.1016/0009-2614(92)85776-7

Chew, D. M., Petrus, J. A., Kenny, G. G., & McEvoy, N. (2017). Rapid high-resolution U–Pb LA-Q-ICPMS age mapping of zircon. *Journal of Analytical Atomic Spectrometry, 32*(2), 262-276. doi:https://doi.org/10.1039/C6JA00404K

Child, A. M. (1995). Microbial taphonomy of archaeological bone. *Studies in conservation, 40*(1), 19-30. doi:https://doi.org/10.1179/sic.1995.40.1.19

Fabbri, M., Wiemann, J., Manucci, F., & Briggs, D. E. (2019). Three-dimensional soft tissue preservation revealed in the skin of a non-avian dinosaur. *Palaeontology*. doi:https://doi.org/10.1111/pala.12470

Filhol, H. (1877). *Recherches sur les phosphorites du Quercy: étude des fossiles qu'on y rencontre et spécialement des mammifères* (Vol. 2): G. Masson.

France, C. A., Thomas, D. B., Doney, C. R., & Madden, O. (2014). FT-Raman spectroscopy as a method for screening collagen diagenesis in bone. *Journal of archaeological Science, 42*, 346-355. doi:https://doi.org/10.1016/j.jas.2013.11.020

Henry, D. G., Jarvis, I., Gillmore, G., & Stephenson, M. (2019). Raman spectroscopy as a tool to determine the thermal maturity of organic matter: Application to sedimentary, metamorphic and structural geology. *Earth-Science Reviews, 198*. doi:https://doi.org/10.1016/j.earscirev.2019.102936

Keenan, S. W., & Engel, A. S. (2017). Early diagenesis and recrystallization of bone. *Geochimica et Cosmochimica Acta, 196*, 209-223. doi:https://doi.org/10.1016/j.gca.2016.09.033

Lafuente, B., Downs, R., Yang, H., & Stone, N. (2015). The power of databases: the RRUFF project. In “Highlights in mineralogical crystallography”, Armbruster, T. & Danisi, RM, eds. W. *De Gruyter, Berlin, Germany, 1*, 30. doi:https://doi.org/10.1515/9783110417104-003

Locher, R. (2018). IDPmisc: 'Utilities of Institute of Data Analyses and Process Design (). Retrieved from https://CRAN.R-project.org/package=IDPmisc

Lumholt, S., Rossum, G. v., Conway, M., Manheimer, K., & Lundh, F. (2020). Tkinter — Python interface to Tcl/Tk (Version 24.1). Retrieved from https://docs.python.org/3/library/tkinter.html#module-tkinter

Lünsdorf, N. K., Kalies, J., Ahlers, P., Dunkl, I., & von Eynatten, H. (2019). Semi-Automated Heavy-Mineral Analysis by Raman Spectroscopy. *Minerals, 9*(7), 385. doi:https://doi.org/10.3390/min9070385

McGowan1, G., & Prangnell, J. (2006). The significance of vivianite in archaeological settings. *Geoarchaeology: An International Journal, 21*(1), 93-111. doi:https://doi.org/10.1002/gea.20090

Menges, F. (2020). Spectragryph-Optical Spectroscopy Software. Retrieved from https://www.effemm2.de/spectragryph/

Mezger, K., & Krogstad, E. (1997). Interpretation of discordant U-Pb zircon ages: An evaluation. *Journal of metamorphic Geology, 15*(1), 127-140. doi:https://doi.org/10.1111/j.1525-1314.1997.00008.x

Muirhead, D. K., Bond, C. E., Watkins, H., Butler, R. W., Schito, A., Crawford, Z., & Marpino, A. (2019). Raman Spectroscopy: an effective thermal marker in low temperature carbonaceous fold-thrust belts. *Geological Society, London, Special Publications, 490*, SP490-2019-2027. doi:https://doi.org/10.1144/SP490-2019-27

Nasdala, L., Irmer, G., & Wolf, D. (1995). The degree of metamictization in zircons: a Raman spectroscopic study. *European Journal of Mineralogy-Ohne Beihefte, 7*(3), 471-478. doi:https://doi.org/10.1127/ejm/7/3/0471

Nasdala, L., Pidgeon, R., Wolf, D., & Irmer, G. (1998). Metamictization and U-Pb isotopic discordance in single zircons: a combined Raman microprobe and SHRIMP ion probe study. *Mineralogy and Petrology, 62*(1-2), 1-27.

Norell, M. A., Wiemann, J., Fabbri, M., Yu, C., Marsicano, C. A., Moore-Nall, A., Varricchio, D. J., Pol, D., & Zelenitsky, D. K. (2020). The first dinosaur egg was soft. *Nature*. doi:https://doi.org/10.1038/s41586-020-2412-8

O'Haver, T. (2020). *Pragmatic Introduction to Signal Processing* Department of Chemistry and Biochemistry, University of Maryland at College Park.

QGIS.org. (2021). QGIS geographic information system. http://www.qgis.org.

Resentini, A., Andò, S., Garzanti, E., Malusà, M. G., Pastore, G., Vermeesch, P., Chanvry, E., & Dall'Asta, M. (2020). Zircon as a provenance tracer: Coupling Raman spectroscopy and UPb geochronology in source-to-sink studies. *Chemical Geology*, 119828. doi:https://doi.org/10.1016/j.chemgeo.2020.119828

Rull, F., Maurice, S., Hutchinson, I., Moral, A., Perez, C., Diaz, C., Colombo, M., Belenguer, T., Lopez-Reyes, G., & Sansano, A. (2017). The Raman laser spectrometer for the ExoMars rover mission to Mars. *Astrobiology, 17*(6-7), 627-654. doi:https://doi.org/10.1089/ast.2016.1567

Savitzky, A., & Golay, M. J. (1964). Smoothing and differentiation of data by simplified least squares procedures. *Analytical chemistry, 36*(8), 1627-1639.

Thomas, D. B., McGoverin, C. M., Fordyce, R. E., Frew, R. D., & Gordon, K. C. (2011). Raman spectroscopy of fossil bioapatite—a proxy for diagenetic alteration of the oxygen isotope composition. *Palaeogeography, Palaeoclimatology, Palaeoecology, 310*(1-2), 62-70. doi:https://doi.org/10.1016/j.palaeo.2011.06.016

Virtanen, P., Gommers, R., Oliphant, T. E., Haberland, M., Reddy, T., Cournapeau, D., Burovski, E., Peterson, P., Weckesser, W., & Bright, J. (2020). SciPy 1.0: fundamental algorithms for scientific computing in Python. Nature methods.

Yang, S., & Akkus, O. (2013). *Fluorescence Background Problem in Raman Spectroscopy: Is 1064 nm Excitation an Improvement of 785 nm*. Wasatch Photonics: Report.

Chapter 5: *Raman and Fluorescence spectroscopy of vein-hosted alpha quartz to characterize tectonic chronology: Novel insights from unconventional methods*

Authors

Odhrán McCarthy[(1)], Pat Meere[(1)], Jurgen Lang[(1)], Alberto Resentini[(2)], Mohit Tunwal[(1)], Richard Unit[(1,)], Hazel Garvie- Cooke, Sergio Andò[(2)].

Affiliations

[1]School of Biological, Environmental and Earth Sciences and iCRAG, University College Cork

[2]Department of Earth and Environmental Sciences, University of Milano –Bicocca.

[3]School of Earth & Environmental Sciences, University of St-Andrews

Abstract

Quartz is an abundant and ideal time capsule that records the formation and deformation history of Earth's lithosphere. However, our understanding of the formation and deformation of quartz is limited due to the absence of a tool to quantify deformation and mineral variance. We demonstrate the first Raman spectroscopy differentiation of vein-hosted alpha quartz by mapping material-fluorescence and Si-O bond variations using Raman Spectroscopy Analysis with potential application in both academia and industry. Analysis of two data sets compiling 917,278 Raman spectra is used to characterise changes of the silicon-oxygen bonds in the SiO_4 quartz tetrahedron. We find that material-fluorescence, accumulated lattice deformation and compositional variance in vein-hosted quartz is effective in construing the history of multiple cross-cutting mineralised fractures. These findings provide a new proxy for constraining tectonic chronology and demonstrate a new application Raman spectroscopy within geosciences.

5.1. **Introduction**

Raman characterisation of mineral chemistry and structure has broad application across numerous academic and industry fields. Quartz is a ubiquitous component of the Earth's crust; its widespread distribution across the upper portion of our planet and stability under diagenetic and weathering conditions makes it an attractive target mineral for Earth Science research. Crystalline structure, inclusion and textural studies that utilise Fluid Inclusion (FI), Cathode Luminescence (CL), Scanning Electron Microscopy – Electron Backscatter Diffraction (SEM-EBSD) and Transmitted Electron Microscopy (TEM) imaging (Randle *et al.*, 2014; Cui *et al.*, 2019) demonstrate the versatility of quartz in examining upper crustal planetary processes. Currently, quantitative image analysis of quartz remains a major challenge because established techniques provide qualitative image-based information lacking workable data sets. Methods like CL imaging depend on variations in rare earth elements (REE) to image zonation without indicating mineral abundance or concentration. More destructive methods like Inductively Coupled Plasma Mass Spectroscopy (ICPMS) are then required to differentiate quartz isotopically, which is expensive and time consuming. Derived qualitative data sets are therefore limited in volume, and the arising interpretations are questionable. Adding to the range of analytical methods for quartz characterisation has a broad appeal to the geoscience community.

Harnessing the "Raman Effect" (Raman, 1928), Raman Spectroscopy Analysis (RSA) is a proven, efficient method to characterise mineral crystal bond variation. Bond variation relates to alteration effects in mineral phases (Kulp *et al.*, 1952; Nasdala *et al.*, 1995; Nasdala *et al.*, 1998; Andò *et al.*, 2014; Rull *et al.*, 2017), the thermodynamic profile of minerals such as quartz and graphite and, to dissolution processes in minerals like feldspars (Bates, 1972; Michel *et al.*, 1976; Mernagh *et al.*, 1991; Pasteris *et al.*, 1991; Chandrabhas *et al.*, 1992; Gout *et al.*, 1997; Gupta *et al.*, 2000; Muirhead *et al.*, 2019). Vein-hosted quartz is largely used to interpret upper crustal history as it can offer insights toward the chronology of multiple tectonic events, the orientation of fracturing (Rusk *et al.*, 2006; Nachon *et al.*, 2014) and to find economically valuable minerals (Landtwing *et al.*, 2005; Bost *et al.*, 2013; Parnell *et al.*, 2014). Raman analysis of quartz and fluid inclusions provides insight into crystal lattice variation, molecular concentration and phase transitions (Shapiro *et al.*, 1967; Talebian *et al.*,

2012). The utility and versatility of RSA is evident today through its inclusion on the ExoMars rover mission 2020 (Bost *et al.*, 2013; Rull *et al.*, 2017). Though its inclusion aims to investigate signs of early life on mars as well as mineral chemistry and structure, it has the potential to provide a deeper level of insight into important veins like those found in Gale crater, Mars (Nachon *et al.*, 2014).

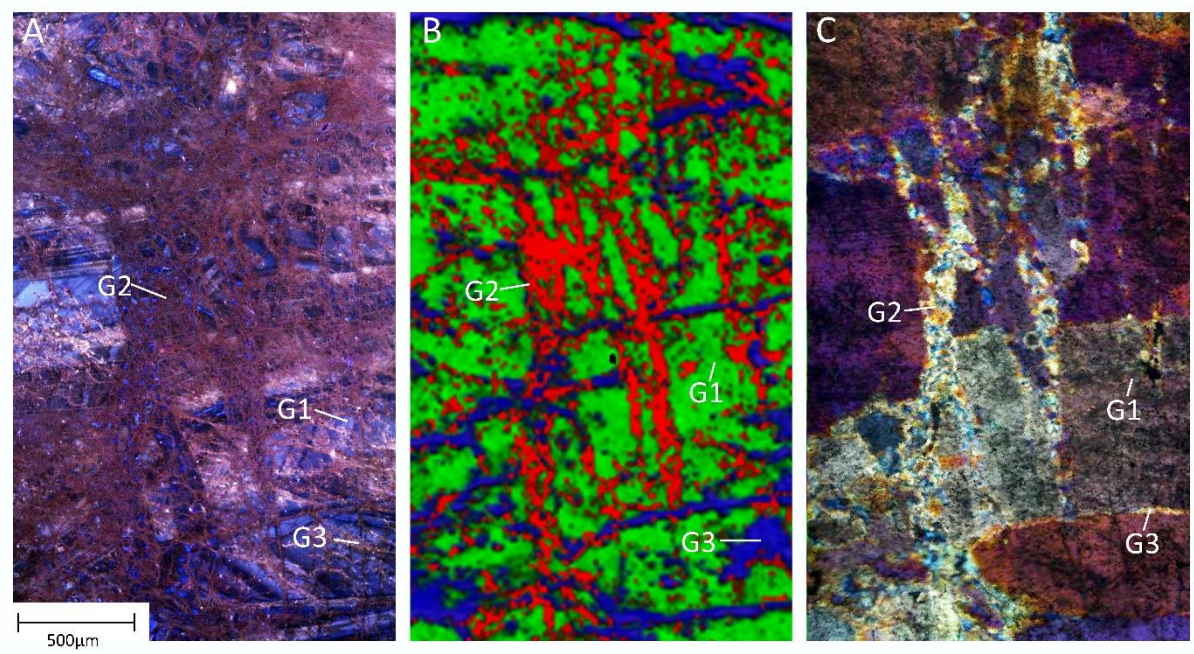

Fig. 29. *Quartz images from the study thick section. (A) Hot CL image of en echelon vein structure associated with pre Variscan quartz in blue (G1) and two cross cutting syn-Variscan veins in bottle brown (G2 & G3). (B) Fluorescence affected RSA false colour image with pre Variscan, G1 quartz in green , G2 syn-Variscan event one and G3 syn-Variscan event two. (C) Cross polarised image where G3 veins and G2 en echelon veins cross cuts G1 quartz.*

Here we demonstrate the utility of RSA and fluorescence spectroscopy in distinguishing multiple generations of vein-hosted alpha quartz using an example from the historic Allihies copper mining area on the Beara Peninsula, southwest Ireland (Fig. 30). One of the challenges in RSA is auto-fluorescence, or the fluorescence effect caused by the excitation of light during Raman analysis (Shreve *et al.*, 1992; Xie *et al.*, 2009). Conversely, Raman or Rayleigh scattering when working in fluorescence landscapes is also a challenge (Eilers *et al.*, 2014). Here we show that RSA combined with the effect of spectral fluorescence can be used to constrain the sequential development of cross cutting vein generations (Fig. 29). This is achieved by applying principal component analysis to Raman data sets before and after fluorescence

correction to capture the impact of fluorescence on Raman spectra and differentiate each generation of quartz growth. Further, characterisation of each quartz generation can then be made using traditional RSA methods like mineral phase identification and measuring molecular vibration variance in each generation of quartz (Passchier *et al.*, 2005). Our method finds new utility in Raman spectroscopy to differentiate vein-hosted quartz and demonstrates a potential benefit of previously removed or avoided material-fluorescence.

5.1.1. The Problem of Fluorescence in Raman Scattering

A brief explanation of RSA and fluorescence is offered to help in the understanding of how each can be used to differentiate mineralogical characteristics. For a more detailed explanation of each, see also Smith *et al.* (2019a) for Raman spectroscopy and Lakowicz (2013) for fluorescence spectroscopy. Raman spectroscopy measures the inelastic scattering (also known as Raman scattering) of light from a solid, liquid or gaseous material (Frezzotti *et al.*, 2012). This inelastic scattering demonstrated by Raman (1928), results in the scattered light having a higher (and sometimes lower) energy state than the incident light. The energy transition which occurs from a molecules ground state to its excited state, is virtual, as the excited state is unstable and the light is instantaneously released as scattered radiation (Vandenabeele *et al.*, 2007; Frezzotti *et al.*, 2012). The amount of light scattered depends on the composition of the sample material as well as vibrational, rotational and the lattice frequency of the material. The vibrational energy of the molecules in a sample are represented in a spectrum made of Raman active bands which appear as peaks. These peaks/active bands are representative of the stretching and bending of a molecule's bonds. A sample is considered Raman active when it is polarized by a monochromatic light source. Raman scattering is a non-resonant process as the energy of the incident photon is not important for scattering to occur and as a result is instantaneous.

Fluorescence is different to Raman scattering as the energy of the incident photon (laser) must be resonant with the molecule, which results in the molecule undergoing an energy transition as it absorbs the photon. When the molecule is excited by the incident photon, it jumps to a higher energy state and emits an extra energy photon known as fluorescence.

Fluorescence exists for a finite time (typically nanoseconds). Consequently, during Raman analysis, material-fluorescence and Raman scattering can occur simultaneously as both are induced by photon radiation. In a Raman spectrum, fluorescence peaks appear as extremely broad and indistinguishable peaks which often have a peak width of more than 700 cm^{-1} (Zięba-Palus *et al.*, 2014). Importantly, fluorescence can be generated by the Raman system (Mosier-Boss *et al.*, 1995) or by the sample making it difficult to identify the source of fluorescence.

If present, fluorescence can artificially increase the Raman baseline or can cause signal saturation resulting in a loss of usable data. For this reason fluorescence is normally avoided or removed in Raman studies often with a baseline subtraction (Yang *et al.*, 2013) or with Fast Fourier Transforms and filtering (Mosier-Boss *et al.*, 1995). Fourier transformation can greatly impact real Raman peaks which are within the same frequency as the fluorescence peaks. Raman peaks are typically characterised by measuring three variables: peak intensity (PI), full width at half maximum height (FWHM), and peak frequency (PF) (Luna, 2017). As fluorescence peaks are so much wider than Raman peaks, when they are present in Raman spectra, they can increase the baseline of the Raman spectra as the limb of the fluorescence peak becomes the baseline of the Raman spectra (Fig. 31). Fluorescence in a Raman spectra may then cause the peak intensity of Raman vibrational modes to be artificially inflated resulting in a biased result. When fluorescence is removed, changes in peak shape and intensity generally reflect an alteration in the lattice structure of crystals (Mosier-Boss *et al.*, 1995). However, directly linking environmental conditions to specific peak variables is challenging as this may also relate to other effects like chemical or topographical variations as well as remaining fluorescence or handling errors. Likewise, the cause of fluorescence in a Raman spectrum is difficult to diagnose because of how broad the peaks are. When combined with additional methods like CL imaging and petrographic studies, we demonstrate that fluorescence in RSA can be used to differentiate generations of mineral growth and vein formation.

5.1.2. Molecule Order – Disorder Transitions in Raman Spectroscopy

Previous research has shown how RSA can be used to measure the effect of temperature and pressure on the vibrational state of molecules (Mernagh *et al.*, 1991; Chandrabhas *et al.*, 1992; Tong *et al.*, 2015). The force needed to bend or compress a bond is determined by the inter atomic binding energy. The frequency at which a molecule vibrates is dependant on the inter atomic binding energy and any change in the order or state of these bonds may induce a change in Raman peak frequency, intensity or width. For example, undulous extinction in quartz is the product of dissociation of molecules altering lattice configuration as a result of strain on the lattice (Passchier *et al.*, 2005) and although this is visible in cross polarized light, it is not directly measurable. Undulous extinction may be measurable with RSA. Geologists currently rely on visible cross cutting relationships to interpret vein chronology; however these are not always present and are often uninterpretable due to the chaotic nature of fracturing (stockwork or cataclastic fracturing). Raman spectroscopy enables for the measurement of the bond variation in minerals (Shapiro *et al.*, 1967; Anderson *et al.*, 2020) meaning that if there is a difference between the molecule vibrational frequency, velocity or composition between two generations of quartz, RSA should measure the difference between each generation. It is difficult to attribute the different Raman peaks between two generations of quartz to a single differentiating factor. For example, a difference in peak intensity between two generations may be due to different molecule concentrations, deformation histories, sample heights, laser strengths, machine or material fluorescence or even post acquisition spectral processing. Here we aim to test the capability for RSA to characterise and differentiate between at least two generations of quartz and offer some cause as to this differentiating factor.

Quartz is grouped into low temperature (< 570 °C), trigonal alpha quartz and high temperature, hexagonal beta quartz. Both are known as reconstructive polymorphs meaning that quartz molecules are progressively becoming more ordered with time as long as the thermodynamic state of the molecule is not altered, i.e. it stays within a state of equilibrium (Broekmans, 2004; Lakshtanov *et al.*, 2007). Beta quartz is not stable at room temperature and will eventually return to a trigonal (alpha) state (Shapiro *et al.*, 1967; Dolino, 1990). Previous research in Raman spectroscopy has characterised 48 vibrational modes where only

some are Raman active (or spectrum peaks) in alpha quartz (Shapiro *et al.*, 1967; Etchepare *et al.*, 1974). The most commonly identified active modes in quartz are the A1 (467 cm^{-1}) and B1 (207 cm^{-1}) modes which measure the symmetrical bending (A1) and stretching (B1) of Si and O molecules (Etchepare *et al.*, 1974). In a vein setting, quartz which is crystalised in a state other than stable equilibrium may have a lesser degree of crystalline order. The influence of pressure, temperature or variable crystallisation conditions on molecule order has not been appropriately explored in the context of Raman spectroscopy. Consequently, it is difficult to explain why one quartz lattice has different Raman peak variables to another. In this study, we demonstrate that it is possible to interpret the relative crystalline order of quartz veinlets.

5.1.3. Geological Context

Analysis was conducted on a thick section from a sample collected in the historic Allihies Copper Mining area on the Beara Peninsula, SW Ireland (Fig. 30). The host rock is a Upper Devonian siliciclastic succession (mainly sandstones and siltstones) that belongs to the 'Upper Old Red Sandstone' sequence of the Munster Basin (MacCarthy, 1990). A pervasive host rock cleavage and minor local faults are attributed to late Carboniferous NNW-directed Variscan compression (Sanderson, 1984; Reilly, 1986; Ford, 1987; Meere, 1995b). Quartz veins that host Cu mineralisation at Allihies are subvertical and strike E-W (Reilly, 1986; Lang *et al.*, 2020), the study sample was collected approximately 225 m north of the Mountain Mine lode. The vein is 2-10 cm wide, subvertical and strikes E-W. Raman analysis targeted two areas of interest from the thick section: i)Data Set 1 includes spectra collected from Investigation site one (Fig. 30). ii)Data Set 2 was collected from Investigation site two (Fig. 30). These areas were chosen as they contain at least two generations of quartz where one cross-cut the other.

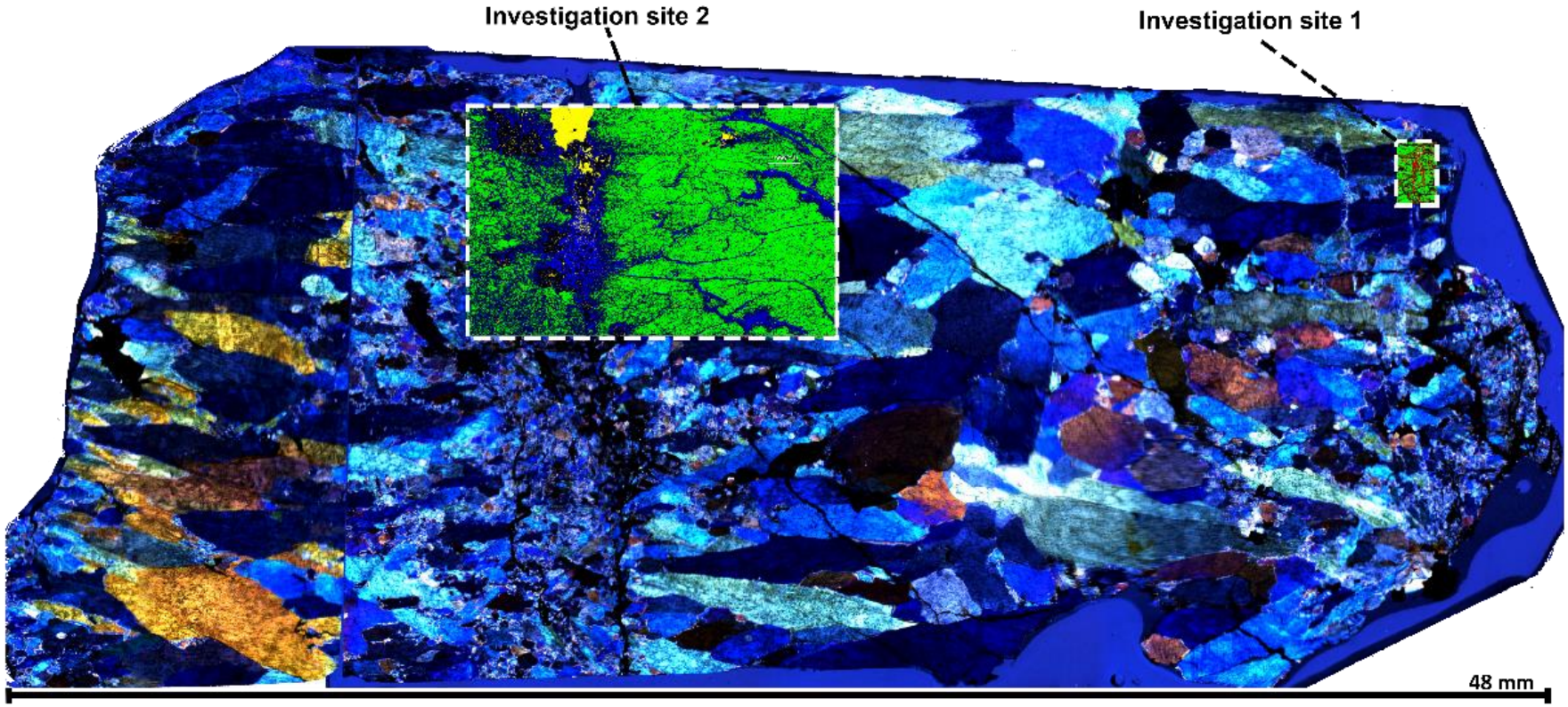

Fig. 30. *Cross polarised image of thin section JL_AH_418 from Allihies Copper Mine. Investigation sites 1 and 2 are outline by white boxes with Raman maps overlayed. (See Figure 2 and 3 for Raman maps)*

5.2. **Methods**

For thick section preparation, Sample JL_AH_418 was cut perpendicular to the Syn-Variscan vein cleavage $S_{1,\ vein}$ = 279/75 . As topography can result in anomalous results during RSA, sections were given a high-grade CL polish to maximise flatness. Additionally, a focus-tracking feature (LiveTrack) on the Raman microscope was used to maintain focus and determine topography over the measured area of the sample. To characterise how topography influenced spectra, the point at which the laser focused (a topographical z value) was recorded to test for correlation between PI and elevation (z). Thick section JL_AH_418 was analysed with petrographic light microscopy, SEM–EDS, Hot CL and Raman spectroscopy. Cross-polarised light petrographic images were collected with a Leica VZ700 C (Fig. 30C & D). Hot CL imaging with the Tescan TIGER MIRA3 FEG-SEM was conducted in the Centre for Microscopy and Analysis, Trinity College Dublin, Ireland (Fig. 31A). CL imaging was conducted with a scan speed of 10, SEM Mag of 242 x, HV of 20.0 Kv and a working distance of 18.00 mm.

Raman spectra were collected with a Renishaw inVia™ confocal Raman microscope in the Biological, Earth and Environmental Sciences department, University College Cork. A 532 nm laser was used for acquisition, with 0.5 second residence time, 100% laser strength and a 50 x objective. Data Set one includes 27,738 spectra collected automatically over 48 minutes from investigation site one (Fig. 31). Data Set 2 includes 889,540 spectra from investigation site two (Fig. 32) was collected automatically over 25 hours. Spectral data was pre-processed with a baseline correction application within WIRE 5.3 which uses a fixed least squares polynomial fit value of 11 to remove background from the data set. A Rayleigh scattering peak can also occur at 120-140 cm^{-1} which is caused by the Rayleigh filter cut off and is an artifact of the machine (Chen *et al.*, 2014). To avoid this artifact affecting results, a spectral truncation was applied to baseline corrected spectra between 0-140 cm^{-1}. Raman maps in Fig. 31 and Fig. 32 were generated with Spectrum Centring and Normalization Scaling Principal Component Analysis (SNV-PCA) (Lee *et al.*, 2008) in WIRE 5.3. Derived principal components which represented the majority of variance in the whole data set were chosen to create each map. Each spectrum equates to one pixel which is designated a colour representing one component. The brightness of each pixel is stretched over its Pearson correlation score with

each principal component, where a high degree of correlation equates to a brightly coloured pixel and inversely, a low correlation equates to a dull or black pixel. In each of these maps, thresholding one principal component against another allows the user to influence the designation of each spectra/pixel to a component to construct these Raman maps. WIRE 5.3 applies an image smoothing iteration reducing the often-pixilated look of maps.

5.3. **Results**

5.3.1. CL Imaging and Optical Petrography

Analysis from CL images and optical petrography of two areas of interest of the fracture zone in thick section BS1 identifies three separate phases of quartz growth during vein formation (Fig. 31A & 3B). In investigation site one, the oldest generation of quartz (G1) comprise euhedral, monocrystalline quartz ranging from 250-1500 µm in maximum diameter. Cathode Luminescence imaging revealed internal growth zones in some larger crystals with a short-lived blue colour which changed to brown with continued electron bombardment. A bottle blue CL colour for quartz is commonly observed in hydrothermal or pegmatitic quartz, however in this case a hydrothermal origin is evident (Götze *et al.*, 2001; Lang *et al.*, 2020). Two later generations of veins (G2 and G3) are evident however it is difficult to distinguish which vein set formed first using CL or petrographic methods. The first set of veins (G1) appears to have been crosscut by a series of subparallel, overlapping fractures identified as G2 veins. As these fractures are 'step like', they appear to be an en-echelon pattern. CL imaging of G2 quartz shows a light-dark brown colour indicating a low grade metamorphic or hydrothermal origin for this quartz. G2 quartz is microcrystalline with most grains being < 20 µm in size. Generation three (G3) is also microcrystalline in origin and in places follows G1 grain boundaries and cross cuts G1 and in places G2 indicating that it may post date G2. It has a light-dark brown CL colour suggesting a similar low grade metamorphic or hydrothermal origin to G2. Generations two and three crosscut G1 ranging from 70-110° angle. It is difficult to disentangle the order of G2 and G3 formation, despite each being distinctly separate textures and fracture sets (Fig. 31).

CL imaging and optical petrography of investigation site two (Fig. 32) identifies two generations of quartz formation. The first generation is related to G1 of investigation site one as these have a hydrothermal, bottle blue CL colour with visible concentric growth rims in large 250 – 1000 + µm quartz crystals. The second generation of veins in this area reveals a chaotic, cataclastic fracture zone with stockwork fracturing in places which is related to G2 or G3 quartz in investigation site one as CL imagery from this area reveals a brown-blue colour similar to G2 and G3 of investigation site one. The complexity of fracturing in this zone makes it difficult to differentiate G2 or G3 veins as observed in investigation site one. Generation one veins are mineralised with quartz, while G2/G3 veins are mineralised by microcrystalline quartz and a small amount of pyrite which is opaque in Fig. 32D. Fracturing of G2/G3 in this area appears to follow grain boundaries in places as well as cross cutting G1 quartz.

5.3.2. RSA and Fluorescence Spectroscopy

Raman spectra from Map1 contain a series of peaks associated with the quartz SiO_4 tetrahedron structure (see Table 9 for raw Raman data). The two strongest peaks in this data set are the A2 (467 cm^{-1}) and B1 (207 cm^{-1}) active modes. Auto-fluorescence was identified in these spectra as the baseline was inflated. To correct for fluorescence, a baseline subtraction was conducted (see Fig. 31). Principal component analysis was conducted before and after baseline subtraction to account for fluorescence in the data set. Non-baseline subtracted PCA results represent 88% of the total variance of the data set and contain A2 (467 cm^{-1}) and B1 (207 cm^{-1}) modes along with smaller associated quartz peaks (Etchepare *et al.*, 1974). The total variance of the total data set which is represented by PC1, PC2 and PC3 is 78, 6 and 5% respectively. The primary difference between each group is the baseline slope (Fig. 31E) as each component contains the same quartz peaks. The PCA map generated from these spectra (Fig. 31B) reveals three distinct quartz generations with different amounts of material fluorescence as the fluorescence appears to be spatially correlated with the location of each vein set, therefore we argue that this fluorescence is likely due to a compositional or structural difference in the minerology of each quartz set and not an artifact of machine noise.

After baseline subtraction, PCA results represent 43% of the total variance of the data set. Due to the corrected baseline, PC1 and PC2 contain different peak variables as fluorescence

has been removed revealing more variance in the data set. Considering the size of the data set, the remaining 57% of variance is likely comprised of noise. The statistical significance of these results set may be improved through noise filtering or smoothing, however these approaches were not conducted as they may introduce bias by further altering peak variables. PC1 incorporates 20% of the total variance of the data set and is correlated with quartz peaks A2 and B1 and is negatively associated with G-band peaks (c. 1500 cm^{-1}). The baseline in PC1 contains more noise and numerous small peaks indicating a more varied composition than PC2 or increased background noise emitted from G1 veins. This is likely due to some compositional variation between G1 and G2 quartz. PC2 represents 5% of total variance in the data set and correlates positively with the A2 peaks and negatively with B1 peaks. The baseline subtracted map differentiates G1 and G2/G3 veins effectively, however due to the removal of the fluorescence affect, G2 and G3 cannot be differentiated (Fig. 31B and C).

Raman analysis results from investigation site two show spectra containing the A1 (467 cm^{-1}) and B1 (207 cm^{-1}) peaks often with a weak, broad peak at 1590 cm^{-1} (Fig. 32G) interpreted to be associated with the simple C-C bond, G- band mode (Muirhead *et al.*, 2019). Epoxy resin is also identified in the area with a characteristic series of peaks (see Table 9 for raw Raman data). Spectra in this data set also contain fluorescence and consequently PCA analysis was conducted before and after truncation and baseline subtraction to profile the fluorescence effect. Principal component analysis before truncation and baseline subtraction accounts for 94% of the total variance of the data set with PC1 (77%), PC2 (10%) and PC3 (3%) representing 91% of total variance of the data set, like PC1 of investigation site 1 before baseline subtraction (Fig. 32G). The differentiating factor in these PCA spectra is the baseline slope as highlighted by the red flat baseline superimposed into Fig. 32G. Here the spatial distribution of fluorescence effects further indicates that this is material fluorescence rather than machine induced fluorescence.

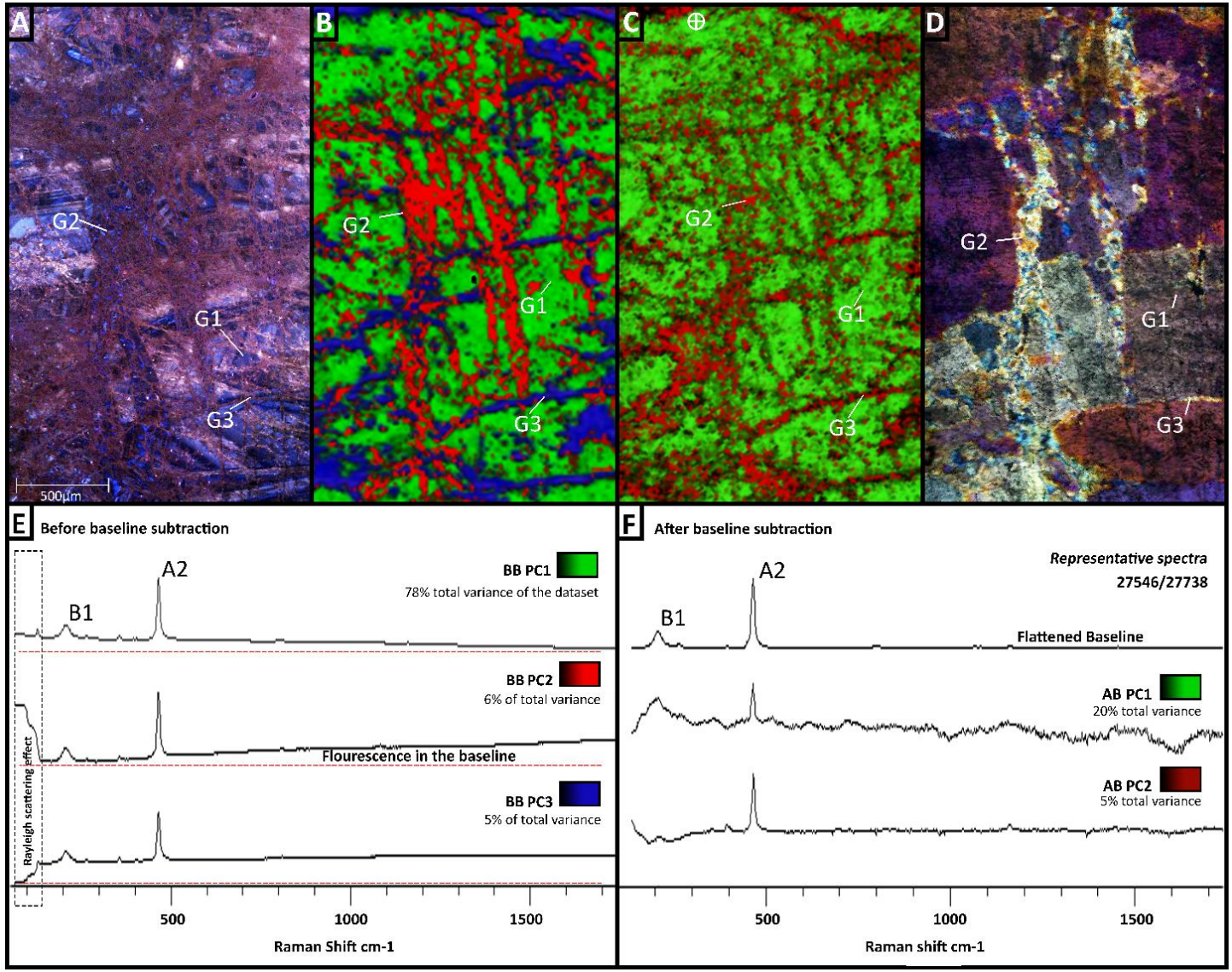

Fig. 31. *Summarised results from the en-echelon fracture zone in investigation site one. (A) CL image with G1 in bottle blue and G2/G3. (B) Non-baseline subtracted RSA Map with G1 (PC1) in green, G2 (PC2) in red, and G3 (PC3) in blue, dark/shaded areas are not clearly associated with any PCA spectra (C) Baseline subtracted RSA map where G1 (PC1) is green and G2 is Red. (D) Petrographic cross polarised image of same area. (E) Principal component analysis (PCA) results from non-baseline subtracted spectra with a red, flat baseline to highlight the effect of fluorescence in the baseline. (F) Baseline subtracted representative spectra and PC1 and PC2 spectra. Note how these spectra do not contain the laser line Rayleigh scattered peaks at c. 150 cm^{-1}. See Table 9 for Raman data*

Principal component analysis of Raman spectra from investigation site two after baseline subtraction identifies three spectra of importance which represent 58% of the total variance in the data set is considered representative of the majority of the data set. Considering the size of this data set, the remaining 42% of variance is likely comprised of small variations in peak characteristics created by noise. Prior to applying the baseline subtraction, fluorescence in the dataset accounted for the majority of variance (BB PC1, BB PC2 and BB, PC3 Fig. 32G). Consequently, more subtle variance in the data set, (like noise or real spectral variance), occupied a smaller proportion of the total variance of the data set. By removing the fluorescence effect, background noise and other influencing factors are better represented by these results (AB PC1, AB PC2 and AB, PC3 Fig. 32G). Principal Component Raman maps generated before and after baseline subtraction look similar and are not included in the main text, however a comparison map is available in Appendix D. Like Investigation site 1, at least two distinct generations of vein formation are present. PC1 contains alpha quartz spectra and represents 47% of total variance. PC2 contains a series of peaks associated with epoxy resin (Lafuente *et al.*, 2015) and represents 5% of total data set variance. PC3 represents 2% of total data set variance and contains quartz peaks and importantly G- band carbon at 1575 cm^{-1} with a D_2 shoulder at 1606 cm^{-1} indicating that carbon in this fluid is thermally matured (Beyssac *et al.*, 2002; Muirhead *et al.*, 2019). The association of disordered carbon with quartz in G2/G3 veins is helpful in distinguishing G1 from G2/G3 veins in this site and explains why PCA maps look similar before and after baseline subtraction. Raman spectroscopy can be used to indicate the thermal maturity of carbon (Beyssac *et al.*, 2002; Lünsdorf, 2016; Muirhead *et al.*, 2019) and better indicate the origin of the hydrothermal fluid. However this is beyond the scope of this study and was not conducted. The noisy baseline of PC3 is likely from the impurities like carbon and different REE as indicated by the CL image in G2 veins (Fig. 32A). Peak intensity is greater in PC1 than PC3 indicating that G2 quartz has a lower molecular order or Si-O molecule concentration than G1 quartz (Shapiro *et al.*, 1967; Dolino, 1990).

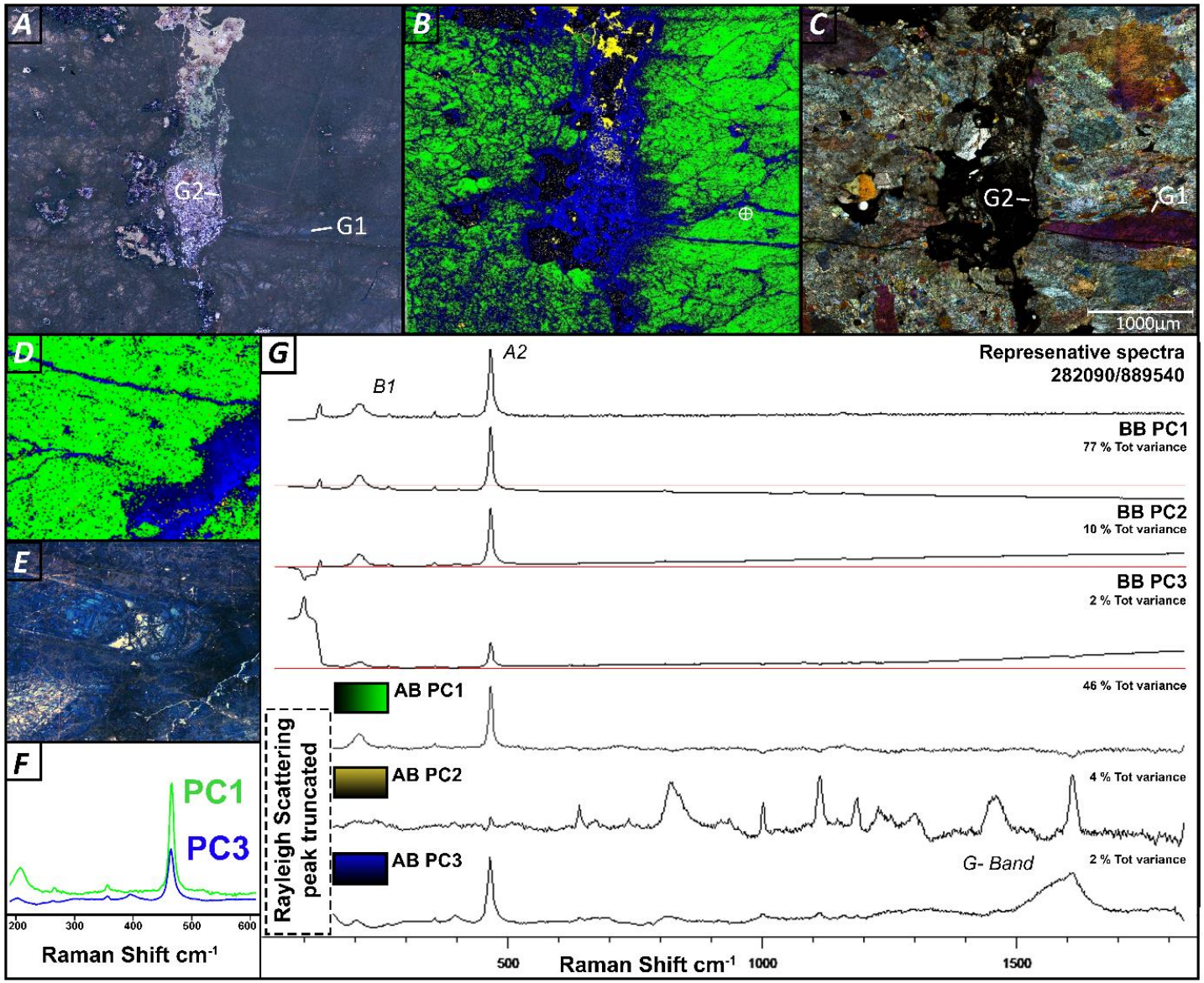

Fig. 32. *Multiple maps of the Cataclastic fracture zone in investigation site 2. (A) Cathode luminescence (CL) image. (B) Close up of Raman PCA map after baseline correction with PC1, PC2 and PC3 coloured as of section G. (C) Cross polarized petrographic image. (D-E) Close up Raman and CL image of large G1 quarts and G2 fracturing. (F) Plot of PC1 and PC3 spectra displaying how PC3 has a lower SiO4 V2 and B1 peak intensity and greater width. (G) Spectral diagram with representative spectra marked by a circled cross in B. Principal component spectra 1-3 before baseline (BB) subtraction and PC1-3 after baseline (AF) subtraction. The total percent of variance which each PC represents is also included. Note how baseline subtraction reveals far more spectral detail (See Table 9 for Raman data).*

5.4. **Discussion**

5.4.1. Investigation Site One

Petrographic, CL and RSA analysis clearly evidence three distinct phases of vein formation as previously observed by Meere (1995a) in the Mountain Mine Lode area. Material fluorescence effects on Raman spectroscopy, as characterised by PCA results (Fig. 31), appear to be the primary differentiating factor between G1, G2 and G3 generations of quartz. After baseline subtraction, only two phases of vein formation are evident from PCA results as G2 and G3 quartz cannot be differentiated. The B1 SiO_4 (220 cm^{-1}) peak is more sensitive to thermally induced alteration than the A2 peak (Shapiro *et al.*, 1967; Schmidt *et al.*, 2000) resulting in the B1 peak increasing in peak intensity with temperature. After baseline correction, the 220 cm^{-1} peak intensity in G2 quartz is lower than in G1 quartz (Fig. 31F). This indicates that as G2 fractured G1 quartz, the pressures and temperatures associated with G2 vein formation disordered G1 veins resulting in an increase in the 220 cm^{-1} peak intensity relative to G2 peak intensity. The A2 (465 cm^{-1}) peak was not as affected by this event. Generally the 465 cm^{-1} peak is more recalcitrant to alteration, unless medium-high grade metamorphic conditions are reached. Medium-high grade metamorphic conditions have not been reported in the Irish Variscides (Lang *et al.*, 2020). It is unlikely that this reduction in 220 cm^{-1} intensity is a product of topographical variation as no correlation between peak variables and topography was recorded. Additionally, this cannot be explained by a reduction in the molecule concentration of Si-O as the B1 and A2 peaks should reduce together in this scenario. After baseline subtraction of Raman spectra, G2 and G3 become less distinct and difficult to differentiate, however G1 remains distinct from G2/G3. These results appear to indicate that material fluorescence and molecule vibrational states can be used to differentiate generations of quartz mineralisation in vein sets. It is important to note that though it is possible to differentiate these quartz generations, it is difficult to interpret the cause for the difference in the Raman spectra from these vein sets.

5.4.2. Investigation Site Two

Investigation site two contains further evidence of at least two generations of vein formation. The cataclastic nature of the fracture zone makes it difficult to visually disentangle more than two phases of quartz formation (Fig. 32). Raman data from this area was greatly affected by material fluorescence which helped to differentiate G1 and G2 quartz, however it was not possible to differentiate G3 from G2 quartz. Interestingly, Raman PCA maps generated before and after baseline subtraction show a similar result revealing the same two generations of quartz, G1 and G2 (see before and after comparison Appendix D-Additional Images file). This is because of the G- band carbon peak present in PC3 helps to differentiate G1 from G2 quartz despite removal of the fluorescence effect. Thermally matured carbon associated with G2 quartz indicates that the hydrothermal fluids which precipitated G2 quartz was possibly sourced from the sedimentary, carbon-rich sequences of the South Munster Basin (MacCarthy, 1987). In addition, Lang *et al.* (2020) demonstrated that hydrothermal fluids which precipitated G2 quartz contained a 28.5 wt% $NaCl_{equiv}$, that indicates that these fluids did not originate from a meteoric source and are either from the surrounding bedrock or a deeper lithospheric source. Recent sulphur isotope work (Spinks *et al.*, 2016) of chalcopyrite from the Allihies mining area demonstrate that a biogenic sedimentary source is most likely. The association of carbon peaks with G2 quartz peaks indicates that the fluids may not have been sourced from the same source as G1 quartz. The absence of altered carbon in G2 and G3 spectra from investigation site one indicates that carbon was not homogeneously present throughout the hyperthermal fluids which infilled G2 and G3 veins in site two and likely reflects a more complex, multi-pulse fluid input as indicated by Lang *et al.* (2020). After baseline subtraction, the 465 cm^{-1} peak intensity is greater in PC1 than PC3 indicating that G2 quartz may have a lower molecular order or Si-O molecule concentration than G1 quartz (Shapiro *et al.*, 1967; Dolino, 1990). As alpha quartz is a reconstructive polymorph and G1 quartz is older than G2, it should have a higher degree of crystallinity and there greater 465 cm^{-1} peak intensity (Broekmans, 2004; Lakshtanov *et al.*, 2007). Alternatively, this may be explained by the contrasting crystallisation conditions of G1 and G2 quartz. Generation one formed in a tectonically extensional setting where quartz had more time to mineralise, without stress in an open space resulting in the euhedral and comparatively higher 465 cm^{-1} peak intensity of G1 quartz spectra. Generation two and three quartz mineralised in a

compressional setting with less space. In contrast to G1, Fluid inclusion, petrography, CL and RSA results demonstrate that G2/G3 fluids had a higher salinity, contained carbonaceous materials as well as ore-forming fluids with less time and space to mineralize. Consequently, these conditions resulted in a microcrystalline texture and less ordered SiO_4 lattice structure in comparison to the monocrystalline, euhedral quartz of G1. These contrasting mineralisation environments and fluid compositions likely account for the different amounts of fluorescence in each generation of quartz as well as the difference in peak variables after baseline correction.

5.4.3. Challenges of Working in a Fluorescent Landscape

Further research on the origin of material fluorescence in a vein setting is required to more accurately account for the observed generation specific material-fluorescence effect observed in these results. Using a focus tracking feature was beneficial during Raman mapping as it enabled changes in fluorescence to be mapped without the effects of a change in beam focus or topography to affect the results. The Raman data sets from each investigation site demonstrates the potential benefits of harnessing and interpreting fluorescence in Raman spectra. Without the fluorescence effect, PCA maps would not have clearly distinguished three each generations of quartz mineralisation (Fig. 31B *vs* C), though the exact cause for this fluorescence remains unclear. Further investigating the cause of this material fluorescence may provide a clearer understanding of quartz precipitation. The potential pitfalls of working in a fluorescence landscape are clearly evident as it can create fake peaks, or a series of quasi-regular ripples as a result of the edge filtering used by the Raman system (Mosier-Boss *et al.*, 1995). Unfortunately, fluorescence removal often requires a heavy-handed approach of extensive data manipulation (e.g., baseline correction, truncation, noise filtering, smoothing, ripple deconvolution and extraction) which can alter the Raman scattered peaks introducing user bias and when conducted incorrectly, can create spurious results. Great care should be taken when handling these types of data sets and additional research into the origins of material fluorescence in the Raman spectra of quartz could greatly help in mitigating the potential pitfalls of this method. It is evident that simply removing or avoiding fluorescence when collecting Raman spectra may result in a loss of important information as demonstrated in Fig. 31.

5.5. **Conclusions**

Three distinct phases of vein formation occurred in Late Devonian siliciclastic sediment of the Upper Devonian sequence of the Munster Basin at the mountain mine, Allihies West Cork. These veins appear to have been infilled by at least three phases of mineralization. Fluorescence effects in Raman spectroscopy maps are fundamental to differentiating these generations of vein mineralization (Fig. 31&32). Degraded carbon G-band molecules present in G2/G3 quartz are also effective in differentiating G1 from G2/G3 and provide an insight as to the potential origin of these fluids. Further work is required to de-risk fluorescence effects in Raman spectra however when measured, this effect can provide novel insights to challenging problems. Results from this study show that Raman characterization of material-fluorescence, the state of molecule vibrations and the compositional differences in veins sets are effective in disentangling the chronology of vein formation and the origin of the fluids which mineralized veins. Although this research uses Raman spectroscopy to investigate quartz mineralization from a tectonics perspective, this study can act as a case study for future work in provenance research focused on diagenesis, thermal alteration, mineral discrimination and provenance fingerprinting linking with objectives in Sections 1.4 and 1.2.2 and 1.2.4.

5.6. **References**

Anderson, A. J., Hanchar, J. M., Hodges, K. V., & van Soest, M. C. (2020). Mapping radiation damage zoning in zircon using Raman spectroscopy: Implications for zircon chronology. *Chemical Geology, 538*, 119494. doi:https://doi.org/10.1016/j.chemgeo.2020.119494

Andò, S., & Garzanti, E. (2014). Raman spectroscopy in heavy-mineral studies. *Geological Society, London, Special Publications, 386*(1), 395-412. doi:https://doi.org/10.1144/SP386.2

Bates, J. B. (1972). Raman spectra of α and β cristobalite. *The Journal of Chemical Physics, 57*(9), 4042-4047. doi:https://doi.org/10.1063/1.1678878

Beyssac, O., Goffé, B., Chopin, C., & Rouzaud, J. (2002). Raman spectra of carbonaceous material in metasediments: a new geothermometer. *Journal of metamorphic Geology, 20*(9), 859-871. doi: https://doi.org/10.1046/j.1525-1314.2002.00408.x

Bost, N., Westall, F., Ramboz, C., Foucher, F., Pullan, D., Meunier, A., Petit, S., Fleischer, I., Klingelhöfer, G., & Vago, J. L. (2013). Missions to Mars: characterisation of Mars analogue rocks for the International Space Analogue Rockstore (ISAR). *Planetary and Space Science, 82*, 113-127.

Broekmans, M. A. (2004). Structural properties of quartz and their potential role for ASR. *Materials Characterization, 53*(2-4), 129-140.

Chandrabhas, N., Shashikala, M., Muthu, D., Sood, A., & Rao, C. (1992). Pressure-induced orientational ordering in C60 crystals as revealed by Raman spectroscopy. *Chemical physics letters, 197*(3), 319-323. doi:https://doi.org/10.1016/0009-2614(92)85776-7

Chen, X., Zhu, B., Zhang, A., Zeng, H., Zhang, Q., & Cui, X. (2014). Electronic Raman Scattering On Individual Semiconducting Single Walled Carbon Nanotubes. *Scientific reports, 4*, 5969. doi:https://doi.org/10.1038/srep05969

Cui, X., Wang, Q., Deng, J., Wu, H., & Shu, Q. (2019). Genesis of the Xiaolonghe quartz vein type Sn deposit, SW China: Insights from cathodoluminescence textures and trace elements of quartz, fluid inclusions, and oxygen isotopes. *Ore Geology Reviews, 111*, 102929. doi:https://doi.org/10.1016/j.oregeorev.2019.05.015

Dolino, G. (1990). The α-inc-β transitions of quartz: a century of research on displacive phase transitions. *Phase Transitions: A Multinational Journal, 21*(1), 59-72. doi:https://doi.org/10.1080/01411599008206882

Eilers, P. H., & Kroonenberg, P. M. (2014). Modeling and correction of Raman and Rayleigh scatter in fluorescence landscapes. *Chemometrics and Intelligent Laboratory Systems, 130*, 1-5. doi:https://doi.org/10.1016/j.chemolab.2013.09.002

Etchepare, J., Merian, M., & Smetankine, L. (1974). Vibrational normal modes of SiO2. I. α and β quartz. *The Journal of Chemical Physics, 60*(5), 1873-1876. doi:https://doi.org/10.1063/1.1681287

Ford, M. (1987). Practical application of the sequential balancing technique: an example from the Irish Variscides. *Journal of the Geological Society, London, 144*(6), 885-891. doi:https://doi.org/10.1144/gsjgs.144.6.0885

Frezzotti, M. L., Tecce, F., & Casagli, A. (2012). Raman spectroscopy for fluid inclusion analysis. *Journal of Geochemical Exploration, 112*, 1-20. doi:https://doi.org/10.1016/j.gexplo.2011.09.009

Götze, J., Plötze, M., & Habermann, D. (2001). Origin, spectral characteristics and practical applications of the cathodoluminescence (CL) of quartz–a review. *Mineralogy and Petrology, 71*(3-4), 225-250.

Gout, R., Oelkers, E. H., Schott, J., & Wick, A. (1997). The surface chemistry and structure of acid-leached albite: New insights on the dissolution mechanism of the alkali feldspars. *Geochimica et Cosmochimica Acta, 61*(14), 3013-3018. doi:https://doi.org/10.1016/S0016-7037(97)00122-1

Gupta, S., Katiyar, R., & Bhalla, A. (2000). Temperature dependent Raman scattering study of order-disorder lead zinc niobate. *Integrated Ferroelectrics, 29*(1-2), 75-85. doi:https://doi.org/10.1080/10584580008216676

Kulp, J. L., Volchok, H. L., & Holland, H. (1952). Age from metamict minerals. *American Mineralogist: Journal of Earth and Planetary Materials, 37*(9-10), 709-718.

Lafuente, B., Downs, R., Yang, H., & Stone, N. (2015). The power of databases: the RRUFF project. In T. Armbruster & R. Danisi (Eds.), *Highlights in mineralogical crystallography* (Vol. 1, pp. 30). De Gruyter, Berlin, Germany 1.

Lakowicz, J. R. (2013). *Principles of fluorescence spectroscopy*: Springer science & business media.

Lakshtanov, D. L., Sinogeikin, S. V., & Bass, J. D. (2007). High-temperature phase transitions and elasticity of silica polymorphs. *Physics and Chemistry of Minerals, 34*(1), 11-22.

Landtwing, M. R., Pettke, T., Halter, W. E., Heinrich, C. A., Redmond, P. B., Einaudi, M. T., & Kunze, K. (2005). Copper deposition during quartz dissolution by cooling magmatic–hydrothermal fluids: the Bingham porphyry. *Earth and Planetary Science Letters, 235*(1-2), 229-243.

Lang, J., Meere, P. A., Unitt, R. P., Johnson, S. C., Solferino, G., Torremans, K., Selby, D., & Kyne, R. (2020). The vein-hosted copper deposits of the Allihies mining area, SW Ireland; a new structural and chronological evaluation. *Journal of the Geological Society, London*. doi:https://doi.org/10.1144/jgs2019-154

Lee, J., Gilmore, I., & Seah, M. (2008). Quantification and methodology issues in multivariate analysis of ToF-SIMS data for mixed organic systems. *Surface and Interface Analysis, 40*(1), 1-14. doi:https://doi.org/10.1002/sia.2713

Luna, A. (2017). *Raman Spectroscopy, Soil Analysis Applications*. Elsevier Ltd.

Lünsdorf, N. K. (2016). Raman spectroscopy of dispersed vitrinite—Methodical aspects and correlation with reflectance. *International Journal of Coal Geology, 153*, 75-86. doi:https://doi.org/10.1016/j.coal.2015.11.010

MacCarthy, I. (1990). Alluvial sedimentation patterns in the Munster Basin, Ireland. *Sedimentology, 37*(4), 685-712. doi:https://doi.org/10.1111/j.1365-3091.1990.tb00629.x

MacCarthy, I. A. (1987). Transgressive facies in the South Munster Basin, Ireland. *Sedimentology, 34*(3), 389-422. doi:https://doi.org/10.1111/j.1365-3091.1987.tb00577.x

Meere, P. A. (1995a). High and low density fluids in a quartz vein from the Irish Variscides. *Journal of Structural Geology, 17*(3), 435-446. doi:https://doi.org/10.1016/0191-8141(94)00066-9

Meere, P. A. (1995b). The structural evolution of the western Irish Variscides: an example of obstacle tectonics? *Tectonophysics, 246*(1-3), 97-112. doi:https://doi.org/10.1016/0040-1951(94)00267-D

Mernagh, T. P., & Liu, L.-g. (1991). Raman spectra from the Al2SiO5 polymorphs at high pressures and room temperature. *Physics and Chemistry of Minerals, 18*(2), 126-130. doi:https://doi.org/10.1007/BF00216605

Michel, D., y Jorba, M. P., & Collongues, R. (1976). Study by Raman spectroscopy of order-disorder phenomena occurring in some binary oxides with fluorite-related structures. *Journal of Raman Spectroscopy, 5*(2), 163-180. doi:https://doi.org/10.1002/jrs.1250050208

Mosier-Boss, P., Lieberman, S., & Newbery, R. (1995). Fluorescence rejection in Raman spectroscopy by shifted-spectra, edge detection, and FFT filtering techniques. *Applied spectroscopy, 49*(5), 630-638.

Muirhead, D. K., Bond, C. E., Watkins, H., Butler, R. W., Schito, A., Crawford, Z., & Marpino, A. (2019). Raman Spectroscopy: an effective thermal marker in low temperature carbonaceous fold-thrust belts. *Geological Society, London, Special Publications, 490*, SP490-2019-2027. doi:https://doi.org/10.1144/SP490-2019-27

Nachon, M., Clegg, S., Mangold, N., Schröder, S., Kah, L., Dromart, G., Ollila, A., Johnson, J., Oehler, D., & Bridges, J. (2014). Calcium sulfate veins characterized by ChemCam/Curiosity at Gale crater, Mars. *Journal of Geophysical Research: Planets, 119*(9), 1991-2016. doi:https://doi.org/10.1002/2013JE004588

Nasdala, L., Irmer, G., & Wolf, D. (1995). The degree of metamictization in zircons: a Raman spectroscopic study. *European Journal of Mineralogy-Ohne Beihefte, 7*(3), 471-478. doi:https://doi.org/10.1127/ejm/7/3/0471

Nasdala, L., Pidgeon, R., Wolf, D., & Irmer, G. (1998). Metamictization and U-Pb isotopic discordance in single zircons: a combined Raman microprobe and SHRIMP ion probe study. *Mineralogy and Petrology, 62*(1-2), 1-27. doi:https://doi.org/10.1007/BF01173760

Parnell, J., McMahon, S., Blamey, N. J., Hutchinson, I. B., Harris, L. V., Ingley, R., Edwards, H. G., Lynch, E., & Feely, M. (2014). Detection of reduced carbon in a basalt analogue for martian nakhlite: a signpost to habitat on Mars. *International Journal of Astrobiology, 13*(2), 124-131.

Passchier, C. W., & Trouw, R. A. (2005). *Microtectonics* (2 ed.): Springer Science & Business Media.

Pasteris, J. D., & Wopenka, B. (1991). Raman spectra of graphite as indicators of degree of metamorphism. *The Canadian Mineralogist, 29*(1), 1-9.

Raman, C. V. (1928). A change of wave-length in light scattering. *Nature, 121*(3051), 619. doi:https://doi.org/10.1038/121619b0

Randle, V., & Engler, O. (2014). *Introduction to texture analysis: macrotexture, microtexture and orientation mapping*: CRC press.

Reilly, T. (1986). A review of vein mineralization in SW County Cork, Ireland. In C. J. Andrew, R. W. A. Crowe, S. Finlay, W. M. Pennell, & J. F. Pyne (Eds.), *Geology and genesis of mineral deposits in Ireland* (pp. 513-544). Irish Association Economic Geologists.

Rull, F., Maurice, S., Hutchinson, I., Moral, A., Perez, C., Diaz, C., Colombo, M., Belenguer, T., Lopez-Reyes, G., & Sansano, A. (2017). The Raman laser spectrometer for the ExoMars rover mission to Mars. *Astrobiology, 17*(6-7), 627-654. doi:https://doi.org/10.1089/ast.2016.1567

Rusk, B. G., Reed, M. H., Dilles, J. H., & Kent, A. J. (2006). Intensity of quartz cathodoluminescence and trace-element content in quartz from the porphyry copper deposit at Butte, Montana. *American Mineralogist, 91*(8-9), 1300-1312. doi:https://doi.org/10.2138/am.2006.1984

Sanderson, D. J. (1984). Structural variation across the northern margin of the Variscides in NW Europe. *Geological Society, London, Special Publications, 14*(1), 149-165. doi:https://doi.org/10.1144/GSL.SP.1984.014.01.15

Schmidt, C., & Ziemann, M. A. (2000). In-situ Raman spectroscopy of quartz: A pressure sensor for hydrothermal diamond-anvil cell experiments at elevated temperatures. *American Mineralogist, 85*(11-12), 1725-1734. doi:https://doi.org/10.2138/am-2000-11-1216

Shapiro, S. M., O'Shea, D. C., & Cummins, H. Z. (1967). Raman scattering study of the alpha-beta phase transition in quartz. *Physical Review Letters, 19*(7), 361. doi:https://doi.org/10.1103/PhysRevLett.19.361

Shreve, A. P., Cherepy, N. J., & Mathies, R. A. (1992). Effective rejection of fluorescence interference in Raman spectroscopy using a shifted excitation difference technique. *Applied spectroscopy, 46*(4), 707-711.

Smith, E., & Dent, G. (2019). *Modern Raman Spectroscopy: A Practical Approach* (2 ed.): John Wiley & Sons Ltd.

Spinks, S. C., Parnell, J., Bellis, D., & Still, J. (2016). Remobilization and mineralization of selenium–tellurium in metamorphosed red beds: Evidence from the Munster Basin, Ireland. *Ore Geology Reviews, 72*, 114-127. doi:https://doi.org/10.1016/j.oregeorev.2015.07.007

Talebian, M., Talebian, E., & Abdi, A. J. P. (2012). The calculation of active Raman modes of α-quartz crystal via density functional theory based on B3LYP Hamiltonian in 6–311+ G (2d) basis set. *PRamana Journal of Physiscs, 78*(5), 803-810. doi:https://doi.org/10.1007/s12043-012-0287-4

Tong, H., Tan, P., & Xu, N. (2015). From crystals to disordered crystals: A hidden order-disorder transition. *Scientific reports, 5*, 15378. doi:https://doi.org/10.1038/srep15378

Vandenabeele, P., Edwards, H. G., & Moens, L. (2007). A decade of Raman spectroscopy in art and archaeology. *Chemical reviews, 107*(3), 675-686. doi:https://doi.org/10.1021/cr068036i

Xie, L., Ling, X., Fang, Y., Zhang, J., & Liu, Z. (2009). Graphene as a substrate to suppress fluorescence in resonance Raman spectroscopy. *Journal of the American Chemical Society, 131*(29), 9890-9891. doi:https://doi.org/10.1021/ja9037593

Yang, S., & Akkus, O. (2013). *Fluorescence Background Problem in Raman Spectroscopy: Is 1064 nm Excitation an Improvement of 785 nm*. Wasatch Photonics: Report.

Zięba-Palus, J., & Michalska, A. (2014). Photobleaching as a useful technique in reducing of fluorescence in Raman spectra of blue automobile paint samples. *Vibrational Spectroscopy, 74*, 6-12. doi:https://doi.org/10.1016/j.vibspec.2014.06.007

Chapter 6: *Synthesis and Core Findings*

Concluding remarks and findings of this thesis are presented below, sequenced in accordance with the project's aims and objectives as outlined in Section 1.1.

6.1. Mesozoic Evolution of Provenance

Findings from this study have greatly improved our understanding of the provenance of Mesozoic basin infill in the Irish and Celtic Sea basins. This work has demonstrated the first-order control of environmental and tectonic factors on sediment sourcing and routing. Provenance research is challenging and requires a multi-proxy approach to limit analytical bias and to gain an insight into the true provenance of basin infill. In relation to the aims outlined in Section 1.1.4. the following conclusions can be drawn:

6.1.A. infill of the Mesozoic basins of the Irish and Celtic Seas did not primarily derive from the Leinster Massif and Welsh Massif. Sedimentation from these sources occurred primarily during periods of marine regression and tectonic activity;

6.1.B. Due to it's significant Laurentian component, the Munster Basin remains a challenging source to differentiate from other Peri-Laurentian and Laurentian source terrains;

6.1.C. marine transgression and regression cycles exhibited a first-order control on distal versus proximal sediment sourcing;

6.1.D. tectonic activity caused recycling of sediment from the surrounding basin margins and greatly influenced inter-basin connectivity throughout the Mesozoic.

The following sections synthesise the temporal evolution of Mesozoic sedimentary provenance in the Irish and Celtic Sea basins.

6.1.1. Early Triassic Provenance

During the deposition of the Lower Triassic Sherwood Sandstone Group, a multi-proxy approach (detrital U-Pb zircon, Ar-Ar white mica, U-Pb apatite geochronology; and trace element analysis) indicates that sediment drained from the Iberian Massif into the Fastnet

Basin, NCSB and SGCB (see Section 3.5.1). This occurred because of long-distance fluvial transportation during a regressive marine period. These findings are significant as they correlate well with other regional studies of the central English Basins and the Wessex Basin demonstrating a broader South-North sediment routing during the Early Triassic. It is also significant as this is the only time within the Mesozoic history of these Basins that the Iberian Massif is shown to be the primary source region. The study shows what can be achieved using such a small amount of sample material and demonstrates the power modern QPA methodologies.

6.1.2. Jurassic Provenance

Lower Jurassic, Lias Group samples from the Fastnet Basin, NCSB and SGCB all indicate a provenance switch from Peri-Gondwanan (400-750 Ma) dominated U-Pb zircon of the Iberian Massif, to a Laurentian (0.9-2.9 Ga) dominated population. This Laurentian population likely drained from the Southern Upland Terrane into the SGCB, while the NCSB appears to have received input from the Laurentian dominated Munster Basin. The Fastnet Basin contains a dominant c. 1.7 Ga U-Pb zircon population which indicates a more distal Laurentian source lacking any Peri-Gondwanan input. Such a source is possibly the Dalradian Supergroup of western Ireland, or the more distal southern Greenland (See section 3.5.2.). Furthermore, it is evident that sediment in the NCSB did not principally derive from the Leinster Massif as proposed by Petrie *et al.* (1989) and Kessler *et al.* (1995).

Throughout the Middle Jurassic, the influence of transgressive conditions on sediment routing appears to have continued as Laurentian dominated U-Pb zircon populations are found in the Eagle Group of the Goban Spur (GS1) and SGCB (SG5). This further emphasises the influence of marine conditions, which facilitated the transport of distally sourced sediments from the north (Southern Uplands and Scottish Massif) into the SGCB and western Laurentian sources into the Goban Spur Basin (See Section 2.6.1.).

A tectonically induced provenance switch is observed by the end of the Middle Jurassic and beginning of the Late Jurassic because of Cimmerian tectonism which exhumed the Fastnet Basin and surrounding marginal areas (See Section 2.6.2.). As a result, samples taken from the

Hook Group of the NCSB record mixed Peri-Gondwanan U-Pb populations likely from the Leinster Massif (Waldron *et al.*, 2014) and Welsh Massif (Waldron *et al.*, 2011). The Laurentian component in these samples is sourced from the Munster Basin and the reworked Eagle and Lias Group successions of the Fastnet Basin. Previous interpretations of Late Jurassic sediment sourcing in the NCSB had hypothesised recycling from marginal basin areas into the Celtic Sea (Caston, 1995). Findings from this study support such hypothesis. HMA results from SGCB indicate a provenance switch between the Middle Jurassic and Late Jurassic signifying more localised sourcing from the Welsh Massif. These results also indicate that the NCSB and SGCB were disconnected during the Late Jurassic.

6.1.3. Cretaceous Provenance

The Purbeck and Wealden Group successions of the Irish and Celtic Sea basins record a provenance switch induced by a local marine regression. During the Late Jurassic, mixed Laurentian and Peri-Gondwanan detrital U-Pb zircon populations were replaced by dominant Peri-Gondwanan populations, deposited by local fluvial mechanisms (See Section 2.6.3.). Findings of this study support the existing hypothesis of Cretaceous sediment routing via fluvial drainage from the Welsh and Irish Massifs (Robinson *et al.*, 1981; Ainsworth *et al.*, 1985).

Peri-Gondwanan detrital U-Pb zircon populations of the Wealden Group were replaced by dominant Grenville (c. 1.0 Ga) populations in the marginal-marine to marine sequences of the Late Cretaceous Selbourne and Chalk Groups in the NCSB and SGCB. This was largely driven by a global marine transgression which enabled more distal sediment sourcing from Dalradian Supergroup of western Ireland likely mixed with input form the Munster Basin. Unimodal U-Pb apatite populations (c. 95 Ma) within these samples indicate that volcanic detritus from the actively rifting Atlantic margin was transported by pyroclastic ash clouds (see Section 2.6.4.).

6.1.4. Concluding Remarks and Future Work in Provenance Research

Chapters 2 and 3 provide unique examples of the influence that environmental and tectonic controls can have on sediment erosion, transport and preservation on sedimentary provenance(Fig. 23). Locally, this study provides insights to the provenance of Mesozoic successions in other comparative basins. On a broader scale, it acts a reference point for basins of the North Sea, and basins offshore of Spain and Portugal's west coast.

A key limiting factor for this study was the scarcity of relevant sample materials. An increased availability of sample material would improve heavy mineral studies, apatite and zircon geochronology and trace element analysis. This in turn may provide a more detailed characterisation of the evolution of sedimentary provenance in the NCSB and SGCB. This study was successful in characterising Mesozoic scale developments in sedimentary provenance but may have overlooked more nuanced provenance changes which could be recognised by detailed investigation of specific intervals. Further detrital zircon or heavy mineral research on Middle-Upper Triassic successions could help in distinguishing the inception of the Triassic-Jurassic provenance switch. K-feldspar Pb-isotope fingerprinting could be very effective in definitively identifying the source of Triassic sediments which appear to have been sourced from the Iberian Massif. Research into the heavy mineral assemblages of the of the Irish Massif would also greatly aid in differentiating the contribution from Irish and British Peri-Gondwanan domains into offshore sedimentary basins. To date, there are no provenance focused heavy mineral studies of onshore Ireland. Findings from this work have further highlighted the importance of using a multi-proxy approach to provenance investigations.

6.2. Part 2: Developments in Raman Spectroscopy methodologies and applications

6.2.1. Raman Spectroscopy Software – Automated Peak Analysis and Rasterisation Application "Ramaster"

Ramaster offers a new solution to batched peak analysis and rasterization of Raman datasets. The software has a demonstrated application in the processing of Raman maps of zircon and could be developed to further distinguish detrital zircon populations as demonstrated by Resentini *et al.* (2020). Great care should be taken during the Raman mapping process as many factors can influence the quality of the results (e.g., fluorescence, topography, material coatings, Raman system configuration). As demonstrated through the analysis and rasterization of Raman data collected from the 40-million-year-old anuran dermal tissue, Ramaster has potential application across broader fields of earth science research. Importantly, Raman spectroscopy is a powerful tool for characterising sample composition as well as molecular state. Ramaster offers a simple and accessible means of processing and imaging mapped Raman datasets.

6.2.A. Ramaster significantly simplifies the processing of Raman datasets processing hundreds of individual datasets in minutes;

6.2.B. Remaster automates data processing and does not require user input after analysis initiation greatly reducing the amount of time it takes to analyze and rasterize data;

6.2.C. Ramaster has demonstrated application in both provenance, geochronology and paleontology fields and potential application in any field of geoscience working with Raman active mineral phases;

6.2.D. The software will be made freely available for use improving the accessibility of Raman processing software.

Future work in this field has potential in petrographic studies, alteration and weathering studies as well as tectonic studies. This tool offers an accessible, accurate and time efficient solution to data processing of multiple spectral datasets and should not be restricted to use

within a tectonics context. In the future, this software may be opened up to community based development help in the development of PCA analysis, spectral truncation, smoothing and noise reduction features to improve the functionality of Ramaster. One significant limitation of the software is the discretization effect calculating FWHM and PF values as these are important factors in peak variation studies. This is also problematic as PI is the most susceptible to alteration by factors outside of the samples composition including, sample topography, beam focus & power as well as machine calibration. Improving the accuracy of the calculated FWHM and PF is primal focus for future development of the software. Other additional features for development include a spectrum viewer and a rasterization map viewer to enable the user to see each spectrum analysed as well as the produced .ascii map without opening up a GIS software.

6.2.2. Raman Spectroscopy of Vein-hosted Alpha Quartz

Findings from this work contribute a novel solution to investigating both mineral growth and the tectonic drivers that cause vein formation. Further, this opens up the potential for investigating mineral crystalisation/growth of any Raman active mineral phase. This study demonstrates the benefit of harnessing material fluorescence in Raman spectra even though fluorescence is typically seen as an unwelcome artifact in such analyses. Findings from this investigation into the vibrational state of alpha quartz SiO_4 molecules demonstrate that:

1.2.E. multiple generations of alpha quartz mineralisation in a vein can be differentiated by characterising spectra from each generation and using a multivariate statistical approach;

1.2.F. material fluorescence can also be used to differentiate generations of quartz growth like CL imaging;

1.2.G. Raman analysis offers insights to the origin of the fluids which precipitated each generation of quartz.

Future research into the cause and effect of fluorescence in the Raman spectra of geological materials could offer new insights into the formation of minerals and fractures. More work is required to clearly define the cause of peak variation in different generations of quartz.

Although this study demonstrates that it is possible to use Raman analysis to differentiate each generation of quartz, it falls short of explaining why these generations can be differentiated. Pressure and temperature experiments with quartz may help to characterise the influence of tectonic or igneous events on quartz lattice structure. Alternatively, the cause of such generational differences may lie in the origin or chemistry of the fluids themselves.

More broadly, using a PCA approach vs a single peak analysis approach to discriminating mineral phases is an important choice and depends largely on the research question. Specrtral PCA and single Peak analysis (as demonstrated in Chapter 4) are effective, however combining these two into a single freely available software package could be very beneficial. The most significant challenge in undertaking this work was the laborious analysis and processing of samples and data taking months of work. Within QPA research, the two approaches demonstrated here utilizing Raman spectroscopy have excellent potential for development within petrography, thermochronology, geochronology, geobarometry and alteration studies. Raman mapping of in-situ minerals which are diagenetically susceptible to alteration or weathering (e.g. feldspar, apatite, rutile) could prove extremely useful in understanding post-depositional petrology providing insights to well porosity and connectivity, basin development and structure as well as exhumation histories. The two applications of mineral characterization and discrimination demonstrated in this thesis (Chapters 4 and 5) are good examples of how to apply Raman spectroscopy to earth science research. These case studies can be used as a benchmark for future work within the field and offer an avenue for new users of Raman technology to understand the versatility of the technique.

6.3. **References**

Ainsworth, N. R., Horton, N. F., & Penney, R. A. (1985). Lower Cretaceous micropalaeontology of the Fastnet Basin, offshore south-west Ireland. *Marine and Petroleum Geology, 2*(4), 341-349. doi:https://doi.org/10.1016/0264-8172(85)90029-7

Allen, P. (1981). Pursuit of Wealden models. *Journal of the Geological Society, London, 138*(4), 375-405. doi:https://doi.org/10.1144/gsjgs.138.4.0375

Allen, P. A., Bennett, S. D., Cunningham, M. J. M., Carter, A., Gallagher, K., Lazzaretti, E., Galewsky, J., Densmore, A. L., Phillips, W. E. A., Naylor, D., & Hach, C. S. (2002). The post-Variscan thermal and denudational history of Ireland. *Geological Society, London, Special Publications, 196*(1), 371-399. doi:10.1144/gsl.sp.2002.196.01.20

Andersen, T. (2002). Correction of common lead in U–Pb analyses that do not report 204 Pb. *Chemical Geology, 192*(1), 59-79.

Andersen, T. O. M. (2012). Age, Hf isotope and trace element signatures of detrital zircons in the Mesoproterozoic Eriksfjord sandstone, southern Greenland: are detrital zircons reliable guides to sedimentary provenance and timing of deposition? *Geological Magazine, 150*(03), 426-440. doi:https://doi.org/10.1017/S0016756812000623

Anderson, A. J., Hanchar, J. M., Hodges, K. V., & van Soest, M. C. (2020). Mapping radiation damage zoning in zircon using Raman spectroscopy: Implications for zircon chronology. *Chemical Geology, 538*, 119494. doi:https://doi.org/10.1016/j.chemgeo.2020.119494

Anderson, C. J., Struble, A., & Whitmore, J. H. (2017). Abrasion resistance of muscovite in aeolian and subaqueous transport experiments. *Aeolian Research, 24*, 33-37. doi:https://doi.org/10.1016/j.aeolia.2016.11.003

Andò, S. (2020). Gravimetric separation of heavy minerals in sediments and rocks. *Minerals, 10*(3), 273.

Andò, S., & Garzanti, E. (2014). Raman spectroscopy in heavy-mineral studies. *Geological Society, London, Special Publications, 386*(1), 395-412. doi:https://doi.org/10.1144/SP386.2

Anell, I., Thybo, H., & Artemieva, I. (2009). Cenozoic uplift and subsidence in the North Atlantic region: Geological evidence revisited. *Tectonophysics, 474*(1-2), 78-105. doi:https://doi.org/10.1016/j.tecto.2009.04.006

ArcGIS-Pro. (2018). ArcMap 10.6 for Desktop. In.

Augier, R., Choulet, F., Faure, M., & Turrillot, P. (2015). A turning-point in the evolution of the Variscan orogen: the ca. 325 Ma regional partial-melting event of the coastal South Armorican domain (South Brittany and Vendée, France). *Bulletin de la Société géologique de France, 186*(2-3), 63-91. doi:https://doi.org/10.2113/gssgfbull.186.2-3.63

Bassoulet, J.-P., Elmi, S., Poisson, A., Cecca, F., Bellion, Y., Guiraud, R., Baudin, F.,. (1993). Middle Toarcian (184-182 Ma). In J. Dercourt, Ricou, L.E., Vrielynck, B. (Ed.), *Atlas Tethys Paleoenvironmental Maps* (pp. 63-84). Gauthier-Villars, Paris.

Bates, J. B. (1972). Raman spectra of α and β cristobalite. *The Journal of Chemical Physics, 57*(9), 4042-4047. doi:https://doi.org/10.1063/1.1678878

Beyssac, O., Goffé, B., Chopin, C., & Rouzaud, J. (2002). Raman spectra of carbonaceous material in metasediments: a new geothermometer. *Journal of metamorphic Geology, 20*(9), 859-871. doi: https://doi.org/10.1046/j.1525-1314.2002.00408.x

Bost, N., Westall, F., Ramboz, C., Foucher, F., Pullan, D., Meunier, A., Petit, S., Fleischer, I., Klingelhöfer, G., & Vago, J. L. (2013). Missions to Mars: characterisation of Mars analogue rocks for the International Space Analogue Rockstore (ISAR). *Planetary and Space Science, 82*, 113-127.

Briggs, D., Kear, A., Martill, D., & Wilby, P. (1993). Phosphatization of soft-tissue in experiments and fossils. *Journal of the Geological Society, London, 150*(6), 1035-1038. doi:https://doi.org/10.1144/gsjgs.150.6.1035

Brodie, J., & White, N. (1994). Sedimentary basin inversion caused by igneous underplating: Northwest European continental shelf. *Geology, 22*(2), 147-150. doi:https://doi.org/10.1130/0091-7613(1994)022<0147:SBICBI>2.3.CO;2

Broekmans, M. A. (2004). Structural properties of quartz and their potential role for ASR. *Materials Characterization, 53*(2-4), 129-140.

Brück, P., Potter, T. L., & Downie, C. (1974). *The Lower Palaeozoic stratigraphy of the northern part of the Leinster Massif.* Paper presented at the Proceedings of the Royal Irish Academy. Section B: Biological, Geological, and Chemical Science.

Buchan, K., Mertanen, S., Park, R., Pesonen, L., Elming, S.-Å., Abrahamsen, N., & Bylund, G. (2000). Comparing the drift of Laurentia and Baltica in the Proterozoic: the importance of key palaeomagnetic poles. *Tectonophysics, 319*(3), 167-198. doi:https://doi.org/10.1016/S0040-1951(00)00032-9

Burke, E. A. (2001). Raman microspectrometry of fluid inclusions. *Lithos, 55*(1-4), 139-158.

Cabrera, L., Roca, E., Garcés, M., & de Porta, J. (2004). Estratigrafía y evolución tectonosedimentaria oligocena superior-neógena del sector central del margen catalán (Cadena Costero-Catalana). *Geología de España*, 569-572.

Cançado, L., Takai, K., Enoki, T., Endo, M., Kim, Y., Mizusaki, H., Jorio, A., Coelho, L., Magalhaes-Paniago, R., & Pimenta, M. (2006). General equation for the determination of the crystallite size L a of nanographite by Raman spectroscopy. *Applied Physics Letters, 88*(16), 163106. doi:https://doi.org/10.1063/1.2196057

Caracciolo, L. (2020). Sediment generation and sediment routing systems from a quantitative provenance analysis perspective: Review, application and future development. *Earth-Science Reviews*, 103226. doi:https://doi.org/10.1016/j.earscirev.2020.103226

Caracciolo, L., Andò, S., Vermeesch, P., Garzanti, E., McCabe, R., Barbarano, M., Paleari, C., Rittner, M., & Pearce, T. (2019). A multidisciplinary approach for the quantitative provenance analysis of siltstone: Mesozoic Mandawa Basin, southeastern Tanzania. *Geological Society, London, Special Publications, 484*, SP484-2018-2136. doi:https://doi.org/10.1144/SP484-2018-136

Caston, V. (1995). The Helvick oil accumulation, Block 49/9, North Celtic Sea Basin. *Geological Society, London, Special Publications, 93*(1), 209-225. doi:10.1144/gsl.sp.1995.093.01.15

Caston, V., Dearnley, R., Harrison, R., Rundle, C., & Styles, M. (1981). Olivine-dolerite intrusionsin the Fastnet Basin. *Journal of the Geological Society, London, 138*(1), 31-46. doi:https://doi.org/10.1144/gsjgs.138.1.0031

Chadwick, R., & Evans, D. (1995). The timing and direction of Permo-Triassic extension in southern Britain. *Geological Society, London, Special Publications, 91*(1), 161-192. doi:https://doi.org/10.1144/GSL.SP.1995.091.01.09

Chandrabhas, N., Shashikala, M., Muthu, D., Sood, A., & Rao, C. (1992). Pressure-induced orientational ordering in C60 crystals as revealed by Raman spectroscopy. *Chemical physics letters, 197*(3), 319-323. doi:https://doi.org/10.1016/0009-2614(92)85776-7

Chen, X., Zhu, B., Zhang, A., Zeng, H., Zhang, Q., & Cui, X. (2014). Electronic Raman Scattering On Individual Semiconducting Single Walled Carbon Nanotubes. *Scientific reports, 4*, 5969. doi:https://doi.org/10.1038/srep05969

Cherniak, D., & Watson, E. (2001). Pb diffusion in zircon. *Chemical Geology, 172*(1-2), 5-24.

Chew, D., Drost, K., & Petrus, J. A. (2019a). Ultrafast,> 50 Hz LA-ICP-MS Spot Analysis Applied to U–Pb Dating of Zircon and other U-Bearing Minerals. *Geostandards and Geoanalytical Research, 43*(1), 39-60. doi:https://doi.org/10.1111/ggr.12257

Chew, D., O'Sullivan, G., Caracciolo, L., Mark, C., & Tyrrell, S. (2020). Sourcing the sand: Accessory mineral fertility, analytical and other biases in detrital U-Pb provenance analysis. *Earth-Science Reviews*, 103093. doi:https://doi.org/10.1016/j.earscirev.2020.103093

Chew, D., Tyrrell, S., Daly, J. S., Cogné, N., Sun, K., & Badenszki, E. (2019b). *The Basement geology of the Porcupine High - A Key Transatlantic link between the Caledonides and Apalachians.* Paper presented at the GSA Annual Meeting in Phoenix, Arizona, USA-2019.

Chew, D. M., Babechuk, M. G., Cogné, N., Mark, C., O'Sullivan, G. J., Henrichs, I. A., Doepke, D., & McKenna, C. A. (2016). (LA, Q)-ICPMS trace-element analyses of Durango and McClure Mountain apatite and implications for making natural LA-ICPMS mineral standards. *Chemical Geology, 435*, 35-48. doi:https://doi.org/10.1016/j.chemgeo.2016.03.028

Chew, D. M., Daly, J. S., Magna, T., Page, L. M., Kirkland, C. L., Whitehouse, M. J., & Lam, R. (2010). Timing of ophiolite obduction in the Grampian orogen. *Bulletin, 122*(11-12), 1787-1799. doi:https://doi.org/10.1130/B30139.1

Chew, D. M., Petrus, J. A., & Kamber, B. S. (2014a). U–Pb LA–ICPMS dating using accessory mineral standards with variable common Pb. *Chemical Geology, 363*, 185-199. doi:https://doi.org/10.1016/j.chemgeo.2013.11.006

Chew, D. M., Petrus, J. A., Kenny, G. G., & McEvoy, N. (2017). Rapid high-resolution U–Pb LA-Q-ICPMS age mapping of zircon. *Journal of Analytical Atomic Spectrometry, 32*(2), 262-276. doi:https://doi.org/10.1039/C6JA00404K

Chew, D. M., & Strachan, R. A. (2014b). The Laurentian Caledonides of Scotland and Ireland. *Geological Society, London, Special Publications, 390*(1), 45-91. doi:https://doi.org/10.1144/SP390.16

Child, A. M. (1995). Microbial taphonomy of archaeological bone. *Studies in conservation, 40*(1), 19-30. doi:https://doi.org/10.1179/sic.1995.40.1.19

Cogné, N., Chew, D., & Stuart, F. M. (2014). The thermal history of the western Irish onshore. *Journal of the Geological Society, London, 171*(6), 779-792. doi:https://doi.org/10.1144/jgs2014-026

Cogné, N., Doepke, D., Chew, D., Stuart, F. M., & Mark, C. (2016). Measuring plume-related exhumation of the British Isles in Early Cenozoic times. *Earth and Planetary Science Letters, 456*, 1-15. doi:https://doi.org/10.1016/j.epsl.2016.09.053

Collins, A., & Buchan, C. (2004). Provenance and age constraints of the South Stack Group, Anglesey, UK: U–Pb SIMS detrital zircon data. *Journal of the Geological Society, London, 161*(5), 743-746. doi:https://doi.org/10.1144/0016-764904-036

Croker, P., & Shannon, P. (1987). *The evolution and hydrocarbon prospectivity of the Porcupine Basin, offshore Ireland.* Paper presented at the Conference on petroleum geology of North West Europe. 3.

Cui, X., Wang, Q., Deng, J., Wu, H., & Shu, Q. (2019). Genesis of the Xiaolonghe quartz vein type Sn deposit, SW China: Insights from cathodoluminescence textures and trace elements of quartz, fluid inclusions, and oxygen isotopes. *Ore Geology Reviews, 111*, 102929. doi:https://doi.org/10.1016/j.oregeorev.2019.05.015

Culver, S. J., & Rawson, P. F. (2006). *Biotic response to global change: the last 145 million years*: Cambridge University Press.

Dallmeyer, R. D., Franke, W., & Weber, K. (2013). *Pre-Permian geology of central and eastern Europe*: Springer Science & Business Media.

Dallmeyer, R. D., & Garcia, E. M. (2012). *Pre-mesozoic geology of Iberia*: Springer Science & Business Media.

Daly, J. S. (1996). Pre-Caledonian history of the Annagh Gneiss Complex North-Western Ireland, and correlation with Laurentia-Baltica. *Irish Journal of Earth Sciences*, 5-18.

Daly, J. S., & Flowerdew, M. J. (2005). Grampian and late Grenville events recorded by mineral geochronology near a basement–cover contact in north Mayo, Ireland. *Journal of the Geological Society, London, 162*(1), 163-174. doi:https://doi.org/10.1144/0016-764903-150

De La Horra, R., Benito, M. I., LÓPEZ-GÓMEZ, J., Arche, A., Barrenechea, J. F., & Luque, J. (2008). Palaeoenvironmental significance of Late Permian palaeosols in the South-Eastern Iberian Ranges, Spain. *Sedimentology, 55*(6), 1849-1873. doi:https://doi.org/10.1111/j.1365-3091.2008.00969.x

Dickinson, W. R. (1970). Interpreting detrital modes of graywacke and arkose. *Journal of Sedimentary Research, 40*(2), 695-707. doi:https://doi.org/10.1306/74D72018-2B21-11D7-8648000102C1865D

Dolino, G. (1990). The α-inc-β transitions of quartz: a century of research on displacive phase transitions. *Phase Transitions: A Multinational Journal, 21*(1), 59-72. doi:https://doi.org/10.1080/01411599008206882

Ducassou, C., Poujol, M., Hallot, E., Bruguier, O., & Ballevre, M. (2011). Petrology and geochronology of the high-K calc-alkaline Mésanger magmatism (Armorican massif, France): a ca. 320 Ma old volcano-plutonic association. *Bulletin de la Société géologique de France, 182*(6), 467-477. doi:https://doi.org/10.2113/gssgfbull.182.6.467

Dunford, G., Dancer, P., & Long, K. (2001). Hydrocarbon potential of the Kish Bank Basin: integration within a regional model for the Greater Irish Sea Basin. *Geological Society, London, Special Publications, 188*(1), 135-154. doi:https://doi.org/10.1144/GSL.SP.2001.188.01.07

Dyment, J., & Bano, M. (1991). Deep crustal features of the Celtic Sea from complementary processing on the SWAT data. *Geophysical Journal International, 105*(1), 71-83. doi:10.1111/j.1365-246X.1991.tb03445.x

Eilers, P. H., & Kroonenberg, P. M. (2014). Modeling and correction of Raman and Rayleigh scatter in fluorescence landscapes. *Chemometrics and Intelligent Laboratory Systems, 130*, 1-5. doi:https://doi.org/10.1016/j.chemolab.2013.09.002

EMODnet, B. C. (2018). EMODnet Digital Bathymetry (DTM 2018) (Publication no. https://doi.org/10.12770/18ff0d48-b203-4a65-94a9-5fd8b0ec35f6). https://sextant.ifremer.fr/record/18ff0d48-b203-4a65-94a9-5fd8b0ec35f6/

Etchepare, J., Merian, M., & Smetankine, L. (1974). Vibrational normal modes of SiO2. I. α and β quartz. *The Journal of Chemical Physics, 60*(5), 1873-1876. doi:https://doi.org/10.1063/1.1681287

Ewins, N. P., & Shannon, P. M. (1995). Sedimentology and diagenesis of the Jurassic and Cretaceous of the North Celtic Sea and Fastnet Basins. *Geological Society, London, Special Publications, 93*(1), 139-169. doi:https://doi.org/10.1144/GSL.SP.1995.093.01.12

Fabbri, M., Wiemann, J., Manucci, F., & Briggs, D. E. (2019). Three-dimensional soft tissue preservation revealed in the skin of a non-avian dinosaur. *Palaeontology*. doi:https://doi.org/10.1111/pala.12470

Fairey, B. J. (2017). *Sediment routing and recycling through multiple basins from Palaeozoic to Mesozoic times: a provenance study of the Devonian Old Red Sandstone of southern Ireland and neighbouring offshore Mesozoic basins.* PhD thesis, University College Cork,

Fairey, B. J., Kerrison, A., Meere, P. A., Mulchrone, K. F., Hofmann, M., Gärtner, A., Sonntag, B.-L., Linnemann, U., Kuiper, K. F., & Ennis, M. (2018). The provenance of the Devonian Old Red Sandstone of the Dingle Peninsula, SW Ireland; the earliest record of Laurentian and peri-Gondwanan sediment mixing in Ireland. *Journal of the Geological Society, London*, jgs2017-2099. doi:https://doi.org/10.1144/jgs2017-099 |

Fernández-Suárez, J., Gutiérrez-Alonso, G., Jenner, G., & Tubrett, M. (2000). New ideas on the Proterozoic-Early Palaeozoic evolution of NW Iberia: insights from U–Pb detrital zircon ages. *Precambrian Research, 102*(3-4), 185-206. doi:https://doi.org/10.1016/S0301-9268(00)00065-6

Fernández-Suárez, J., Gutiérrez-Alonso, G., Pastor-Galán, D., Hofmann, M., Murphy, J., & Linnemann, U. (2014). The Ediacaran–Early Cambrian detrital zircon record of NW Iberia: possible sources and paleogeographic constraints. *International Journal of Earth Sciences, 103*(5), 1335-1357. doi:https://doi.org/10.1007/s00531-013-0923-3

Ferreira, J., dos Santos, T. B., Pereira, I., & Mata, J. (2019). Tectonically assisted exhumation and cooling of Variscan granites in an anatectic complex of the Central Iberian Zone, Portugal: constraints from LA-ICP-MS zircon and apatite U–Pb ages. *International Journal of Earth Sciences, 108*(7), 2153-2175. doi:https://doi.org/10.1007/s00531-019-01755-1

Filhol, H. (1877). *Recherches sur les phosphorites du Quercy: étude des fossiles qu'on y rencontre et spécialement des mammifères* (Vol. 2): G. Masson.

Fitzpatrick, R. W., & Raven, M. D. (2019). The forensic comparison of trace amounts of soil on a pyjama top with hypersulfidic subaqueous soil from a river as evidence in a homicide cold case. *Geological Society, London, Special Publications, 492*, SP492-2019-2059.

Ford, M. (1987). Practical application of the sequential balancing technique: an example from the Irish Variscides. *Journal of the Geological Society, London, 144*(6), 885-891. doi:https://doi.org/10.1144/gsjgs.144.6.0885

France, C. A., Thomas, D. B., Doney, C. R., & Madden, O. (2014). FT-Raman spectroscopy as a method for screening collagen diagenesis in bone. *Journal of archaeological Science, 42*, 346-355. doi:https://doi.org/10.1016/j.jas.2013.11.020

Franklin, J., Tyrrell, S., Morton, A., Frei, D., & Mark, C. (2019). Triassic sand supply to the Slyne Basin, offshore western Ireland–new insights from a multi-proxy provenance approach. *Journal of the Geological Society, 176*(6), 1120-1135. doi:https://doi.org/10.1144/jgs2019-085

Franklin, J., Tyrrell, S., O'Sullivan, G., Nauton-Fourteu, M., & Raine, R. (2020). Provenance of Triassic sandstones in the basins of Northern Ireland—Implications for NW European Triassic palaeodrainage. *Geological Journal*. doi:https://doi.org/10.1002/gj.3697

Frezzotti, M. L., Tecce, F., & Casagli, A. (2012). Raman spectroscopy for fluid inclusion analysis. *Journal of Geochemical Exploration, 112*, 1-20. doi:https://doi.org/10.1016/j.gexplo.2011.09.009

Fritschle, T., Daly, J. S., Whitehouse, M. J., McConnell, B., & Buhre, S. (2018). Multiple intrusive phases in the Leinster Batholith, Ireland: geochronology, isotope geochemistry and constraints on the deformation history. *Journal of the Geological Society, London, 175*(2), 229-246. doi:https://doi.org/10.1144/jgs2017-034

Fullea, J., Muller, M., Jones, A., & Afonso, J. (2014). The lithosphere–asthenosphere system beneath Ireland from integrated geophysical–petrological modeling II: 3D thermal and compositional structure. *Lithos, 189*, 49-64. doi:https://doi.org/10.1016/j.lithos.2013.09.014

García-Mondéjar, J. (1996). Plate reconstruction of the Bay of Biscay. *Geology, 24*(7), 635-638. doi:https://doi.org/10.1130/0091-7613(1996)024<0635:PROTBO>2.3.CO;2

Garzanti, E. (2017). The Maturity Myth In Sedimentology and Provenance AnalysiS. *Journal of Sedimentary Research, 87*(4), 353-365. doi:https://doi.org/10.2110/jsr.2017.17

Garzanti, E., Andò, S., & Vezzoli, G. (2009). Grain-size dependence of sediment composition and environmental bias in provenance studies. *Earth and Planetary Science Letters, 277*(3), 422-432. doi:https://doi.org/10.1016/j.epsl.2008.11.007

Garzanti, E., Vermeesch, P., Andò, S., Lustrino, M., Padoan, M., & Vezzoli, G. (2014). Ultra-long distance littoral transport of Orange sand and provenance of the Skeleton Coast Erg (Namibia). *Marine Geology, 357*, 25-36. doi:https://doi.org/10.1016/j.margeo.2014.07.005

Gehrels, G., Valencia, V., & Pullen, A. (2006). Detrital zircon geochronology by laser-ablation multicollector ICPMS at the Arizona LaserChron Center. *The Paleontological Society Papers, 12*, 67-76. doi:DOI: https://doi.org/10.1017/S1089332600001352

Gilligan, A., Bastow, I. D., & Darbyshire, F. A. (2016). Seismological structure of the 1.8 Ga Trans-Hudson Orogen of North America. *Geochemistry, Geophysics, Geosystems, 17*(6), 2421-2433. doi:https://doi.org/10.1002/2016GC006419

Götze, J., Plötze, M., & Habermann, D. (2001). Origin, spectral characteristics and practical applications of the cathodoluminescence (CL) of quartz–a review. *Mineralogy and Petrology, 71*(3-4), 225-250.

Gout, R., Oelkers, E. H., Schott, J., & Wick, A. (1997). The surface chemistry and structure of acid-leached albite: New insights on the dissolution mechanism of the alkali feldspars. *Geochimica et Cosmochimica Acta, 61*(14), 3013-3018. doi:https://doi.org/10.1016/S0016-7037(97)00122-1

Gower, C. F. (1996). The evolution of the Grenville Province in eastern Labrador, Canada. *Geological Society, London, Special Publications, 112*(1), 197-218. doi:https://doi.org/10.1144/GSL.SP.1996.112.01.11

Grobe, R., Alvarez-Marrón, J., Glasmacher, U., & Stuart, F. (2014). Mesozoic exhumation history and palaeolandscape of the Iberian Massif in eastern Galicia from apatite fission-track and (U+ Th)/He data. *International Journal of Earth Sciences, 103*(2), 539-561. doi:https://doi.org/10.1007/s00531-013-0976-3

Guerrot, C., & Peucat, J. (1990). U-Pb geochronology of the Upper Proterozoic Cadomian orogeny in the northern Armorican Massif, France. *Geological Society, London, Special Publications, 51*(1), 13-26. doi:https://doi.org/10.1144/GSL.SP.1990.051.01.02

Gupta, S., Katiyar, R., & Bhalla, A. (2000). Temperature dependent Raman scattering study of order-disorder lead zinc niobate. *Integrated Ferroelectrics, 29*(1-2), 75-85. doi:https://doi.org/10.1080/10584580008216676

Gutiérrez-Alonso, G., Fernández-Suárez, J., Collins, A. S., Abad, I., & Nieto, F. (2005). Amazonian Mesoproterozoic basement in the core of the Ibero-Armorican Arc: 40Ar/39Ar detrital mica ages complement the zircon's tale. *Geology, 33*(8), 637-640. doi:https://doi.org/10.1130/G21485AR.1

Hames, W. E., & Cheney, J. (1997). On the loss of 40Ar∗ from muscovite during polymetamorphism. *Geochimica et Cosmochimica Acta, 61*(18), 3863-3872. doi:https://doi.org/10.1016/S0016-7037(97)00207-X

Hancock, J. M. (1989). Sea-level changes in the British region during the Late Cretaceous. *Proceedings of the Geologists' Association, 100*(4), 565-IN561.

Haq, B. U. (2014). Cretaceous eustasy revisited. *Global and Planetary change, 113*, 44-58. doi:https://doi.org/10.1016/j.gloplacha.2013.12.007

Harrison, T. M., Célérier, J., Aikman, A. B., Hermann, J., & Heizler, M. T. (2009). Diffusion of 40Ar in muscovite. *Geochimica et Cosmochimica Acta, 73*(4), 1039-1051. doi:https://doi.org/10.1016/j.gca.2008.09.038

Hartley, A. (1995). Sedimentology of the Cretaceous Greensand, Quadrants 48 and 49, North Celtic Sea Basin: a progradational shoreface deposit. *Geological Society, London, Special Publications, 93*(1), 245-257. doi:https://doi.org/10.1144/GSL.SP.1995.093.01.17

Henderson, B. J., Collins, W. J., Murphy, J. B., Gutierrez-Alonso, G., & Hand, M. (2016). Gondwanan basement terranes of the Variscan–Appalachian orogen: Baltican, Saharan and West African hafnium isotopic fingerprints in Avalonia, Iberia and the Armorican Terranes. *Tectonophysics, 681*, 278-304. doi:https://doi.org/10.1016/j.tecto.2015.11.020

Henrique-Pinto, R., Guilmette, C., Bilodeau, C., & McNicoll, V. (2017). Evidence for transition from a continental forearc to a collisional pro-foreland basin in the eastern Trans-Hudson Orogen: Detrital zircon provenance analysis in the Labrador Trough, Canada. *Precambrian Research, 296*, 181-194. doi:https://doi.org/10.1016/j.precamres.2017.04.035

Henry, D. G., Jarvis, I., Gillmore, G., & Stephenson, M. (2019). Raman spectroscopy as a tool to determine the thermal maturity of organic matter: Application to sedimentary, metamorphic and structural geology. *Earth-Science Reviews, 198*. doi:https://doi.org/10.1016/j.earscirev.2019.102936

Hesselbo, S. P., Ogg, J.G. & Ruhl., M. (2020). The Jurassic Period. In F. M. Gradstein, J. G. Ogg, M. D. Schmitz, & G. M. Ogg (Eds.), *The Geologic Time Scale 2020* (Vol. 2, pp. 955 – 1021): Amsterdam: Elsevier.

Hibbard, J. P., Van Staal, C. R., & Rankin, D. W. (2007). A comparative analysis of pre-Silurian crustal building blocks of the northern and the southern Appalachian orogen. *American Journal of Science, 307*(1), 23-45. doi:https://doi: 10.2475/01.2007.02

Hietpas, J., Samson, S., Moecher, D., & Chakraborty, S. (2011). Enhancing tectonic and provenance information from detrital zircon studies: assessing terrane-scale sampling and grain-scale characterization. *Journal of the Geological Society, London, 168*(2), 309-318. doi:https://doi.org/10.1144/0016-76492009-163

Higgs, K., & Beese, A. (1986). A Jurassic microflora from the Colbond Clay of Cloyne, County Cork. *Irish Journal of Earth Sciences*, 99-109.

Hoffman, P. F. (1990). Subdivision of the Churchill Province and the extent of the Trans-Hudson Orogen. In L. J.F & S. M.R. (Eds.), *The Early Proterozoic Trans-Hudson Orogen of North America* (pp. 15-39). Geological Association of Canada.

Hounslow, M., & Ruffell, A. (2006). Triassic: seasonal rivers, dusty deserts and saline lakes. In *The Geology of England & Wales* (pp. 295-325): Geological Society of London.

ISPSG, I. S. P. S. G. (2019). *The Standard Stratigraphic Nomenclature of Offshore Ireland: An Integrated Lithostratigraphic, Biostratigraphic and Sequence Stratigraphic Framework, Dublin: Irish Petroleum Infrastructure Programme (PIP).* Retrieved from

Jennings, E., Marschall, H., Hawkesworth, C., & Storey, C. (2011). Characterization of magma from inclusions in zircon: Apatite and biotite work well, feldspar less so. *Geology, 39*(9), 863-866. doi:https://doi.org/10.1130/G32037.1

Jones, S. M., White, N., Clarke, B. J., Rowley, E., & Gallagher, K. (2002). Present and past influence of the Iceland Plume on sedimentation. *Geological Society, London, Special Publications, 196*(1), 13-25. doi:https://doi.org/10.1144/GSL.SP.2002.196.01.02

Keeley, M. (1995). New evidence of Permo-Triassic rifting, onshore southern Ireland, and its implications for Variscan structural inheritance. *Geological Society, London, Special Publications, 91*(1), 239-253. doi:https://doi.org/10.1144/GSL.SP.1995.091.01.12

Keenan, S. W., & Engel, A. S. (2017). Early diagenesis and recrystallization of bone. *Geochimica et Cosmochimica Acta, 196*, 209-223. doi:https://doi.org/10.1016/j.gca.2016.09.033

Kessler, L., & Sachs, S. D. (1995). Depositional setting and sequence stratigraphic implications of the Upper Sinemurian (Lower Jurassic) sandstone interval, North Celtic Sea/St George's Channel Basins, offshore Ireland. *Geological Society, London, Special Publications, 93*(1), 171-192. doi:https://doi.org/10.1144/GSL.SP.1995.093.01.13

Kirkland, C., Yakymchuk, C., Szilas, K., Evans, N., Hollis, J., McDonald, B., & Gardiner, N. (2018). Apatite: a U-Pb thermochronometer or geochronometer? *Lithos, 318*, 143-157.

Kirstein, L., Davies, G., & Heeremans, M. (2006). The petrogenesis of Carboniferous–Permian dyke and sill intrusions across northern Europe. *Contributions to Mineralogy and Petrology, 152*(6), 721-742. doi:https://doi.org/10.1007/s00410-006-0129-9

Koglin, N., Frimmel, H. E., Minter, W. L., & Brätz, H. (2010). Trace-element characteristics of different pyrite types in Mesoarchaean to Palaeoproterozoic placer deposits. *Mineralium Deposita, 45*(3), 259-280.

Kuiper, K., Deino, A., & Hilgen, F. (2008). Synchronizing Rock Clocks of Earth History. *Synchronizing rock clocks of Earth history: Science, 320*, 500-504. doi:https://doi:10.1126/science.1154339

Kulp, J. L., Volchok, H. L., & Holland, H. (1952). Age from metamict minerals. *American Mineralogist: Journal of Earth and Planetary Materials, 37*(9-10), 709-718.

Lafuente, B., Downs, R., Yang, H., & Stone, N. (2015). The power of databases: the RRUFF project. In T. Armbruster & R. Danisi (Eds.), *Highlights in mineralogical crystallography* (Vol. 1, pp. 30). De Gruyter, Berlin, Germany 1.

Lakowicz, J. R. (2013). *Principles of fluorescence spectroscopy*: Springer science & business media.

Lakshtanov, D. L., Sinogeikin, S. V., & Bass, J. D. (2007). High-temperature phase transitions and elasticity of silica polymorphs. *Physics and Chemistry of Minerals, 34*(1), 11-22.

Landtwing, M. R., Pettke, T., Halter, W. E., Heinrich, C. A., Redmond, P. B., Einaudi, M. T., & Kunze, K. (2005). Copper deposition during quartz dissolution by cooling magmatic–hydrothermal fluids: the Bingham porphyry. *Earth and Planetary Science Letters, 235*(1-2), 229-243.

Lang, J., Meere, P. A., Unitt, R. P., Johnson, S. C., Solferino, G., Torremans, K., Selby, D., & Kyne, R. (2020). The vein-hosted copper deposits of the Allihies mining area, SW Ireland; a new structural and chronological evaluation. *Journal of the Geological Society, London*. doi:https://doi.org/10.1144/jgs2019-154

Lee, J.-Y., Marti, K., Severinghaus, J. P., Kawamura, K., Yoo, H.-S., Lee, J. B., & Kim, J. S. (2006). A redetermination of the isotopic abundances of atmospheric Ar. *Geochimica et Cosmochimica Acta, 70*(17), 4507-4512. doi:https://doi.org/10.1016/j.gca.2006.06.1563

Lee, J., Gilmore, I., & Seah, M. (2008). Quantification and methodology issues in multivariate analysis of ToF-SIMS data for mixed organic systems. *Surface and Interface Analysis, 40*(1), 1-14. doi:https://doi.org/10.1002/sia.2713

Lenz, C., & Nasdala, L. (2015a). A photoluminescence study of REE3+ emissions in radiation-damaged zircon. *American Mineralogist, 100*(5-6), 1123-1133.

Lenz, C., Nasdala, L., Talla, D., Hauzenberger, C., Seitz, R., & Kolitsch, U. (2015b). Laser-induced REE3+ photoluminescence of selected accessory minerals—An "advantageous artefact" in Raman spectroscopy. *Chemical Geology, 415*, 1-16.

Li, Z.-X., Wartho, J.-A., Occhipinti, S., Zhang, C.-L., Li, X.-H., Wang, J., & Bao, C. (2007). Early history of the eastern Sibao Orogen (South China) during the assembly of Rodinia: new mica 40Ar/39Ar dating and SHRIMP U–Pb detrital zircon provenance constraints. *Precambrian Research, 159*(1-2), 79-94.

Locher, R. (2018). IDPmisc: 'Utilities of Institute of Data Analyses and Process Design Retrieved from https://CRAN.R-project.org/package=IDPmisc

Long, C. B., Max, M. D., & Yardley, B. W. (1983). Compilation Caledonian metamorphic map of Ireland. In P. E. Schenk (Ed.), *Regional Trends in the Geology of the Appalachian-Caledonian-Hercynian-Mauritanide Orogen* (pp. 221-233): Springer.

Ludwig, K. (2012). Isoplot 3.75-4.15 manual. *A Geochronological Toolkit for Microsoft Excel, 4*, 1-70.

Lumholt, S., Rossum, G. v., Conway, M., Manheimer, K., & Lundh, F. (2020). Tkinter — Python interface to Tcl/Tk (Version 24.1). Retrieved from https://docs.python.org/3/library/tkinter.html#module-tkinter

Luna, A. (2017). *Raman Spectroscopy, Soil Analysis Applications*. Elsevier Ltd.

Lünsdorf, N. K. (2016). Raman spectroscopy of dispersed vitrinite—Methodical aspects and correlation with reflectance. *International Journal of Coal Geology, 153*, 75-86. doi:https://doi.org/10.1016/j.coal.2015.11.010

Lünsdorf, N. K., Kalies, J., Ahlers, P., Dunkl, I., & von Eynatten, H. (2019). Semi-Automated Heavy-Mineral Analysis by Raman Spectroscopy. *Minerals, 9*(7), 385. doi:https://doi.org/10.3390/min9070385

MacCarthy, I. (1990). Alluvial sedimentation patterns in the Munster Basin, Ireland. *Sedimentology, 37*(4), 685-712. doi:https://doi.org/10.1111/j.1365-3091.1990.tb00629.x

MacCarthy, I. A. (1987). Transgressive facies in the South Munster Basin, Ireland. *Sedimentology, 34*(3), 389-422. doi:https://doi.org/10.1111/j.1365-3091.1987.tb00577.x

Maddox, S. J., Blow, R., & Hardman, M. (1995). Hydrocarbon prospectivity of the Central Irish Sea Basin with reference to Block 42/12, offshore Ireland. *Geological Society, London, Special Publications, 93*(1), 59-77. doi:https://doi.org/10.1144/GSL.SP.1995.093.01.08

Malusà, M. G., Resentini, A., & Garzanti, E. (2016). Hydraulic sorting and mineral fertility bias in detrital geochronology. *Gondwana Research, 31*, 1-19.

Mange, M. A., & Maurer, H. (1992). *Heavy minerals in colour*: Springer Science & Business Media.

Mange, M. A., & Wright, D. T. (2007). *Heavy minerals in use*: Elsevier.

Max, M., Barber, A., & Martinez, J. (1990). Terrane assemblage of the Leinster Massif, SE Ireland, during the Lower Palaeozoic. *Journal of the Geological Society, London, 147*(6), 1035-1050. doi:https://doi.org/10.1144/gsjgs.147.6.1035

McAteer, C. A., Daly, J. S., Flowerdew, M. J., Connelly, J. N., Housh, T. B., & Whitehouse, M. J. (2010a). Detrital zircon, detrital titanite and igneous clast U–Pb geochronology and basement–cover relationships of the Colonsay Group, SW Scotland: Laurentian provenance and correlation with the Neoproterozoic Dalradian Supergroup. *Precambrian Research, 181*(1-4), 21-42.

McAteer, C. A., Daly, J. S., Flowerdew, M. J., Whitehouse, M. J., & Kirkland, C. L. (2010b). A Laurentian provenance for the Dalradian rocks of north Mayo, Ireland, and evidence for an original basement–cover contact with the underlying Annagh Gneiss Complex. *Journal of the Geological Society, London, 167*(5), 1033-1048. doi:https://doi.org/10.1144/0016-76492009-147

McAteer, C. A., Daly, J. S., Flowerdew, M. J., Whitehouse, M. J., & Monaghan, N. M. (2014). Sedimentary provenance, age and possible correlation of the Iona Group SW Scotland. *Scottish Journal of Geology, 50*(2), 143-158. doi:https://doi.org/10.1144/sjg2013-019

McConnell, B., Rogers, R., & Crowley, Q. (2016). Sediment provenance and tectonics on the Laurentian margin: implications of detrital zircons ages from the Central Belt of the Southern Uplands–Down–Longford Terrane in Co. Monaghan, Ireland. *Scottish Journal of Geology, 52*(1), 11-17. doi:https://doi.org/10.1144/sjg2015-013

McGowan1, G., & Prangnell, J. (2006). The significance of vivianite in archaeological settings. *Geoarchaeology: An International Journal, 21*(1), 93-111. doi:https://doi.org/10.1002/gea.20090
Meere, P. A. (1995a). High and low density fluids in a quartz vein from the Irish Variscides. *Journal of Structural Geology, 17*(3), 435-446. doi:https://doi.org/10.1016/0191-8141(94)00066-9
Meere, P. A. (1995b). The structural evolution of the western Irish Variscides: an example of obstacle tectonics? *Tectonophysics, 246*(1-3), 97-112. doi:https://doi.org/10.1016/0040-1951(94)00267-D
Meere, P. A., & Mulchrone, K. F. (2006). Timing of deformation within Old Red Sandstone lithologies from the Dingle Peninsula, SW Ireland. *Journal of the Geological Society, London, 163*(3), 461-469. doi:https://doi.org/10.1144/0016-764905-099
Menges, F. (2020). Spectragryph-Optical Spectroscopy Software. Retrieved from https://www.effemm2.de/spectragryph/
Mernagh, T. P., & Liu, L.-g. (1991). Raman spectra from the Al2SiO5 polymorphs at high pressures and room temperature. *Physics and Chemistry of Minerals, 18*(2), 126-130. doi:https://doi.org/10.1007/BF00216605
Mezger, K., & Krogstad, E. (1997). Interpretation of discordant U-Pb zircon ages: An evaluation. *Journal of metamorphic Geology, 15*(1), 127-140. doi:https://doi.org/10.1111/j.1525-1314.1997.00008.x
Michel, D., y Jorba, M. P., & Collongues, R. (1976). Study by Raman spectroscopy of order-disorder phenomena occurring in some binary oxides with fluorite-related structures. *Journal of Raman Spectroscopy, 5*(2), 163-180. doi:https://doi.org/10.1002/jrs.1250050208
Miles, A. J., & Woodcock, N. (2018). A combined geochronological approach to investigating long lived granite magmatism, the Shap granite, UK. *Lithos, 304*, 245-257. doi:https://doi.org/10.1016/j.lithos.2018.02.012
Millson, J. (1987). *The Jurassic evolution of the Celtic Sea basins.* Paper presented at the Conference on petroleum geology of North West Europe. 3.
Min, K., Mundil, R., Renne, P. R., & Ludwig, K. R. (2000). A test for systematic errors in 40Ar/39Ar geochronology through comparison with U/Pb analysis of a 1.1-Ga rhyolite. *Geochimica et Cosmochimica Acta, 64*(1), 73-98. doi:https://doi.org/10.1016/S0016-7037(99)00204-5
Monaghan, A., & Pringle, M. (2004). 40Ar/39Ar geochronology of Carboniferous-Permian volcanism in the Midland Valley, Scotland. *Geological Society, London, Special Publications, 223*(1), 219-241. doi:https://doi.org/10.1144/GSL.SP.2004.223.01.10
Monster, M. W. L. (2016). *Multi-method palaeointensity data of the geomagnetic field during the past 500 kyrs from European volcanoes.* UU Dept. of Earth Sciences, Retrieved from https://dspace.library.uu.nl/handle/1874/340862
Morton, A. (1984). Stability of detrital heavy minerals in Tertiary sandstones from the North Sea Basin. *Clay minerals, 19*(3), 287-308.
Morton, A., Hounslow, M. W., & Frei, D. (2013). Heavy-mineral, mineral-chemical and zircon-age constraints on the provenance of Triassic sandstones from the Devon coast, southern Britain. *Geologos, 19*(1-2), 67-85.
Morton, A., Knox, R., & Frei, D. (2016). Heavy mineral and zircon age constraints on provenance of the Sherwood Sandstone Group (Triassic) in the eastern Wessex Basin, UK. *Proceedings of the Geologists' Association, 127*(4), 514-526. doi:https://doi.org/10.1016/j.pgeola.2016.06.001
Morton, A., Waters, C., Fanning, M., Chisholm, I., & Brettle, M. (2015). Origin of Carboniferous sandstones fringing the northern margin of the Wales-Brabant Massif: insights from detrital zircon ages. *Geological Journal, 50*(5), 553-574. doi:https://doi.org/10.1002/gj.2572
Morton, A. C. (1982). The provenance and diagenesis of Palaeogene sandstones of southeast England as indicated by heavy mineral analysis. *Proceedings of the Geologists' Association, 93*(3), 263-274.
Morton, A. C., & Hallsworth, C. (1994). Identifying provenance-specific features of detrital heavy mineral assemblages in sandstones. *Sedimentary Geology, 90*(3-4), 241-256. doi:https://doi.org/10.1016/0037-0738(94)90041-8
Morton, A. C., & Hallsworth, C. R. (1999). Processes controlling the composition of heavy mineral assemblages in sandstones. *Sedimentary Geology, 124*(1), 3-29.
Mosier-Boss, P., Lieberman, S., & Newbery, R. (1995). Fluorescence rejection in Raman spectroscopy by shifted-spectra, edge detection, and FFT filtering techniques. *Applied spectroscopy, 49*(5), 630-638.
Muirhead, D. K., Bond, C. E., Watkins, H., Butler, R. W., Schito, A., Crawford, Z., & Marpino, A. (2019). Raman Spectroscopy: an effective thermal marker in low temperature carbonaceous fold-thrust belts. *Geological Society, London, Special Publications, 490*, SP490-2019-2027. doi:https://doi.org/10.1144/SP490-2019-27

Murdoch, L. M., Musgrove, F. W., & Perry, J. S. (1995). Tertiary uplift and inversion history in the North Celtic Sea Basin and its influence on source rock maturity. *Geological Society, London, Special Publications, 93*(1), 297-319. doi:10.1144/gsl.sp.1995.093.01.22

Murphy, J. B., Nance, R. D., Gabler, L. B., Martell, A., & Archibald, D. A. (2019). Age, geochemistry and origin of the Ardara appinite plutons, northwest Donegal, Ireland. *Geoscience Canada: Journal of the Geological Association of Canada/Geoscience Canada: journal de l'Association Géologique du Canada, 46*(1), 31-48. doi:https://doi.org/10.12789/geocanj.2019.46.144

Murphy, N. J., & Ainsworth, N. R. (1991). Stratigraphy of the Triassic, Lower Jurassic and Middle Jurassic (Aalenian) from the Fastnet Basin, offshore south-west Ireland. *Marine and Petroleum Geology, 8*(4), 417-429. doi:https://doi.org/10.1016/0264-8172(91)90064-8

Nachon, M., Clegg, S., Mangold, N., Schröder, S., Kah, L., Dromart, G., Ollila, A., Johnson, J., Oehler, D., & Bridges, J. (2014). Calcium sulfate veins characterized by ChemCam/Curiosity at Gale crater, Mars. *Journal of Geophysical Research: Planets, 119*(9), 1991-2016. doi:https://doi.org/10.1002/2013JE004588

Naemat, A., Elsheikha, H. M., Al-Sandaqchi, A., Kong, K., Ghita, A., & Notingher, I. (2015). Analysis of interaction between the apicomplexan protozoan Toxoplasma gondii and host cells using label-free Raman spectroscopy. *Analyst, 140*(3), 756-764.

Nance, R. D., Murphy, J. B., Strachan, R. A., Keppie, J. D., Gutiérrez-Alonso, G., Fernández-Suárez, J., Quesada, C., Linnemann, U., D'lemos, R., & Pisarevsky, S. A. (2008). Neoproterozoic-early Palaeozoic tectonostratigraphy and palaeogeography of the peri-Gondwanan terranes: Amazonian v. West African connections. *Geological Society, London, Special Publications, 297*(1), 345-383. doi:https://doi.org/10.1144/SP297.17

Nance, R. D., Neace, E. R., Braid, J. A., Murphy, J. B., Dupuis, N., & Shail, R. K. (2015). Does the Meguma terrane extend into SW England? *Geoscience Canada*, 61-76. doi:https://doi.org/10.12789/geocanj.2014.41.056

Nasdala, L., Corfu, F., Schoene, B., Tapster, S. R., Wall, C. J., Schmitz, M. D., Ovtcharova, M., Schaltegger, U., Kennedy, A. K., & Kronz, A. (2018). GZ 7 and GZ 8–Two Zircon Reference Materials for SIMS U-Pb Geochronology. *Geostandards and Geoanalytical Research, 42*(4), 431-457. doi: https://doi.org/10.1111/ggr.12239

Nasdala, L., Irmer, G., & Wolf, D. (1995). The degree of metamictization in zircons: a Raman spectroscopic study. *European Journal of Mineralogy-Ohne Beihefte, 7*(3), 471-478. doi:https://doi.org/10.1127/ejm/7/3/0471

Nasdala, L., Pidgeon, R., Wolf, D., & Irmer, G. (1998). Metamictization and U-Pb isotopic discordance in single zircons: a combined Raman microprobe and SHRIMP ion probe study. *Mineralogy and Petrology, 62*(1-2), 1-27. doi:https://doi.org/10.1007/BF01173760

Nauton-Fourteu, M., Tyrrell, S., Morton, A., Mark, C., O'Sullivan, G. J., & Chew, D. M. (2020). Constraining recycled detritus in quartz-rich sandstones: insights from a multi-proxy provenance study of the Mid-Carboniferous, Clare Basin, western Ireland. *Basin Research*. doi:https://doi.org/10.1111/bre.12469

Naylor, D., & Shannon, P. (1982). *Geology of offshore Ireland and west Britain*. United Kingdom.

Naylor, D., & Shannon, P. (2011). *Petroleum geology of Ireland*: Dunedin Academic Press Limited.

Norell, M. A., Wiemann, J., Fabbri, M., Yu, C., Marsicano, C. A., Moore-Nall, A., Varricchio, D. J., Pol, D., & Zelenitsky, D. K. (2020). The first dinosaur egg was soft. *Nature*. doi:https://doi.org/10.1038/s41586-020-2412-8

O'Connor, P., & Brück, P. (1978). Age and origin of the Leinster Granite. *Journal of Earth Sciences*, 105-113.

O'Haver, T. (2020). *Pragmatic Introduction to Signal Processing* Department of Chemistry and Biochemistry, University of Maryland at College Park.

O'Reilly, B. M., Shannon, P. M., & Vogt, U. (1991). Seismic studies in the North Celtic Sea Basin: implications for basin development. *Journal of the Geological Society, London, 148*(1), 191-195. doi:https://10.1144/gsjgs.148.1.0191

O'Sullivan, G., Chew, D., Kenny, G., Henrichs, I., & Mulligan, D. (2020). The trace element composition of apatite and its application to detrital provenance studies. *Earth-Science Reviews, 201*, 103044. doi:https://doi.org/10.1016/j.earscirev.2019.103044

Parnell, J., McMahon, S., Blamey, N. J., Hutchinson, I. B., Harris, L. V., Ingley, R., Edwards, H. G., Lynch, E., & Feely, M. (2014). Detection of reduced carbon in a basalt analogue for martian nakhlite: a signpost to habitat on Mars. *International Journal of Astrobiology, 13*(2), 124-131.

Pascoe, R., Power, M., & Simpson, B. (2007). QEMSCAN analysis as a tool for improved understanding of gravity separator performance. *Minerals engineering, 20*(5), 487-495. doi:https://doi.org/10.1016/j.mineng.2006.12.012
Passchier, C. W., & Trouw, R. A. (2005). *Microtectonics* (2 ed.): Springer Science & Business Media.
Pasteris, J. D., & Wopenka, B. (1991). Raman spectra of graphite as indicators of degree of metamorphism. *The Canadian Mineralogist, 29*(1), 1-9.
Paton, C., Hellstrom, J., Paul, B., Woodhead, J., & Hergt, J. (2011). Iolite: Freeware for the visualisation and processing of mass spectrometric data. *Journal of Analytical Atomic Spectrometry, 26*(12), 2508-2518. doi:https://10.1039/C1JA10172B
Payton, C. E. (1977). *Seismic stratigraphy: applications to hydrocarbon exploration* (Vol. 26): American Association of Petroleum Geologists Tulsa, OK.
Pereira, M. F., Fernández, R. D., Gama, C., Hofmann, M., Gärtner, A., & Linnemann, U. (2018). S-type granite generation and emplacement during a regional switch from extensional to contractional deformation (Central Iberian Zone, Iberian autochthonous domain, Variscan Orogeny). *International Journal of Earth Sciences, 107*(1), 251-267.
Petrie, S., Brown, J., Granger, P., & Lovell, J. (1989). Mesozoic history of the Celtic Sea basins. *Extensional Tectonics and Stratigraphy of the North Atlantic Margins American Association of Petroleum Geologists Memoirs, 46*, 433-445.
Petrus, J. A., & Kamber, B. S. (2012). VizualAge: A Novel Approach to Laser Ablation ICP-MS U-Pb Geochronology Data Reduction. *Geostandards and Geoanalytical Research, 36*(3), 247-270. doi:https://10.1111/j.1751-908X.2012.00158.x
Pettijohn, F. J., Potter, P. E., & Siever, R. (2012). *Sand and sandstone*: Springer Science & Business Media.
Pollock, J. C., Hibbard, J. P., & van Staal, C. R. (2012). A paleogeographical review of the peri-Gondwanan realm of the Appalachian orogen. *Canadian Journal of Earth Sciences, 49*(1), 259-288. doi:https://doi.org/10.1139/e11-049
Pothier, H. D., Waldron, J. W., Schofield, D. I., & DuFrane, S. A. (2015). Peri-Gondwanan terrane interactions recorded in the Cambrian–Ordovician detrital zircon geochronology of North Wales. *Gondwana Research, 28*(3), 987-1001. doi:https://doi.org/10.1016/j.gr.2014.08.009
QGIS.org. (2021). QGIS geographic information system. http://www.qgis.org.
Rainbird, R. H., Hamilton, M. A., & Young, G. M. (2001). Detrital zircon geochronology and provenance of the Torridonian, NW Scotland. *Journal of the Geological Society, London, 158*(1), 15-27. doi:https://doi.org/10.1144/jgs.158.1.15
Raman, C. V. (1928). A change of wave-length in light scattering. *Nature, 121*(3051), 619. doi:https://doi.org/10.1038/121619b0
Ramkumar, M. (2015). Toward standardization of terminologies and recognition of chemostratigraphy as a formal stratigraphic method. In *Chemostratigraphy* (pp. 1-21): Elsevier.
Randle, V., & Engler, O. (2014). *Introduction to texture analysis: macrotexture, microtexture and orientation mapping*: CRC press.
Rawson, P., & Riley, L. (1982). Latest Jurassic-Early Cretaceous events and the "late Cimmerian unconformity" in North Sea area. *AAPG Bulletin, 66*(12), 2628-2648. doi:https://doi.org/10.1306/03B5AC87-16D1-11D7-8645000102C1865D
Reilly, T. (1986). A review of vein mineralization in SW County Cork, Ireland. In C. J. Andrew, R. W. A. Crowe, S. Finlay, W. M. Pennell, & J. F. Pyne (Eds.), *Geology and genesis of mineral deposits in Ireland* (pp. 513-544). Irish Association Economic Geologists.
Resentini, A., Andò, S., Garzanti, E., Malusà, M. G., Pastore, G., Vermeesch, P., Chanvry, E., & Dall'Asta, M. (2020). Zircon as a provenance tracer: Coupling Raman spectroscopy and UPb geochronology in source-to-sink studies. *Chemical Geology*, 119828. doi:https://doi.org/10.1016/j.chemgeo.2020.119828
Roberts, D. G. (1989). Basin inversion in and around the British Isles. *Geological Society, London, Special Publications, 44*(1), 131-150. doi:10.1144/gsl.sp.1989.044.01.09
Robinson, K., Shannon, P., & Young, G. M. (1981). The Fastnet Basin: An integrated analysis. In L. G. Illing & G. D. Hobson (Eds.), *Petroleum Geology of the Continental Shelf of North-West Europe* (pp. 444–454). London: Heyden and Son Ltd.
Rodriguez-Salgado, P. (2019). *Structural and Kinematic Analysis of the Celtic Sea Basins.* (PhD). University College Dublin,

Rodríguez-Salgado, P., Childs, C., Shannon, P. M., & Walsh, J. J. (2019). Structural evolution and the partitioning of deformation during basin growth and inversion: A case study from the Mizen Basin Celtic Sea, offshore Ireland. *Basin Research*. doi:https://doi.org/10.1111/bre.12402

Rowell, P. (1995). Tectono-stratigraphy of the North Celtic Sea Basin. *Geological Society, London, Special Publications, 93*(1), 101-137. doi:10.1144/gsl.sp.1995.093.01.11

Ruffell, A., & Shelton, R. (1999). The control of sedimentary facies by climate during phases of crustal extension: examples from the Triassic of onshore and offshore England and Northern Ireland. *Journal of the Geological Society, London, 156*(4), 779-789. doi:https://doi.org/10.1144/gsjgs.156.4.0779

Ruffell, A. H., & Rawson, P. F. (1994). Palaeoclimate control on sequence stratigraphic patterns in the late Jurassic to mid-Cretaceous, with a case study from Eastern England. *Palaeogeography, Palaeoclimatology, Palaeoecology, 110*(1-2), 43-54. doi:https://doi.org/10.1016/0031-0182(94)90109-0

Rull, F., Maurice, S., Hutchinson, I., Moral, A., Perez, C., Diaz, C., Colombo, M., Belenguer, T., Lopez-Reyes, G., & Sansano, A. (2017). The Raman laser spectrometer for the ExoMars rover mission to Mars. *Astrobiology, 17*(6-7), 627-654. doi:https://doi.org/10.1089/ast.2016.1567

Rusk, B. G., Reed, M. H., Dilles, J. H., & Kent, A. J. (2006). Intensity of quartz cathodoluminescence and trace-element content in quartz from the porphyry copper deposit at Butte, Montana. *American Mineralogist, 91*(8-9), 1300-1312. doi:https://doi.org/10.2138/am.2006.1984

Sanderson, D. J. (1984). Structural variation across the northern margin of the Variscides in NW Europe. *Geological Society, London, Special Publications, 14*(1), 149-165. doi:https://doi.org/10.1144/GSL.SP.1984.014.01.15

Savitzky, A., & Golay, M. J. (1964). Smoothing and differentiation of data by simplified least squares procedures. *Analytical chemistry, 36*(8), 1627-1639.

Schmidt, C., & Ziemann, M. A. (2000). In-situ Raman spectroscopy of quartz: A pressure sensor for hydrothermal diamond-anvil cell experiments at elevated temperatures. *American Mineralogist, 85*(11-12), 1725-1734. doi:https://doi.org/10.2138/am-2000-11-1216

Shannon, P. (1991a). The development of Irish offshore sedimentary basins. *Journal of the Geological Society, London, 148*(1), 181-189. doi:https://doi.org/10.1144/gsjgs.148.1.0181

Shannon, P. (1996). Current and future potential of oil and gas exploration in Ireland. In K. Glennie & A. Hurst (Eds.), *AD1995-NW Europe's Hydrocarbon Industry. Geol. Soc, London* (Vol. 1, pp. 51-62): Journal of the Geological Society, London.

Shannon, P., & MacTiernan, B. (1993). Triassic prospectivity in the Celtic Sea, Ireland-a case history. *First Break, 11*(2), 47-57. doi:https://doi.org/10.3997/1365-2397.1993003

Shannon, P., & Naylor, D. (1998). An assessment of Irish offshore basins and petroleum plays. *Journal of Petroleum Geology, 21*(2), 125-152. doi:https://doi.org/10.1111/j.1747-5457.1998.tb00651.x

Shannon, P. M. (1991b). The development of Irish offshore sedimentary basins. *Journal of the Geological Society, London, 148*(1), 181-189. doi:https://doi.org/10.1144/gsjgs.148.1.0181

Shannon, P. M. (1995). Permo-Triassic development of the Celtic Sea region, offshore Ireland. *Geological Society London Special Publication, 91*, 215-237. doi:https://doi.org/10.1144/GSL.SP.1995.091.01.11

Shannon, P. M., Corcoran, D. V., & Haughton, P. D. W. (2001). The petroleum exploration of Ireland's offshore basins: introduction. *Geological Society, London, Special Publications, 188*(1), 1-8. doi:https://10.1144/gsl.sp.2001.188.01.01

Shapiro, S. M., O'Shea, D. C., & Cummins, H. Z. (1967). Raman scattering study of the alpha-beta phase transition in quartz. *Physical Review Letters, 19*(7), 361. doi:https://doi.org/10.1103/PhysRevLett.19.361

Shreve, A. P., Cherepy, N. J., & Mathies, R. A. (1992). Effective rejection of fluorescence interference in Raman spectroscopy using a shifted excitation difference technique. *Applied spectroscopy, 46*(4), 707-711.

Sibuet, J. C., Dyment, J., Bois, C., Pinet, B., & Ondreas, H. (1990). Crustal structure of the Celtic Sea and Western Approaches from gravity data and deep seismic profiles: constraints on the formation of continental basins. *Journal of Geophysical Research: Solid Earth, 95*(B7), 10999-11020. doi:https://doi.org/10.1029/JB095iB07p10999

SÌtolfovÃ¡, K. i., & Shannon, P. M. (2009). Permo-Triassic development from Ireland to Norway: basin architecture and regional controls. *Geological Journal, 44*(6), 652-676. doi:10.1002/gj.1187

Sláma, J., Košler, J., Condon, D. J., Crowley, J. L., Gerdes, A., Hanchar, J. M., Horstwood, M. S., Morris, G. A., Nasdala, L., & Norberg, N. (2008). Plešovice zircon—a new natural reference material for U–Pb and Hf isotopic microanalysis. *Chemical Geology, 249*(1-2), 1-35. doi:https://doi.org/10.1016/j.chemgeo.2007.11.005

Smith, E., & Dent, G. (2019a). *Modern Raman Spectroscopy: A Practical Approach* (2 ed.): John Wiley & Sons Ltd.
Smith, W. D., Darling, J., Bullen, D., Lasalle, S., Pereira, I., Moreira, H., Allen, C. J., & Tapster, S. (2019b). Zircon perspectives on the age and origin of evolved S-type granites from the Cornubian Batholith, Southwest England. *Lithos, 336*, 14-26. doi:https://doi.org/10.1016/j.lithos.2019.03.025
Smyth, H. R., Morton, A., Richardson, N., & Scott, R. A. (2014). Sediment provenance studies in hydrocarbon exploration and production: An introduction. *Geological Society, London, Special Publications, 386*(1), 1-6.
Somerville, I. D., Strogen, P., & Jones, G. L. (1992). Biostratigraphy of Dinantian limestones and associated volcanic rocks in the Limerick Syncline, Ireland. *Geological Journal, 27*(3), 201-220. doi:https://doi.org/10.1002/gj.3350270302
Soper, N., & Hutton, D. (1984). Late Caledonian sinistral displacements in Britain: implications for a three-plate collision model. *Tectonics, 3*(7), 781-794. doi:https://10.1029/TC003i007p00781
Spinks, S. C., Parnell, J., Bellis, D., & Still, J. (2016). Remobilization and mineralization of selenium–tellurium in metamorphosed red beds: Evidence from the Munster Basin, Ireland. *Ore Geology Reviews, 72*, 114-127. doi:https://doi.org/10.1016/j.oregeorev.2015.07.007
Stampfli, G. M., & Kozur, H. W. (2006). Europe from the Variscan to the Alpine cycles. *Journal of the Geological Society, London, 32*, 57-82. doi:https://doi.org/10.1144/GSL.MEM.2006.032.01.04
Strachan, R., Collins, A., Buchan, C., Nance, R., Murphy, J., & D'Lemos, R. (2007). Terrane analysis along a Neoproterozoic active margin of Gondwana: insights from U–Pb zircon geochronology. *Journal of the Geological Society, London, 164*(1), 57-60. doi:https://doi.org/10.1144/0016-76492006-014
Taber, D., Vickers, M., & Winn, R. (1995). The definition of the Albian 'A'Sand reservoir fairway and aspects of associated gas accumulations in the North Celtic Sea Basin. *Geological Society, London, Special Publications, 93*(1), 227-244. doi:https://doi.org/10.1144/GSL.SP.1995.093.01.16
Talebian, M., Talebian, E., & Abdi, A. J. P. (2012). The calculation of active Raman modes of α-quartz crystal via density functional theory based on B3LYP Hamiltonian in 6–311+ G (2d) basis set. *Pramana Journal of Physiscs, 78*(5), 803-810. doi:https://doi.org/10.1007/s12043-012-0287-4
Tartese, R., Poujol, M., Ruffet, G., Boulvais, P., Yamato, P., & Košler, J. (2011). New U-Pb zircon and 40Ar/39Ar muscovite age constraints on the emplacement of the Lizio syn-tectonic granite (Armorican Massif, France). *Comptes Rendus Geoscience, 343*(7), 443-453. doi:https://doi.org/10.1016/j.crte.2011.07.005
Tate, M., & Dobson, M. (1988). Syn-and post-rift igneous activity in the Porcupine Seabight Basin and adjacent continental margin W of Ireland. *Geological Society, London, Special Publications, 39*(1), 309-334. doi:https://doi.org/10.1144/GSL.SP.1988.039.01.28
Taylor, G. K. (2007). Pluton shapes in the Cornubian Batholith: new perspectives from gravity modelling. *Journal of the Geological Society, London, 164*(3), 525-528. doi:https://doi.org/10.1144/0016-76492006-104
Thomas, D. B., McGoverin, C. M., Fordyce, R. E., Frew, R. D., & Gordon, K. C. (2011). Raman spectroscopy of fossil bioapatite—a proxy for diagenetic alteration of the oxygen isotope composition. *Palaeogeography, Palaeoclimatology, Palaeoecology, 310*(1-2), 62-70. doi:https://doi.org/10.1016/j.palaeo.2011.06.016
Thomson, S. N., Gehrels, G. E., Ruiz, J., & Buchwaldt, R. (2012). Routine low-damage apatite U-Pb dating using laser ablation–multicollector–ICPMS. *Geochemistry, Geophysics, Geosystems, 13*(2). doi:https://10.1029/2011GC003928
Todd, S. (2015). Structure of the Dingle Peninsula, SW Ireland: evidence for the nature and timing of Caledonian, Acadian and Variscan tectonics. *Geological Magazine, 152*(2), 242-268. doi:https://doi.org/10.1017/S0016756814000260
Tong, H., Tan, P., & Xu, N. (2015). From crystals to disordered crystals: A hidden order-disorder transition. *Scientific reports, 5*, 15378. doi:https://doi.org/10.1038/srep15378
Tyrrell, S. (2005). *Investigations of Sandstone Provenance.* (PhD
). University College Dublin,
Tyrrell, S., Haughton, P. D., & Daly, J. S. (2007). Drainage reorganization during breakup of Pangea revealed by in-situ Pb isotopic analysis of detrital K-feldspar. *Geology, 35*(11), 971-974. doi:https://doi.org/10.1130/G4123A.1
Tyrrell, S., Haughton, P. D., Souders, A. K., Daly, J. S., & Shannon, P. M. (2012). Large-scale, linked drainage systems in the NW European Triassic: insights from the Pb isotopic composition of detrital K-feldspar. *Journal of the Geological Society, London, 169*(3), 279-295. doi:https://doi.org/10.1144/0016-76492011-104

Van der Voo, R. (1988). Paleozoic paleogeography of North America, Gondwana and intervening. displaced terranes: Comparisons of palaeomagnetism with paleoclimatology and biogeographical patterns. *Geological Society of America Bulletin, 100*, 411-423. doi:https://doi.org/10.1130/0016-7606(1988)100<0311:PPONAG>2.3.CO;2

van Staal, C. R., Sullivan, R. W., & Whalen, J. B. (1996). Provenance of tectonic history of the Gander Zone in the Caledonian/Appalachian Orogen: Implications for the origin and assembly of Avalon. In M. D. T. Damian Nance (Ed.), *Avalonian and Related Peri-Gondwanan Terranes of the Circum-North Atlantic* (Vol. 304, pp. 347-367): Geological Society of America.

Vandenabeele, P., Edwards, H. G., & Moens, L. (2007). A decade of Raman spectroscopy in art and archaeology. *Chemical reviews, 107*(3), 675-686. doi:https://doi.org/10.1021/cr068036i

Vermeesch, P. (2018). IsoplotR: A free and open toolbox for geochronology. *Geoscience Frontiers, 9*(5), 1479-1493. doi:https://doi.org/10.1016/j.gsf.2018.04.001

Vermeesch, P., Resentini, A., & Garzanti, E. (2016). An R package for statistical provenance analysis. *Sedimentary Geology, 336*, 14-25. doi:https://doi.org/10.1016/j.sedgeo.2016.01.009

Vermeesch, P., Rittner, M., Petrou, E., Omma, J., Mattinson, C., & Garzanti, E. (2017). High throughput petrochronology and sedimentary provenance analysis by automated phase mapping and LAICPMS. *Geochemistry, Geophysics, Geosystems, 18*(11), 4096-4109. doi:https://doi.org/10.1002/2017GC007109

Vickers, M. L., Fernandez, A., Hesselbo, S. P., Price, G. D., Bernasconi, S. M., Lode, S., Ullmann, C. V., Thibault, N., Hougaard, I. W., & Korte, C. (2020). Unravelling Middle to Late Jurassic palaeoceanographic and palaeoclimatic signals in the Hebrides Basin using belemnite clumped isotope thermometry. *Earth and Planetary Science Letters, 546*, 116401.

Virtanen, P., Gommers, R., Oliphant, T. E., Haberland, M., Reddy, T., Cournapeau, D., Burovski, E., Peterson, P., Weckesser, W., & Bright, J. (2020). SciPy 1.0: fundamental algorithms for scientific computing in Python. Nature methods.

Von Eynatten, H., & Wijbrans, J. (2003). Precise tracing of exhumation and provenance using 40Ar/39Ar geochronology of detrital white mica: the example of the Central Alps. *Geological Society, London, Special Publications, 208*(1), 289-305. doi:https://doi.org/10.1144/GSL.SP.2003.208.01.14

von Raumer, J. F., Stampfli, G. M., Arenas, R., & Martínez, S. S. (2015). Ediacaran to Cambrian oceanic rocks of the Gondwana margin and their tectonic interpretation. *International Journal of Earth Sciences, 104*(5), 1107-1121. doi:https://doi.org/10.1007/s00531-015-1142-x

Waldron, J. W., Floyd, J. D., Simonetti, A., & Heaman, L. M. (2008). Ancient Laurentian detrital zircon in the closing Iapetus ocean, Southern Uplands terrane, Scotland. *Geology, 36*(7), 527-530. doi:https://doi.org/10.1130/G24763A.1

Waldron, J. W., Schofield, D. I., Dufrane, S. A., Floyd, J. D., Crowley, Q. G., Simonetti, A., Dokken, R. J., & Pothier, H. D. (2014). Ganderia–Laurentia collision in the Caledonides of Great Britain and Ireland. *Journal of the Geological Society, London, 171*(4), 555-569. doi:https://doi.org/10.1144/jgs2013-131

Waldron, J. W., Schofield, D. I., & Murphy, J. B. (2019a). Diachronous Paleozoic accretion of peri-Gondwanan terranes at the Laurentian margin. *Geological Society, London, Special Publications, 470*(1), 289-310. doi:https://doi.org/10.1144/SP470.11

Waldron, J. W., Schofield, D. I., Pearson, G., Sarkar, C., Luo, Y., & Dokken, R. (2019b). Detrital zircon characterization of early Cambrian sandstones from East Avalonia and SE Ireland: implications for terrane affinities in the peri-Gondwanan Caledonides. *Geological Magazine, 156*(7), 1217-1232. doi:https://doi.org/10.1017/S0016756818000407

Waldron, J. W., Schofield, D. I., White, C. E., & Barr, S. M. (2011). Cambrian successions of the Meguma Terrane, Nova Scotia, and Harlech Dome, North Wales: dispersed fragments of a peri-Gondwanan basin? *Journal of the Geological Society, London, 168*(1), 83-98. doi:https://doi.org/10.1144/0016-76492010-068

Warr, L. (2012). The Variscan orogeny: the welding of Pangaea. In N. Woodcock & R. Strachan (Eds.), *Geological history of Britain and Ireland* (2nd ed., pp. 274-298): John Wiley & Sons.

Warrington, G., & Ivimey-Cook, H. (1992). Triassic. In J. Cope, J. Ingham, & P. Rawson (Eds.), *Atlas of palaeogeography and lithofacies.* (Vol. 13, pp. 97-106): Geological Society of London Memoir.

Welch, M. J., & Turner, J. P. (2000). Triassic–Jurassic development of the St. George's Channel basin, offshore Wales, UK. *Marine and Petroleum Geology, 17*(6), 723-750. doi:https://doi.org/10.1016/S0264-8172(00)00017-9

Weltje, G. J., & von Eynatten, H. (2004). Quantitative provenance analysis of sediments: review and outlook. *Sedimentary Geology, 171*(1-4), 1-11.

White, C., Palacios, T., Jensen, S., & Barr, S. (2012). Cambrian–Ordovician acritarchs in the Meguma terrane, Nova Scotia, Canada: Resolution of early Paleozoic stratigraphy and implications for paleogeography. *GSA Bulletin, 124*(11-12), 1773-1792. doi:https://doi.org/10.1130/B30638.1

Wiedenbeck, M., Alle, P., Corfu, F., Griffin, W., Meier, M., Oberli, F. v., Quadt, A. v., Roddick, J., & Spiegel, W. (1995). Three natural zircon standards for U-Th-Pb, Lu-Hf, trace element and REE analyses. *Geostandards newsletter, 19*(1), 1-23. doi:https://doi.org/10.1111/j.1751-908X.1995.tb00147.x

Willner, A. P., Gerdes, A., Massonne, H.-J., van Staal, C. R., & Zagorevski, A. (2014). Crustal evolution of the northeast Laurentian margin and the Peri-Gondwanan microcontinent Ganderia prior to and during closure of the Iapetus Ocean: detrital zircon U–Pb and Hf isotope evidence from Newfoundland. *Geoscience Canada*, 345-364. doi:https://doi.org/10.12789/geocanj.2014.41.046

Winn Jr, R. D. (1994). Shelf sheet-sand reservoir of the Lower Cretaceous Greensand, North Celtic Sea Basin, offshore Ireland. *AAPG Bulletin, 78*(11), 1775-1789. doi:https://doi.org/10.1306/A25FF28D-171B-11D7-8645000102C1865D

Xie, L., Ling, X., Fang, Y., Zhang, J., & Liu, Z. (2009). Graphene as a substrate to suppress fluorescence in resonance Raman spectroscopy. *Journal of the American Chemical Society, 131*(29), 9890-9891. doi:https://doi.org/10.1021/ja9037593

Yang, P., Welford, J. K., Peace, A. L., & Hobbs, R. (2020). Investigating the Goban Spur rifted continental margin, offshore Ireland, through integration of new seismic reflection and potential field data. *Tectonophysics, 777*, 228364. doi:https://doi.org/10.1016/j.tecto.2020.228364

Yang, S., & Akkus, O. (2013). *Fluorescence Background Problem in Raman Spectroscopy: Is 1064 nm Excitation an Improvement of 785 nm*. Wasatch Photonics: Report.

Zhang, X., Pease, V., Omma, J., & Benedictus, A. (2015). Provenance of Late Carboniferous to Jurassic sandstones for southern Taimyr, Arctic Russia: a comparison of heavy mineral analysis by optical and QEMSCAN methods. *Sedimentary Geology, 329*, 166-176. doi:https://doi.org/10.1016/j.sedgeo.2015.09.008

Zięba-Palus, J., & Michalska, A. (2014). Photobleaching as a useful technique in reducing of fluorescence in Raman spectra of blue automobile paint samples. *Vibrational Spectroscopy, 74*, 6-12. doi:https://doi.org/10.1016/j.vibspec.2014.06.007

Ziegler, P. A. (1990). *Geological Atlas of Western and Central Europe* (2 ed.): Shell Internationale Petroleum Maatschappij B.V. 239pp.

Ziegler, P. A., Cloetingh, S., & van Wees, J.-D. (1995). Dynamics of intra-plate compressional deformation: the Alpine foreland and other examples. *Tectonophysics, 252*(1-4), 7-59.

Zimmermann, S., Mark, C., Chew, D., & Voice, P. J. (2018). Maximising data and precision from detrital zircon U-Pb analysis by LA-ICPMS: The use of core-rim ages and the single-analysis concordia age. *Sedimentary Geology, 375*, 5-13. doi:https://doi.org/10.1016/j.sedgeo.2017.12.020

Zoleikhaei, Y., Frei, D., Morton, A., & Zamanzadeh, S. M. (2016). Roundness of heavy minerals (zircon and apatite) as a provenance tool for unraveling recycling: A case study from the Sefidrud and Sarbaz rivers in N and SE Iran. *Sedimentary Geology, 342*, 106-117. doi:https://doi.org/10.1016/j.sedgeo.2016.06.016

Appendices

Explanation of Appendices

These appendices provide additional information which was excluded from the previous chapters of the thesis to improve readability. Appendix A outlines the contribution of the authors in each manuscript. Appendix B is a list of conference presentations, workshops and courses undertaken during this project. Appendix C lists all samples collected for this study as well as a list of samples used in each study. Appendix D contains all geochronology, trace element and heavy mineral data which is provided in the external USB. See Appendix D text for notes on each folder.

Appendix A: Author Contribution

Multiple authors have contributed to the conception, analysis and discussions which lead to the formation of the four major chapters in this study. The original project was conceived by the supervisor of this project Dr Pat Meere. This project was awarded funding under sediment tracking group within hydrocarbons spoke of the Irish Centre of Research in Applied Geosciences (iCRAG). The role of Dr Meere was to provide project oversight, editorial and data interpretation support as well as numerous beneficial and constructive discussions. All the major interpretations and conclusions in this thesis are the work of the lead author Odhrán McCarthy. Secondary supervisor Dr David Chew provided sample preparation, analysis, processing, interpretation, and editorial support.

Chapters one and two which addressed the provenance of Mesozoic sediments in the Irish and Celtic Sea basins received input from several authors. Odhrán McCarthy collected samples form the Petroleum Affairs Division (PAD) core store in Dublin and BGS core shed in Keyworth. To prepare these samples, Odhrán attended several workshops and courses (Appendixes C) in addition to significant background reading to set up a crushing facility and heavy mineral separation laboratory in University College Cork. This process took several months of learning, sample processing and polishing. Detrital zircon and apatite analysis and preliminary processing was conducted in Trinity College Dublin by Dr David Chew with the help of his laboratory assistant Dr Foteini Drakou. Heavy mineral analysis via QEMSCAN imaging was conducted by Rocktype Ltd. under the supervision of Dr Jenny Omma. Raman analysis of heavy minerals and mapping of zircon grains was conducted by Odhrán McCarthy in UCC. Dr Brenton Fairey provided unpublished detrital zircon and mica data from offshore wells as well as providing editorial support. Co-authors Aidan Kerrison, Dr Mandy Hoffman, Dr Andreas Gartner, Benita-Lisette Sonntag, Prof. Klaudia Kuiper, and Prof. Ulf Linnemann assisted in the analysis and processing of Dr Fairey's data set and were included as co-authors to acknowledge their contribution this work. A full list of the samples which were collected by Dr Fairey and Odhrán McCarthy are provided in Appendixes D.

Chapter 4 which presented the Ramaster software was principally conceived, programmed and writing by Odhrán McCarthy with support from Dr Meere. During a two-month academic

visit to the University of Milano, Biccoca in 2018, Dr Sergio Ando and Dr Alberto Resentini helped to construct the first R based peak analysis script used in this chapter. Fellow PhD student Gerrard Summers and software engineer Artsiom Vahin helped to construct the batch processing and rasterization components of the software. The user interface for this software was developed by Odhrán McCarthy and Artsiom Vahin. Dr Mohit Tunwal and Dr Richard Unitt provided Raman expertise and mathematical support during this process. Dr Meere provided editorial support.

Chapter 5 presents the Raman and Fluorescence spectroscopy differentiation of alpha quartz from the Allihies Copper Mine. It was conceived and developed by Odhrán McCarthy. Dr Meere and Jurgen Lang provided sample material and geological expertise of the area as well as editorial support. Dr Alberto Resentini, Dr Sergio Ando and Dr William McCarthy provided expertise and advice in the application and development of this project. Dr Tunwal and Dr Unitt provided expert advice in Raman spectroscopy and data interpretation. Dr Hazel Garvie-Cooke provided expert advice as a Renishaw application specialist to ensure that results and chemical interpretations were accurate.

All interpretations presented in this thesis are the work of the PhD candidate, Odhrán McCarthy.

Appendix B: Conferences and Workshops

This section presents a list of conference presentations and workshops attended throughout the course of this PhD.

Conferences

McCarthy O., Fairey B., Kerrison A., Chew D., Meere P., 2020. Provenance of Mesozoic sediments in the North Celtic Sea and Saint George's Channel Basins: Results from Detrital Zircon and Apatite studies. Oral Presentation delivered at iCRAG's Energy Security virtual Technical Advisory Committee meeting, Athlone, 17 June 2020.

McCarthy O., Meere P., Resentini A., Garvie-Cook H., Tunwal M., Ando S., Unitt R., McCarthy W., 2020. Constraining tectonic chronology: Quantifying deformation in quartz via Raman spectroscopy. Poster Presentation delivered at the Irish Geological Research Meeting, Athlone, 28 February-1 March 2020.

McCarthy O., Fairey B., Kerrison A., Chew D., Meere P., 2020. Provenance of Mesozoic sediments in the North Celtic Sea and Saint Georges Channel Basins: Results from Detrital Zircon and Apatite studies. Oral Presentation delivered at the Irish Geological Research Meeting, Athlone, 28 February-1 March 2020.

McCarthy O., Fairey B., Kerrison A., Chew D., Meere P., 2020. Provenance of Mesozoic sediments in the North Celtic Sea and Saint George's Channel Basins: Results from Detrital Zircon, Apatite and Mica studies. Poster Presentation delivered at the Atlantic Ireland Conference, Dublin, 29-30 November 2020.

McCarthy O., Meere P., Mulchrone K., Chew D., 2019. Provenance of Mesozoic sediments in the North Celtic Sea and St. George's Channel Basins: Heavy Mineral Results. Poster Presentation delivered at the Atlantic Ireland Conference, Dublin, 1-3 November 2019.

McCarthy O., Meere P., Chew D., 2019. Heavy Mineral analysis of the NCSB and SGCB: Temporal and spatial variations through the Mesozoic. Oral presentation delivered at the Offshore Irish Basins meeting, Dublin, 8 October 2019.

McCarthy O., Meere P., Mulchrone K., Chew D., 2019. Sediment Hunting: Provenance of the Upper Jurassic NCSV and what we know. Oral Presentation delivered by Tyrell S. at the iCRAG site visit, Dublin, 15 March 2019.

McCarthy O., Meere P., Resentini A., Garvie-Cook H., Tunwal M., Ando S., Unitt R., McCarthy W., 2019. Innovations in Raman Spectroscopy Analysis: Testing Raman spectroscopy as an age dating tool. Oral Presentation for my one-year review, University College Dublin, 2 February 2019.

McCarthy O., Meere P., Mulchrone K., Chew D., 2018. Provenance of Mesozoic sediments in the North Celtic Sea and St. George's Channel Basins: Heavy Mineral Results. Oral Presentation delivered Master students in the University of Milano-Bicocca, Italy, 14 December 2018.

McCarthy O., Meere P., Mulchrone K., Chew D., Pastor-Galan D., 2018. A provenance study of Mesozoic sediments in the North Celtic Sea Basin and St. George's Channel. Poster Presentation delivered at the Atlantic Ireland Conference, Dublin, 1-3 November 2018.

McCarthy O., Meere P., Mulchrone K., Chew D., Pastor-Galan D., 2018. A provenance study of Mesozoic sediments in the North Celtic Sea Basin and St. George's Channel. Poster presentation at the 1st school on "Controls on Sandstone Diagenesis", Erlangen, Germany, 27-29 August 2018.

McCarthy O., Meere P., Mulchrone K., Chew D., Pastor-Galan D., 2018. A provenance study of Mesozoic sediments in the North Celtic Sea Basin and St. George's Channel. Oral Presentation for my one-year review, UCC, 5 May 2018.

McCarthy O., Fairey B., Kerrison A., Chew D., Meere P., 2018. Sediment hunting: fingerprinting the palaeocontinents of Ireland and the UK. Oral Presentation delivered at the Irish Geological Research Meeting, Dublin, 25 February 2018.

McCarthy O., Fairey B., Kerrison A., Chew D., Meere P., 2018. Sediment hunting: fingerprinting the palaeocontinents of Ireland and the UK. Poster/oral presentation delivered at the Heavy Mineral School 2018, Milan, 19-24 February 2018.

McCarthy O., Meere P., Mulchrone K., Chew D., Pastor-Galan D., 2017. The temporal evolution of provenance in the Mesozoic rocks of the North Celtic Sea and St. George's Channel Basins. Poster Presentation delivered at the Atlantic Ireland Conference, Dublin, 31 October-1 November 2017.

McCarthy O., Meere P., Mulchrone K., Chew D., Pastor-Galan D., 2017. The temporal evolution of provenance in the Mesozoic rocks of the North Celtic Sea and St. George's Channel Basins. Poster/oral Presentation delivered at Sedimentary Provenance Analysis short course at the University of Gottingen, Dublin, 18-22 September 2017.

McCarthy O., 2017. Overview of sedimentary provenance activities at University College Cork. Oral presentation at the iCRAG sediment tracking meeting, University College Dublin, Dublin, 7 June 2017.

Workshops

2020: Viva workshop for PhD students – University College Cork, Ireland
2019: Project Management for Researchers – University College Cork, Ireland
2018: Postgraduate teaching and learning – University College Cork, Ireland
2018: Sedimentary Petrography – University of Milan Biccoca, Italy
2018: The geology of sedimentary Basins – University of Milan Biccoca, Italy
2018: Controls on Sandstone Diagenesis – FAU Erlangen-Nurnberg, Germany
2018: Heavy Mineral School – University of Milan Biccoca, Italy
2018: Sediment budget course-WGSG-Dublin, Ireland

2017: BSRG Field Trip – Coastal to Deep water sedimentology of the Culm Basin, UK

2017: Sedimentary Provenance Analysis Course-Gottingen, Germany

Appendix C: Sample Lists

Table 3. Original samples collected from BGS and PAD core stores. All samples were taken from the NCSB or SGCB. Note that Sample No. refer to the original sample ID, to see the ID used in text, refer to Table 2 of Appendix C. Samples from the NCSB were originally labeled with "s", this was a bad decision as s is generic and will not be used in future work.

Well No.	Sample No.	Period	Age	Sample Type	Depth
50/03-01	S1	Cretaceous	Purbeck	Unwashed Chips	1340
50/03-01	S2	Cretaceous	Purbeck	Unwashed Chips	1370
50/03-01	S3	Cretaceous	Purbeck	Unwashed Chips	1310
50/03-01	S4	Cretaceous	Purbeck	Unwashed Chips	1340
50/03-01	S5	Jurassic	Kimmeridgian/Oxfordian	Unwashed Chips	2420
50/03-01	S6	Jurassic	Kimmeridgian/Oxfordian	Unwashed Chips	2450
50/03-01	S7	Jurassic	Kimmeridgian/Oxfordian	Unwashed Chips	2420
50/03-01	S9	Jurassic	Kimmeridgian/Oxfordian	Unwashed Chips	2510
50/03-01	S10	Jurassic	Kimmeridgian/Oxfordian	Unwashed Chips	2480-2510
50/03-01	S10.5	Jurassic	Pleinsbachian	Core	8383
50/03-01	S11	Jurassic	Pleinsbachian	Core	8384
50/03-01	S12	Jurassic	Pleinsbachian	Core	8389
50/03-01	S13	Jurassic	Pleinsbachian	Core	8384
50/03-02	S14	Cretaceous	Purbeck	Unwashed Chips	1390
50/03-02	S15	Cretaceous	Purbeck	Unwashed Chips	1420
50/03-02	S16	Cretaceous	Purbeck	Unwashed Chips	1480
50/03-02	S17	Cretaceous	Purbeck	Unwashed Chips	1510
50/03-02	S18	Cretaceous	Purbeck	Unwashed Chips	1540
50/03-02	S19	Cretaceous	Purbeck	Unwashed Chips	2390
50/03-02	S20	Cretaceous	Purbeck	Unwashed Chips	2400
50/03-02	S21	Cretaceous	Purbeck	Unwashed Chips	2410
50/03-02	S23	Jurassic	Kimmeridgian	Core	4066
50/03-02	S24	Jurassic	Kimmeridgian	Core	4068
50/03-02	S25	Jurassic	Kimmeridgian	Core	4070
50/03-02	S26	Jurassic	Kimmeridgian	Unwashed Chips	4660
50/03-02	S26.2	Jurassic	Kimmeridgian	Core	4068
50/03-02	S27	Jurassic	Oxfordian	Unwashed Chips	5300
50/03-02	S28	Jurassic	Oxfordian	Unwashed Chips	5310
50/03-02	S29	Jurassic	Oxfordian	Unwashed Chips	5320
50/03-02	S30	Jurassic	Oxfordian	Unwashed Chips	5750
50/03-02	S31	Jurassic	Oxfordian	Unwashed Chips	5780

Well No.	Sample No.	Period	Age	Sample Type	Depth
50/03-02	S32	Jurassic	Oxfordian	Unwashed Chips	5770
50/03-02	S33	Jurassic	Oxfordian	Unwashed Chips	5719
50/03-02	S34	Jurassic	Oxfordian	Unwashed Chips	5311
50/03-02	S35.1	Jurassic	Oxfordian	Unwashed Chips	5308
50/03-02	S35.2	Jurassic	Oxfordian	Unwashed Chips	5308
50/03-03	S37	Jurassic	Sinemurian-Pleinsbachian	Unwashed Chips	1480
50/03-03	S38 & S39	Jurassic	Sinemurian-Pleinsbachian	Unwashed Chips	1490
50/03-03		Jurassic	Sinemurian-Pleinsbachian	Unwashed Chips	1500
50/03-03	S40	Triassic	undefined	Unwashed Chips	3680
50/03-03	S41	Triassic	undefined	Unwashed Chips	3690
50/03-03	S42	Triassic	undefined	Unwashed Chips	3700
50/07-01	S43	Cretaceous	Albian	Unwashed Chips	1480
50/07-01	S44	Cretaceous	Albian	Unwashed Chips	1490
50/07-01	S45	Cretaceous	Albian	Unwashed Chips	1510
50/07-01	S46	Jurassic	Kimmeridgian/Oxfordian	Unwashed Chips	4020
50/07-01	S47	Jurassic	Kimmeridgian/Oxfordian	Unwashed Chips	4030
50/10-01	S48	Jurassic	Oxfordian	Unwashed Chips	3230
50/10-01	S49	Jurassic	Oxfordian	Unwashed Chips	3260
50/10-01	S50	Jurassic	Oxfordian	Unwashed Chips	3290
50/10-01	S51	Jurassic	Oxfordian	Unwashed Chips	3710
50/10-01	S52	Jurassic	Oxfordian	Unwashed Chips	3740
50/10-01	S53	Jurassic	Oxfordian	Unwashed Chips	3770
50/10-01	S54	Jurassic	Pleinsbachian	Unwashed Chips	5930
50/10-01	S55	Triassic	Triassic	Unwashed Chips	8010
50/10-01	S56	Triassic	Triassic	Unwashed Chips	8030
50/10-01	S57	Triassic	Triassic	Unwashed Chips	8040

Table 4. Samples taken from the SGCB at the start of the project.

Well No.	Sample No.	Period	Age	Sample Type	Depth
103/01-1	SG 1	Jurassic	Kimmeridgian	Washed Chips	5250
103/01-1	SG 2	Jurassic	Kimmeridgian	Washed Chips	5310
103/01-1	SG 3	Jurassic	Oxfordian	Washed Chips	7020
103/01-1	SG 4	Jurassic	Oxfordian	Washed Chips	7080
103/01-1	SG 5	Jurassic	Oxfordian	Washed Chips	7110
103/01-1	SG 6	Jurassic	Oxfordian	Washed Chips	7300
103/01-1	SG 7	Jurassic	Oxfordian	Washed Chips	7310
103/01-1	SG 8	Jurassic	Oxfordian	Washed Chips	7320
103/01-1	SG 9	Jurassic	Oxfordian	Washed Chips	7330
103/01-1	SG 10	Jurassic	Oxfordian	Washed Chips	7340
103/01-1	SG 11	Jurassic	Oxfordian	Washed Chips	7350
103/01-1	SG 12	Jurassic	Bathonian	Washed Chips	7910
103/01-1	SG 13	Jurassic	Bathonian	Washed Chips	7920
103/01-1	SG 14	Jurassic	Bathonian	Washed Chips	7930
103/01-1	SG 15	Jurassic	Bathonian	Washed Chips	7940
103/01-1	SG 16	Jurassic	Bathonian	Washed Chips	7950
103/01-1	SG 17	Jurassic	Aalenian	Washed Chips	10220
103/01-1	SG 18	Jurassic	Aalenian	Washed Chips	10230
103/01-1	SG 19	Jurassic	Aalenian	Washed Chips	10240
103/01-1	SG 20	Jurassic	Aalenian	Washed Chips	10250
103/01-1	SG 21	Jurassic	Aalenian	Washed Chips	10260
103/01-1	SG 22	Jurassic	Aalenian	Washed Chips	10270
103/01a-2	SG 23	Jurassic	Kimmeridgian	Washed Chips	6500
103/01a-2	SG 24	Jurassic	Kimmeridgian	Washed Chips	6550
103/01a-2	SG 25	Jurassic	Oxfordian	Washed Chips	9350
103/01a-2	SG 26	Jurassic	Oxfordian	Washed Chips	9400
103/01a-2	SG 27	Jurassic	Oxfordian	Washed Chips	10560
103/01a-2	SG 28	Jurassic	Oxfordian	Washed Chips	10580
103/01a-2	SG 29	Jurassic	Oxfordian	Washed Chips	10600
103/01a-2	SG 30	Jurassic	Oxfordian	Washed Chips	10620
106/28-1	SG 35	Jurassic	Aalenian	Washed Chips	3020
106/28-1	SG 36	Jurassic	Aalenian	Washed Chips	3040
107/16-1	SG 40	Jurassic	Kimmeridgian	Washed Chips	1520
107/16-1	SG 41	Jurassic	Kimmeridgian	Washed Chips	1640
107/21-1	SG 42	Jurassic	Kimmeridgian	Washed Chips	1680
107/21-1	SG 43	Jurassic	Kimmeridgian	Washed Chips	1760
107/21-1	SG 44	Jurassic	Kimmeridgian	Washed Chips	1780
107/16-1	SG 45	Jurassic	Oxfordian	Washed Chips	2300
107/16-1	SG 46	Jurassic	Oxfordian	Washed Chips	2320
107/16-1	SG 47	Jurassic	Oxfordian	Washed Chips	2400

Well No.	Sample No.	Period	Age	Sample Type	Depth
107/16-1	SG 48	Jurassic	Oxfordian	Washed Chips	2360
107/21-1	SG 49	Jurassic	Aalenian	Washed Chips	6100
107/21-1	SG 50	Jurassic	Aalenian	Washed Chips	6140
107/21-1	SG 51	Jurassic	Aalenian	Washed Chips	6160
107/16-1	SG 52	Jurassic	Aalenian	Core	6190
107/16-1	SG 53	Jurassic	Aalenian	Core	6205
107/16-1	SG 54	Jurassic	Aalenian	Core	6214
103/02-1	SG 31	Triassic	Skythian	Washed Chips	8800
103/02-1	SG 32	Triassic	Skythian	Washed Chips	8810
103/02-1b	SG 33	Triassic	Skythian	Washed Chips	9370
103/02-1b	SG 34	Triassic	Skythian	Washed Chips	9390
106/28-1	SG 37	Triassic	undefined	Washed Chips	9670
106/28-1	SG 38	Triassic	undefined	Washed Chips	9690
106/28-1	SG 39	Triassic	undefined	Washed Chips	9710
42/21-1	S66	Jurassic	Bathonian	Unwashed Chips	1280
42/21-1	S67	Jurassic	Bathonian	Unwashed Chips	1290
42/21-2	S68	Jurassic	Bathonian	Unwashed Chips	1320
42/21-3	S69	Jurassic	Bathonian	Unwashed Chips	1350
42/21-4	S70	Jurassic	Pleinsbachian	Unwashed Chips	6390
42/21-5	S71	Jurassic	Pleinsbachian	Unwashed Chips	3400
42/21-6	S72	Jurassic	Pleinsbachian	Unwashed Chips	6420

Table 5. List of samples included in Chapters two and three. The original ID is the id used during collection, the QEMSCAN ID is the ID selected by Rocktype for analyzing samples and the Publication ID was used to improve the interpretability between samples from different basins. In samples collected specifically for this study, samples were split into four grain size fractions using three different sieves. Each sample ID (e.g., SG35) was then given an additional number from 1-4 (e.g., SG35.2.) indicating the grain size fraction it represents where .1 = 0-65 µm, .2 = 65-125 µm, .3 = 125-250 µm and .4 = > 250 µm. The third numbered ID in these samples refers to whether it is the heavy fraction (SG35.2.101) or the light fraction (SG35.2.201) of the sample after heavy mineral separation. In hindsight this sample ID system was overly complex and confusing and a simpler sample ID system, as used during publication, would have been preferable.

Well No.	Original ID	QEMSCAN ID	Publication ID	Period	Age	Sample Type	Depth (Ft'/M)
106_28_1	SG35.2.101	R59-060	SG16	Cretaceous	Cenomanian	Cuttings	3020 m
50_07_01	S43.2.101	R59-027	NC22	Cretaceous	Cenomanian	Cuttings	1480 m
49/09-02	BF1		NC17	Cretaceous	Albian	Cuttings	2460' - 2496'
50_03_02	S18.2.101	R59-013	NC23	Cretaceous	Purbeck	Cuttings	1540 m
50_03_01	S2.2.101	R59-007	NC24	Cretaceous	Purbeck	Cuttings	1370 m
50_03_02	S21.2.101	R59-015	NC25	Cretaceous	Purbeck	Cuttings	2410 m
48/18-01	BF2		NC18	Cretaceous	Cretaceous	Cuttings	850 m-1160 m
48/24-04	BF4	BF4	NC19	Cretaceous	Aptian-Barremian	Cuttings	3276'-3323.2'
48/28-01	BF5	BF5	NC20	Cretaceous	Hauterivian	Cuttings	4600'-5420'
58/03-01	BF9	BF9	SC1	Cretaceous	Berriasian-Hauterivan	Cuttings	3258'-3910'
56/22-1	AK26	AK26	NC26	Cretaceous	Valanginian-Barremian	Cuttings	3500'-3846'
56/26-2	AK25		FB4	Cretaceous	Valanginian-Barremian	Cuttings	1220'-1380'
56/15-1	AK23	AK23	NC27	Cretaceous	Valanginian	Cuttings	3700'-3800'
50_03_01	S5.2.101	R59-009	NC9	Jurassic	Oxfordian	Cuttings	2420 m
103_01_02	SG24.2.101	R59-052	SG6	Jurassic	Kimmeridgian	Cuttings	6550 m
107_16_1	SG40.2.101	R59-064	SG7	Jurassic	Kimmeridgian	Cuttings	1520 m
103_01_01	SG4.2.101	R59-044	SG8	Jurassic	Oxfordian	Cuttings	7080 m
103_01_01	SG6.2.101	R59-046	SG9	Jurassic	Oxfordian	Cuttings	7300 m
107_16_1	SG45.2.101	R59-066	SG10	Jurassic	Oxfordian	Cuttings	2300 m
103_01_02	SG25.2.101	R59-054	SG11	Jurassic	Oxfordian	Cuttings	9350 m
50_03_02	S24.2.101	R59-017	NC10	Jurassic	Kimmeridgian	Cuttings	4068 m
50_03_02	S262.2.101	R59-019	NC11	Jurassic	Kimmeridgian	Core	4068 m
50_07_01	S47.2.101	R59-029	NC12	Jurassic	Oxfordian	Cuttings	4030 m
50_10_01	S49.2.101	R59-031	NC13	Jurassic	Oxfordian	Cuttings	3260 m

50_10_01	S51.2.101	R59-033	NC14	Jurassic	Oxfordian	Cuttings	3710 m
50_03_02	S53.2.101	R59-041	NC15	Jurassic	Oxfordian	Cuttings	3770 m
50_03_02	S30.2.101	R59-021	NC16	Jurassic	Oxfordian	Cuttings	5750 m
49/15-01	BF10		NC6	Jurassic	Oxfordian	Cuttings	3630'-4100'
49/09-03	BF8		NC7	Jurassic	Kimmeridgian	Cuttings	7854.5'-7876.92'
49/10-01	BF7		NC8	Jurassic	Upper Jurassic	Cuttings	6246'-6282'
50_03_01	S12.2.101	R59-011	NC4	Jurassic	Pleinsbachian	Core	8389 m
42_21_1	S72.2.101	R59-039	SG4	Jurassic	Pleinsbachian	Cuttings	6420 m
50_03_03	S3839.2.101	R59-023	NC5	Jurassic	Sinemurian-Pleinsbachian	Cuttings	1500
63/10-1	AK27		FB1	Jurassic	Sinemurian	Cuttings	2856-2910
107_16_1	SG52.2.101	R59-070	SG5	Jurassic	Bajocian-Callovian	Core	6190
42_21_1	S67.2.101	R59-037	SG12	Jurassic	Bathonian	Cuttings	1290
103_01_01	SG12.2.101	R59-048	SG13	Jurassic	Bathonian	Cuttings	7910
103_01_01	SG17.2.101	R59-050	SG14	Jurassic	Aalenian	Cuttings	10220
107_21_1	SG49.2.101	R59-068	SG15	Jurassic	Aalenian	Cuttings	6100
62/07-1	AK22		GS1	Jurassic	Callovian-Bathonian	Cuttings	10200'-10350'
106_28_1	SG38.2.101	R59-062	SG1	Triassic	Ladinian-anisian	Cuttings	9690
103_01_02	SG33.2.101	R59-058	SG2	Triassic	Skythian	Cuttings	9370
50_10_01	S55b.2.101	R59-035	NC2	Triassic	Ladinian-anisian	Cuttings	8010
103_01_02	SG31.2.101	R59-056	SG3	Triassic	Skythian	Cuttings	8800
50_03_03	S40.2.101	R59-025	NC3	Triassic	Mercia Mudstone	Cuttings	3680
56/26-2	AK24		NC1	Triassic	Ladinian-anisian	Cuttings	3102-3136

Original ID	QEMSCAN ID	Publication ID	Stratigraphy/Age	System	Well	Depth (Ft'/M)	Co
SG35.2.101	R59-060	SG16	Cenomanian	Late Cretaceous	106_28_1	3020 m	
S43.2.101	R59-027	NC22	Cenomanian	Late Cretaceous	50_07_01	1480 m	
BF1		NC17	Albian	Late Cretaceous	49/09-02	2460' - 2496'	
S18.2.101	R59-013	NC23	Purbech	Lower Cretaceous	50_03_02	1540 m	
S2.2.101	R59-007	NC24	Purbeck	Lower Cretaceous	50_03_01	1370 m	
S21.2.101	R59-015	NC25	Purbech	Lower Cretaceous	50_03_02	2410 m	
BF2		NC18	Cretaceous	Lower Cretaceous	48/18-01	850 m - 1160 m	
BF4	BF4	NC19	Aptian - Berremian	Lower Cretaceous	48/24-04	3276' - 3323.2'	
BF5	BF5	NC20	Hauterivian	Lower Cretaceous	48/28-01	4600' - 5420'	
BF9	BF9	SC1	Berriasian - Hauterivan	Lower Cretaceous	58/03-01	3258' - 3910'	
AK26	AK26	NC26	Valanginian- Barremian	Lower Cretaceous	56/22-1	3500' - 3846'	
AK25	AK25	FB4	Valanginian- Barremian		56/26-2		

				Lower Cretaceous		1220' - 1380'	
AK23	AK23	NC27	Valangian	Lower Cretaceous	56/15-1	3700'-3800'	
S5.2.101	R59-009	NC9	Oxfordian	Late Jurassic	50_03_01	2420 m	
SG24.2.101	R59-052	SG6	Kimmeridgian	Late Jurassic	103_01_02	6550 m	
SG40.2.101	R59-064	SG7	Kimmeridgian	Late Jurassic	107_16_1	1520 m	
SG4.2.101	R59-044	SG8	Oxfordian	Late Jurassic	103_01_01	7080 m	
SG6.2.101	R59-046	SG9	Oxfordian	Late Jurassic	103_01_01	7300 m	
SG45.2.101	R59-066	SG10	Oxfordian	Late Jurassic	107_16_1	2300 m	
SG25.2.101	R59-054	SG11	Oxfordian	Late Jurassic	103_01_02	9350 m	
S24.2.101	R59-017	NC10	Kimmeridgian	Late Jurassic	50_03_02	4068 m	
S262.2.101	R59-019	NC11	Kimmeridgian	Late Jurassic	50_03_02	4068 m	
S47.2.101	R59-029	NC12	Oxfordian	Late Jurassic	50_07_01	4030 m	
S49.2.101	R59-031	NC13	Oxfordian	Late Jurassic	50_10_01	3260 m	
S51.2.101	R59-033	NC14	Oxfordian	Late Jurassic	50_10_01	3710 m	
S53.2.101	R59-041	NC15	Oxfordian	Late Jurassic	50_03_02	3770 m	
S30.2.101	R59-021	NC16	Oxfordian	Late Jurassic	50_03_02	5750 m	
BF10		NC6	Oxfordian	Late Jurassic	49/15-01	3630' - 4100'	
BF8		NC7	Kimmeridgian	Late Jurassic	49/09-03	7854.5' - 7876.92'	
BF7		NC8	Upper Jurassic	Late Jurassic	49/10-01	6246' - 6282'	
S12.2.101	R59-011	NC4	Pleinsbachian	Lower Jurassic	50_03_01	8389 m	
S72.2.101	R59-039	SG4	Pleinsbachian	Lower Jurassic	42_21_1	6420 m	
S3839.2.101	R59-023	NC5	Sinemurian-Pleinsbachian	Lower Jurassic	50_03_03	1500	
AK27		FB1	Sinemurian	Lower Jurassic	63/10-1	2856-2910	
SG52.2.101	R59-070	SG5	Bajocian-Callovian	Middle Jurassic	107_16_1	6190	
S67.2.101	R59-037	SG12	Bathonian	Middle Jurassic	42_21_1	1290	
SG12.2.101	R59-048	SG13	Bathonian	Middle Jurassic	103_01_01	7910	
SG17.2.101	R59-050	SG14	Aalenian	Middle Jurassic	103_01_01	10220	
SG49.2.101	R59-068	SG15	Aalenian	Middle Jurassic	107_21_1	6100	
AK22		GS1	Callovian-Bathonian	Middle Jurassic	62/07-1	10200'-10350'	
SG38.2.101	R59-062	SG1	Ladinian-anisian	Lower Triassic	106_28_1	9690	
SG33.2.101	R59-058	SG2	Skythian	Lower Triassic	103_01_02	9370	
S55b.2.101	R59-035	NC2	Ladinian-anisian	Lower Triassic	50_10_01	8010	
SG31.2.101	R59-056	SG3	Skythian	Lower Triassic	103_01_02	8800	
S40.2.101	R59-025	NC3	Mercia Mudstone	Lower Triassic	50_03_03	3680	
AK24		NC1	Ladinian-anisian	Lower Triassic	56/26-2	3102-3136	

Appendix D

This USB contains the data sets which were too large to be included in the body of this thesis. For sample details see samples list provided in Appendixes C. U-Pb Zircon and apatite geochronology data is reported in the format required for publication in the Journal of the

Geological Society, London all values are reported to within two decimal places of analytical uncertainty (See Table 2., Table 3. and Table 4.). Ar-Ar data is also reported to within this uncertainty (See Table 5.). In addition, there is an image folder for each manuscript where additional, Raman maps and QEMSCAN maps which were not included in the body of the thesis are provided (see folder entitled “additional images”). Note that samples/data used from Fairey (2017), have CL images which are not included in this appendix. Heavy mineral data is reported in Table 6. Raman mapping data for detrital zircon grains and fossilized anuran skin are found in Table 7 and Table 8, respectively. Table 9 contains the raw Raman spectra for Chapter 5. Raman maps of zircon grains from 9 samples was collected but is not included in this appendix as the file sizes are extremely large and the images are often poor but can be provided upon request.